

The Pennsylvania State University  
The Graduate School  
College of Earth and Mineral Sciences

**MECHANISMS OF SINTERING AND SECOND PHASE  
FORMATION IN BAYER ALUMINA**

A Dissertation in  
Materials Science and Engineering  
by  
Tobias Frueh

© 2017 Tobias Frueh

Submitted in Partial Fulfillment  
of the Requirements  
for the Degree of

Doctor of Philosophy

December 2017

The dissertation of Tobias Frueh was reviewed and approved\* by the following:

Gary L. Messing  
Distinguished Professor of Ceramic Science and Engineering  
Dissertation Advisor, Chair of Committee

James H. Adair  
Professor of Materials Science and Engineering, Biomedical Engineering and  
Pharmacology

John R. Hellmann  
Professor of Materials Science and Engineering  
Associate Dean for Graduate Education and Research

Douglas E. Wolfe  
Professor of Materials Science and Engineering  
Department Head, Advanced Coatings at the Applied Research Laboratory  
Senior Scientist

Charles E. Compson  
Global Technical Director, CPO  
Almatis, Inc.  
Special Member

Suzanne E. Mohney  
Professor of Materials Science and Engineering and Electrical Engineering  
Chair, Intercollege Graduate Degree Program in Materials Science and  
Engineering

\*Signatures are on file in the Graduate School.

# Abstract

The vast majority of industrial  $\text{Al}_2\text{O}_3$  applications use powders derived from Bayer feedstocks with purity levels of 99.0 - 99.9%. This dissertation explores how the extrinsic powder chemistry of Bayer alumina influences densification, microstructure evolution, and fundamental sintering mechanisms.

To determine how grain-boundary composition affects the sintering of MgO-free Bayer  $\text{Al}_2\text{O}_3$ , dilatometry and sintering kinetics experiments of samples with  $\text{Na}_2\text{O}$  and  $\text{SiO}_2$  concentrations up to 1029 ppm and 603 ppm, respectively, were performed. It was shown that  $\text{Na}_2\text{O}$  and  $\text{SiO}_2$  form a nanometer thick siliceous grain boundary film. The estimated viscosities (20 - 400 Pa·s) indicate that diffusion greatly depends on the composition of the liquid grain-boundary phase, and densification strongly depends on the  $\text{Na}_2\text{O}/\text{SiO}_2$  ratio in the samples. For low  $\text{Na}_2\text{O}/\text{SiO}_2$  ratios, densification of Bayer  $\text{Al}_2\text{O}_3$  at 1525°C is controlled by diffusion of  $\text{Al}^{3+}$  through the grain-boundary liquid, whereas for high  $\text{Na}_2\text{O}/\text{SiO}_2$  ratios, densification can be governed by either the interface reaction of  $\text{Al}_2\text{O}_3$  or diffusion of  $\text{Al}^{3+}$ . Increasing  $\text{Na}_2\text{O}$  in  $\text{SiO}_2$ -doped samples increases diffusion of  $\text{Al}^{3+}$  and  $\text{Al}_2\text{O}_3$  solubility in the liquid, and thus densification increases by 1-2.5%. Based on these findings, it is concluded that Bayer  $\text{Al}_2\text{O}_3$  densification is controlled by the  $\text{Na}_2\text{O}$  to  $\text{SiO}_2$  ratio.

The stages at which MgO influences densification of  $\text{Al}_2\text{O}_3$  were identified by comparing dilatometry measurements and sintering kinetics of MgO-free and 380 ppm MgO-doped Bayer  $\text{Al}_2\text{O}_3$  powder. Using high-resolution TEM it was shown that MgO reduces the grain boundary thickness during final stage sintering. It was shown by EDS that MgO increases the solubility of  $\text{SiO}_2$  in  $\text{Al}_2\text{O}_3$  grains near the boundaries. First-principles DFT calculations demonstrated that the co-dissolution of MgO and  $\text{SiO}_2$  in  $\text{Al}_2\text{O}_3$  is thermodynamically favored over the dissolution of MgO or  $\text{SiO}_2$  individually in  $\text{Al}_2\text{O}_3$ . For the first time, it was experimentally demonstrated that removal of  $\text{SiO}_2$  from the grain boundary during final stage sintering is a key process by which MgO enhances the sintering of  $\text{Al}_2\text{O}_3$ .

A physical model that describes the dynamic development of grain boundary chemistry and thickness from initial to final stage sintering as a function of chemical and physical powder parameters was developed. The liquid glass phase initially accumulates in the particle contacts due to capillarity and during densification the glass phase distribution changes due to the formation of grain boundaries and grain growth, leading to a dynamic change in grain boundary thickness during densification. Grain boundary thicknesses measured from high-resolution TEM images agree well with predicted film thicknesses. The model shows that the grain boundary thickness is determined by either the concentration of the glass phase in the sample or by an equilibrium film thickness, which is controlled by a balance between attractive and repulsive interparticle forces. Variations in powder chemistry, such as changing the  $\text{Na}_2\text{O}/\text{SiO}_2$  ratio or changing the  $\text{MgO}$  concentration, can affect the grain boundary thickness by influencing the interparticle force balance or by changing the amount of glass phase in the grain boundaries.

The formation of  $\beta\text{-Al}_2\text{O}_3$  ( $\text{Na}_2\text{O}\cdot11\text{Al}_2\text{O}_3$ ) is sometimes observed during sintering of Bayer  $\text{Al}_2\text{O}_3$ , and the conditions and mechanisms of formation were investigated. Formation kinetics showed that the majority of  $\beta\text{-Al}_2\text{O}_3$  grains form between 0 and 1 hour at  $1525^\circ\text{C}$ , at densities  $>90\%$ . The amount of  $\beta\text{-Al}_2\text{O}_3$  increases with increasing  $\text{Na}_2\text{O}$  and  $\text{MgO}$  concentrations, and decreases with increasing  $\text{SiO}_2$  concentration.  $\text{SiO}_2$  increases the solubility of  $\text{Na}_2\text{O}$  in the grain boundaries by forming a glassy film, and thereby counteracts the formation of  $\beta\text{-Al}_2\text{O}_3$ . At final sintering stage  $\text{SiO}_2$  is removed from the grain boundaries because  $\text{SiO}_2$  and  $\text{MgO}$  form a solid solution in  $\alpha\text{-Al}_2\text{O}_3$ , which leads to the supersaturation of grain boundaries and the nucleation and growth of  $\beta\text{-Al}_2\text{O}_3$ .

The Master Sintering Curve (MSC) approach and the factors affecting its accuracy were explored for analyzing the complete sintering profile of Bayer  $\text{Al}_2\text{O}_3$ . MSC analysis is sensitive to shrinkage anisotropy, which can be accounted for by directional shrinkage measurements, and to powder chemistry and forming technique effects that result in mechanistic changes that cannot be sufficiently described by MSC analysis. It is concluded that  $Q$  should not be interpreted as the sintering activation energy, or used to interpret mechanistic differences between powders since  $Q$  includes several mechanisms that influence densification throughout the sintering cycle. Despite these limitations, the MSC approach is a useful and practical tool for predicting the effects of thermal load (i.e. time and temperature) on densification of a specific powder and forming process.

# Table of Contents

<b>List of Figures</b>	<b>viii</b>
<b>List of Tables</b>	<b>xiv</b>
<b>Acknowledgments</b>	<b>xv</b>
<b>Chapter 1</b>	
<b>Introduction</b>	<b>1</b>
1.1 Motivation . . . . .	1
1.2 Sintering of Ceramics . . . . .	2
1.3 Effects of Impurities and Dopants on the Sintering of $\text{Al}_2\text{O}_3$ . . . . .	4
1.3.1 MgO in Ultrahigh Purity $\text{Al}_2\text{O}_3$ . . . . .	4
1.3.2 Effects of Impurities during sintering of $\text{Al}_2\text{O}_3$ . . . . .	5
1.3.3 Effects of MgO on Liquid Phase Sintering of $\text{Al}_2\text{O}_3$ . . . . .	6
1.3.4 Grain Boundaries During Sintering of $\text{Al}_2\text{O}_3$ . . . . .	7
1.4 Sintering of Bayer Alumina . . . . .	10
1.4.1 The Bayer Process . . . . .	10
1.4.2 Influence of $\text{Na}_2\text{O}$ and $\text{SiO}_2$ on the Sintering Behavior of $\text{Al}_2\text{O}_3$	11
<b>Chapter 2</b>	
<b>The Effects of <math>\text{Na}_2\text{O}</math> and <math>\text{SiO}_2</math> on Liquid Phase Sintering of     Bayer <math>\text{Al}_2\text{O}_3</math></b>	<b>17</b>
2.1 Introduction . . . . .	17
2.2 Experimental . . . . .	18
2.3 Results . . . . .	19
2.3.1 Effects of $\text{Na}_2\text{O}$ -doping . . . . .	19
2.3.2 Effects of $\text{Na}_2\text{O}/\text{SiO}_2$ co-doping . . . . .	20
2.4 Discussion . . . . .	21
2.5 Summary . . . . .	26

<b>Chapter 3</b>	
<b>Powder Chemistry Effects on the Sintering Behavior of MgO-doped Bayer Alumina</b>	<b>39</b>
3.1 Introduction . . . . .	39
3.2 Experimental . . . . .	41
3.3 Computational Methodology . . . . .	42
3.4 Sintering and Microstructure Analysis . . . . .	44
3.5 Mechanistic Interpretation . . . . .	47
3.6 Summary and Conclusion . . . . .	53
<b>Chapter 4</b>	
<b>Dynamic development of nanometer scale grain boundaries during liquid phase sintering</b>	<b>69</b>
4.1 Introduction . . . . .	69
4.2 Experiment . . . . .	71
4.3 Grain boundary thickness in MgO-free alumina . . . . .	72
4.4 The equilibrium film thickness model . . . . .	74
4.5 Calculation of the theoretical Equilibrium Film Thicknesses . . . . .	75
4.6 High-resolution TEM . . . . .	79
4.7 The effect of changes in powder chemistry . . . . .	80
4.7.1 Na <sub>2</sub> O/SiO <sub>2</sub> ratio . . . . .	80
4.7.2 MgO-doped Bayer alumina . . . . .	81
4.8 Conclusion . . . . .	81
<b>Chapter 5</b>	
<b>Second phase formation in Bayer alumina</b>	<b>95</b>
5.1 Introduction . . . . .	95
5.2 Experimental . . . . .	96
5.3 Results . . . . .	97
5.4 Interpretation and mechanisms of $\beta$ -Al <sub>2</sub> O <sub>3</sub> formation . . . . .	99
5.5 Summary . . . . .	102
<b>Chapter 6</b>	
<b>A Critique of the Master Sintering Curve Analysis of Sintering Processes</b>	<b>116</b>
6.1 Introduction . . . . .	116
6.2 Experimental Procedure . . . . .	119
6.3 Results and Discussion . . . . .	121
6.3.1 The effect of forming on $Q$ . . . . .	121
6.3.2 MSC at high densities . . . . .	123

6.3.3	Quantification of the MSC shape . . . . .	124
6.3.4	Influence of powder chemistry . . . . .	125
6.3.5	Limitations of the MSC analysis . . . . .	125
6.3.6	Practical use of the MSC analysis . . . . .	127
6.4	Summary . . . . .	128
<b>Chapter 7</b>		
<b>Summary and Future Work</b>		<b>141</b>
7.1	Summary . . . . .	141
7.1.1	The Effects of Na <sub>2</sub> O and SiO <sub>2</sub> on Liquid Phase Sintering of Bayer Al <sub>2</sub> O <sub>3</sub> . . . . .	141
7.1.2	Powder Chemistry Effects on the Sintering of MgO-doped Specialty Al <sub>2</sub> O <sub>3</sub> . . . . .	142
7.1.3	Dynamic development of nanometer scale grain boundaries during liquid phase sintering . . . . .	143
7.1.4	Second phase formation in Bayer alumina . . . . .	144
7.1.5	A Critique of Master Sintering Curve Analysis of Sintering Processes . . . . .	145
7.2	Future work . . . . .	145
<b>Bibliography</b>		<b>148</b>

# List of Figures

1.1 Segregation and precipitation map of MgO-doped alumina based on the results in the literature [1] . . . . .	14
1.2 SIMS maps of Al <sub>2</sub> O <sub>3</sub> doped with 500 ppm MgO (a) and 1000 ppm SiO <sub>2</sub> (b). Samples were sintered for 8 h at 1650°C [2]. . . . .	15
1.3 SIMS maps of Al <sub>2</sub> O <sub>3</sub> co-doped with 500 ppm MgO and 1000 ppm SiO <sub>2</sub> and sintered at 1650°C for 8h. (a) shows the distribution of SiO <sub>2</sub> , (b) the distribution of MgO in the same samples [2]. . . . .	16
2.1 SEM image of as-received chemically purified Bayer Al <sub>2</sub> O <sub>3</sub> powder used in this study. . . . .	30
2.2 Dilatometer curves of as-received and singly Na <sub>2</sub> O-doped samples heated at 10°C/min to 1525°C. . . . .	31
2.3 Densification kinetics of Bayer Al <sub>2</sub> O <sub>3</sub> doped with different Na <sub>2</sub> O concentrations and sintered at 1525°C. . . . .	32
2.4 Microstructures of as-received and singly 529 ppm Na <sub>2</sub> O doped samples after 30 min, 3 h and 8 h at 1525°C. . . . .	33
2.5 Dilatometer curves of as-received, singly SiO <sub>2</sub> -doped, and Na <sub>2</sub> O/SiO <sub>2</sub> co-doped Bayer Al <sub>2</sub> O <sub>3</sub> heated at 10°C/min to 1525°C. . . . .	34
2.6 Densification kinetics of Bayer Al <sub>2</sub> O <sub>3</sub> doped with different concentrations of Na <sub>2</sub> O and SiO <sub>2</sub> at 1525°C. . . . .	35
2.7 Microstructures of Bayer Al <sub>2</sub> O <sub>3</sub> doped with a) 603 ppm SiO <sub>2</sub> and b) 529 ppm Na <sub>2</sub> O and 603 ppm SiO <sub>2</sub> after heating at 1525°C for 8h. . . . .	36
2.8 Micrographs of a sample doped with 1029 ppm Na <sub>2</sub> O after sintering at 1525°C for 3 h. The micrographs were recorded using a) a secondary electron detector and b) a backscattered electron detector. The arrows point at the platelet shaped $\beta$ -alumina grains that form in samples doped with Na <sub>2</sub> O. The samples were not thermally etched. . . . .	37

2.9	Liquidus projection of the $\text{Al}_2\text{O}_3$ - $\text{SiO}_2$ - $\text{Na}_2\text{O}$ ternary phase diagram. The red solid lines are isoplethal cuts representing the samples investigated in this study. The red dashed line is the 1525°C isotherm where $\alpha$ - $\text{Al}_2\text{O}_3$ and liquid are in equilibrium. The blue dash-dot line and green dotted line are eutectic lines at which $\alpha$ - $\text{Al}_2\text{O}_3$ and liquid is in equilibrium with $\beta$ - $\text{Al}_2\text{O}_3$ or mullite, respectively. . . . .	38
3.1	SEM image of 380 ppm MgO-doped Bayer alumina powder used in this work. . . . .	57
3.2	Dilatometer curves of a) 380 ppm MgO-doped and b) MgO-free [3] Bayer alumina samples with different $\text{Na}_2\text{O}/\text{SiO}_2$ levels heated at 10°C/min to 1525°C. . . . .	58
3.3	Densification kinetics of Bayer processed alumina containing different amounts $\text{Na}_2\text{O}$ and $\text{SiO}_2$ and a) 380 ppm MgO sintered at 1450°C, b) 380 ppm MgO sintered at 1525°C, and c) 2 ppm MgO sintered at 1525°C [3]. . . . .	59
3.4	Microstructures of 380 ppm MgO-doped Bayer alumina samples with different $\text{Na}_2\text{O}$ and $\text{SiO}_2$ concentrations sintered at 1525°C for 8 h. . . . .	60
3.5	Sintering trajectories (grain size vs. relative density) for 380 ppm MgO-doped Bayer alumina samples with different $\text{Na}_2\text{O}$ and $\text{SiO}_2$ concentrations. . . . .	61
3.6	Grain boundary of a sample containing 529 ppm $\text{Na}_2\text{O}$ , 603 ppm $\text{SiO}_2$ , and 2 ppm MgO after 3 h at 1525°C. . . . .	62
3.7	Grain boundaries of samples containing 560 ppm $\text{Na}_2\text{O}$ , 582 ppm $\text{SiO}_2$ , and 380 ppm MgO after a) 0 h and b) 3 h at 1525°C. . . . .	63
3.8	EDS of grain boundaries of samples containing 560 ppm $\text{Na}_2\text{O}$ , 582 ppm $\text{SiO}_2$ , and 380 ppm MgO after a) 0 h and b) 3 h at 1525°C showing the Si distribution. After 0 h Si shows a stronger segregation to the grain boundaries than after 3 h. . . . .	64
3.9	EDS line scan across a grain boundary of a sample containing 560 ppm $\text{Na}_2\text{O}$ , 582 ppm $\text{SiO}_2$ , and 380 ppm MgO after sintering at 1525°C for a) 0 h and b) 3 h. . . . .	65
3.10	Comparison of the formation energy of $\alpha$ - $\text{Al}_2\text{O}_3$ with an Mg-cluster ( $E_{Form}^{Mg}$ ), Si-cluster ( $E_{Form}^{Si}$ ) and Mg+Si-cluster ( $E_{Form}^{Mg+Si}$ ) as a function of temperature. The formation energy difference ( $\Delta E_{Form}$ ) between the structures was calculated from Eq. 3.9 to compare the formation energy values and show that it is energetically favorable to form Mg+Si-clusters over Si-clusters and Mg-clusters. . . . .	66

3.11 EDS maps of different oxides in 380 ppm MgO-doped Bayer alumina samples after sintering at 1525°C for a-d) 0 h and e-h) 3 h. a) and e) show the distribution of Mg, b) and f) show the distribution of Fe, c) and g) show the distribution of Na, and d) and h) show the distribution of Ca. . . . .	67
3.12 Na <sub>2</sub> O concentration (ICP measurements) of 380 ppm MgO-doped Bayer alumina samples with 560 ppm Na <sub>2</sub> O as a) function of sintering temperature and b) as a function of sintering time at 1525°C. . . . .	68
4.1 Increase in concentration of liquid phase as a function of temperature for MgO-free powder samples with 529 ppm Na <sub>2</sub> O and different SiO <sub>2</sub> concentrations. . . . .	83
4.2 Relative density as a function of temperature and hold time determined from dilatometry for MgO-free powder samples with 529 ppm Na <sub>2</sub> O and different SiO <sub>2</sub> concentrations. . . . .	84
4.3 Liquid phase concentration as a function of relative density for MgO-free powder samples with 529 ppm Na <sub>2</sub> O and different SiO <sub>2</sub> concentrations. . . . .	85
4.4 Grain size - density trajectories as a function of Na <sub>2</sub> O and SiO <sub>2</sub> concentration for MgO-free alumina. . . . .	86
4.5 Change in Na/Al ion ratio in the liquid phase during sintering of samples with Na <sub>2</sub> O/SiO <sub>2</sub> ratios > 0.5. . . . .	87
4.6 Development of the electrostatic potential as a function of relative density. For MgO-free powder samples with 529 ppm Na <sub>2</sub> O and different SiO <sub>2</sub> concentrations. . . . .	88
4.7 Contributions to the equilibrium film thickness as a function of film thickness for MgO-free powder samples with 529/603 ppm Na <sub>2</sub> O/SiO <sub>2</sub> at a relative density of 93%. . . . .	89
4.8 Calculated equilibrium film thickness for MgO-free powder samples at different chemistries as a function of relative density. . . . .	90
4.9 Calculated grain boundary thicknesses as a function of relative density for MgO-free powder samples. The trajectories labeled with 529/603 ppm Na <sub>2</sub> O/SiO <sub>2</sub> , 529/203 ppm Na <sub>2</sub> O/SiO <sub>2</sub> , and 529 ppm Na <sub>2</sub> O/SiO <sub>2</sub> were calculated based on the liquid phase concentration and sintering stage. The equilibrium film thickness was calculated based on Clarke's model. The calculated grain boundary thicknesses are compared to measured grain boundary thicknesses (data points a: 1000/1000 ppm Na <sub>2</sub> O/SiO <sub>2</sub> , b) 529/603 ppm Na <sub>2</sub> O/SiO <sub>2</sub> , c) 529/203 ppm Na <sub>2</sub> O/SiO <sub>2</sub> after heating at 1525°C for 3 h). . . . .	91

4.10	TEM images of MgO-free powder samples with a) 529/203 ppm Na <sub>2</sub> /SiO <sub>2</sub> , b) 529/603 ppm Na <sub>2</sub> /SiO <sub>2</sub> , c) 1000/1000 ppm Na <sub>2</sub> /SiO <sub>2</sub> , and d) 29/103 ppm Na <sub>2</sub> /SiO <sub>2</sub> after sintering at 1525°C for 3 h . . . . .	92
4.11	TEM image of a MgO-free powder sample with 29/603 ppm Na <sub>2</sub> O/SiO <sub>2</sub> . . . . .	93
4.12	TEM images of MgO-doped (380 ppm) powder samples with a) 60/82 ppm Na <sub>2</sub> O/SiO <sub>2</sub> , b) 60/582 ppm Na <sub>2</sub> O/SiO <sub>2</sub> , and c) 560/582 ppm Na <sub>2</sub> O/SiO <sub>2</sub> . After heating at 1525°C for 3 h. . . . .	94
5.1	Micrographs of MgO-doped Bayer doped with 560 ppm Na <sub>2</sub> O and 82 ppm SiO <sub>2</sub> after 3 h at 1525°C obtained using a) a secondary electron detector and b) a backscattered electron detector. . . . .	105
5.2	a) XRD pattern and b) zoomed-in XRD pattern of a sample with 1060 ppm Na <sub>2</sub> O, 82 ppm SiO <sub>2</sub> , and 380 ppm MgO after sintering at 1525°C for 5 h. All observed peaks except for one (*) can be assigned to either $\alpha$ -Al <sub>2</sub> O <sub>3</sub> or $\beta$ -Al <sub>2</sub> O <sub>3</sub> . . . . .	106
5.3	Micrographs showing $\beta$ -Al <sub>2</sub> O <sub>3</sub> grains (red circles) in MgO-doped Bayer alumina samples with 82 ppm SiO <sub>2</sub> and 560 ppm Na <sub>2</sub> O after sintering at 1525°C for a) 0 h, b) 1 h, and c) 8 h. . . . .	107
5.4	Kinetics of $\beta$ -Al <sub>2</sub> O <sub>3</sub> formation for different powder chemistries of MgO-doped powder samples. . . . .	108
5.5	Micrographs showing $\beta$ -Al <sub>2</sub> O <sub>3</sub> grains (red circles) in MgO-doped Bayer alumina samples with 82 ppm SiO <sub>2</sub> and a) 185 ppm Na <sub>2</sub> O, b) 560 ppm Na <sub>2</sub> O, and c) 1060 ppm Na <sub>2</sub> O after sintering at 1525°C for 3 h. . . . .	109
5.6	Formation of $\beta$ -Al <sub>2</sub> O <sub>3</sub> a function of Na <sub>2</sub> O concentration in MgO-doped Bayer alumina. . . . .	110
5.7	Formation of $\beta$ -Al <sub>2</sub> O <sub>3</sub> in MgO-doped powder samples a function of a) SiO <sub>2</sub> concentration for different Na <sub>2</sub> O concentrations, and b) Na <sub>2</sub> O/SiO <sub>2</sub> ratio. In b) the black diamonds are samples with 82 ppm SiO <sub>2</sub> and the blue squares are samples with 182 and 582 ppm SiO <sub>2</sub> . . . . .	111
5.8	Micrographs showing $\beta$ -Al <sub>2</sub> O <sub>3</sub> grains (red circles) in MgO-doped Bayer alumina samples with a) 185/182 ppm Na <sub>2</sub> O/SiO <sub>2</sub> and b) 560/182 ppm Na <sub>2</sub> O/SiO <sub>2</sub> after sintering at 1525°C for 3 h. . . . .	112
5.9	Formation of $\beta$ -Al <sub>2</sub> O <sub>3</sub> in MgO-free powder samples as a function of a) MgO concentration (29 ppm Na <sub>2</sub> O) and b) Na <sub>2</sub> O concentration (2 ppm MgO) after 3 h at 1525°C. . . . .	113

5.10	Micrographs showing $\beta$ -Al <sub>2</sub> O <sub>3</sub> grains (red circles) in Bayer alumina samples with a) 1002 ppm MgO, 1000 ppm SiO <sub>2</sub> , 29 ppm Na <sub>2</sub> O, b) 2 ppm MgO, 1000 ppm SiO <sub>2</sub> , 1029 ppm Na <sub>2</sub> O, c) 1002 ppm MgO, 1000 ppm SiO <sub>2</sub> , 1029 ppm Na <sub>2</sub> O after 3 h at 1525°C. . . . .	114
5.11	Micrograph showing $\beta$ -Al <sub>2</sub> O <sub>3</sub> grains (red circles) in an ultra high purity powder sample with 502 ppm Na <sub>2</sub> O, 2 ppm MgO, and 11 ppm SiO <sub>2</sub> after sintering at 1525°C for 3 h. . . . .	115
6.1	Dilatometry curves of non-aqueous slip cast CT3000 LS SG samples heated at a) 5°C/min, b) 10°C/min, and c) 20°C/min to 1525°C measured parallel to (z-direction) and perpendicular to (x/y-direction) the capillary force acting during slip casting. . . . .	130
6.2	Development of the shrinkage anisotropy factor for shrinkage, $k$ , during densification of non-aqueous slip cast samples as a function of relative density for CT3000 LS SG samples heated at different rates. . . . .	131
6.3	Development of the relative density corrected for shrinkage anisotropy as a function of temperature for non-aqueous slip cast CT3000 LS SG samples heated at different rates. . . . .	132
6.4	Mean residuals of the MSCs assuming different values for $Q$ for non-aqueous slip cast CT3000 LS SG samples. . . . .	133
6.5	MSCs of CT3000 LS SG samples prepared by non-aqueous slip casting using a) the $Q$ -value obtained by accounting for shrinkage anisotropy ( $Q=550$ kJ/mol) and b) using $Q$ -value when shrinkage anisotropy was uncorrected for ( $Q = 625$ kJ/mol). . . . .	134
6.6	MSCs and $Q$ -values of CT3000LS-SG samples obtained from the minimum mean residuals for samples prepared by different forming techniques and accounting for shrinkage anisotropy. . . . .	135
6.7	a) Densification of dry pressed CT3000 LS SG samples at different heating rates, b) mean residuals as a function of $Q$ , and c) MSC for $Q = 700$ kJ/mol obtained from the minimum mean residuals, showing divergence at densities >90%. . . . .	136
6.8	$Q$ -values for dry pressed CT3000 LS SG samples as a function of relative density obtained from iso-density analysis. . . . .	137
6.9	Development of the microstructural parameters, summarized in the $C$ parameter, as a function of relative density for dry pressed CT3000 LS SG samples. . . . .	138
6.10	MSCs and $Q$ -values for CT3000 LS SG samples prepared by non-aqueous slip casting with different Na <sub>2</sub> O concentrations. . . . .	139

6.11 Equivalent time/temperature diagram for CT3000 LS SG samples prepared by non-aqueous slip casting heated at 10°C/min. The contours may be used to predict heat treatments requirements to achieve a desired density. . . . .	140
---	-----

# List of Tables

2.1	Physical and chemical characteristics of the as-received Bayer Al <sub>2</sub> O <sub>3</sub> powder used in this study. . . . .	28
2.2	Calculated compositions and amounts of liquid in as-received, singly doped and co-doped samples at 1525°C ( $\alpha = \alpha\text{-Al}_2\text{O}_3$ , $\beta = \beta\text{-Al}_2\text{O}_3$ , L = liquid, M = mullite). . . . .	29
3.1	Physical and chemical characteristics of the as-received 380 ppm MgO-doped Bayer alumina powder used in this study. . . . .	54
3.2	Calculated compositions and amounts of liquid in 380 ppm MgO-doped Bayer alumina samples of different chemistries at 1450°C and 1525°C. . . . .	55
3.3	Lattice parameters and equilibrium energy ( $E_0$ ) compared to previous first-principles and experimental values. . . . .	56
5.1	Physical and chemical characteristics of the alumina powder used in this study. . . . .	103
5.2	Estimated amount of $\beta\text{-Al}_2\text{O}_3$ in MgO-doped Bayer alumina samples after 3 h at 1525°C. . . . .	104
6.1	$Q$ values obtained by MSC analysis for different alumina powders. .	129

# Acknowledgments

The completion of graduate school and this dissertation could not have been possible without the support from many people that I would like to thank now. First, I would like to thank Prof. Gary Messing for guiding this research and helping me develop as a scientist. I learned a lot from Prof. Messing and I will always be indebted to him for his time, patience, and experience. I would like to thank my dissertation committee, Prof. James Adair, Prof. Douglas Wolfe, Prof. John Hellmann and Dr. Charles Compson for their time, constructive criticism and advice. I would like to thank Dr. Charles Compson and Dr. Joe Atria from Almatis, Inc. for funding this research and for many discussions that contributed substantially to the quality of this research. The staff of the Materials Characterization Laboratory was always supportive and helpful and I enjoyed working with them. Specifically, I would like to thank Joshua Maier and Haiying Wang for preparing my samples for TEM, and Dr. Jennifer Gray for spending many hours at the TEM with me. I would like to thank the past and present members of the Messing Research Group, (Dr. Elizabeth Kupp, Jesse Matson, Alexandra Wadja, Elisabeth Roch, Ryan Sommerhuber, Dr. Nuerxida Pulati, Marie Arnoult, Yi Yuan, Dr. Yunfei Chang, Beecher Watson, Rebecca Walton, Michael Brova, Anna Hofer, Kuo-Hao Lee, Jie Wu, Howard Payne, Dr. Raul Bermejo) for a great time in the lab and in the office, and many great discussions. It was an honor to get to work with so many great people. I want to thank the staff, faculty, and students of the Penn State Materials Science and Engineering Department for always being helpful and for creating a positive and great work environment. I want to thank all the friends I made at Penn State over the past few years, within and outside the Department of Materials Science (Christopher Rotella, Lyndsey Denis, Daniel Schuman, Tim Lichtenstein, Ethan Kahn, Nathan Smith, Tim Pillsbury, and many more). I am proud that I can call them my friends. I would like to thank my significant other, Cassie Marker for her support. She also contributed significantly to this dissertation by performing the first-principles DFT calculations, which I could not have done without her. Finally, I want to thank my family. My parents, grandparents, uncle, and brother always

supported and encouraged me, even when I decided to move half way across the globe for grad school. I am very grateful for their constant support.

# Chapter 1

## Introduction

### 1.1 Motivation

With an estimated total market of 2.8 million tons per year, specialty aluminas for non-metallurgical applications are arguably the most extensively used material in the field of ceramics. They are used in large volume applications such as high temperature refractories, technical ceramics, high voltage insulators, and functional fillers. The majority of  $\text{Al}_2\text{O}_3$  applications use synthetic or specialty aluminas derived from Bayer feedstocks (Bayer aluminas), such as aluminum trihydrate ( $\text{Al}(\text{OH})_3$ ), smelter grade  $\text{Al}_2\text{O}_3$  and others. Bayer aluminas are typically 99.0 - 99.9% pure and contain  $\text{Na}_2\text{O}$ ,  $\text{CaO}$ ,  $\text{Fe}_2\text{O}_3$ , and  $\text{SiO}_2$  impurities that originate from the bauxite ore and/or Bayer process reagents (e.g.,  $\text{NaOH}$ ). The vast majority of research on the sintering of  $\text{Al}_2\text{O}_3$ , however, focuses on ultrahigh purity ( $\geq 99.99\%$ ) aluminas derived from specialty feedstocks, such as ammonium alum ( $(\text{NH}_4\text{Al}(\text{SO}_4)_2 \cdot 12\text{H}_2\text{O})$ ), boehmite ( $\gamma\text{-AlOOH}$ ) and aluminum chloride ( $\text{AlCl}_3$ ). Due to the higher cost involved in producing the high purity chemicals and to maintain the purity during subsequent processes to obtain ultrahigh-purity aluminas, these powders are typically one to two orders of magnitude more expensive than Bayer aluminas. Therefore, for many industrial applications aluminas derived from the Bayer process constitute an overwhelming majority of the global market share of over 90%.

While ultrahigh purity aluminas provide the purest platform from which to conduct fundamental sintering research, that research does not usually explore the types and amounts of impurities typical of Bayer aluminas. Commercial Bayer

$\text{Al}_2\text{O}_3$  powders exist in a range of reactive grades that differ in the amount and types of these impurities, and additionally to impurities the manufacturer commonly adds  $\text{MgO}$  to commercial alumina powders since it is known for its beneficial effect during sintering. A fundamental understanding of the mechanisms of densification, grain growth and second phase formation is key for predicting and tailoring the sintering behavior and microstructure evolution of Bayer alumina powders based on their chemistry, and will provide valuable information to industrial users.

The purpose of this dissertation is to develop a fundamental, in-depth understanding about how the chemistry of commercial Bayer alumina powder affects sintering mechanisms, densification, grain growth, and the formation of second phases. Specifically, this dissertation will focus on investigating the effects and cross effects of  $\text{MgO}$ ,  $\text{Na}_2\text{O}$  and  $\text{SiO}_2$  on densification and microstructure evolution of Bayer aluminas, and provide insight into the fundamental mechanisms that are responsible for changes in sintering behavior. Furthermore, a model is developed to describe the dynamic development of grain boundaries during densification as a function of powder chemistry. It is crucial to understand the structure and chemistry of grain boundaries during sintering, as grain boundary diffusion is the dominant mechanism for mass transport. The methodology developed to analyze densification, microstructure evolution, sintering mechanisms, and grain boundaries during densification will serve as an example for investigating and tailoring the mechanisms of sintering in ceramic powders as a function of powder chemistry. Finally, the Master Sintering Curve approach is evaluated as a tool to identify powder chemistry effects on the sintering of Bayer alumina in a fundamental, predictive way.

## 1.2 Sintering of Ceramics

Sintering is the heat treatment of a particle mass, or high surface area powder, that results in a strength increase, reduction in surface area and, usually, densification. Sintering is used to fabricate bulk ceramic components and powder metallurgical parts [4], and can be divided into two main types; solid state sintering and liquid phase sintering. The difference between these two types of sintering is the absence or presence of a liquid phase, respectively, which results in fundamental differences in sintering mechanisms.

The sintering process can be divided into three stages; initial, intermediate, and final stage sintering [4]. Initial stage sintering accounts for the first few percent of densification, during which particles rearrange as a result of capillarity and contacts between particles form. The majority of densification occurs from  $\sim$ 65 to  $\sim$ 92% relative density occurs and is termed intermediate stage sintering. During this stage the microstructure is characterized by pore channels along the grain edges. Little to no grain growth occurs during intermediate stage sintering since the presence of pore channels limits the mobility of grain boundaries. Intermediate stage solid state sintering is governed by densifying mechanisms, such as grain boundary and volume diffusion. In the presence of a liquid phase, grain boundary diffusion occurs by a solution-precipitation mechanism, where material from the particle - grain boundary interface dissolves into the liquid grain boundary phase, diffuses through the liquid grain boundary phase, and precipitates at sites of highest negative curvature, which is usually at the particle necks. In solid state sintering this diffusion process occurs by solid-state diffusion along the grain boundaries. At densities  $>$ 92% the pore channels that have formed during intermediate sintering close and form isolated pores on grain boundaries, which are eliminated during final stage sintering until full density is reached. Grain growth sets in after the closing of the pore channels at densities  $>$ 92% since grain boundaries with isolated pores are more mobile than grain boundaries with pore channels. As long as the mobility of the grain boundaries do not exceed the mobility of the pores, full density can be obtained. However, in many ceramic systems abnormal grain growth sets in at some point during sintering, and a limited number of grains grow abnormally fast, which results in a bimodal grain size distribution. Microstructures exhibit a few large grains, which are surrounded by a fine-grained matrix with grains that are orders of magnitude smaller than the large grains. The fast growth of these grains is due to a higher mobility of the grain boundaries of the large grains, which is much faster than the mobility of the pores. In this case pores cannot be removed fast enough from these grain boundaries, get trapped in the grains and remain in the final microstructure. Hence, the final density of a ceramic is often limited by the onset of abnormal grain growth.

## **1.3 Effects of Impurities and Dopants on the Sintering of Al<sub>2</sub>O<sub>3</sub>**

### **1.3.1 MgO in Ultrahigh Purity Al<sub>2</sub>O<sub>3</sub>**

For a long time the performance and application of alumina as a technical ceramic was limited because it is known to exhibit abnormal grain growth. In 1961 Coble discovered that MgO-doping can suppress abnormal grain growth and high-density translucent alumina can be produced this way [5–7]. Since then numerous studies have attempted to understand the underlying mechanisms. Initially Coble proposed four possible mechanisms for the suppression of abnormal grain growth by MgO. As a first possible mechanism he proposed that spinel particles precipitate, pin the grain boundaries and prevent abnormal grain growth. The second mechanism he proposed was a solid-solution pinning mechanism, which assumed that MgO is preferentially adsorbed in the grain boundaries and inhibits abnormal grain growth by lowering the grain boundary mobility. The third proposed mechanism was that MgO could affect the pore shape and thereby increase the effect of pore pinning on grain boundary movement. The fourth proposed mechanism, which was the explanation Coble favored at that time, was that a minimum amount of time is required to nucleate abnormal grains after a critical density is reached, and that MgO increases the densification rate sufficiently to prevent the nucleation of abnormal grains. Since then multiple researchers have found arguments that support all of these mechanisms [8]. Jorgensen and Westbrook [9, 10] showed indirect evidence for MgO segregation to the grain boundaries and explained the effect of MgO on the sintering of Al<sub>2</sub>O<sub>3</sub> by a solute pinning mechanism, where MgO influences the diffusion coefficient or surface energy through defect chemistry effects. Johnson and Coble [11] did not find evidence for MgO segregation in their experiments, and proposed that sintering kinetics change due to an increase in diffusion coefficient by the formation of a solid solution of MgO in Al<sub>2</sub>O<sub>3</sub>, which causes a change in grain growth and pore elimination rate. An alternative model was proposed by Heuer [12], which assumed that MgO increases the pore mobility by increasing the surface diffusivity and, therefore, prevents pore-grain boundary breakaway and abnormal grain growth.

A variety of the mechanisms described above were summarized in a segrega-

tion and precipitation map in unpublished work by Carry, Legros, Bowen, and Lartigue [1] as shown in Figure 1.1. They proposed that when the MgO content in  $\text{Al}_2\text{O}_3$  exceeds the maximum solubility of MgO in the  $\text{Al}_2\text{O}_3$  lattice and a critical concentration of MgO in the grain boundaries, the excess MgO and  $\text{Al}_2\text{O}_3$  form spinel precipitates. Schottky defects are formed below the solubility limit of MgO in the  $\text{Al}_2\text{O}_3$  crystal, and the increased concentration of point defects facilitates diffusion and hence promotes the sintering by enhancing densification and grain growth. MgO concentrations that exceed the solubility of MgO in the  $\text{Al}_2\text{O}_3$  lattice segregate to the grain boundaries, and when the solubility of MgO in the  $\text{Al}_2\text{O}_3$  crystal and grain boundaries is exceeded, spinel precipitates form on the grain boundaries, which reduces the grain boundary mobility by a pinning mechanism, and thus inhibits grain growth. With increasing grain size the required MgO concentration for the formation of spinel decreases, as seen from the segregation and precipitation map in Figure 1.1. The total area of the grain-boundary interface decreases with increasing grain size, and hence the critical concentration of MgO in the  $\text{Al}_2\text{O}_3$  grain boundaries changes. While this proposed segregation precipitation map explains the observed segregation of MgO to grain boundaries and the precipitation of spinel, the key mechanism by which MgO improves the sintering of alumina cannot be identified. However, the segregation precipitation map implies that several of the described mechanisms may contribute to the effect of MgO on the sintering of alumina.

### 1.3.2 Effects of Impurities during sintering of $\text{Al}_2\text{O}_3$

After it was discovered that ppm levels of MgO are sufficient to drastically affect the sintering behavior of alumina [5–7], there has been high academic and commercial interest in understanding how small concentrations of other dopants or impurities such as  $\text{Na}_2\text{O}$ ,  $\text{CaO}$ ,  $\text{Fe}_2\text{O}_3$ , and  $\text{SiO}_2$  affect the sintering kinetics, density and microstructure evolution of alumina. An overwhelming amount of literature exists on how impurities, specifically  $\text{SiO}_2$  and  $\text{CaO}$ , affect the sintering of ultrahigh purity aluminas, and the literature is in agreement that  $\text{SiO}_2$  and  $\text{CaO}$  can form a liquid phase, which allows abnormal and anisotropic grain growth. Bae and Baik [13, 14] showed that there is no abnormal grain growth in  $\text{Al}_2\text{O}_3$ , as long as the total impurity content is below 10 ppm, and it was realized that abnormal grain

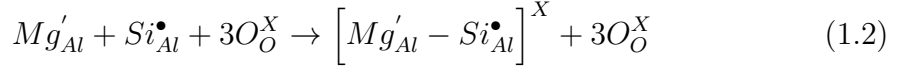
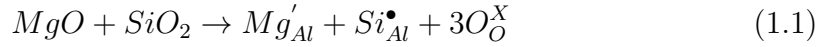
growth during sintering is not intrinsic to alumina, but depends on the presence of trace amounts of impurities on the ppm level, which form a liquid film on grain boundaries [2,8,15,16]. By co-doping of  $\text{Al}_2\text{O}_3$  with  $\text{SiO}_2$  and  $\text{CaO}$  Bae and Baik [13] were able to show that a liquid forms during sintering as soon as the solubility of  $\text{SiO}_2$  and  $\text{CaO}$  in  $\text{Al}_2\text{O}_3$  is exceeded. They estimated the solubility of  $\text{SiO}_2$  and  $\text{CaO}$  in  $\text{Al}_2\text{O}_3$  to be 100 and 20 ppm, and that abnormal grain growth sets in after a critical thickness of the amorphous grain boundary has formed. This implies that impurity contents in commercial alumina powders with purity levels from 99.7 - 99.9% are high enough to form a liquid phase during sintering, if glass-forming impurities are present, as demonstrated by Hansen and Philips [17]. Harmer [18] reported that even in 99.98% pure alumina the impurity level is high enough for the formation of a liquid phase during sintering and it was concluded that abnormal grain growth could only be prevented by adding sintering additives such as  $\text{MgO}$ .

### 1.3.3 Effects of $\text{MgO}$ on Liquid Phase Sintering of $\text{Al}_2\text{O}_3$

Since it was established that abnormal grain growth is due to the presence of glass forming impurities in alumina, the role of  $\text{MgO}$  in alumina needed to be addressed in the context of these impurities, since  $\text{MgO}$  prohibits the deleterious effect of small amounts of liquid phase-forming impurities during sintering and facilitates the formation of a dense and homogeneous submicron microstructure. Several reasonable explanations can be found in the literature to explain this positive effect of  $\text{MgO}$  on the sintering behavior of  $\text{Al}_2\text{O}_3$  containing small amounts of other impurities [8,19]. Regardless of the presence of other impurities, the solute-pinning mechanism and the pinning-by-particle-precipitation mechanism are commonly accepted interpretations of the role of  $\text{MgO}$  on sintering of  $\text{Al}_2\text{O}_3$  [20,21]. Bae and Baik [15] suggested, that  $\text{MgO}$  acts as a glass modifier in glassy grain boundary films and changes the kinetics of dissolution precipitation mass transport by modifying the viscosity. Additionally, a reduction of the kinetics for dissolution into and precipitation from the liquid phase was considered as a key mechanism for sintering of  $\text{MgO}$ -doped alumina [8,19].

Handwerker et al. [16] proposed that  $\text{MgO}$  can increase the solubility of  $\text{SiO}_2$  in  $\text{Al}_2\text{O}_3$  by co-dissolving  $\text{MgO}$ , since the difference in size and charge of  $\text{Mg}^{2+}$  and  $\text{Si}^{4+}$  relative to  $\text{Al}^{3+}$  in the alumina lattice can compensate each other. This

co-dissolution mechanism is supported by the work by Gavrilov et al. [2], who investigated the distribution of impurities in sintered  $\text{Al}_2\text{O}_3$  by high-resolution scanning secondary mass spectrometry (SIMS). Figure 1.2 shows the SIMS maps of sintered  $\text{Al}_2\text{O}_3$  singly doped with (a) 500 ppm  $\text{MgO}$  and (b) 1000 ppm  $\text{SiO}_2$ . Areas of high dopant concentrations appear bright, and in both cases it can be seen that the dopants segregate to the grain boundaries. Furthermore, they showed that if  $\text{Al}_2\text{O}_3$  is co-doped with 500 ppm  $\text{MgO}$  and 1000 ppm  $\text{SiO}_2$ , both dopants segregate to the grain boundaries, but show a substantially higher  $\text{MgO}$  and  $\text{SiO}_2$  concentration towards the grain center, as shown in the SIMS maps in Figure 1.3. The authors concluded that the solubility of  $\text{MgO}$  and  $\text{SiO}_2$  in  $\text{Al}_2\text{O}_3$  is increased by co-doping via the following defect compensation mechanism:



A similar reaction was proposed by Coble and Roy [22] to explain a higher solubility of  $\text{TiO}_2$  in  $\text{Al}_2\text{O}_3$  when an equimolar amount of  $\text{MgO}$  is added. Gavrilov et al. [2] concluded that  $\text{MgO}$  increases the solubility of glass forming impurities in  $\text{Al}_2\text{O}_3$  and therefore prevents the formation of a liquid phase during sintering. However, while they showed that there are higher Si and Mg concentrations in the alumina grains, they did not prove that no liquid phase exists in these samples.

### 1.3.4 Grain Boundaries During Sintering of $\text{Al}_2\text{O}_3$

After the importance of grain boundaries for sintering of ceramics with ppm amounts of impurities and dopants was discovered, more recent literature has focused on developing general models based on grain boundary structures and chemistries to explain the sintering behavior and grain growth of ceramics. For example Harmer and his group [23–26] proposed that impurities form thermodynamically stable grain boundary "phases", which they refer to as "complexions". Depending on the thickness of the adsorbed layer, i.e. the grain boundary thickness, they distinguish between six complexions: clean, monolayer, bilayer, multilayer, nanolayer and wetted, which can be either ordered or amorphous and show transitions from one to another during sintering.

According to their model the mobility of the grain boundaries is determined by the type of complexion, which depends on impurity type and concentration, temperature and crystal orientation of adjacent crystals. During densification and grain growth impurities remain in the grain boundaries after the solubility in the crystal is exceeded. Grain boundaries can be sites for supersaturation during sintering because of the reduction of grain boundary area due to grain growth. The authors argue that there are only two possibilities for the excess impurities to reduce the free energy of the system; the formation of a new phase, or the transition to another complexion [24]. The predominance of either events depends on the relative activation energies. Since crystal planes of different orientation have different grain boundary or interface energies different complexions may co-exist in a microstructure. How many and what type of complexions coexist mainly depends on the temperature. Inhomogeneous impurity distribution may also be considered as a reason for the formation of different complexions.

Using this concept the authors interpret the microstructure development of  $\text{Al}_2\text{O}_3$  with different impurities.  $\text{CaO}$  impurities in  $\text{Al}_2\text{O}_3$  can form calcium hexaluminate, which shows epitaxy on the basal planes of  $\alpha\text{-}\text{Al}_2\text{O}_3$ . The interface energy between the basal planes of  $\alpha\text{-}\text{Al}_2\text{O}_3$  and calcium hexaluminate is low and therefore also the activation energy for formation. But for crystal planes with other orientations the activation energy for formation of calcium hexaluminate is high. Therefore, the theory suggests that complexion transitions are preferred on these planes and that the different grain boundary mobilities of the basal planes compared to all other planes lead to anisotropic abnormal grain growth, which is often observed in  $\text{CaO}$  containing alumina.

$\text{SiO}_2$  in  $\text{Al}_2\text{O}_3$  does not have a preferred crystal plane on which it can form precipitations with low interfacial energy. The activation energy for precipitation is high for all crystal orientations and, therefore, this system is interpreted to prefer complexion transitions rather than the formation of a new phase. It is stated that complexions with higher grain boundary mobilities form upon heating and that grain growth is enhanced. Dillon and Harmer's [23, 27] interpretation for  $\text{MgO}$  in  $\text{Al}_2\text{O}_3$  is that spinel precipitates are formed, and that this system behaves isotropically and exhibits low interface energies on several crystal planes. Therefore, it is stated that the activation energy for precipitation is low as well and that complexion transitions are prevented by the formation of spinel precipitates, or the

precipitations occur uniformly throughout the microstructure.

While this model can fundamentally explain the grain growth behavior in fully dense microstructures, it cannot explain observed differences in densification and how different chemistries, i.e. concentration and ratios of different impurities, and grain boundary structures affect the rate-limiting sintering mechanisms.

A different model, based on the activation energy and the driving force for atoms to cross the grain boundary, was developed by Kang et al. [4, 28, 29] to explain microstructure evolution in ceramics and metals. According to this model grains grow normal and an equiaxed microstructure develops if the critical driving force for grain boundary migration is zero and the grain interface is atomically rough. The critical driving force for grain boundary migration is determined by factors such as temperature, dopant concentration, and oxygen partial pressure, and if the critical driving force is zero then the step free energy, i.e. the additional surface energy created during nucleation and growth of grains (the ledges of the nucleus), has to be zero. If the critical driving force is not zero, then grains grow faceted, and if the maximum driving force, i.e. the driving force for the largest grains to grow, is larger than the critical driving force, then abnormal grain growth occurs. If the maximum driving force is much larger than the critical driving force, i.e. the driving force of many grains is larger than the critical driving force, many grains start growing fast ("abnormally") forming a microstructure that looks like a normally grown microstructure, and this is defined as pseudo-normal grain growth. If the maximum driving force is less than the critical driving force, then grain growth is stagnant, i.e. the microstructure does not change.

Kang et al. [28, 29] investigated a variety of parameters such as partial pressure, temperature, dopants, and impurities for different material systems, but explained the microstructure evolution only qualitatively with the described model, and the majority of observations from experiments were fitted into the model rather than predicted by the model. For example, it is concluded that MgO lowers the step free energy of alumina since the addition of MgO to alumina results in a homogeneous and equiaxed microstructure [30]. However, it is not explained why MgO lowers the step free energy, and why MgO is the only material that lowers the step free energy in that manner. Furthermore the model only takes into account the microstructural evolution in fully dense bodies and does not address densification.

## 1.4 Sintering of Bayer Alumina

### 1.4.1 The Bayer Process

The Bayer process is a hydrothermal precipitation process in which bauxite ore is digested in an aqueous solution of caustic soda ( $\text{NaOH}$ ) at temperatures up to  $230^\circ\text{C}$  and pressures up to 40 bar. Bauxite consists of a variety of minerals, including gibbsite ( $\text{Al}(\text{OH})_3$ ), boehmite ( $\gamma\text{-AlO(OH)}$ ), diasporite ( $\alpha\text{-AlO(OH)}$ ), goethite ( $\text{FeO(OH)}$ ), haematite ( $\text{Fe}_2\text{O}_3$ ), and kaolinite ( $\text{Al}_2\text{Si}_2\text{O}_5(\text{OH})_4$ ). During digestion in  $\text{NaOH}$  the Al-containing minerals form  $\text{NaAl}(\text{OH})_4$ , which dissolves as a complex. Fe- and Si-containing minerals and other accessory minerals are insoluble under these conditions and can be separated as red mud. The temperature of the sodium aluminate solution is decreased to  $50\text{-}70^\circ\text{C}$  and the addition of  $\gamma\text{-Al}(\text{OH})_3$  seed crystals results in the precipitation of  $\gamma\text{-Al}(\text{OH})_3$  from the solution. Heat treatment and calcination of the  $\gamma\text{-Al}(\text{OH})_3$  at  $1100\text{-}1200^\circ\text{C}$  leads to the formation of  $\alpha\text{-Al}_2\text{O}_3$ .

$\text{SiO}_2$  and  $\text{Fe}_2\text{O}_3$  are the main components of the Bauxite ore, additionally to  $\text{Al}_2\text{O}_3$ , and hence low concentrations of  $\text{SiO}_2$  and  $\text{Fe}_2\text{O}_3$  are present in the final powder. Additional  $\text{SiO}_2$  impurities may originate from the milling media that is used by the manufacturer to grind the calcined powder to the desired particle size [8, 31].  $\text{Na}_2\text{O}$  impurities result from the digestion of the bauxite in  $\text{NaOH}$  and the consequent precipitation of  $\text{Al}(\text{OH})_3$  crystals from the  $\text{NaAl}(\text{OH})_4$  solution. Small amounts of  $\text{Na}_2\text{O}$  are precipitated within the  $\text{Al}(\text{OH})_3$  crystals [31]. To remove  $\text{NaOH}$  from the powder surface, the  $\text{Al}(\text{OH})_3$  is washed after precipitation. However, small amounts of  $\text{NaOH}$  or rather  $\text{Na}_2\text{O}$  after calcination, remain on the powder surface. Hence,  $\text{Na}_2\text{O}$  impurities are either distributed on the surface, or entrapped in the alumina grains in Bayer process alumina powders. Other impurities such as gallium, calcium and magnesium originate from accessory minerals in the bauxite [8].

### **1.4.2 Influence of Na<sub>2</sub>O and SiO<sub>2</sub> on the Sintering Behavior of Al<sub>2</sub>O<sub>3</sub>**

The Bayer process illustrates that alumina powders obtained by this process inevitably contain trace amounts of impurities, such as Na<sub>2</sub>O and SiO<sub>2</sub>. Despite the extensive use of Bayer alumina there are relatively few published studies on the effects of Na<sub>2</sub>O on its sintering. Sumita and Bowen reported on the effect of adding 1 wt.% Na<sub>2</sub>O to a high purity alumina powder (Sumitomo, AKP-HP) [32]. However, they determined that only ~8 ppm Na<sub>2</sub>O was present in the alumina after sintering at 1400°C for 2 h, without additional details to explain the large discrepancy between the doping concentration and the amount determined by inductively coupled plasma (ICP) spectrometry after sintering. Smothers and Reynolds [33] investigated the influence of 1 wt.% of different additives on the sintering of 99.3% pure alumina (Alcoa A-11) and showed that Na<sub>2</sub>CO<sub>3</sub> or NaF retard sintering and inhibit grain growth.

Cahoon and Christensen [34] reported a deleterious effect of Na<sub>2</sub>O on the sintering of alumina as well. They added between 0.03 and 5.9 wt.% Na<sub>2</sub>O to their alumina powder (Alcoa A-14, no purity specifications given) and heated the samples in a 5 days cycle (2 days heating, 3 days cooling) to temperatures between 1600°C and 1835°C for 1 h. A very strong retardation of sintering and inhibition of abnormal grain growth was reported for increasing Na<sub>2</sub>O concentration. They observed cracking of their samples and inferior compressive strengths and suggested that this deleterious effect might be due to the formation of  $\beta$ - or  $\xi$ -Al<sub>2</sub>O<sub>3</sub>. They also studied the effect of SiO<sub>2</sub> on the sintering of Al<sub>2</sub>O<sub>3</sub> and reported a "moderately deleterious effect" of SiO<sub>2</sub>. They claim that it strongly inhibits abnormal grain growth at concentrations as low as 0.1% and that this effect is enhanced with increasing SiO<sub>2</sub> content. They reported that the deleterious effect of Na<sub>2</sub>O was moderated in Na<sub>2</sub>O/SiO<sub>2</sub> co-doped Al<sub>2</sub>O<sub>3</sub>.

Louet et al. [35] studied the effect of Na<sub>2</sub>O and SiO<sub>2</sub> doping on densification and microstructure evolution of a Bayer process alumina (Rhone-Poulenc, P172SB), containing 550 ppm Na<sub>2</sub>O, 770 ppm SiO<sub>2</sub>, 1010 ppm MgO, 600 ppm CaO and 115 ppm Fe<sub>2</sub>O<sub>3</sub>. Na<sub>2</sub>O and SiO<sub>2</sub> levels were adjusted by adding CH<sub>3</sub>COOH-Na and silica gel. When they added Na<sub>2</sub>O, the concentrations in the samples after sintering for 2 h at 1540°C, as measured by ICP spectrometry, were less than 50% of the targeted

amount, and they explained this difference by the low vaporization temperature of Na<sub>2</sub>O [35]. Louet et al. concluded that Na<sub>2</sub>O slows the sintering process and decreases the sintered density from 98 to 97% for Na<sub>2</sub>O concentrations of 550 ppm and 1150 ppm, respectively, when sintered at 1540°C for 2h. The authors reported that a high level of Na<sub>2</sub>O results in a fine, homogeneous microstructure. They observed a drop in grain size from 4 - 5 μm to 3 μm when exceeding 1000 ppm Na<sub>2</sub>O. This work also showed that increasing SiO<sub>2</sub> concentration from 770 ppm to as high as 1500 ppm in the presence of Na<sub>2</sub>O does not affect the final density but does cause anisotropic grain growth. Even though one can see an increase in grain size but no abnormal grain growth as the SiO<sub>2</sub> concentration increases in the presented micrographs, the authors state that increasing the SiO<sub>2</sub> concentration has no effect on the average grain size but leads to abnormal grain growth. As noted by the authors, these results are difficult to interpret in terms of Na<sub>2</sub>O and SiO<sub>2</sub> effects due to the large number and high concentrations of impurities in the as-received powder.

Compson et al. [31] investigated the effect of SiO<sub>2</sub> and Na<sub>2</sub>O concentration on the sintering behavior of alumina. They chose four commercial alumina powders with similar specific surface areas, particle diameter and particle distributions. All powders were 99.8% pure, but showed different concentrations for the single impurities. Particularly, the Na<sub>2</sub>O and SiO<sub>2</sub> concentrations varied from 0.02 to 0.1% and 0.01 to 0.04%, respectively. Using dilatometry they showed that the four powders exhibit different shrinkage, sintering and densification behavior in the temperature range from 1150°C to 1500°C. They concluded that SiO<sub>2</sub> has a deleterious effect on the sintering of Al<sub>2</sub>O<sub>3</sub>, but they could not detect an influence of Na<sub>2</sub>O.

This literature survey shows that there is some disagreement about whether ppm levels of Na<sub>2</sub>O and SiO<sub>2</sub> have a positive, negative, or no effect on sintering of alumina, and unfortunately none of the literature reports investigated fundamental mechanisms that would explain their observations. While most authors acknowledged the presence of other impurities and dopants, such as MgO, their effect and possible cross effects with other impurities or dopants were not considered. The lack of understanding of this system was the motivation to investigate the fundamental mechanisms that are responsible for changes in sintering behavior as a function of powder chemistry in Bayer process-derived Al<sub>2</sub>O<sub>3</sub>.

The chapters of this dissertation have either been published, submitted for publication, or will be submitted for publication in peer-reviewed scientific journals. As a result some degree of self-plagiarism was necessary to construct this dissertation.

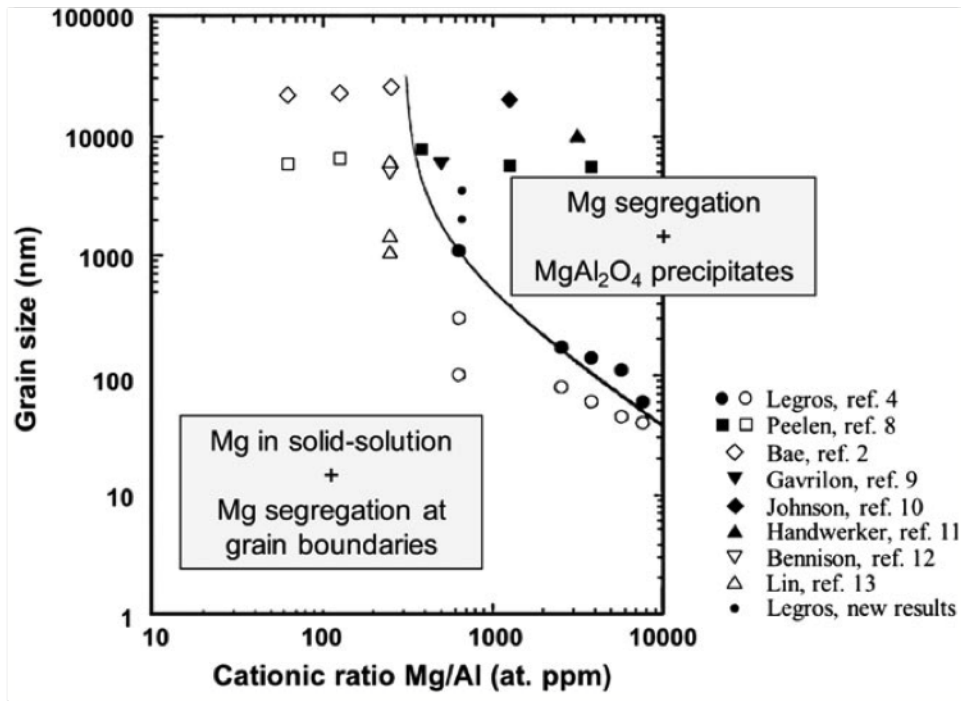


**Figure 1.1.** Segregation and precipitation map of MgO-doped alumina based on the results in the literature [1].

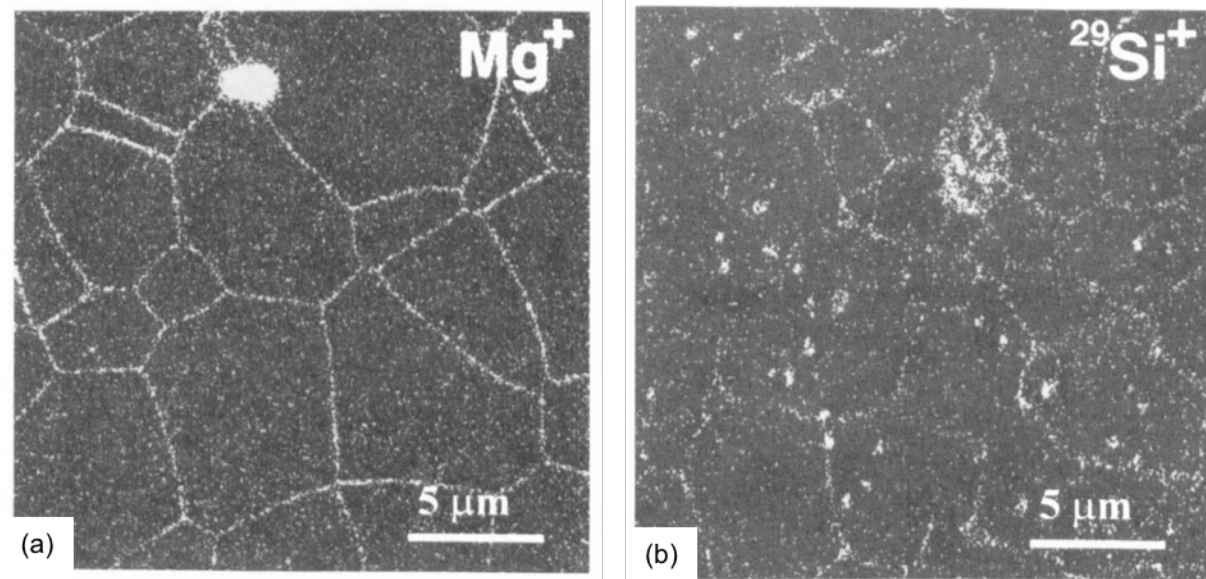


**Figure 1.2.** SIMS maps of  $\text{Al}_2\text{O}_3$  doped with 500 ppm  $\text{MgO}$  (a) and 1000 ppm  $\text{SiO}_2$  (b). Samples were sintered for 8 h at  $1650^\circ\text{C}$  [2].

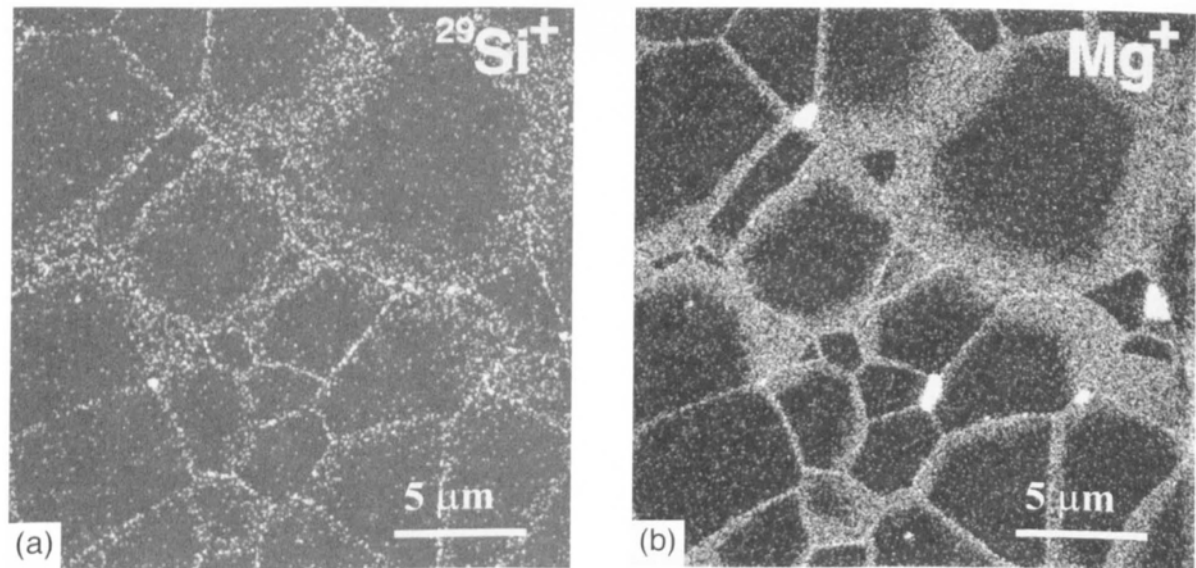


**Figure 1.3.** SIMS maps of  $\text{Al}_2\text{O}_3$  co-doped with 500 ppm  $\text{MgO}$  and 1000 ppm  $\text{SiO}_2$  and sintered at 1650°C for 8h. (a) shows the distribution of  $\text{SiO}_2$ , (b) the distribution of  $\text{MgO}$  in the same samples [2].

# **Chapter 2 |**

# **The Effects of Na<sub>2</sub>O and SiO<sub>2</sub>**

# **on Liquid Phase Sintering of Bayer**

# **Al<sub>2</sub>O<sub>3</sub>**

## **2.1 Introduction**

Al<sub>2</sub>O<sub>3</sub> is arguably the most extensively used and researched ceramic material because it is used in many large volume applications such as high temperature refractories, technical ceramics, high voltage insulators, and functional fillers. The majority of Al<sub>2</sub>O<sub>3</sub> applications use synthetic or specialty aluminas derived from Bayer feedstocks, such as aluminum trihydrate (Al(OH)<sub>3</sub>), smelter grade Al<sub>2</sub>O<sub>3</sub> and others. Bayer process aluminas are typically 99.0 - 99.9% pure and contain Na<sub>2</sub>O, CaO, Fe<sub>2</sub>O<sub>3</sub>, and SiO<sub>2</sub> impurities that originate from the bauxite ore and/or Bayer process reagents (e.g., NaOH). The vast majority of research on the sintering of Al<sub>2</sub>O<sub>3</sub>, however, focuses on ultra-high purity ( $\geq 99.99\%$ ) aluminas derived from specialty feedstocks, such as ammonium alum (NH<sub>4</sub>Al(SO<sub>4</sub>)<sub>2</sub>·12H<sub>2</sub>O), boehmite ( $\gamma$ -AlOOH) and aluminum chloride (AlCl<sub>3</sub>). While ultra-high purity aluminas provide the purest platform from which to conduct fundamental sintering research, that research does not usually explore the types and amounts of impurities typical of Bayer aluminas. Commercial Bayer Al<sub>2</sub>O<sub>3</sub> powders exist in a range of reactive grades that differ in the amount and types of these impurities. Therefore, the evaluation of specialty reactive aluminas, within the context of previous work on ultra-high purity aluminas, is a valuable contribution to industrial users and bridges

fundamental sintering research with ultra-high purity aluminas.

## 2.2 Experimental

A chemically purified 0.4  $\mu\text{m}$  median particle size Bayer process  $\text{Al}_2\text{O}_3$  powder (Almatis, Inc., Leetsdale, PA, USA) with only 2 ppm  $\text{MgO}$  was used to study the sintering of near  $\text{MgO}$ -free Bayer  $\text{Al}_2\text{O}_3$  (Figure 2.1). The powder was chemically purified by the manufacturer so that impurity levels similar to commercial high purity Bayer process aluminas were obtained after doping with  $\text{Na}_2\text{O}$  and/or  $\text{SiO}_2$ . The physical and chemical characteristics of the as-received powder are shown in Table 2.1. Chemical analysis of the as-received  $\text{Al}_2\text{O}_3$  was performed by inductively coupled plasma (ICP) emission spectroscopy (iCap 6000, Thermo Fischer Scientific, Inc., Waltham, MA, USA) after  $\text{Al}_2\text{O}_3$  samples were acid digested in a microwave digestion unit in a Teflon<sup>TM</sup> sample holder. It should be noted that the as-received Bayer  $\text{Al}_2\text{O}_3$  contained impurity levels of 90 ppm  $\text{Fe}_2\text{O}_3$ , 62  $\text{CaO}$ , and 22 ppm  $\text{TiO}_2$ . The  $\text{Na}_2\text{O}$  and  $\text{SiO}_2$  concentrations reported after doping include the impurity concentrations in the as-received powder (29 ppm  $\text{Na}_2\text{O}$  and 103 ppm  $\text{SiO}_2$ ).

The  $\text{Al}_2\text{O}_3$  powders were doped with up to 1000 ppm  $\text{Na}_2\text{O}$  using sodium acetate ( $\text{NaC}_2\text{H}_3\text{O}_2 \cdot 3\text{H}_2\text{O}$ , ACS grade, BDH, West Chester, PA, USA), based on the procedure reported by Louet et al. [35]. The  $\text{Al}_2\text{O}_3$  powders were dispersed in a solution of sodium acetate dissolved in de-ionized water. The suspension was stirred on a magnetic stir plate for 5 h at room temperature, and held at 80°C for 24 h while stirring until the mixture was too viscous to stir, and then dried at 100°C for 24 h.

Samples were doped with up to 500 ppm  $\text{SiO}_2$  by first dissolving tetraethyl orthosilicate (TEOS,  $\text{Si}(\text{OC}_2\text{H}_5)_4$ , 98%, Aldrich Chemical Company, Inc., Milwaukee, WI, USA) in 200 proof ethanol with a few drops of de-ionized water to hydrolyze the TEOS and immediately mixed at room temperature for 5 h with either the as-received or  $\text{Na}_2\text{O}$ -doped  $\text{Al}_2\text{O}_3$  powder. The mixture was subsequently stirred at 70°C for an additional 12 h. The powder was then dried at 100°C for 2 h, followed by crushing in a mortar and pestle, and sieving to -106  $\mu\text{m}$  (US Standard 140 mesh).

Samples were prepared for sintering studies by uniaxially dry pressing the powders at 170 MPa and then cold isostatic pressing at 200 MPa (CIP, Autoclave

Engineers, Erie, PA, USA) to obtain cylindrical samples (3.0-3.5 mm long by 12.7 mm diameter or 8.5-10 mm long by 6 mm diameter) with green densities of 59.0%  $\pm$  0.5% of theoretical density. To investigate the sintering process, dry pressed 8.5-10 mm long by 6 mm diameter cylinders were heated at 10°C/min to 1525°C in a thermomechanical analyzer (TMA, Linseis PT1600, Robbinsville, NJ, USA). The kinetics of sintering and grain growth were evaluated on 3.0-3.5 mm long by 12.7 mm diameter samples heated at 10°C/min to 1200 °C then 5°C/min to 1525°C followed by sintering at 1525°C for up to 8 h. The density of three samples of each condition was measured by the Archimedes method according to ASTM standard B962-15 [36] and the average density reported for each sintering time and temperature. For microstructure analysis, samples were first polished to a surface finish of 1  $\mu$ m and then thermally etched in air at 1425°C for 40 min. Average grain sizes were measured on SEM (ESEM, Quanta 200, FEI Company, Hillsboro, OR, USA) micrographs using a linear intercept method (ASTM Standard E112-96) [37].

## 2.3 Results

### 2.3.1 Effects of Na<sub>2</sub>O-doping

The doping experiments were designed to uniformly distribute Na<sub>2</sub>O and SiO<sub>2</sub> on the surfaces of the Al<sub>2</sub>O<sub>3</sub> particles. Upon heating the dopant NaC<sub>2</sub>H<sub>3</sub>O<sub>2</sub>·3H<sub>2</sub>O first dehydrates and then decomposes to form Na<sub>2</sub>CO<sub>3</sub> above 385°C [38]. Using a video recorder, we observed that anhydrous sodium acetate melts and rapidly spreads on the surface of an Al<sub>2</sub>O<sub>3</sub> substrate at  $\sim$ 420°C. Na<sub>2</sub>CO<sub>3</sub> melts at 851°C and subsequently decomposes to Na<sub>2</sub>O [38]. As a result of the rapid wetting of the Na<sub>2</sub>O precursor on the Al<sub>2</sub>O<sub>3</sub> substrate we conclude that Na<sub>2</sub>O is uniformly distributed on the powder surface by the acetate doping process.

Figure 2.2 shows the shrinkage behavior of Bayer Al<sub>2</sub>O<sub>3</sub> doped with different Na<sub>2</sub>O concentrations during heating to 1525°C at 10°C/min. The as-received Al<sub>2</sub>O<sub>3</sub> (intrinsic impurities: 29 ppm Na<sub>2</sub>O, 103 ppm SiO<sub>2</sub>) begins to shrink at  $\sim$ 1050 °C, whereas shrinkage begins at  $\sim$ 1100°C for samples doped with 1029 ppm Na<sub>2</sub>O. The difference in density at the beginning of densification continues throughout the heating cycle. However, above  $\sim$ 1350°C the densification rate of the Na<sub>2</sub>O doped samples surpasses that of the as-received sample. Overall, the Na<sub>2</sub>O-doped samples

are 2.5% less dense than the as-received  $\text{Al}_2\text{O}_3$  after heating to 1525°C.

Figure 2.3 shows the influence of  $\text{Na}_2\text{O}$  concentration on the densification kinetics at 1525°C. Clearly, the degree of densification decreases with increasing  $\text{Na}_2\text{O}$  concentration for up to 30 min with the  $\text{Na}_2\text{O}$ -doped samples being as much as 2% less dense than the as-received  $\text{Al}_2\text{O}_3$ . However, after  $\geq 30$  min at 1525°C densification is independent of  $\text{Na}_2\text{O}$  content and all samples are 97.5-98.0% dense after  $\geq 3$  h.

The microstructures of as-received samples (29 ppm  $\text{Na}_2\text{O}$ ) and doped samples with 529 ppm  $\text{Na}_2\text{O}$  sintered for 30 min, 3 h and 8 h at 1525°C are compared in Figure 2.4. It is seen that higher  $\text{Na}_2\text{O}$  concentration does not affect the average grain size for all hold times. Microstructures of as-received samples are predominantly equiaxed with a small number of faceted grains, whereas samples doped with  $\text{Na}_2\text{O}$  appear to have an increasing number of faceted grain boundaries with increasing  $\text{Na}_2\text{O}$  concentration. A few tabular grains of up to  $60 \mu\text{m}$  were seen in both as-received and  $\text{Na}_2\text{O}$ -doped samples after 8 h at 1525°C (see Figure 2.4c and 2.4f). Those faceted grains are larger in the as-received powder samples compared to  $\text{Na}_2\text{O}$ -doped samples, whereas the  $\text{Na}_2\text{O}$ -doped samples show more large tabular grains than samples from the as-received powder.

### 2.3.2 Effects of $\text{Na}_2\text{O}/\text{SiO}_2$ co-doping

As seen in Figure 2.5, the presence of 603 ppm  $\text{SiO}_2$  significantly retards densification of as-received alumina. Starting at  $\sim 1250^\circ\text{C}$ , all of the  $\text{SiO}_2$ -doped samples densify less than as-received and singly  $\text{Na}_2\text{O}$ -doped samples. The densification rate of the  $\text{SiO}_2$ -doped samples from 1250 to 1525°C is slower than the as-received alumina.  $\text{SiO}_2$  reduces the linear shrinkage by  $\sim 3.0\%$  and thus the samples are 8.7% less dense than the as-received  $\text{Al}_2\text{O}_3$  after 8 h at 1525°C.

The densification kinetics of the  $\text{Al}_2\text{O}_3$  powders doped with different amounts of  $\text{Na}_2\text{O}$  (154 and 529 ppm) and  $\text{SiO}_2$  (203 and 603 ppm) are compared in Figure 2.6. It is seen that the addition of  $\text{SiO}_2$  significantly reduces sintered density for all hold times. For example, samples containing as much as 603 ppm  $\text{SiO}_2$  have densities of 81.5% after 0 h and 93.8% after 8 h at 1525°C, whereas the as-received and singly  $\text{Na}_2\text{O}$ -doped  $\text{Al}_2\text{O}_3$  samples are 98% dense after 3 h at 1525°C.

Figure 2.6 shows the effect of  $\text{Na}_2\text{O}$  on the densification of  $\text{SiO}_2$ -doped samples.

For hold times < 1 h, samples doped with 529 ppm Na<sub>2</sub>O and 203 ppm SiO<sub>2</sub> are ~ 1.5% denser than samples doped with 154 ppm Na<sub>2</sub>O and 203 ppm SiO<sub>2</sub>. A difference in Na<sub>2</sub>O concentration does not affect the final density of samples containing 203 ppm SiO<sub>2</sub> (96.5 - 97.0%) after 3 h at 1525°C. For higher SiO<sub>2</sub> concentrations (603 ppm), singly SiO<sub>2</sub> doped samples are 1 - 2.5% less dense than samples co-doped with 529 ppm Na<sub>2</sub>O and 603 ppm SiO<sub>2</sub> for all hold times at 1525°C.

The average grain sizes of the as-received and Na<sub>2</sub>O-doped samples are nominally the same and increase from 1.6  $\mu\text{m}$  to 2.5  $\mu\text{m}$  after 30 min and 8 h at 1525°C, respectively. There was little grain growth (1.4  $\mu\text{m}$  to 2.1  $\mu\text{m}$ ) in singly SiO<sub>2</sub>-doped samples (603 ppm) after 30 min and 8 h at 1525°C, respectively. In samples co-doped with 529 ppm Na<sub>2</sub>O and 603 ppm SiO<sub>2</sub> the average grain size is 1.6  $\mu\text{m}$  for hold times between 30 min and 8 h at 1525°C. The limited grain growth is attributed primarily to the large fraction of porosity. Micrographs of 603 ppm SiO<sub>2</sub> singly doped and 529 ppm Na<sub>2</sub>O and 603 ppm SiO<sub>2</sub> co-doped samples heated for 8 h after heating for 8 h at 1525°C are compared in Figure 2.7. Both samples are only 92-94% dense and thus it was difficult to prepare polished micrographs without some grain pull-out.

## 2.4 Discussion

To understand the above effects, we first note from the Al<sub>2</sub>O<sub>3</sub>-Na<sub>2</sub>O phase diagram [39] that Na<sub>2</sub>O is insoluble in  $\alpha$ -Al<sub>2</sub>O<sub>3</sub>. A few platelet shaped grains with high aspect ratios were observed in the microstructures of sintered Na<sub>2</sub>O-doped samples (Figure 2.8). Due to their morphology and literature reports [40–44], it is assumed that these grains are a type of  $\beta$ -Al<sub>2</sub>O<sub>3</sub>. Four types of  $\beta$ -Al<sub>2</sub>O<sub>3</sub> exist; two of them,  $\beta$ -Al<sub>2</sub>O<sub>3</sub> (Na<sub>2</sub>O·11Al<sub>2</sub>O<sub>3</sub>) and  $\beta''$ -Al<sub>2</sub>O<sub>3</sub> (Na<sub>2</sub>O·5Al<sub>2</sub>O<sub>3</sub>), form in the binary system Na<sub>2</sub>O-Al<sub>2</sub>O<sub>3</sub> [45, 46]. The formation of this second phase is investigated in greater detail in chapter 5.

Sodium aluminate (NaAlO<sub>2</sub>) is reported to form at temperatures as low as 900°C, [47] and  $\beta''$ -Al<sub>2</sub>O<sub>3</sub> (Na<sub>2</sub>O·5Al<sub>2</sub>O<sub>3</sub>) can be synthesized at temperatures as low as 1100°C [40, 48, 49]. Therefore, we hypothesize that either sodium aluminate or  $\beta''$ -Al<sub>2</sub>O<sub>3</sub> forms before the onset of densification and that the presence of the second phases on the surface of the Al<sub>2</sub>O<sub>3</sub> particles retards the initial shrinkage of

$\text{Na}_2\text{O}$ -doped samples at  $\sim 1050^\circ\text{C}$ . However, we did not observe any  $\beta$ - $\text{Al}_2\text{O}_3$  type grains in the samples at this temperature. Alternatively, as discussed below,  $\text{Na}_2\text{O}$  may interact with the 103 ppm of intrinsic  $\text{SiO}_2$  in the sample.

We hypothesize that the initial grain boundaries in the as-received  $\text{Al}_2\text{O}_3$  are wetted with the intrinsic impurities such as  $\text{Na}_2\text{O}$ ,  $\text{CaO}$ ,  $\text{TiO}_2$  and  $\text{SiO}_2$ . Doping with  $\text{Na}_2\text{O}$  and  $\text{SiO}_2$  changes the relative grain boundary chemistries and the properties of the respective grain boundary liquids. In the presence of a grain boundary liquid, densification occurs by a solution-precipitation sintering process, and thus, the rate of densification is controlled by either interface reaction between the grain boundary liquid and  $\text{Al}_2\text{O}_3$  grains, or by the diffusion of  $\text{Al}^{3+}$  through the liquid grain boundary film.  $\text{Al}^{3+}$  diffusion is rate-limiting at  $1525^\circ\text{C}$  since it has been shown for molten glass systems that  $\text{Al}^{3+}$  has lower ionic diffusion rates than  $\text{O}^{2-}$  [50]. For diffusion-controlled densification, the densification rate is given by [51, 52]

$$\frac{d\left(\frac{\Delta\rho}{\rho}\right)}{dt} = \frac{A\delta D_l C_0 \gamma_{l\nu} \Omega}{kT} r_s^{-4} \quad (2.1)$$

and for interface reaction-controlled densification, the densification rate is given by

$$\frac{d\left(\frac{\Delta\rho}{\rho}\right)}{dt} = \frac{BKC_0 \gamma_{l\nu} \Omega}{kT} r_s^{-2} \quad (2.2)$$

where  $A$  and  $B$  are geometric factors,  $\delta$  is the thickness of the liquid film,  $D_l$  is the diffusion coefficient of  $\text{Al}^{3+}$  in the liquid,  $C_0$  is the equilibrium solute concentration,  $K$  the interface reaction constant,  $\gamma_{l\nu}$  is the liquid surface tension,  $\Omega$  is the molecular volume of the solid,  $r_s$  is the particle radius,  $k$  is the Boltzmann constant and  $T$  is absolute temperature.

Equations 2.1 and 2.2 can be used to gain insights into the rate-limiting densification mechanisms during liquid phase sintering by evaluating their ratio [51, 52]

$$\alpha = \frac{A\delta D_l}{BK} r_s^{-2} \quad (2.3)$$

In general, for  $\alpha > 1$ , densification is controlled by the interface reaction, since  $D_l$  is relatively high. For  $\alpha < 1$ , densification is controlled by diffusion, and for  $\alpha = 1$  both mechanisms contribute equally to densification [52]. Since the product of the grain boundary thickness and the diffusion coefficient greatly influences

the rate-determining mechanism,  $\delta D_l$  and the interface reaction constant  $K$  were examined in more detail.

Due to the main impurities in Bayer aluminas being  $\text{SiO}_2$  and  $\text{Na}_2\text{O}$ , the  $\text{Al}_2\text{O}_3$ - $\text{SiO}_2$ - $\text{Na}_2\text{O}$  ternary phase diagram [39] was utilized to evaluate the effects of dopant type and concentration on solubility of  $\text{Al}_2\text{O}_3$  in the grain boundary liquid. It is assumed that the system approaches thermodynamic equilibrium upon holding at 1525°C, and thus the equilibrium composition of the liquid at 1525°C can be calculated from the ternary phase diagram (Figure 2.9). For simplification, we considered only  $\text{Al}_2\text{O}_3$ ,  $\text{SiO}_2$  and  $\text{Na}_2\text{O}$  for the analysis, and assumed that all impurities/dopants are located in the grain boundaries. It was stated earlier that  $\text{Na}_2\text{O}$  is not soluble in  $\text{Al}_2\text{O}_3$ , and it has been reported in the literature that  $\text{SiO}_2$  segregates at the grain boundaries in  $\text{Al}_2\text{O}_3$  [53]. Figure 2.9 shows the liquidus projection of the  $\text{Al}_2\text{O}_3$ - $\text{SiO}_2$ - $\text{Na}_2\text{O}$  ternary phase diagram. The red solid lines connecting the  $\text{Al}_2\text{O}_3$  end member to the  $\text{Na}_2\text{O}$ - $\text{SiO}_2$  side are binary cuts through the ternary (isoplethal sections) and correspond to some of the  $\text{Na}_2\text{O}/\text{SiO}_2$  ratios investigated in this study. The red dashed line is the isotherm at 1525°C for the part of the phase diagram where  $\alpha$ - $\text{Al}_2\text{O}_3$  and liquid are in equilibrium. The blue dash-dot line and the green dotted line are eutectic lines along which  $\beta$ - $\text{Al}_2\text{O}_3$  or mullite is stable with  $\alpha$ - $\text{Al}_2\text{O}_3$  and a liquid. The isotherm and the eutectic lines are important for determining the stable phases and the composition of the liquid in the samples. If a binary cut intersects the isotherm (red dashed line) only  $\alpha$ - $\text{Al}_2\text{O}_3$  and liquid are stable phases at 1525°C and the intersection point determines the composition of the liquid. If a binary cut intersects one of the two marked eutectic lines (blue dash-dot or green dotted) a third phase ( $\beta$ - $\text{Al}_2\text{O}_3$  or mullite) is stable in those samples, and the composition of the liquid at 1525°C is determined by the intersection point of the respective intersected eutectic line with the isotherm at 1525°C.

The  $\text{Al}_2\text{O}_3$ - $\text{SiO}_2$ - $\text{Na}_2\text{O}$  phase diagram demonstrates that a small amount of liquid is stable at 1525°C for all compositions investigated. Note that these overall compositions are all very close to the  $\text{Al}_2\text{O}_3$  end member ( $\sim 99.8\%$   $\text{Al}_2\text{O}_3$ ) and  $\text{Na}_2\text{O}$  and  $\text{SiO}_2$  are insoluble in  $\text{Al}_2\text{O}_3$ . Isoplethal sections (red solid lines in Figure 2.9) can be used to determine the stability and equilibrium composition of a liquid since the volume fractions of  $\text{Na}_2\text{O}$  and  $\text{SiO}_2$  are known. Lambotte and Chartrand [39] calculated isoplethal sections of the ternary phase diagram, and based on their

calculations, the solubility of  $\text{Al}_2\text{O}_3$  in the liquid at 1525°C in the samples was estimated based on the respective  $\text{Na}_2\text{O}:\text{SiO}_2$  ratios (assuming a constant liquid density of 2.45 g/cm<sup>3</sup> [37, 54]). Likewise, the volume fractions of liquid and solid phases can be estimated since the doping and impurity concentrations of  $\text{SiO}_2$  and  $\text{Na}_2\text{O}$  are known. Table 2.2 summarizes the stable phases, the liquid compositions, and the total amount of liquid in the as-received and doped samples. Stable liquids at 1525°C are predicted for liquid compositions with  $\text{Na}_2\text{O}:\text{SiO}_2$  ratios between 0.25 and 0.5. As described above, for higher  $\text{Na}_2\text{O}$  concentrations in the samples (global  $\text{Na}_2\text{O}:\text{SiO}_2$  ratio > 0.5),  $\alpha$ - $\text{Al}_2\text{O}_3$ ,  $\beta$ - $\text{Al}_2\text{O}_3$  and a liquid with a  $\text{Na}_2\text{O}:\text{SiO}_2$  ratio of 0.5 are stable. For sample compositions with higher  $\text{SiO}_2$  concentrations (global  $\text{Na}_2\text{O}:\text{SiO}_2$  ratio < 0.25)  $\alpha$ - $\text{Al}_2\text{O}_3$ , mullite and a liquid with a  $\text{Na}_2\text{O}:\text{SiO}_2$  ratio of 0.25 are stable. Since the global  $\text{Na}_2\text{O}:\text{SiO}_2$  ratio in most of the samples investigated in this work is either > 0.5 or < 0.25, the liquid in those samples had compositions of 0.5 or 0.25, respectively. As the  $\text{Na}_2\text{O}:\text{SiO}_2$  ratio in the liquid increases from 0.25 to 0.5 the solubility of  $\text{Al}_2\text{O}_3$  in the liquid increases from 18.4 vol.% to 21.6 vol.% [39]. The increased  $\text{Al}_2\text{O}_3$  solubility leads to higher densification rates and higher densities in  $\text{Na}_2\text{O}/\text{SiO}_2$  co-doped samples compared to singly  $\text{SiO}_2$ -doped samples, regardless of the rate-limiting process.

Assuming fully dense samples and the liquid volume fractions reported in Table 2.2, we calculated the grain boundary thickness  $\delta$  using:

$$\delta = 2 \frac{V_g \phi}{S_g (1 - \phi)} \quad (2.4)$$

where  $\phi$  is the liquid volume fraction and  $V_g$  and  $S_g$  are the volume and the surface area based on the average grain size, respectively. For as-received and singly  $\text{Na}_2\text{O}$ -doped samples the grain boundary thickness is < 0.3 nm for all observed grain sizes. For  $\text{Na}_2\text{O}/\text{SiO}_2$  co-doped samples (603 ppm  $\text{SiO}_2$ ) the grain boundary thickness is between 0.8 and 1.8 nm for grain sizes of 1  $\mu\text{m}$  and 2.5  $\mu\text{m}$ , respectively. The calculated grain boundary thickness of singly  $\text{SiO}_2$ -doped samples is similar to that of as-received samples, since mullite is predicted to form in the  $\text{Al}_2\text{O}_3\text{-SiO}_2\text{-Na}_2\text{O}$  system for low  $\text{Na}_2\text{O}$  concentrations at 1525°C. However, mullite may not form in Bayer process  $\text{Al}_2\text{O}_3$  due to the presence of other impurities, such as  $\text{CaO}$ , which, similar to  $\text{Na}_2\text{O}$ , lowers the eutectic temperature and acts as a network modifier in the glass. Therefore, the grain boundary thicknesses of singly  $\text{SiO}_2$ -doped and

$\text{Na}_2\text{O}/\text{SiO}_2$  co-doped samples are expected to be similar at  $\sim 1.8$  nm. The amount of liquid in the samples and, therefore, the grain boundary thickness, is governed mainly by the amount of glass forming species in the samples, i.e.  $\text{SiO}_2$ .

The diffusion coefficient of  $\text{Al}^{3+}$  through the liquid grain boundary phase can be calculated with the Eyring relation

$$D_l = \frac{kT}{\eta\lambda} \quad (2.5)$$

where  $\eta$  is the viscosity of the grain boundary liquid and  $\lambda$  is the jump distance of the diffusion species, taken as the ionic diameter of an  $\text{Al}^{3+}$  ( $1.07$  Å). Using viscosity data (range of  $20$  -  $400$  Pa·s) from the literature [55], we estimated the diffusion coefficients to be  $\sim 1 \cdot 10^{-7}$  and  $\sim 5 \cdot 10^{-9}$  cm<sup>2</sup>/s for  $\text{Na}_2\text{O}/\text{SiO}_2$  co-doped and singly  $\text{SiO}_2$ -doped samples, respectively.

Although we can calculate values for grain boundary thickness ( $\delta$ ) and viscosity ( $\eta$ ), an exact  $\alpha$ -ratio cannot be determined using Equation 2.3 because we do not know the interface reaction constant ( $K$ ). Nevertheless, assuming a reasonable  $K$  value from the literature ( $K = 5 \cdot 10^{-8}$  m/s) [52] and assuming that the A/B ratio (A and B being geometrical factors) is on the order of 1, we estimated  $\alpha$  to be  $\sim 10^{-2}$  and  $\sim 1$  for singly  $\text{SiO}_2$ -doped samples (603 ppm  $\text{SiO}_2$ ) and  $\text{Na}_2\text{O}/\text{SiO}_2$  co-doped samples (529/603 ppm), respectively. Thus, we conclude that at  $1525^\circ\text{C}$  densification of Bayer aluminas with low  $\text{Na}_2\text{O}/\text{SiO}_2$  concentration ratios is governed by diffusion, whereas densification of Bayer aluminas with high  $\text{Na}_2\text{O}/\text{SiO}_2$  concentration ratios can be governed by either diffusion or interface reaction.

The enhanced densification of  $\text{Na}_2\text{O}/\text{SiO}_2$  co-doped samples compared to singly  $\text{SiO}_2$ -doped is attributed to two factors; the increased solubility of  $\text{Al}_2\text{O}_3$  in the liquid grain boundary phase, and the enhanced diffusion of  $\text{Al}^{3+}$  ( $\sim 5 \cdot 10^{-9}$  to  $\sim 1 \cdot 10^{-7}$  cm<sup>2</sup>/s) through the liquid grain boundary. This effect of enhanced densification of  $\text{Na}_2\text{O}/\text{SiO}_2$  co-doped samples compared to singly  $\text{SiO}_2$ -doped samples is observed in both the dilatometry curves and the densification kinetics data shown in Figure 2.2 and Figure 2.6, respectively.

It should be noted that a particular challenge for thermal processing studies with soda-based ceramics is  $\text{Na}_2\text{O}$  volatilization at relatively lower temperature than the sintering temperature. Soda by itself is highly volatile at temperatures  $< 1000^\circ\text{C}$  and the evaporation of soda from  $\text{Na}_2\text{O}$  containing technical ceramics

such as sodium niobates [56] and  $\beta$ -Al<sub>2</sub>O<sub>3</sub> during sintering is often reported. For example,  $\beta$ -Al<sub>2</sub>O<sub>3</sub> ( $\text{Na}_2\text{O}\cdot11\text{Al}_2\text{O}_3$ ) has an appreciable Na<sub>2</sub>O vapor pressure at temperatures  $> 1400^\circ\text{C}$  [48], and when heated in air to  $> 1500^\circ\text{C}$ ,  $\beta$ -Al<sub>2</sub>O<sub>3</sub> converts to  $\alpha$ -Al<sub>2</sub>O<sub>3</sub> by volatilization of Na<sub>2</sub>O [48, 57]. Therefore, Na<sub>2</sub>O evaporation from the samples during heating should be considered as samples might have somewhat lower Na<sub>2</sub>O concentrations than assumed for the above calculations. Thus, for samples with low Na<sub>2</sub>O/SiO<sub>2</sub> ratios, the liquid grain boundary phase may contain somewhat less Na<sub>2</sub>O and the grain boundary thickness may be somewhat less than calculated. However, for singly Na<sub>2</sub>O-doped samples and for co-doped samples with high Na<sub>2</sub>O/SiO<sub>2</sub> ratios (e.g. Na<sub>2</sub>O  $\geq 529$  ppm for samples with 603 ppm SiO<sub>2</sub>) the composition of the grain boundary liquid and the grain boundary thickness is not expected to change very much if Na<sub>2</sub>O volatilizes. Consequently, even with Na<sub>2</sub>O volatilization, the proposed sintering mechanisms do not change. The evaporation of Na<sub>2</sub>O from Bayer Al<sub>2</sub>O<sub>3</sub> samples will be further discussed in more detail in the following chapter.

## 2.5 Summary

High concentrations of Na<sub>2</sub>O in Bayer process Al<sub>2</sub>O<sub>3</sub> powders inhibit densification in the initial sintering stage and retard densification up to the final sintering stage compared to powders with low Na<sub>2</sub>O concentrations. However, Na<sub>2</sub>O shows no adverse effect on the final density after longer hold times ( $\geq 3$  h at  $1525^\circ\text{C}$ ). The addition of SiO<sub>2</sub> to Bayer process Al<sub>2</sub>O<sub>3</sub> powders substantially retards densification, starting at  $\sim 1250^\circ\text{C}$ , and samples containing as much as 603 ppm SiO<sub>2</sub> are 4% less dense than samples containing 103 ppm SiO<sub>2</sub>, even after hold times as long as 8 h at  $1525^\circ\text{C}$ . Co-doping with Na<sub>2</sub>O and SiO<sub>2</sub> increases densification by 1 - 2.5% relative density relative to singly SiO<sub>2</sub>-doped samples. The observed differences in sintering behavior can be explained by a liquid phase sintering model. Diffusion and solubility of Al<sub>2</sub>O<sub>3</sub> in the SiO<sub>2</sub>-based liquid in the grain boundaries is low at the temperatures used in this study, which explains the substantial retardation of densification by SiO<sub>2</sub>. As predicted from the phase diagram Na<sub>2</sub>O increases the solubility of Al<sub>2</sub>O<sub>3</sub> in the siliceous grain boundary phase. As predicted from viscosity data Na<sub>2</sub>O enhances diffusion of Al<sup>3+</sup> through the liquid grain boundary phase. Both factors contribute to the enhanced densification rates of samples with

high Na<sub>2</sub>O/SiO<sub>2</sub> ratios compared to samples with low Na<sub>2</sub>O/SiO<sub>2</sub> ratios.

**Table 2.1.** Physical and chemical characteristics of the as-received Bayer Al<sub>2</sub>O<sub>3</sub> powder used in this study.

BET (m <sup>2</sup> /g)	7.4
D <sub>50</sub> (μm)	0.4
D <sub>90</sub> (μm)	1.5
	ICP (ppm)
Al <sub>2</sub> O <sub>3</sub>	99.96 %
SiO <sub>2</sub>	103
Na <sub>2</sub> O (total)	29
Fe <sub>2</sub> O <sub>3</sub>	90
CaO	62
TiO <sub>2</sub>	22
MgO	2

**Table 2.2.** Calculated compositions and amounts of liquid in as-received, singly doped and co-doped samples at 1525°C ( $\alpha = \alpha\text{-Al}_2\text{O}_3$ ,  $\beta = \beta\text{-Al}_2\text{O}_3$ , L = liquid, M = mullite).

Global dopant concentration		Global Na <sub>2</sub> O/SiO <sub>2</sub> ratio	Na <sub>2</sub> O:SiO <sub>2</sub> ratio in liquid	Composition of liquid (mol %)			Amount of liquid (vol. %)	Stable phases
ppm (wt.)	ppm (mol)			Na <sub>2</sub> O	SiO <sub>2</sub>	Al <sub>2</sub> O <sub>3</sub>		
Na <sub>2</sub> O/SiO <sub>2</sub>	Na <sub>2</sub> O/SiO <sub>2</sub>							
As-received 29/103	48/175	0.27	0.25	17.9	63.4	19.7	0.03%	$\alpha + L$
154/103- 1029/103	253/175- 1693/175	1.45-9.67	0.5	26.1	52.3	21.6	0.03%	$\alpha + L + \beta$
29/603	48/1023	0.05	0.25	16.3	65.3	18.4	0.03%	$\alpha + L + M$
154/603	253/1023	0.25	0.25	16.3	65.3	18.4	0.16%	$\alpha + L$
279/603	459/1023	0.45	0.45	24.5	54.6	20.8	0.19%	$\alpha + L$
529/603	870/1023	0.85	0.5	26.1	52.3	21.6	0.22%	$\alpha + L + \beta$
1029/603	1693/1023	1.65	0.5	26.1	52.3	21.6	0.22%	$\alpha + L + \beta$

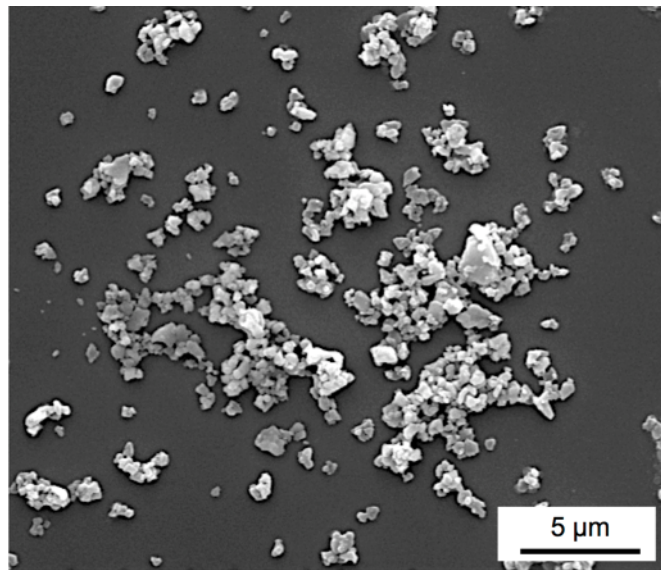


**Figure 2.1.** SEM image of as-received chemically purified Bayer  $\text{Al}_2\text{O}_3$  powder used in this study.

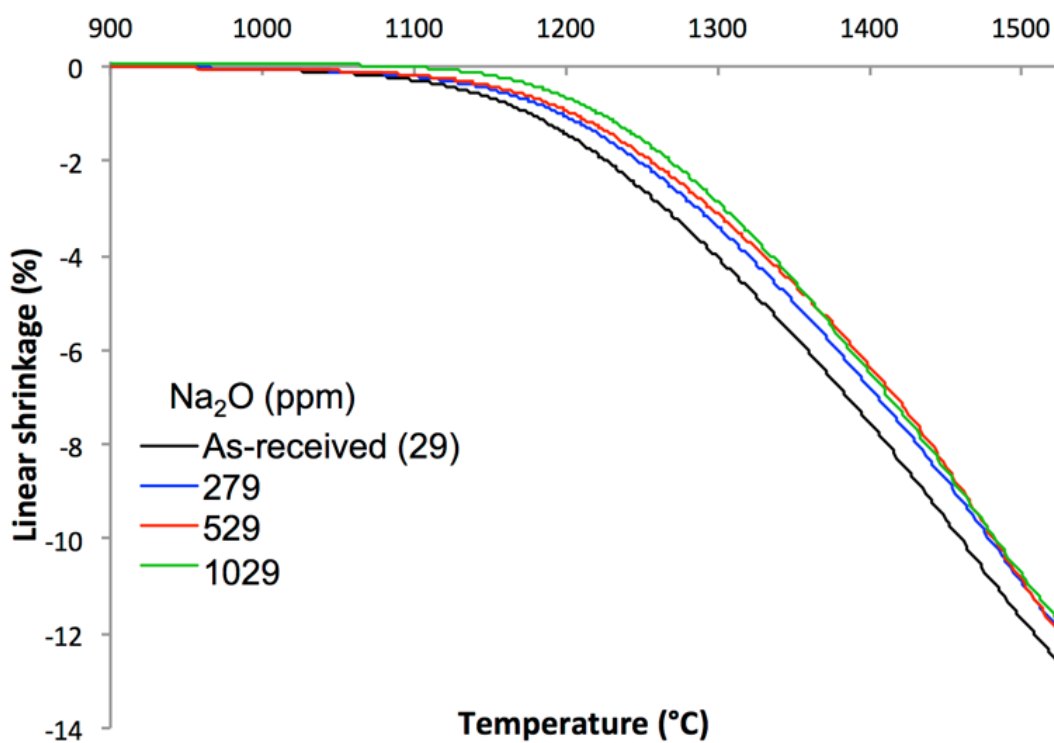


**Figure 2.2.** Dilatometer curves of as-received and singly  $\text{Na}_2\text{O}$ -doped samples heated at  $10^\circ\text{C}/\text{min}$  to  $1525^\circ\text{C}$ .

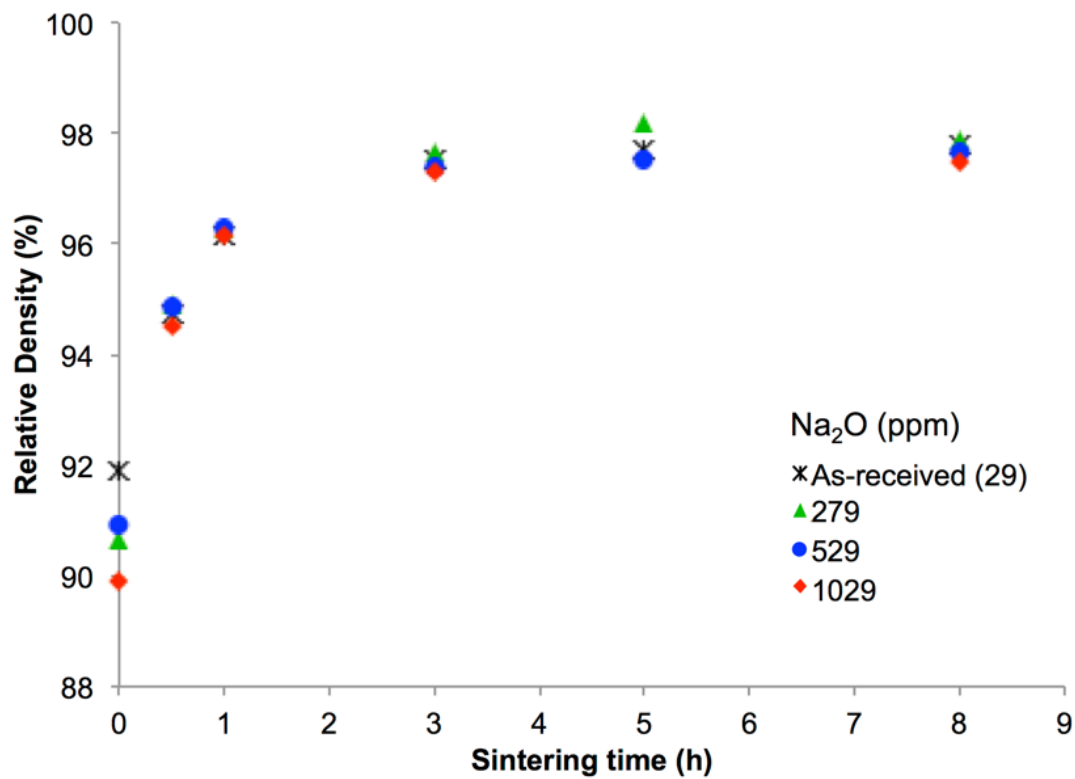


**Figure 2.3.** Densification kinetics of Bayer  $\text{Al}_2\text{O}_3$  doped with different  $\text{Na}_2\text{O}$  concentrations and sintered at  $1525^\circ\text{C}$ .

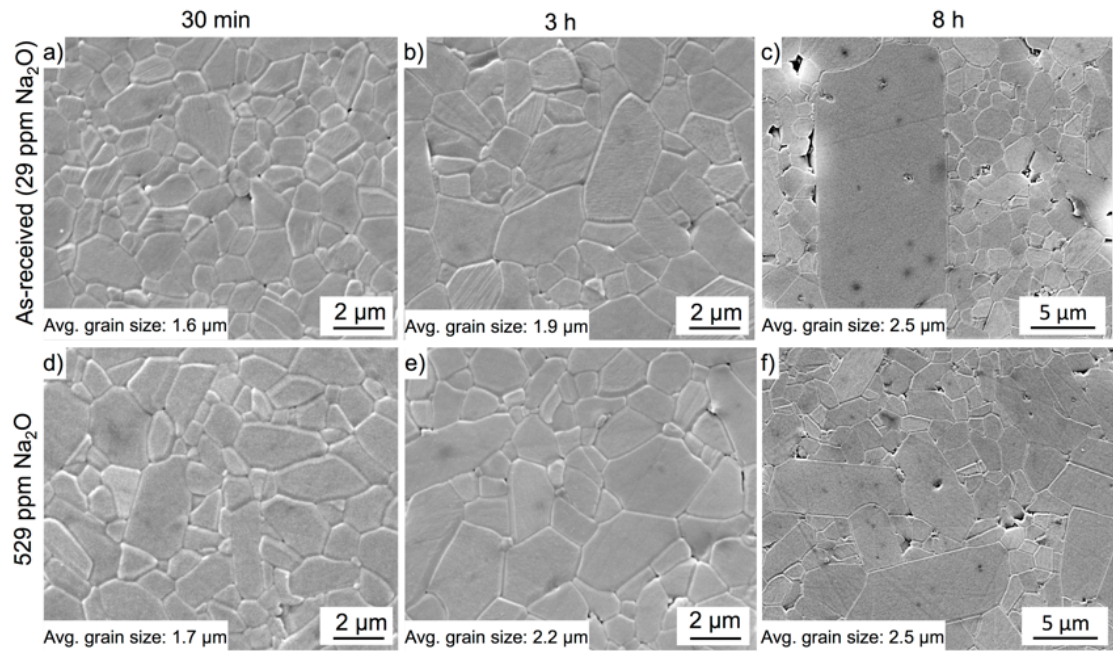


**Figure 2.4.** Microstructures of as-received and singly 529 ppm  $\text{Na}_2\text{O}$  doped samples after 30 min, 3 h and 8 h at 1525°C.

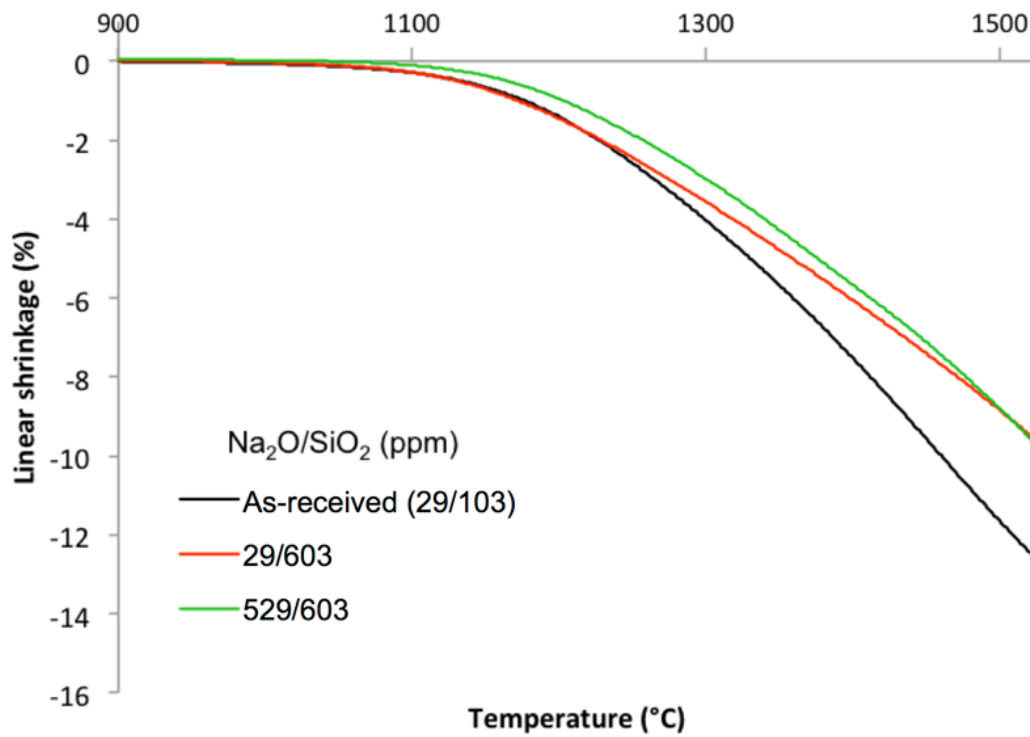


**Figure 2.5.** Dilatometer curves of as-received, singly SiO<sub>2</sub>-doped, and Na<sub>2</sub>O/SiO<sub>2</sub> co-doped Bayer Al<sub>2</sub>O<sub>3</sub> heated at 10°C/min to 1525°C.

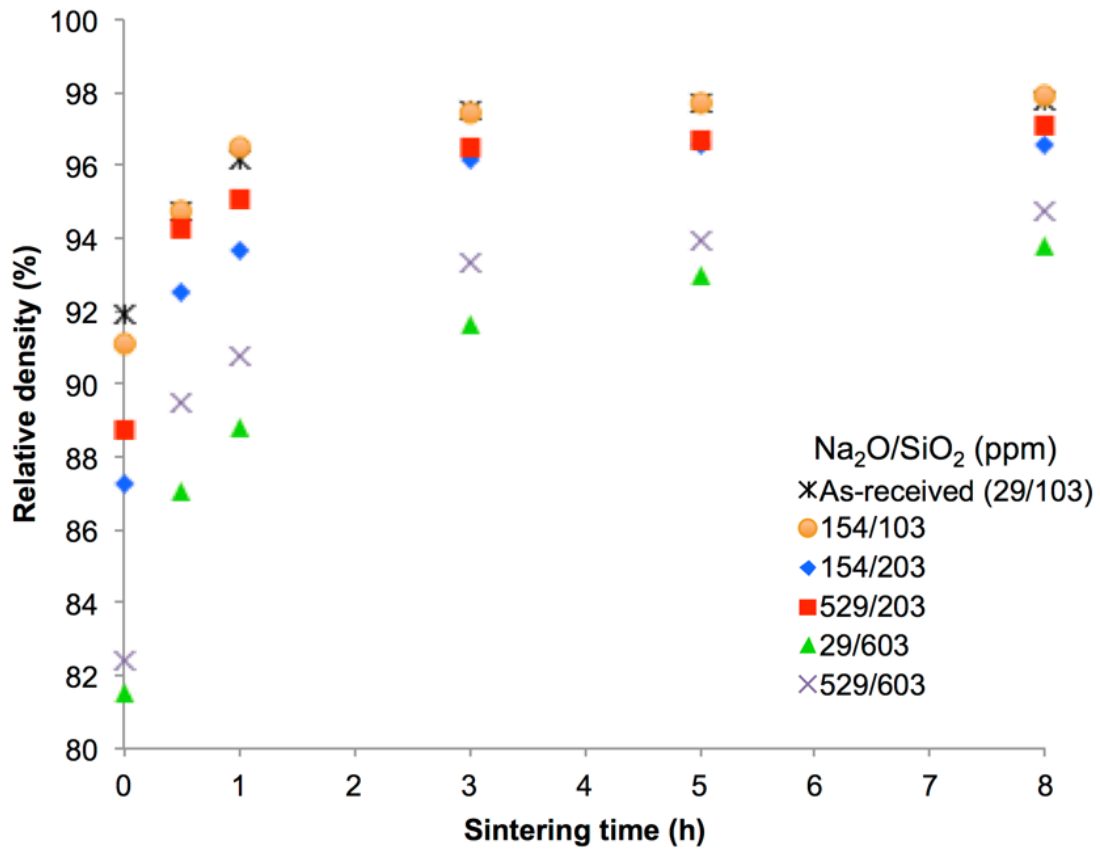


**Figure 2.6.** Densification kinetics of Bayer  $\text{Al}_2\text{O}_3$  doped with different concentrations of  $\text{Na}_2\text{O}$  and  $\text{SiO}_2$  at  $1525^\circ\text{C}$ .

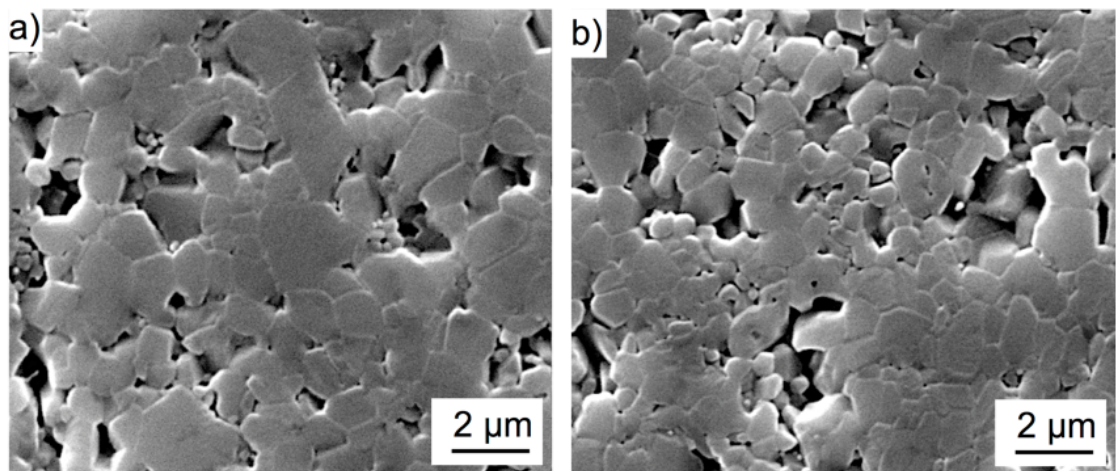


**Figure 2.7.** Microstructures of Bayer  $\text{Al}_2\text{O}_3$  doped with a) 603 ppm  $\text{SiO}_2$  and b) 529 ppm  $\text{Na}_2\text{O}$  and 603 ppm  $\text{SiO}_2$  after heating at  $1525^\circ\text{C}$  for 8h.

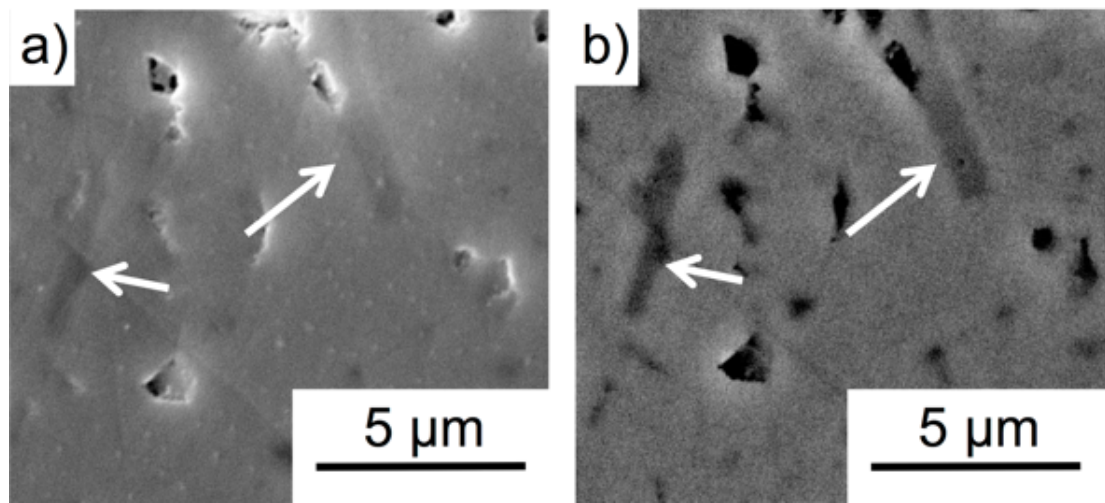


**Figure 2.8.** Micrographs of a sample doped with 1029 ppm  $\text{Na}_2\text{O}$  after sintering at  $1525^\circ\text{C}$  for 3 h. The micrographs were recorded using a) a secondary electron detector and b) a backscattered electron detector. The arrows point at the platelet shaped  $\beta$ -alumina grains that form in samples doped with  $\text{Na}_2\text{O}$ . The samples were not thermally etched.

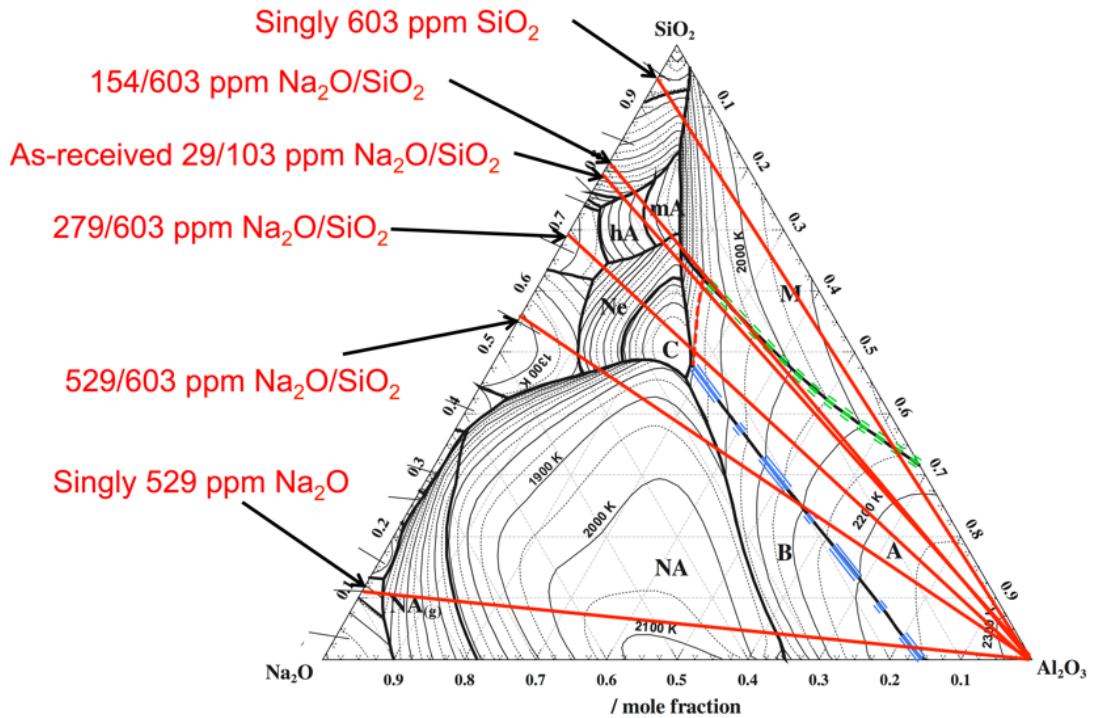


**Figure 2.9.** Liquidus projection of the  $\text{Al}_2\text{O}_3$ - $\text{SiO}_2$ - $\text{Na}_2\text{O}$  ternary phase diagram. The red solid lines are isoplethal cuts representing the samples investigated in this study. The red dashed line is the 1525°C isotherm where  $\alpha$ - $\text{Al}_2\text{O}_3$  and liquid are in equilibrium. The blue dash-dot line and green dotted line are eutectic lines at which  $\alpha$ - $\text{Al}_2\text{O}_3$  and liquid is in equilibrium with  $\beta$ - $\text{Al}_2\text{O}_3$  or mullite, respectively.

# **Chapter 3 | Powder Chemistry Effects on the Sintering Behavior of MgO- doped Bayer Alumina**

## **3.1 Introduction**

Most commercial alumina products use Bayer processed powder because it is a lower cost option for products with purity levels of up to 99.9%. The remaining 0.1% consists of the intentionally added MgO dopant, and impurities such as Na<sub>2</sub>O, CaO, Fe<sub>2</sub>O<sub>3</sub>, and SiO<sub>2</sub> that originate from the bauxite ore or the Bayer process itself. It is well known that trace (ppm) amounts of dopants or impurities can have a significant influence on the sintering of alumina [14, 15, 58]. Since Coble's discovery of MgO doping to produce high-density translucent alumina, there has been high academic and commercial interest in understanding how small concentrations of dopants and impurities characteristic of Bayer alumina affect sintering [8, 10, 12, 35, 59].

In chapter 2, the influence of Na<sub>2</sub>O and SiO<sub>2</sub> on the sintering of MgO-free Bayer alumina was investigated. Na<sub>2</sub>O was shown to initially retard the densification of MgO-free Bayer alumina samples, but no effect was observed after extended sintering time (> 30 min) at 1525°C, whereas the addition of SiO<sub>2</sub> to MgO-free Bayer alumina formed a liquid phase and significantly retarded densification throughout the entire sintering process. Na<sub>2</sub>O addition to SiO<sub>2</sub>-doped samples increased the densification rate and degree of densification compared to singly SiO<sub>2</sub>-doped samples. Based on phase equilibria, the solubility of Al<sub>2</sub>O<sub>3</sub> in the liquid phase was shown to increase as

the  $\text{Na}_2\text{O}$  concentration in the liquid grain boundary phase increases. Furthermore, a higher  $\text{Na}_2\text{O}$  concentration decreases the viscosity of the liquid phase, which further increases the densification rate [3]. Hence, samples with high  $\text{Na}_2\text{O}/\text{SiO}_2$  ratios ( $\geq 0.5$ ) have higher densities than samples with lower  $\text{Na}_2\text{O}/\text{SiO}_2$  ratios.

$\text{MgO}$  is commonly added to commercial alumina powders because it is known to improve sintering. Several reasonable mechanistic explanations for the beneficial effect of  $\text{MgO}$  include solute-drag, particle-pinning, modification of defect chemistry, increase of surface diffusivity, modification of a liquid phase, and modification of interfacial properties [15]. A model that takes into account the redistribution of  $\text{MgO}$  and  $\text{SiO}_2$  during the sintering of high purity alumina was reported by Handwerker et al. [16] They proposed that  $\text{MgO}$  changes the segregation behavior of glass forming impurities such as  $\text{SiO}_2$  by increasing their solubility in  $\text{Al}_2\text{O}_3$ . This mechanism was supported by the work of Gavrilov et al. [2] who demonstrated by high resolution secondary ion mass spectrometry that the dopants segregate strongly to grain boundaries when high purity  $\text{Al}_2\text{O}_3$  is singly doped with either  $\text{SiO}_2$  or  $\text{MgO}$ , but show a higher solubility in  $\text{Al}_2\text{O}_3$  when co-doped with  $\text{MgO}$  and  $\text{SiO}_2$  due to a defect mechanism in which  $\text{Mg}^{2+}$  and  $\text{Si}^{4+}$  occupy  $\text{Al}^{3+}$  sites and compensate for each other's charge and strain. This model is of particular interest since it considers the direct interaction of  $\text{MgO}$  and  $\text{SiO}_2$ ; an impurity known to negatively affect alumina densification.

In this chapter it is reported how  $\text{Na}_2\text{O}$  and  $\text{SiO}_2$  influence the sintering of 99.8 - 99.9% pure Bayer alumina doped with 380 ppm  $\text{MgO}$ . Dilatometry and sintering kinetics of  $\text{MgO}$ -free Bayer alumina samples with similar  $\text{Na}_2\text{O}$  and  $\text{SiO}_2$  concentrations from chapter 2 are compared to the present results to identify the stages at which  $\text{MgO}$  affects densification, and to identify key mechanisms that are responsible for the beneficial effect of  $\text{MgO}$  on the sintering of Bayer alumina. High-resolution transmission electron microscopy (TEM) and energy dispersive spectroscopy (EDS) measurements show the distribution of dopants/impurities on grain boundaries. First-principles calculations based on the density functional theory (DFT) were carried out to estimate the relative thermodynamic stability of  $\text{MgO}$ ,  $\text{SiO}_2$ , and  $\text{MgO}+\text{SiO}_2$  in the alumina lattice.

## 3.2 Experimental

A chemically purified MgO-doped Bayer alumina powder (Almatis, Inc., Leetsdale, PA, USA) was chosen for this study. Earlier we studied the influence of SiO<sub>2</sub> and Na<sub>2</sub>O on the sintering of MgO-free Bayer alumina using a powder with similar physical and chemical characteristics as the powder used in this study. Since the sample preparation procedures of the two powders were identical, the differences in sintering behavior after doping with similar Na<sub>2</sub>O and SiO<sub>2</sub> concentrations should be attributable primarily to the difference in MgO concentration and its cross effects with Na<sub>2</sub>O and SiO<sub>2</sub>.

Physical and chemical characteristics of the powder are shown in Table 3.1 and Figure 3.1. The powder was doped with up to 1000 ppm Na<sub>2</sub>O and 500 ppm SiO<sub>2</sub> using sodium acetate (NaC<sub>2</sub>H<sub>3</sub>O<sub>2</sub>·3H<sub>2</sub>O, ACS grade, BDH, VWR International LLC, West Chester, PA, USA) and tetraethyl orthosilicate (Si(OC<sub>2</sub>H<sub>5</sub>)<sub>4</sub>), 98%, Aldrich Chemical Company, Inc. Milwaukee, WI, USA), respectively, to obtain chemistries similar to commercial high purity Bayer aluminas with different liquid volume fractions and different Na<sub>2</sub>O/SiO<sub>2</sub> ratios, as shown in Table 3.2. The amount of liquid in the samples at 1525°C was estimated from the Al<sub>2</sub>O<sub>3</sub>-Na<sub>2</sub>O-SiO<sub>2</sub> and Al<sub>2</sub>O<sub>3</sub>-MgO-SiO<sub>2</sub> phase diagrams [3, 39, 60] based on the concentrations of SiO<sub>2</sub>, Na<sub>2</sub>O and MgO. The detailed doping procedures are described in chapter 2.

Samples with green densities of 59.0 ± 0.5% were fabricated for sintering studies by uniaxial and cold isostatic dry pressing (CIP, Autoclave engineers, Erie, Pa, USA) at 170 MPa and 200 MPa, respectively. The dry pressed cylinders were heated at 10°C/min to 1525°C in a thermomechanical analyzer (TMA, Linseis PT1600, Robbinsville, NJ, USA) to record the shrinkage during heating. The kinetics of sintering of samples at 1450°C and 1525°C were investigated for up to 8 h. The samples were heated at 10°C/min to 1200°C and then at 5°C/min to the final sintering temperature. The average grain size and density were measured by the linear intercept (ASTM Standard E112-96) [37] and Archimedes methods (ASTM standard B962-15) [36], respectively. The structure and chemistry of grain boundaries were investigated by transmission electron microscopy (TEM) and energy dispersive x-ray spectroscopy EDS using a dual aberration corrected FEI Titan<sup>3</sup> field emission microscope operated at 300 kV and FEI Talos (FEI, Hillsboro, OR, USA) field emission microscope at 200 kV. The EDS on both microscopes is

an FEI Super-X system consisting of four SDDs (Silicon Drift Detectors) with a solid angle of 0.9 sr ad. The samples for TEM and EDS were air-quenched from the sintering temperature by pulling the samples out of the box furnace at temperature and prepared using a focused ion beam (Quanta 200 3D Dual Beam FIB, FEI, Hillsboro, OR, USA). Grain boundaries were chosen for analysis that were oriented parallel to the TEM beam in order to accurately measure grain boundary widths in the 2D projection images and EDS profiles. Chemical analyses were performed by inductively coupled plasma (ICP) emission spectroscopy (iCap 6000, Thermo Fischer Scientific, Inc., Waltham, MA, USA) after alumina samples were acid digested in a microwave digestion unit equipped with a Teflon<sup>TM</sup> sample holder (MARS M, CEM Corp., Matthews, NC, USA).

### 3.3 Computational Methodology

DFT-based first-principles calculations were carried out at 0 K to investigate the thermodynamic stability of clustered defects in the  $\alpha$ -alumina structure. The energy at 0 K without the contribution of the zero-point vibrational energy  $E_0$  was obtained by an equation of state (EOS) fitting using the four-parameter Birch-Murnaghan (BM4) equation as follows [61]:

$$E_0(V) = a + bV^{-\frac{2}{3}} + cV^{-\frac{4}{3}} + dV^{-2} \quad (3.1)$$

where  $a$ ,  $b$ ,  $c$ , and  $d$  are fitting parameters. The EOS fitting is achieved through an energy-volume (E-V) curve of at least 5 different volumes based on the methodology discussed by Shang et al. [61]. The Helmholtz energy  $F(V, T)$  can be predicted as a function of temperature  $T$  and volume  $V$  via [61, 62]:

$$F(V, T) = E_0(V) + F_{vib}(V, T) + F_{T-el}(V, T) \quad (3.2)$$

where  $F_{vib}$  is the temperature-dependent vibrational contribution, and  $F_{T-el}$  is the thermal electronic contribution. At ambient pressure, the Helmholtz energy of the system is equal to the Gibbs energy.

The vibrational contribution was obtained using the Debye-Grüneisen model [61]:

$$F_{vib}(V, T) = \frac{9}{8}k_B\theta_D(V) - k_BT \left[ D \left( \frac{\theta_D(V)}{T} \right) + 3\ln \left( 1 - e^{-\theta_D(V)/T} \right) \right] \quad (3.3)$$

where  $\theta_D$  is the Debye temperature,  $T$  the temperature, and  $D[\theta_D(V)/T]$  the Debye function. The Debye temperature can be calculated by:

$$\theta_D = s \frac{(6\pi^2)^{\frac{1}{3}}\hbar}{k_B} V_0^{\frac{1}{6}} \left( \frac{B_0}{M} \right)^{\frac{1}{2}} \left( \frac{V_0}{V} \right)^\gamma \quad (3.4)$$

where  $s$  is the Debye temperature scaling factor,  $\gamma$  the Grüneisen parameter determined by the pressure derivative of bulk modulus  $B'$ ,  $B_0$  the equilibrium bulk modulus,  $M$  the atomic mass, and  $V_0$  the equilibrium volume. Here, the equilibrium properties  $V_0$ ,  $B_0$ , and  $B'$  are estimated from the EOS of Eq. 3.1. The methodology by Liu et al. [63] was used to calculate the scaling factor of Al<sub>2</sub>O<sub>3</sub>:

$$s(\nu) = 3^{\frac{5}{6}} \left( 4\sqrt{2} \left( \frac{1+\nu}{1-\nu} \right)^{\frac{3}{2}} + \left( \frac{1+\nu}{1-\nu} \right)^{\frac{3}{2}} \right)^{-\frac{1}{3}} \quad (3.5)$$

where  $\nu$  is the Poisson's ratio, which was calculated by Shang et al. [64]. The thermal electronic contribution was estimated based on the electronic density of states and the Fermi-Dirac statistics [62].

In the present work, the Vienna Ab-initio Simulation Package (VASP) was used to perform the first-principles calculations [65]. The projector augmented-wave (PAW) [66, 67] method was utilized to describe the electron-ion interactions with the exchange correlation functional given by the generalized gradient approximation (GGA-PW91) [68]. A sigma value of 0.2 eV and a plane wave energy cutoff of 1.3 times higher than the highest default cutoff were adopted, which was 520 eV. The Brillouin zone sampling was carried out with Blöchl corrections using a gamma centered Monkhorst-Pack (MP) scheme [67, 69]. The automated k-points grid generator in VASP was employed with a subdivision length of 80. The k-points generated by VASP for these calculations was 19x19x6. The energy convergence criterion of the electronic self-consistency was set at 10<sup>-5</sup> eV/atom for all calculations.

The energies of charge, site, and mass balanced defects in  $\alpha$ -alumina were calculated for defect clusters, i.e. the defects are located next to each other, since

this has been shown to be the most stable configuration [70]. The geometric arrangements of each of the clusters were chosen based on previous computational work. Multiple authors showed that a 30-40 atom supercell of  $\text{Al}_2\text{O}_3$  is sufficient to calculate non-charged defects [70–74]. Multiple authors have studied charged and clustered defects in  $\text{Al}_2\text{O}_3$  [70–74]. They showed that different geometric arrangements and supercell size result in little difference in energy and that the impurity atoms prefer to be clustered due to the binding energy [70–74]. Using this methodology, supercells were generated in the present work with Mg and/or Si clustered, i.e. the Mg-cluster having two Mg atoms substituted for two Al atoms and an oxygen vacancy as nearest neighbors, the Si-cluster having three Si atoms substituted for three Al atoms and an Al vacancy, and the Mg+Si-cluster having one Mg and one Si substituted for two Al atoms.

### 3.4 Sintering and Microstructure Analysis

In chapter 2, it was shown that a glass phase can form during sintering of Bayer alumina. Table 3.2 shows the amounts of liquid in the samples at 1525°C estimated from the  $\text{Al}_2\text{O}_3\text{-Na}_2\text{O}\text{-SiO}_2$  and  $\text{Al}_2\text{O}_3\text{-MgO}\text{-SiO}_2$  phase diagrams based on the amount of  $\text{SiO}_2$ ,  $\text{Na}_2\text{O}$  and  $\text{MgO}$  [60]. It can be seen that the glass volume fraction increases from 0.03 vol.% for  $\text{SiO}_2$  concentrations of 82 ppm to 0.21 vol.% for  $\text{SiO}_2$  concentrations of 582 ppm at 1525°C.

Figure 3.2 shows the dilatometry curves of MgO-doped and MgO-free samples with different  $\text{Na}_2\text{O}$  and  $\text{SiO}_2$  concentrations heated at 10°C/min to 1525°C. For samples with  $\text{SiO}_2$  concentrations of 582 ppm the estimated amount of liquid increases from 0.18 vol.% to 0.21 vol.% during heating from 1250°C to 1525°C, and for samples with 82 ppm  $\text{SiO}_2$  the amount of liquid phase is estimated from the phase diagram to increase from 0.026 vol.% to 0.030 vol.% during heating from 1250°C to 1525°C.

Figure 3.2a shows that the onset of densification (taken as the temperature at which the sample shrinkage is 0.1%) of MgO-doped specialty alumina is shifted from  $\sim 1050^\circ\text{C}$  for samples with 60 ppm  $\text{Na}_2\text{O}$  to  $\sim 1100^\circ\text{C}$  for samples with 560 ppm  $\text{Na}_2\text{O}$ . Samples with 560 ppm  $\text{Na}_2\text{O}$  shrink 1% less than samples with 60 ppm  $\text{Na}_2\text{O}$  after heating to 1525°C. In both the MgO-doped and the MgO-free powders, higher  $\text{SiO}_2$  concentrations retard densification at  $\sim 1250^\circ\text{C}$ . However, the

retardation caused by higher  $\text{SiO}_2$  concentrations is less severe in the MgO-doped powder than in the MgO-free powder; e.g. already at 1300°C, MgO-doped powder samples with 582 ppm  $\text{SiO}_2$  (after the addition of 500 ppm  $\text{SiO}_2$ ) shrink 0.2% less and are 0.5% less dense than samples with 82 ppm  $\text{SiO}_2$ , whereas samples of the MgO-free powder with 603 ppm  $\text{SiO}_2$  shrink 0.5% less and are 3.2% less dense than samples with 103 ppm  $\text{SiO}_2$ . After reaching 1525°C the dilatometry curves show that MgO-doped samples with 582 ppm  $\text{SiO}_2$  (0.21 vol.% glass) shrink 1.8% less and are 5.4% less dense than MgO-doped samples with 82 ppm  $\text{SiO}_2$  (0.03 vol.% glass). In contrast, the retardation of densification caused by the addition of 500 ppm  $\text{SiO}_2$  to the MgO-free powder results in 3.0% less linear shrinkage and 8.7% lower relative densities after heating to 1525°C. MgO-doped (380 ppm) powder samples with 560 ppm  $\text{Na}_2\text{O}$  and 582 ppm  $\text{SiO}_2$  shrink  $\sim$ 2.5% less than samples with 60 ppm  $\text{Na}_2\text{O}$  and 82 ppm  $\text{SiO}_2$  after reaching 1525°C, and MgO-free powder samples with 529 ppm  $\text{Na}_2\text{O}$  and 603 ppm  $\text{SiO}_2$  shrink  $\sim$ 3.0% less than samples with 29 ppm  $\text{Na}_2\text{O}$  and 103 ppm  $\text{SiO}_2$  after reaching 1525°C.

Figure 3.3a and b show how the sintering kinetics of MgO-doped and MgO-free alumina are affected by  $\text{Na}_2\text{O}$  and  $\text{SiO}_2$  after heating at 1450°C and 1525°C for up to 8 h. The density of samples with higher  $\text{SiO}_2$  concentrations, i.e. higher glass concentrations, is lower for all hold times at 1450°C and 1525°C. At 1450°C MgO-doped powder samples with 0.19 vol.% glass phase (582 ppm  $\text{SiO}_2$ ) are 6-7% less dense than samples with 0.027 vol.% glass phase (82 ppm  $\text{SiO}_2$ ), for all hold times (Figure 3.3a). At 1525°C MgO-doped powder samples with 0.21 vol.% glass phase are  $\sim$ 11% and  $\sim$ 2% less dense than samples with 0.03 vol.% glass phase after heating for 0 h and 8 h, respectively, and samples with 0.03 vol.% glass phase reach densities  $>$ 98% after 1 h, whereas samples with 0.066 and 0.21 vol.% glass phase are only  $\sim$ 96% and  $\sim$ 94% dense, respectively (Figure 3.3b).

The effect of  $\text{Na}_2\text{O}$  concentration on densification strongly depends on glass phase concentration. In all samples a higher  $\text{Na}_2\text{O}$  concentration initially retards densification. For example, after 0 h at 1450°C the relative density of samples with 0.03 vol.% glass phase and 560 ppm  $\text{Na}_2\text{O}$  is  $\sim$ 3% lower than the relative density of samples containing the same amount of glass phase and 60 ppm  $\text{Na}_2\text{O}$ . However, there is no difference in sintered density after 3 h at either 1450°C or 1525°C. For samples with higher glass phase concentrations (e.g., 0.21 vol.%) the effect of  $\text{Na}_2\text{O}$  on the densification is more complicated, due to the changing  $\text{Na}_2\text{O}/\text{SiO}_2$  ratio from

0.1 to 0.9 (Table 3.2). Samples with 0.21 vol.% glass phase and  $\text{Na}_2\text{O}/\text{SiO}_2$  ratios of 0.9 are 1-2% denser than samples with 0.21 vol.% glass phase and  $\text{Na}_2\text{O}/\text{SiO}_2$  ratios of 0.1. However, after 30 min at 1525°C the relative density of samples with 0.21 vol.% glass phase and  $\text{Na}_2\text{O}/\text{SiO}_2$  ratios of 0.9 in the glass phase is 0.9% lower than the relative density of samples with 0.21 vol.% glass phase and  $\text{Na}_2\text{O}/\text{SiO}_2$  ratios of 0.1 in the glass phase, and after 1 h or longer at 1525°C there is no difference in relative density. Samples with 0.066 vol.% glass phase are 98.3 - 98.6% dense after 8 h at 1525°C, and samples with 0.21 vol.% glass phase are 97.1% - 97.5% dense after 8 h at 1525°C.

Comparing the as-received MgO-free and MgO-doped powders with 0.03 vol.% glass phase shows that doping with 380 ppm MgO leads to 1% higher densities for all hold times at 1525°C (Figure 3.3b and c). After 8 h at 1525°C the MgO-doped samples with 0.21 vol.% glass phase are ~2% less dense than samples with 0.03 vol.% glass phase, whereas the addition of 500 ppm  $\text{SiO}_2$  (total of 603 ppm  $\text{SiO}_2$  and 0.22 vol.% glass) to the MgO-free powder leads to ~4% less dense samples. MgO-free and MgO-doped Bayer alumina samples containing 0.22 and 0.21 vol.% glass phase, respectively, and global  $\text{Na}_2\text{O}/\text{SiO}_2$  ratios of 0.9 show initial retardation of densification compared to samples with  $\text{Na}_2\text{O}/\text{SiO}_2$  ratios of 0.1, but have higher densities than samples with  $\text{Na}_2\text{O}/\text{SiO}_2$  ratios of 0.1 after further heating. This increased densification can be explained by the increased solubility of  $\text{Al}_2\text{O}_3$  into the liquid grain boundary phase and the higher diffusivity (lower viscosity of the grain boundary phase) as the  $\text{Na}_2\text{O}/\text{SiO}_2$  ratio increases [3,52]. However, after hold times of 1 h or longer at 1525°C, MgO-free powder samples with 0.22 vol.% glass phase and  $\text{Na}_2\text{O}/\text{SiO}_2$  ratios of 0.9 are 1% denser than samples with 0.22 vol.% glass phase and  $\text{Na}_2\text{O}/\text{SiO}_2$  ratios of 0.1, whereas MgO-doped powder samples with 0.21 vol.% and  $\text{Na}_2\text{O}/\text{SiO}_2$  ratios of 0.9 have the same densities as samples with 0.21 vol.% glass phase and  $\text{Na}_2\text{O}/\text{SiO}_2$  ratios of 0.1.

The microstructures of samples with different vol.% glass phase and different  $\text{Na}_2\text{O}/\text{SiO}_2$  ratios heated at 1525°C for 8 h are shown in Figure 3.4. Samples with 60 ppm  $\text{Na}_2\text{O}$  show mostly equiaxed grains, regardless of the glass phase concentration in the samples (Figures 3.4a and c). Samples with 560 ppm  $\text{Na}_2\text{O}$  (Figures 3.4b and d) show more faceted  $\alpha\text{-Al}_2\text{O}_3$  grains and appear to have a wider grain size distribution than samples with 60 ppm  $\text{Na}_2\text{O}$ . These effects are more pronounced in samples with higher glass concentrations. The grain sizes of samples

with 0.21 vol.% glass are less than the grain sizes of samples with 0.03 vol.% glass phase.

The average grain sizes of samples with different vol.% glass phase and different  $\text{Na}_2\text{O}/\text{SiO}_2$  ratios are plotted as a function of relative density in Figure 3.5. Grain growth starts when the final sintering stage is reached, between 85 and 92% relative density. Samples with 0.03 vol.% glass phase and 60 ppm  $\text{Na}_2\text{O}$  show a three-fold increase in grain size, from  $0.5 \mu\text{m}$  to  $\sim 1.5 \mu\text{m}$ , when the relative density increases from 68% to 99%, and samples with 0.03 vol.% glass phase and 560 ppm  $\text{Na}_2\text{O}$  have a somewhat larger grain size of  $2.2 \mu\text{m}$  at 99% relative density. When relative densities of  $\sim 99\%$  are reached in samples with 0.03 vol.% glass, the grain size increases to  $3.1 - 3.4 \mu\text{m}$  when heated at  $1525^\circ\text{C}$  for 8 h. Samples with higher glass concentrations have a similar trajectory up to 92% density. However, at densities  $>92\%$  the grain size of samples with higher glass phase concentrations increases stronger at lower densities compared to samples with lower densities. For example, 97.0-97.5% dense samples with glass phase concentrations of 0.21 and 0.17 vol.% have grain sizes of  $2.6$  and  $2.4 \mu\text{m}$ , respectively, whereas samples with glass phase concentrations of 0.03 vol.% have a grain size of  $1.5 \mu\text{m}$  at the same relative density.

## 3.5 Mechanistic Interpretation

If the mechanism of  $\text{MgO}$  increasing the solubility of  $\text{SiO}_2$  in alumina, as proposed by Handwerker et al. [16], is responsible for the improved sintering behavior of alumina, then the amount of liquid phase in  $\text{MgO}$ -doped alumina should be less than calculated and less than in  $\text{MgO}$ -free samples, and, the grain boundary thickness in  $\text{MgO}$ -doped alumina should be less than in  $\text{MgO}$ -free powder. The reduced grain boundary thickness in  $\text{MgO}$ -doped alumina should lead to a change in grain boundary chemistry and different sintering behavior after this co-dissolution has occurred compared to  $\text{MgO}$ -free alumina.

Comparing the dilatometry curves and sintering kinetics of  $\text{MgO}$ -doped and  $\text{MgO}$ -free Bayer alumina powders with different chemistries shows that there are two stages at which  $\text{MgO}$  affects densification. At  $1250^\circ\text{C}$  increased  $\text{SiO}_2$  concentrations retard densification, and at the same stage there is an enhancement of densification due to  $\text{MgO}$ . This suggests that there is a direct interaction between  $\text{SiO}_2$  and  $\text{MgO}$  at this stage, where  $\text{MgO}$  mitigates the negative effect of  $\text{SiO}_2$ . In ultrahigh purity

alumina  $\text{SiO}_2$  has been reported to decrease the concentration of Al interstitials and O vacancies, which decreases the diffusion rate during intermediate stage sintering ( $>1200^\circ\text{C}$ ) [76]. However, a liquid phase forms during the sintering of Bayer alumina at temperatures as low as  $1200^\circ\text{C}$  due to the presence of other impurities and dopants such as  $\text{Na}_2\text{O}$  and  $\text{MgO}$ . Therefore, Bayer alumina densifies by liquid phase sintering. The  $\text{Al}_2\text{O}_3$ - $\text{SiO}_2$ - $\text{MgO}$  phase diagram suggests that  $\text{MgO}$  increases the solubility of  $\text{Al}_2\text{O}_3$  in the liquid, and  $\text{MgO}$  can lower the viscosity of the glass melt [55], which results in higher diffusion coefficients. The enhanced diffusion associated with the lower viscosity and higher solubility of  $\text{Al}_2\text{O}_3$  in the glass phase can explain why  $\text{MgO}$  positively affects the sintering of alumina at stages when  $\text{SiO}_2$  would negatively affect densification.

The second stage at which  $\text{MgO}$  affects densification is after 1 h at  $1525^\circ\text{C}$ .  $\text{MgO}$ -free powder samples with 0.22 vol.% glass phase and  $\text{Na}_2\text{O}/\text{SiO}_2$  ratios of 0.9 have 1-2% higher relative densities than samples with 0.22 vol.% glass phase and  $\text{Na}_2\text{O}/\text{SiO}_2$  ratios of 0.1 for all hold times at  $1525^\circ\text{C}$ . In previous work we calculated an expected grain boundary thickness of 1.3 nm for samples with 0.22 vol.% glass phase after 3 h at  $1525^\circ\text{C}$ , based on the observed grain size of  $1.6 \mu\text{m}$  assuming spherical monodispersed grains as an approximation.. The addition of 500 ppm  $\text{Na}_2\text{O}$  increases the  $\text{Na}_2\text{O}/\text{SiO}_2$  ratio from 0.1 to 0.9, which modifies the liquid grain boundary phase and enhances densification as shown in Chapter 2. Figure 3.6 shows a high-resolution TEM image of a grain boundary of a  $\text{MgO}$ -free powder sample (2 ppm  $\text{MgO}$ ) with 0.22 vol.% glass phase and a  $\text{Na}_2\text{O}/\text{SiO}_2$  ratio of 0.9 after 3 h at  $1525^\circ\text{C}$ . It can be seen that the measured grain boundary thickness of 1.7 nm is close to the grain boundary thickness calculated based on the amount of glass phase in the sample.  $\text{MgO}$ -doped powder samples with 0.21 vol.% glass phase and  $\text{Na}_2\text{O}/\text{SiO}_2$  ratios of 0.9 have 1-2% higher densities than samples with 0.21 vol.% glass phase and  $\text{Na}_2\text{O}/\text{SiO}_2$  ratios of 0.1 for most hold times at  $1450^\circ\text{C}$  and for hold times  $< 30$  min at  $1525^\circ\text{C}$ . This difference in densification behavior is similar to the densification behavior of  $\text{MgO}$ -free powder samples, which suggests the presence of a liquid phase that is modified by  $\text{Na}_2\text{O}$ , as seen in the  $\text{MgO}$ -free alumina samples.

Figure 3.7a shows a high resolution TEM image of a grain boundary in an  $\text{MgO}$ -doped alumina sample with 0.21 vol.% glass phase and a  $\text{Na}_2\text{O}/\text{SiO}_2$  ratio of 0.9 after 0 h at  $1525^\circ\text{C}$ . The measured grain boundary thickness of  $\sim 1.4$  nm for

this sample is in agreement with the theoretically estimated [3] grain boundary thickness. However, after 1 h or longer at 1525°C, samples with 0.21 vol.% glass and Na<sub>2</sub>O/SiO<sub>2</sub> ratios of 0.9 have the same densities as samples with 0.21 vol.% glass and Na<sub>2</sub>O/SiO<sub>2</sub> ratios of 0.1, and the grain boundary thicknesses of those samples after 3 h at 1525°C are ~0.5 nm (Figure 3.7b) and substantially thinner than the calculated grain boundary thickness of 1.4 nm.

The thinner grain boundary demonstrates that the addition of MgO causes a reduction of the amount of liquid phase in the grain boundaries after longer time at 1525°C. In the literature it is reported that excess liquid phase, after an equilibrium grain boundary thickness [75] is reached, can accumulate in triple pockets. However, we did not observe any triple pockets in the 380 ppm MgO-doped samples with 0.21 vol.% glass. Therefore, the impurities and dopants that formed the liquid phase after 0 h have to be distributed elsewhere in the sample after 3 h at 1525°C. Since SiO<sub>2</sub>-containing second phases, such as mullite or cordierite, were not observed in the samples, we hypothesize that SiO<sub>2</sub> and MgO form a solid solution in  $\alpha$ -alumina, as proposed by Handwerker et al. [16]. This co-dissolution mechanism could significantly reduce the total amount of SiO<sub>2</sub> and, therefore, the liquid phase content in the samples and in the grain boundaries.

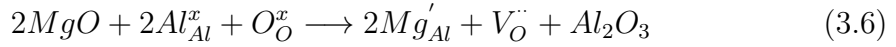
The EDS maps in Figure 3.8 show the distribution of Si around a grain boundary in MgO-doped samples with a calculated glass concentration of 0.21 vol.% after 0 h and 3 h at 1525°C. Figure 3.9 shows the corresponding EDS line scans for Si and Mg across the grain boundaries. After 0 h at 1525°C SiO<sub>2</sub> and MgO are strongly concentrated in the grain boundaries, and a chemical grain boundary thickness,  $\delta_{chem}$ , of ~1.7 nm is estimated (Figures 3.8a and 3.9a), which is close to the structural grain boundary thickness of 1.4 nm measured from the high resolution TEM image (Figure 3.7a). After 3 h at 1525°C MgO and SiO<sub>2</sub> are still concentrated on the grain boundary, however, the chemical grain boundary thickness,  $\delta_{chem}$ , is ~3.2 nm (Figure 3.8b and 3.9b) and substantially thicker than the observed structural grain boundary thickness,  $\delta_{str}$ , of ~0.5 nm (Figure 3.7b). This difference in structural and chemical grain boundary thickness after 3 h supports the argument that MgO and SiO<sub>2</sub> form a solid solution in the alumina lattice in the near grain boundary region. If we assume that equal amounts of MgO and SiO<sub>2</sub> dissolve into the alumina lattice to form the proposed defect complex, and that all MgO in the sample is consumed by this process, then 380 ppm SiO<sub>2</sub> must be removed from the

amorphous grain boundary phase. This would leave 202 ppm SiO<sub>2</sub> in the grain boundaries to form the amorphous film with a calculated grain boundary thickness of 0.5 nm, which agrees with the observed grain boundary thickness of 0.5 nm.

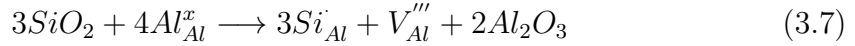
To further evaluate whether MgO and SiO<sub>2</sub> form a solid solution in  $\alpha$ -alumina we conducted first-principles calculations based on density functional theory to gain insight into the thermodynamic stability of Mg<sup>2+</sup> and Si<sup>4+</sup> by themselves and together in the  $\alpha$ -alumina structure. To ensure the accuracy of the calculations, the lattice parameters and energy of the  $\alpha$ -alumina structure without any substitutions are compared with previous experiments and calculations in Table 3.3. The calculated lattice parameters match well with experimental values and lattice parameters from previous first-principles calculations [70, 77–81]. The difference between the present and past first-principles calculations can be attributed to the different input parameters used.

We calculated the energy of a unit cell of the  $\alpha$ -alumina structure with substitutions according to the following balanced equations:

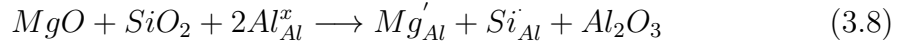
Mg-Cluster:



Si-Cluster:



Mg+Si-Cluster:



Defect simulations of aliovalent cation substitutions in alumina [70] showed that the dominant compensation mechanisms for Mg<sup>2+</sup> and Si<sup>4+</sup> by themselves in alumina are the formation of oxygen and aluminum vacancies, respectively (Eq. 3.6 and 3.7). In Eq. 3.8 Mg<sup>2+</sup> and Si<sup>4+</sup> compensate for each other's charge and the formation of vacancies or interstitials is unnecessary to account for dissolution in the alumina lattice. The calculations were carried out for clustered defects since they are lower in energy than isolated defects [70]. The structures were relaxed and the formation

energies as a function of temperature with bulk  $\text{Al}_2\text{O}_3$  as the reference state are plotted in Figure 3.10. It can be seen that the formation energy for the Mg+Si-cluster,  $E_{Form}^{Mg+Si}$ , is lower than the formation energies of the Mg-cluster,  $E_{Form}^{Mg}$ , and the Si-cluster,  $E_{Form}^{Si}$ , which shows that the Mg+Si-cluster is more stable than the Mg-cluster and the Si-cluster. Since two  $\text{Mg}^{2+}$  ions and three  $\text{Si}^{4+}$  ions are necessary to form the Mg-cluster and Si-cluster, respectively, but only one  $\text{Mg}^{2+}$  and one  $\text{Si}^{4+}$  are required to form the Mg+Si-cluster, the formation energies of the clusters can be compared by

$$\Delta E_{Form} = E_{Form}^{Mg+Si} - \left( \frac{1}{3}E_{Form}^{Si} + \frac{1}{2}E_{Form}^{Mg} \right) \quad (3.9)$$

The formation energy difference,  $\Delta E_{Form}$ , is plotted in Figure 3.10 and it can be seen that  $\Delta E_{Form}$  is negative at all temperatures, which means that the Mg+Si-cluster is more energetically favored to form than the Mg-cluster or Si-cluster. This shows that  $\text{MgO}$  and  $\text{SiO}_2$  have a higher co-solubility in  $\alpha$ -alumina than  $\text{MgO}$  or  $\text{SiO}_2$  by themselves. In  $\alpha$ -alumina the  $\text{Al}^{3+}$  cation sites are 6-fold coordinated and  $\text{Al}^{3+}$  has an effective ionic radius of 53.5 pm, while the radii of  $\text{Mg}^{2+}$  and  $\text{Si}^{4+}$  are 72 pm and 40 pm, respectively. Therefore,  $\text{Mg}^{2+}$  and  $\text{Si}^{4+}$  can compensate for each other's size and charge difference relative to  $\text{Al}^{3+}$  in the  $\alpha$ -alumina lattice, which explains the lower energy of the Mg+Si-cluster. The stable phases for  $\text{MgO}$  and/or  $\text{SiO}_2$  and  $\text{Al}_2\text{O}_3$  are spinel, cordierite, and mullite. However, we hypothesize that if both  $\text{MgO}$  and  $\text{SiO}_2$  are present at low concentrations, then it is more favorable for  $\text{MgO}$  and  $\text{SiO}_2$  to form a solid solution in the  $\alpha$ -alumina structure than to form a second phase or remain in the grain boundaries as a siliceous liquid phase.

The described mechanism could also influence the distribution of other oxides in the samples, such as  $\text{Fe}_2\text{O}_3$ ,  $\text{CaO}$ , and  $\text{Na}_2\text{O}$ . Figure 3.11 shows the element distribution obtained from EDS of two grain boundaries in samples sintered at 1525°C for 0 h and 3 h, respectively. Figures 3.11a and e show the segregation of  $\text{MgO}$  to the grain boundaries after 0 h and 3 h, respectively, and it can be seen that after 0 h at 1525°C Mg is more strongly concentrated in the grain boundary than after 3 h at 1525°C, due to the mechanism described above. From Figures 3.11b and f it can be seen that there is no segregation of  $\text{Fe}_2\text{O}_3$ , which indicates that  $\text{Fe}_2\text{O}_3$  is in solid solution in the alumina lattice [70], since  $\alpha$ - $\text{Al}_2\text{O}_3$  and  $\alpha$ - $\text{Fe}_2\text{O}_3$  are isostructural and the  $\text{Al}_2\text{O}_3$ - $\text{Fe}_2\text{O}_3$  phase diagram shows considerable solubility [82].

Figures 3.11c, d, g, and h show that there is a slightly higher Na and Ca signal coming from the grain boundaries, showing that Na and Ca segregate to the grain boundaries and are components of the liquid grain boundary phase. Ca is more concentrated in the grain boundary after 3 h at 1525°C, due to the narrower grain boundary thickness (Figure 3.7b).

It can be seen that the Na signal after 0 h at 1525°C (Figure 3.11c) shows a slight segregation of Na to the grain boundary, but after 3 h at 1525°C (Figure 3.11g) no segregation can be observed. It should also be noted that it is challenging to detect Na using EDS since the Na signal disappears quickly after the high-voltage electron beam is focused on the grain boundary. Therefore, we believe that there is still Na on the grain boundaries, even though the EDS map does not show an increased Na signal. However, since the Na signal is lower, we believe that after 3 h at 1525°C there is less Na<sub>2</sub>O on the grain boundaries than after 0 h at 1525°C. The reduced amount of Na might be a result of volatilization of Na<sub>2</sub>O during sintering. Figure 3.12 shows the influence of sintering time and temperature on the Na<sub>2</sub>O concentration, obtained by ICP analysis, during sintering for samples with target concentrations of 560 ppm Na<sub>2</sub>O. Between 1300°C and 1525°C the Na<sub>2</sub>O concentration is constant at ~510 ppm, which is 50 ppm below the target level. The lower Na<sub>2</sub>O concentration might be due to volatilization at earlier stages. After heating to 1600°C there is a loss of ~250 ppm or a ~50% decrease in Na<sub>2</sub>O concentration (Figure 3.12a). After sintering at 1525°C for 30 min the Na<sub>2</sub>O concentration decreases by about 210 ppm or 40%, but remains constant at ~300 ppm when heated to 1525°C for up to 8 h (Figure 3.12b). This Na<sub>2</sub>O loss between 0 and 30 min at 1525°C can explain the lower Na signal in Figure 3.11g.

As explained earlier, the described dissolution of MgO and SiO<sub>2</sub> into the alumina lattice reduces the amount of glass phase in the grain boundaries. Since only SiO<sub>2</sub> is removed from the glass phase and other components of the glass phase, such as CaO and Na<sub>2</sub>O remain, the grain boundaries can supersaturate. This can eventually lead to the nucleation of second phases, which was observed for samples with lower SiO<sub>2</sub> concentrations of 82 and 182 ppm.

## 3.6 Summary and Conclusion

The effect of MgO on the sintering of Bayer alumina powders with different chemistry was analyzed by comparing the sintering kinetics of MgO-free and MgO-doped Bayer aluminas with different impurity levels and ratios of Na<sub>2</sub>O and SiO<sub>2</sub>. TEM images of grain boundaries shows that the grain boundary thickness of MgO-doped Bayer alumina is reduced during densification at 1525°C and are thinner than observed in MgO-free Bayer alumina. EDS analysis suggests that MgO and SiO<sub>2</sub> have an increased co-solubility in the alumina lattice when present together. This co-dissolution mechanism was supported by DFT-based first-principles calculations showing that the formation energy of MgO and SiO<sub>2</sub> together in the alumina lattice is lower than the formation energies of MgO or SiO<sub>2</sub> by themselves in the alumina lattice. The reduced amount of SiO<sub>2</sub> on the grain boundaries of MgO-doped alumina leads to enhanced densification compared to MgO-free alumina because SiO<sub>2</sub> has been shown to retard densification.

The present study supports the hypothesis of Handwerker et al. [16] and high resolution SIMS observations of Gavrilov et al. [2] that the key mechanism responsible for the beneficial effect of MgO on the sintering of alumina is the reduction of amorphous phase in the grain boundaries by increasing the solubility of SiO<sub>2</sub> in the alumina lattice.

**Table 3.1.** Physical and chemical characteristics of the as-received 380 ppm MgO-doped Bayer alumina powder used in this study.

BET ( $\text{m}^2/\text{g}$ )	7.3
$D_{50}$ ( $\mu\text{m}$ )	0.4
$D_{90}$ ( $\mu\text{m}$ )	1.4
	ICP (ppm)
$\text{Al}_2\text{O}_3$	99.92 %
$\text{SiO}_2$	82
$\text{Na}_2\text{O}$	60
$\text{Fe}_2\text{O}_3$	140
$\text{CaO}$	51
$\text{TiO}_2$	8
MgO	380

**Table 3.2.** Calculated compositions and amounts of liquid in 380 ppm MgO-doped Bayer alumina samples of different chemistries at 1450°C and 1525°C.

Na <sub>2</sub> O/SiO <sub>2</sub> concentration		Global Na <sub>2</sub> O/SiO <sub>2</sub> ratio	Na <sub>2</sub> O:SiO <sub>2</sub> ratio in the liquid	Vol. % of liquid in sample	
ppm by wt.	ppm by mole			1450°C	1525°C
60/82 - 560/82	99/139 - 921/139	0.7 - 6.6	0.5	0.027	0.030
185/182 - 560/182	304/309 - 921/309	1.0 - 3.0	0.5	0.060	0.066
60/582	99/987	0.1	0.1	0.19	0.21
560/582	921/987	0.9	0.5	0.19	0.21

**Table 3.3.** Lattice parameters and equilibrium energy ( $E_0$ ) compared to previous first-principles and experimental values.

Reference	$E_0$ (eV/atom)	$a$ (Å)	$b$ (Å)	$c$ (Å)
This work	-7.48	4.76	4.76	12.99
Calc. [77–81]	-7.48	4.78	4.78	13.00
Expt. [70]		4.76	4.76	13.00

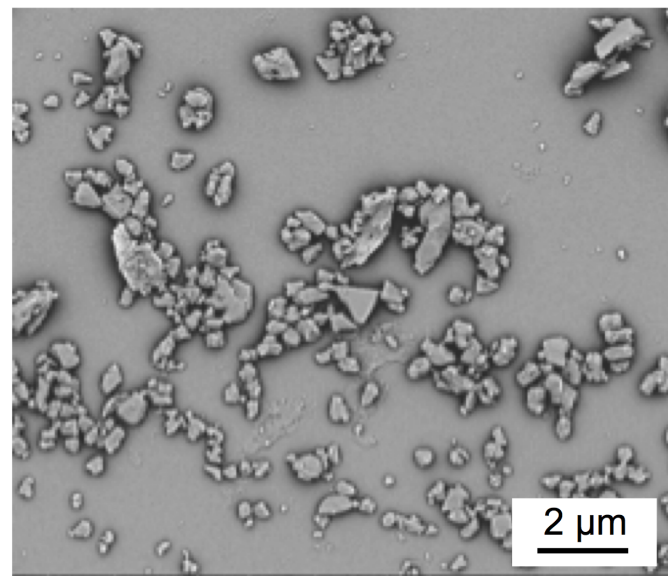


**Figure 3.1.** SEM image of 380 ppm MgO-doped Bayer alumina powder used in this work.

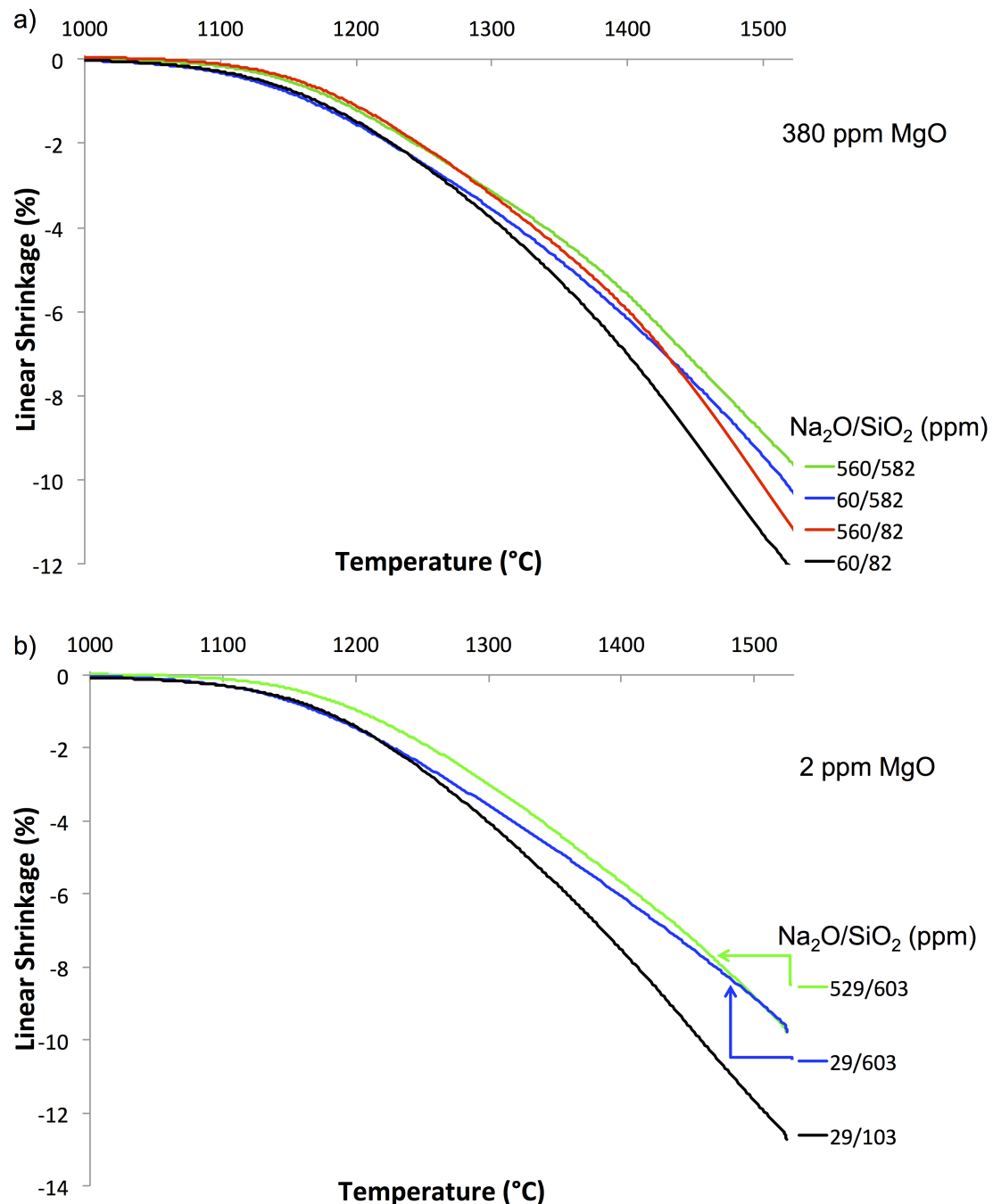


**Figure 3.2.** Dilatometer curves of a) 380 ppm MgO-doped and b) MgO-free [3] Bayer alumina samples with different  $\text{Na}_2\text{O}/\text{SiO}_2$  levels heated at  $10^\circ\text{C}/\text{min}$  to  $1525^\circ\text{C}$ .

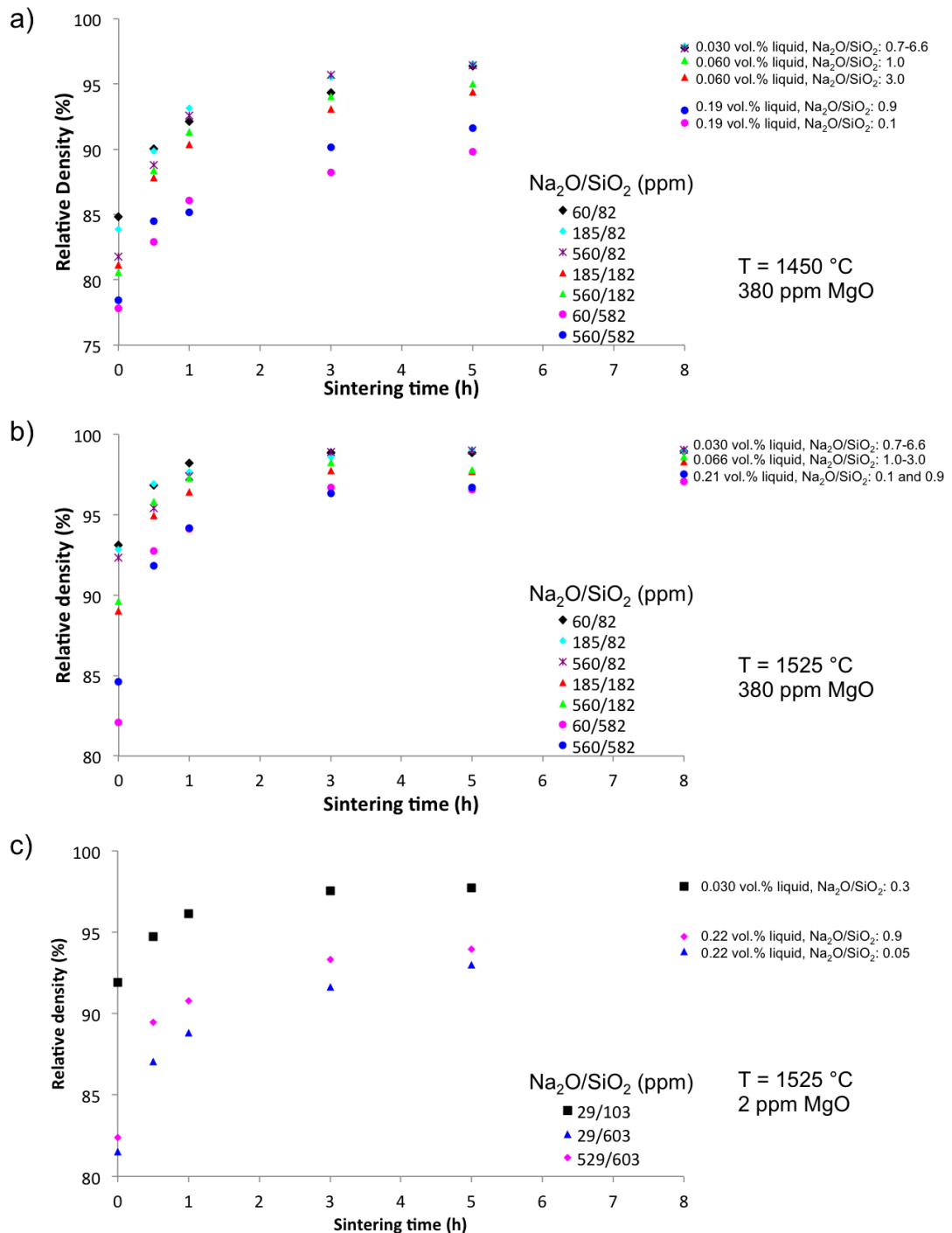


**Figure 3.3.** Densification kinetics of Bayer processed alumina containing different amounts Na<sub>2</sub>O and SiO<sub>2</sub> and a) 380 ppm MgO sintered at 1450°C, b) 380 ppm MgO sintered at 1525°C, and c) 2 ppm MgO sintered at 1525°C [3].

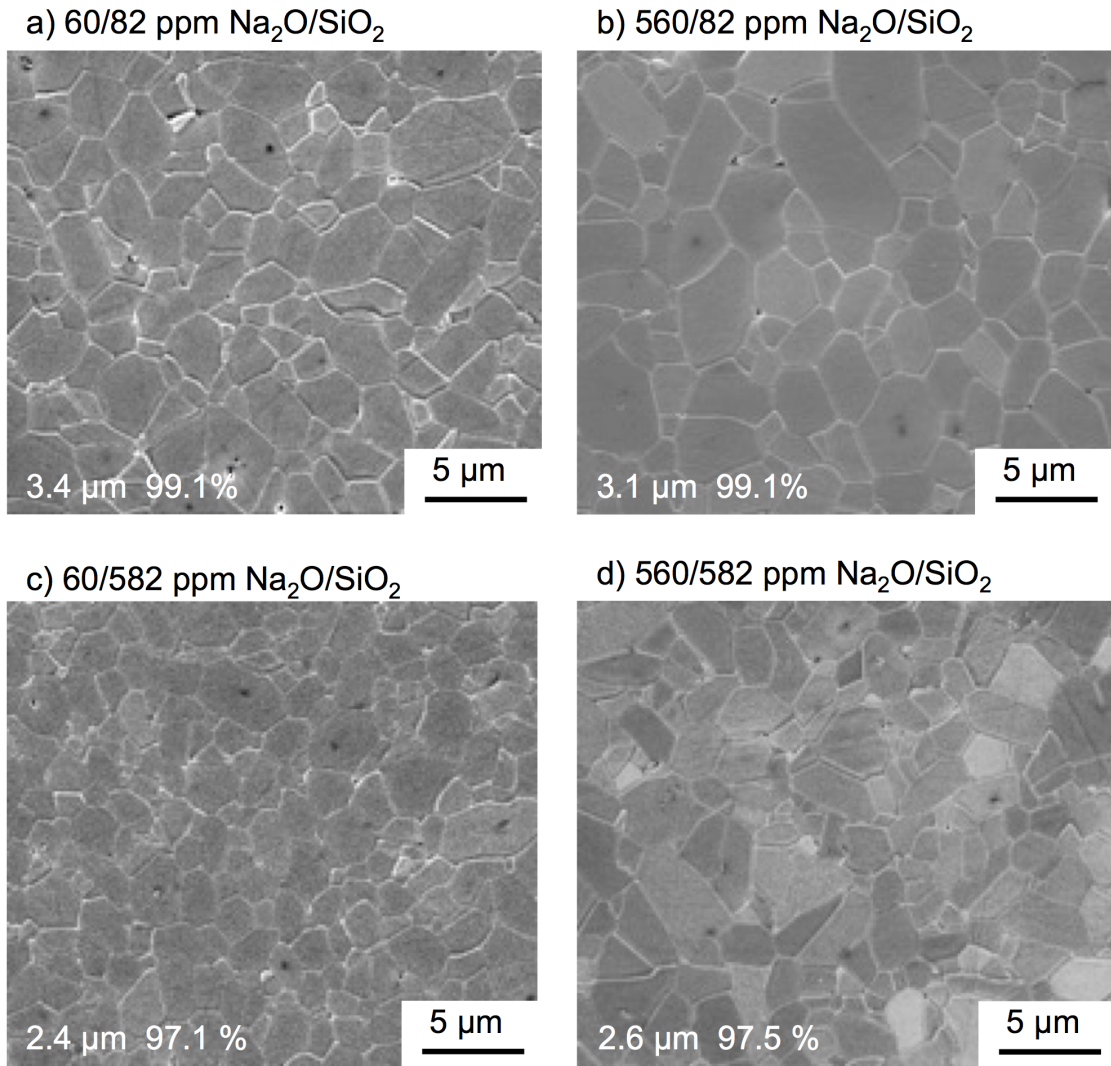


**Figure 3.4.** Microstructures of 380 ppm MgO-doped Bayer alumina samples with different  $\text{Na}_2\text{O}$  and  $\text{SiO}_2$  concentrations sintered at 1525°C for 8 h.

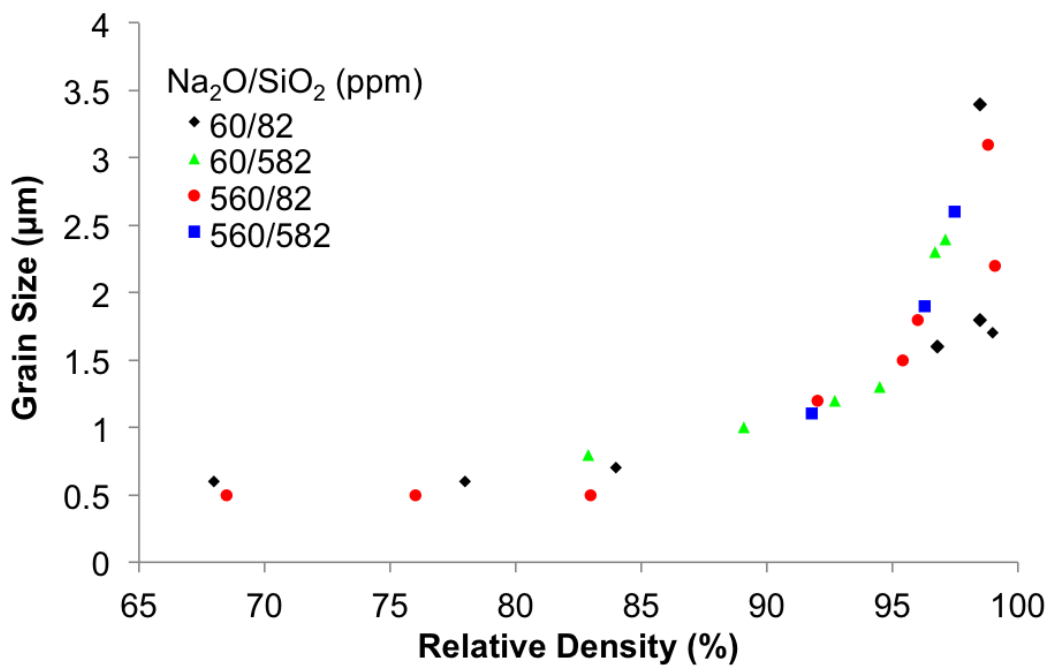


**Figure 3.5.** Sintering trajectories (grain size vs. relative density) for 380 ppm MgO-doped Bayer alumina samples with different Na<sub>2</sub>O and SiO<sub>2</sub> concentrations.

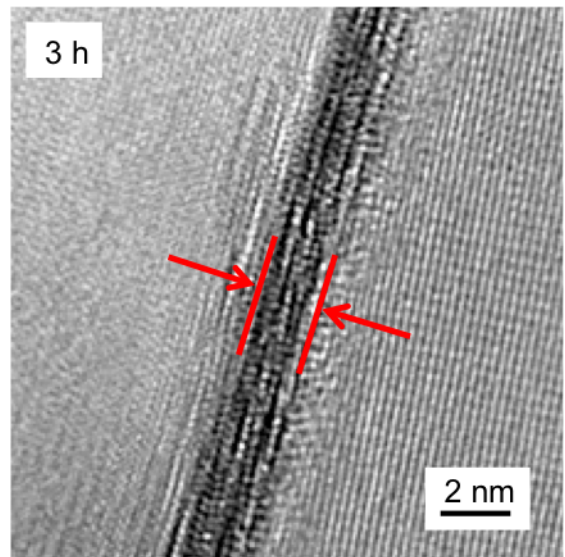


**Figure 3.6.** Grain boundary of a sample containing 529 ppm Na<sub>2</sub>O, 603 ppm SiO<sub>2</sub>, and 2 ppm MgO after 3 h at 1525°C.

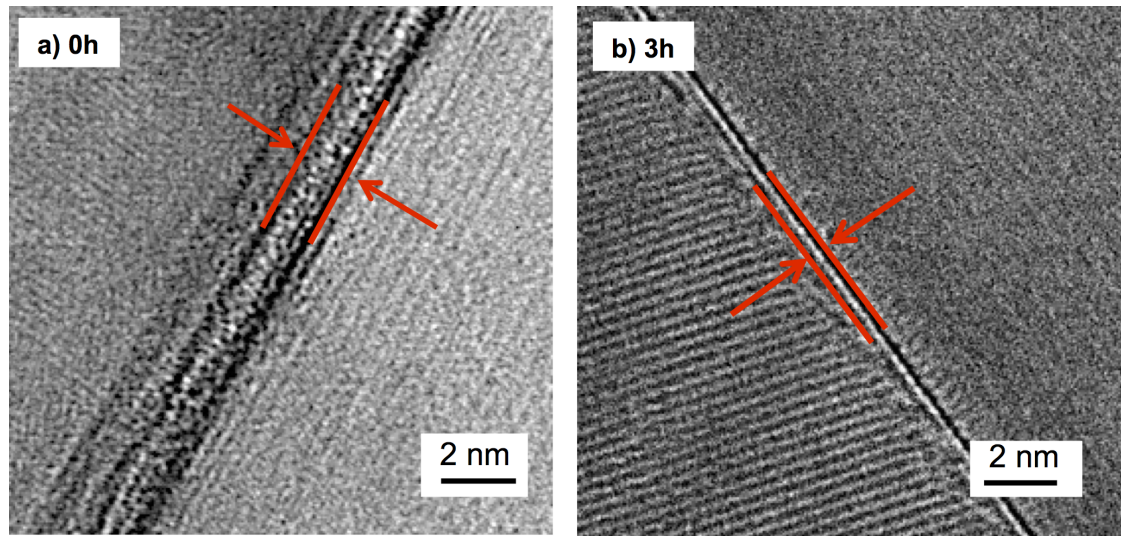


**Figure 3.7.** Grain boundaries of samples containing 560 ppm Na<sub>2</sub>O, 582 ppm SiO<sub>2</sub>, and 380 ppm MgO after a) 0 h and b) 3 h at 1525°C.

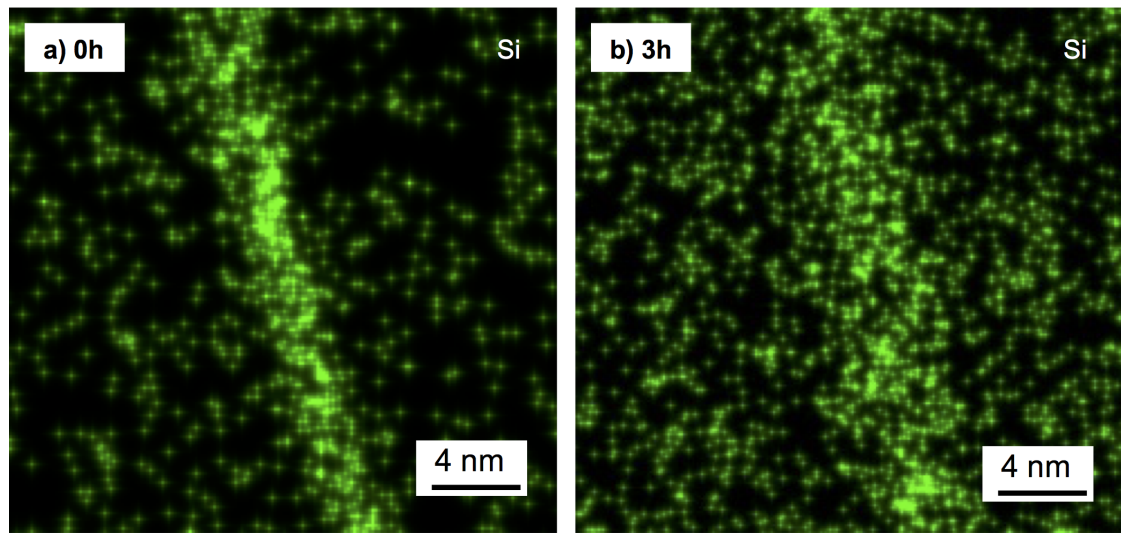


**Figure 3.8.** EDS of grain boundaries of samples containing 560 ppm Na<sub>2</sub>O, 582 ppm SiO<sub>2</sub>, and 380 ppm MgO after a) 0 h and b) 3 h at 1525°C showing the Si distribution. After 0 h Si shows a stronger segregation to the grain boundaries than after 3 h.

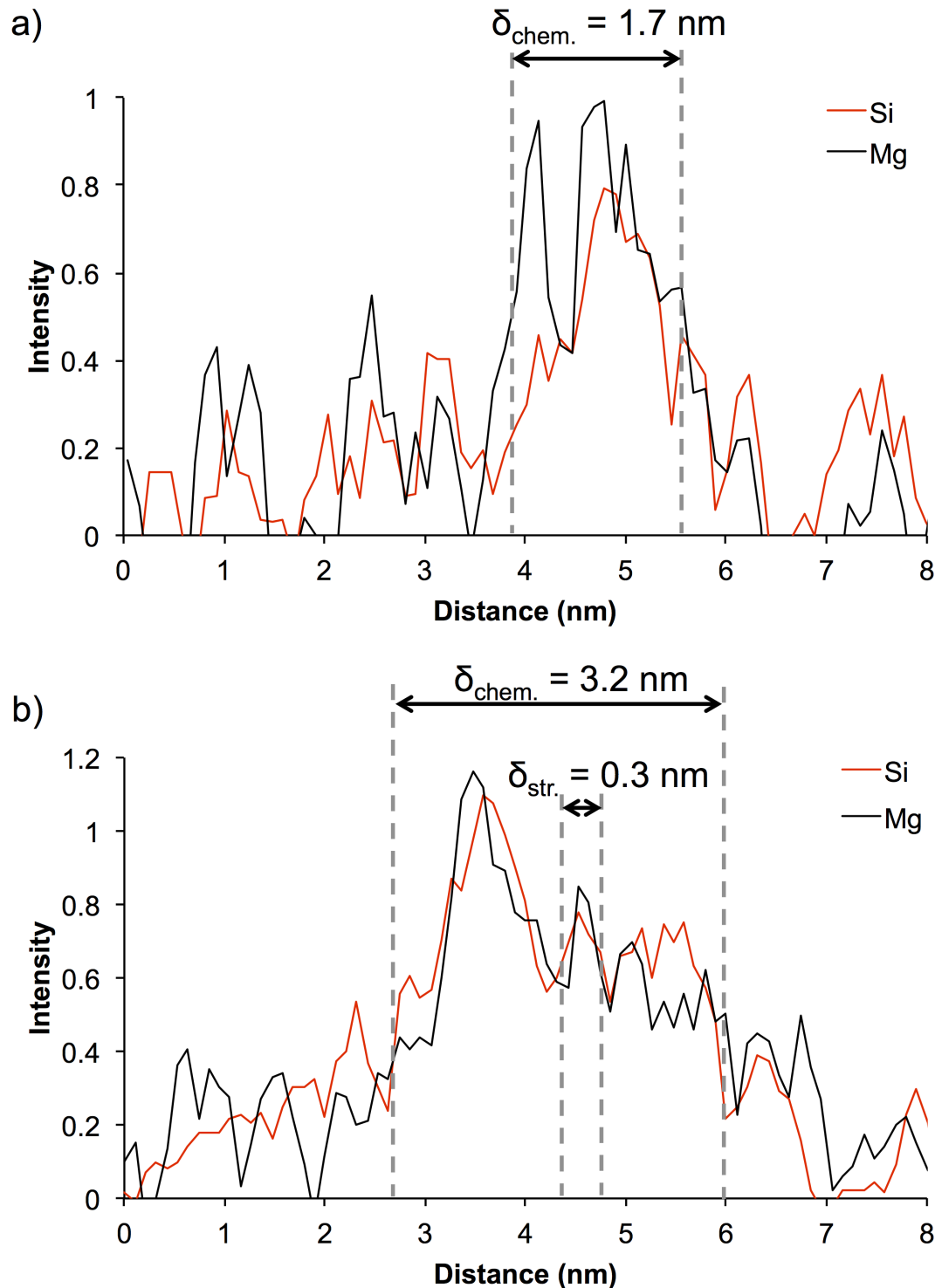


**Figure 3.9.** EDS line scan across a grain boundary of a sample containing 560 ppm Na<sub>2</sub>O, 582 ppm SiO<sub>2</sub>, and 380 ppm MgO after sintering at 1525°C for a) 0 h and b) 3 h.

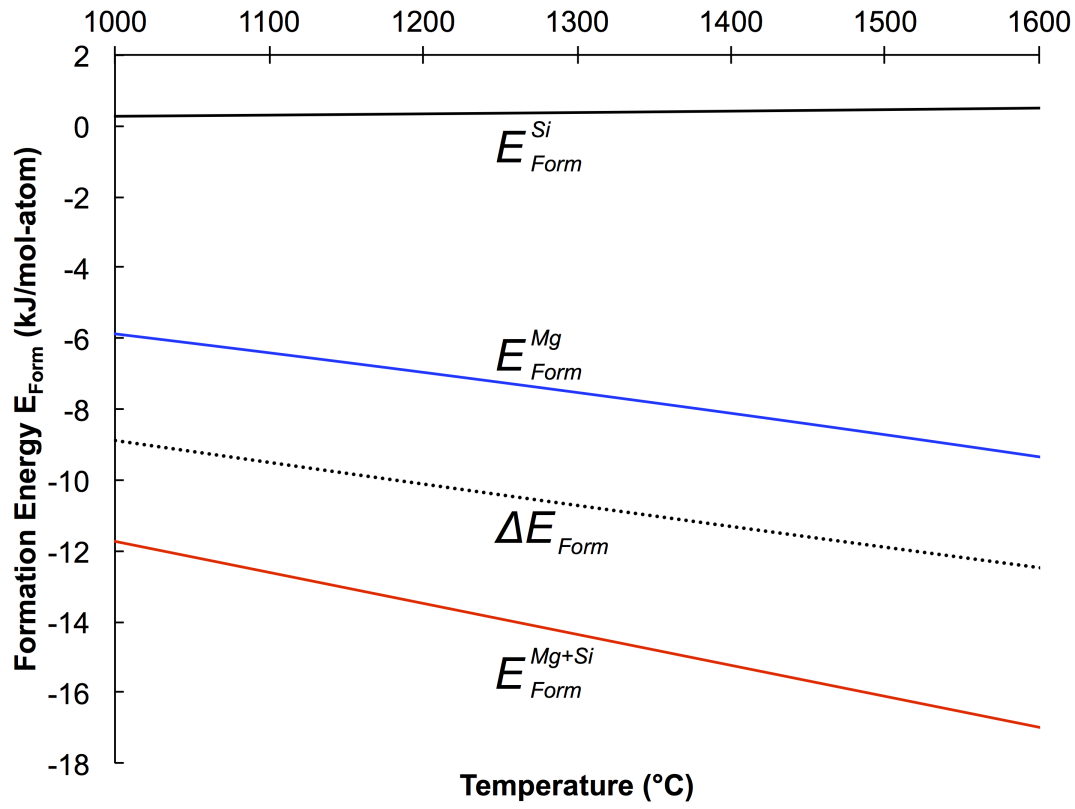


**Figure 3.10.** Comparison of the formation energy of  $\alpha\text{-Al}_2\text{O}_3$  with an Mg-cluster ( $E_{Form}^{Mg}$ ), Si-cluster ( $E_{Form}^{Si}$ ) and Mg+Si-cluster ( $E_{Form}^{Mg+Si}$ ) as a function of temperature. The formation energy difference ( $\Delta E_{Form}$ ) between the structures was calculated from Eq. 3.9 to compare the formation energy values and show that it is energetically favorable to form Mg+Si-clusters over Si-clusters and Mg-clusters.

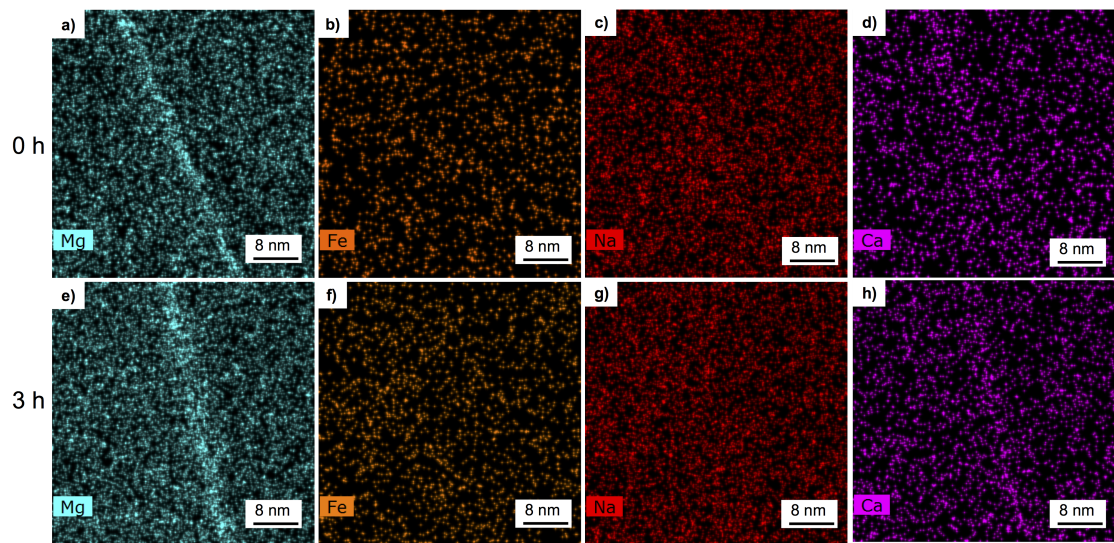


**Figure 3.11.** EDS maps of different oxides in 380 ppm MgO-doped Bayer alumina samples after sintering at 1525°C for a-d) 0 h and e-h) 3 h. a) and e) show the distribution of Mg, b) and f) show the distribution of Fe, c) and g) show the distribution of Na, and d) and h) show the distribution of Ca.

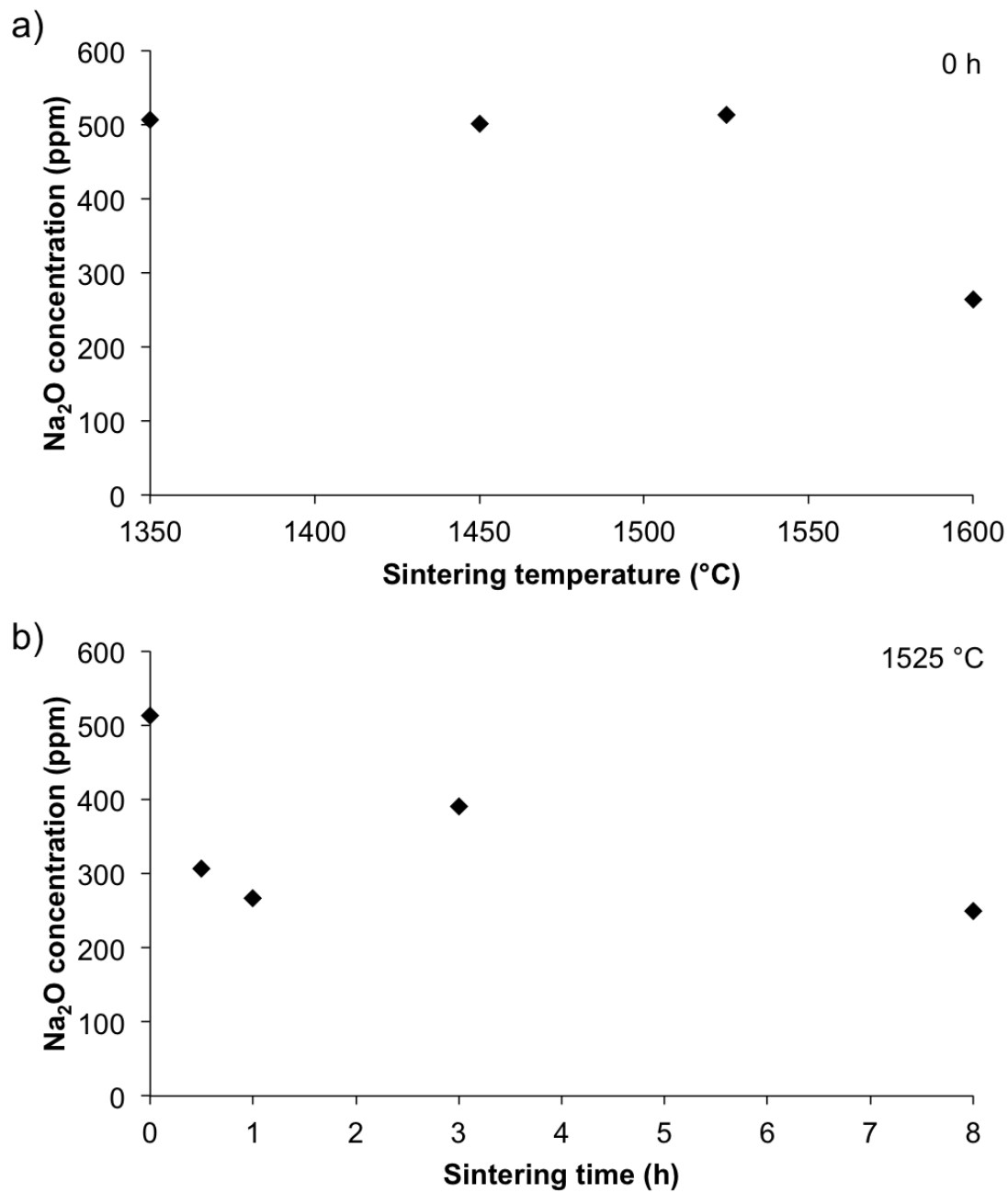


**Figure 3.12.**  $\text{Na}_2\text{O}$  concentration (ICP measurements) of 380 ppm MgO-doped Bayer alumina samples with 560 ppm  $\text{Na}_2\text{O}$  as a) function of sintering temperature and b) as a function of sintering time at 1525  $^{\circ}\text{C}$ .

# **Chapter 4**

# **Dynamic development of nanometer scale grain boundaries during liquid phase sintering**

## **4.1 Introduction**

During sintering of ceramics insoluble impurities and dopants can accumulate in the grain boundaries and form an amorphous grain boundary film that significantly influences the sintering behavior and properties of ceramics. Recently, it has been established that grain boundaries in fully dense microstructures can possess different characteristics, depending on chemistry and temperature. Based on their structure and thickness, grain boundaries have been classified into different types of thermodynamically stable complexions [25]. The type of complexion strongly affects transport kinetics and determines the mobility of a grain boundary, and if multiple complexions coexist at a time, multi-modal grain-size distributions and anisotropic microstructures can develop. One class of grain boundaries that is well investigated in dense ceramics are intergranular films (IGF), since they are often observed in a variety of systems such as  $\text{Si}_3\text{N}_4$ ,  $\text{SiC}$ , and  $\text{Al}_2\text{O}_3$  [75, 83]. IGFs are amorphous grain boundary films with an equilibrium thickness of typically 1-2 nm. Clarke et al. showed that the equilibrium film thickness results from a balance of attractive and repulsive interparticle forces, similar to those seen in colloidal systems [83, 84].

In classical sintering theories the differences in grain boundary structures are

considered by distinguishing between solid state and liquid phase sintering with fundamental differences in their respective sintering mechanisms. Solid state sintering occurs by solid state diffusion throughout the entire sintering process. During initial stage sintering surface diffusion leads to the formation of necks between particles. Most of the densification up to  $\sim 92\%$  occurs during intermediate stage, where grain boundaries between particles and pore channels along the grain edges form. At densities  $>92\%$  the pore channels close and isolated pores first form and are then eliminated during final stage sintering. The dominant diffusion mechanisms during intermediate and final stage sintering are volume and grain boundary diffusion, which can be affected by solute segregated to the grain boundaries [25].

In contrast, for liquid phase sintering [85] the particle compact is penetrated by a liquid film and during the initial sintering stage the powder compact begins to densify by particle rearrangement after the liquid phase has formed. Further densification during intermediate and final stage sintering is controlled by a solution-precipitation mechanism, where the particles of the sinter are dispersed in a liquid glass matrix, and material from the grain boundary area dissolves into the liquid grain boundary phase and diffuses to the particle necks, where it precipitates, leading to a particle contact flattening and densification.

Additional models were developed in the literature that account for the liquid phase redistribution during densification. For example, a number of models describe the filling of pores during liquid phase sintering due to capillarity [86, 87]. However, the existing models in the literature that address liquid phase redistribution typically deal with liquid concentrations of at least a few volume percent. In this case it can be assumed that the concentration of liquid phase is high enough to form a continuous liquid film of equilibrium thickness [75, 83, 84] in the grain boundaries and that excess liquid phase accumulates in necks, pores and glass pockets. For example, Svoboda et al. [88] assumed a constant equilibrium intergranular film thickness of 1.5 nm when they developed their liquid phase sintering model, and Kwon and Messing [52] estimated a grain boundary thickness of  $\sim 1$  nm based on a squeeze film analysis.

The redistribution of liquid phase becomes more complicated as the liquid phase concentration in a sinter is reduced, for example to concentrations  $<0.2$  vol.%. In this case the glass phase concentration could be insufficient to form a liquid

film of equilibrium thickness, and if the glass phase concentration is low enough the grain boundaries may be considered rather solid than liquid, which changes the sintering model that can be applied. This case is interesting specifically in commercial powders used in industry, since they typically contain higher impurity levels than the ultrahigh purity powders studied in academia. For example, most fundamental research on alumina uses ultrahigh purity aluminas of >99.99% Al<sub>2</sub>O<sub>3</sub> and, therefore, sintering is analyzed using solid state sintering models. In contrast commercial alumina powders are typically produced by the Bayer process and are ~99.8% pure with ppm levels of Na<sub>2</sub>O, SiO<sub>2</sub>, CaO, and Fe<sub>2</sub>O<sub>3</sub>, and added MgO as a sintering additive. The concentration and ratios of these impurities and additives can vary substantially by the commercial grade and can form a small amount of liquid phase. Despite considerable interest no research has been done on determining what volume fraction of liquid phase is necessary to consider grain boundaries liquid and when to apply a liquid phase sintering model in such a system.

Concentration, chemistry, and distribution of a liquid phase change during densification as a result of increasing temperature during heating and as a result of changing grain boundary area during densification and grain growth. This implies that grain boundaries undergo a dynamic change in physical and chemical character during densification. This dynamic change in chemistry and structure and possible transitions of grain boundaries from solid to liquid or vice versa can significantly impact densification as densification typically occurs via grain boundary diffusion. While most liquid phase sintering models imply that grain boundaries may change during densification, no work has been done on identifying these changes.

In this work we develop a model to predict the dynamic development of grain boundaries from initial to final stage sintering as a function of chemical and physical parameters of a sintering powder. The predicted grain boundary thicknesses are compared with grain boundaries examined by high-resolution TEM.

## 4.2 Experiment

Two chemically purified Bayer process alumina powders (Almatis, Inc., Leetsdale, PA, USA) were chosen for study. Powder characteristics and experimental details are described in previous chapter. The main difference between the two powders

are the MgO concentrations of 2 ppm (MgO-free powder) and 380 ppm (MgO-doped powder), respectively. The powders were doped with up to 1000 ppm Na<sub>2</sub>O and 1000 ppm SiO<sub>2</sub> using sodium acetate (NaC<sub>2</sub>H<sub>3</sub>O<sub>2</sub>·3H<sub>2</sub>O, ACS grade, BDH, VWR International LLC, West Chester, PA, USA) and tetraethyl orthosilicate (Si(OC<sub>2</sub>H<sub>5</sub>)<sub>4</sub>, 98%, Aldrich Chemical Company, Inc. Milwaukee, WI, USA), respectively, to obtain chemistries similar to commercial high purity Bayer aluminas at different glass concentrations. Samples with green densities of 59.0 ± 0.5% were fabricated for sintering studies by uniaxial and cold isostatic dry pressing (CIP, Autoclave engineers, Erie, Pa, USA) at 170 MPa and 200 MPa, respectively. The dry pressed cylinders were heated at 10°C/min to 1525°C in a thermomechanical analyzer (TMA, Linseis PT1600, Robbinsville, NJ, USA) to record the shrinkage during heating. Samples were heated at 10°C/min to 1200°C and then at 5°C/min to 1525°C for different hold times. Microstructure and density were measured by the linear intercept (ASTM Standard E112-96) [37] and Archimedes methods (ASTM standard B962-15), [36] respectively. The structure and chemistry of grain boundaries were investigated by transmission electron microscopy (TEM) and energy dispersive x-ray spectroscopy (EDS) using a dual aberration corrected FEI Titan [84] field emission microscope operated at 300 kV and FEI Talos (FEI, Hillsboro, OR, USA) field emission microscope at 200 kV. The EDS on both microscopes is an FEI Super-X system consisting of four SDDs (Silicon Drift Detectors) with a solid angle of 0.9 sr. The samples for TEM and EDS were air-quenched from the sintering temperature and prepared using a focused ion beam (Quanta 200 3D Dual Beam FIB, FEI, Hillsboro, OR, USA). Grain boundaries were chosen for analysis that were oriented parallel to the TEM beam in order to accurately measure grain boundary thicknesses in the 2D projection images and EDS profiles.

### 4.3 Grain boundary thickness in MgO-free alumina

The development of the grain boundary thickness during densification is described for MgO-free powder samples with 529/103 ppm Na<sub>2</sub>O/SiO<sub>2</sub>, 529/203 ppm Na<sub>2</sub>O/SiO<sub>2</sub>, and 529/603 ppm Na<sub>2</sub>O/SiO<sub>2</sub>. As shown in the previous chapter, the main difference of the samples is the concentration of glass phase that forms. The liquidus projection of the Al<sub>2</sub>O<sub>3</sub>-Na<sub>2</sub>O-SiO<sub>2</sub> phase diagram [88] was used to predict the equilibrium composition of the glass phase during heating as a function

of temperature [3], and based on the concentration of Na<sub>2</sub>O and SiO<sub>2</sub> the glass phase concentration  $\phi(T)$  was estimated as a function of temperature, as shown in Figure 4.1.

The liquid glass is expected to accumulate in particle contacts due to capillary forces [87], and during densification it is assumed that the liquid phase accumulates in the grain boundaries until an equilibrium film thickness [75] is reached. After this equilibrium thickness is reached it is assumed that the excess liquid phase accumulates in the particle necks. The fraction of a particle/grain surface that is in contact with another particle/grain, i.e. the fraction of grain boundary area, increases with increasing density [89]:

$$\alpha(\rho) = 1 - r(\rho) \left(1 - \frac{\rho}{100}\right)^{\frac{1}{2}} \quad (4.1)$$

where  $r$  is a factor between 1.4 and 1.7, depending on the relative density. With these assumptions the grain boundary thickness based on the amount of impurities in the samples can be estimated by:

$$\delta = 2 \frac{V_g \phi(T)}{S_g (1 - \phi(T)) \alpha(\rho)} \quad (4.2)$$

where  $V_g$  and  $S_g$  are the average volume and average surface area of a particle/grain. The parameters of this equation are specific to the system investigated and change during sintering.

If the calculated grain boundary thickness is smaller than a monolayer, e.g. the size of a SiO<sub>4</sub><sup>4-</sup> tetrahedron ( $\sim 0.3$  nm), the liquid phase concentration in the sample is not high enough to form a liquid grain boundary phase, assuming a homogeneous distribution of the liquid phase in the sample. We assume that a grain boundary thickness  $> 0.6$  nm, i.e. a bilayer of SiO<sub>4</sub><sup>4-</sup> tetrahedra, is necessary to consider the grain boundary liquid or liquid like. For calculated grain boundary thicknesses  $> 0.6$  nm the grain boundary thickness is assumed to be limited by an equilibrium film thickness, if the concentration of the liquid phase is high enough to form an amorphous film of equilibrium thickness. If the concentration of the liquid phase is not high enough to form an amorphous film of equilibrium thickness, the grain boundary thickness is limited by the concentration of glass phase in the sample.

Dilatometry was used to determine the development of relative density as a function of temperature (Figure 4.2), assuming isotropic shrinkage of the samples.

Now the increase in liquid phase concentration can be expressed as a function of relative density, as seen in Figure 4.3.  $V_g$  and  $S_g$  were estimated using the average particle/grain size determined from micrographs, assuming spherical particles of the same size. Using the sintering trajectories shown in Figure 4.4,  $V_g$  and  $S_g$  can be expressed as a function of relative density. The grain boundary thickness can be calculated as a function of relative density since all parameters in Eq. 4.2 can be expressed as a function of the relative density.

## 4.4 The equilibrium film thickness model

In 1987 Clarke proposed a model to calculate the equilibrium grain boundary thickness based on the equilibrium between attractive van der Waals and capillary pressures ( $P_{vdW}$  and  $P_C$ ) and repulsive electric double layer and structural disjoining pressures ( $P_{ELD}$  and  $P_{ST}$ ) [83, 84]:

$$P_{vdW} + P_C = P_{ELD} + P_{ST} \quad (4.3)$$

The van der Waals pressure is given by

$$P_{vdW} = \frac{H}{6\pi h^3} \quad (4.4)$$

where  $h$  is the grain boundary thickness and  $H$  is the Hamaker constant, which can be estimated by:

$$H = \frac{3}{4}kT \left( \frac{\varepsilon_\alpha - \varepsilon_\beta}{\varepsilon_\alpha + \varepsilon_\beta} \right)^2 + \frac{3\pi\hbar v}{8\sqrt{2}} \frac{(n_\alpha^2 - n_\beta^2)^2}{(n_\alpha^2 + n_\beta^2)^{\frac{3}{2}}} \quad (4.5)$$

where  $k$  is the Boltzmann constant,  $T$  is the absolute temperature,  $\varepsilon_\alpha$  and  $\varepsilon_\beta$  are the dielectric constants of the ceramic and the glass phase, respectively, and  $n_\alpha$  and  $n_\beta$  are the refractive indices of the ceramic and the glass phase, respectively.

In Clarke's original work the capillary pressure was assumed to be constant, which is a valid assumption for samples at constant densities. However, during densification the capillary pressure changes and can be estimated by [52]:

$$P_C = \frac{\left(0.59 - 0.79(1-\rho)^{\frac{1}{2}}\right)\rho^{\frac{1}{3}}}{0.39(1-\rho)^{\frac{1}{2}}\left(0.59 - 0.39(1-\rho)^{\frac{1}{2}}\right)} \frac{\gamma_{lv}}{r_s} \quad (4.6)$$

where  $\gamma_{lv}$  is the surface tension of the liquid,  $r_s$  is the particle radius, and  $\rho$  is the relative sintered density.

The structural disjoining force is given by [84]:

$$P_{ST} = -\alpha\tau_0^2 \left(\sinh^2\left(\frac{h}{2\xi}\right)\right)^{-1} \quad (4.7)$$

where  $a$  is a constant that can be approximated by the heat of fusion,  $\tau_0$  is a coefficient for the degree of ordering between 0 and 1, and  $\xi$  is a structural correlation length. The electric double layer force is given by [83]

$$P_{ELD} = \frac{16kT}{z^2\pi b_L h^2} \left(\tanh\frac{ze\psi_s}{4kT}\right)^2 (\kappa h)^2 e^{(-\kappa h)} \quad (4.8)$$

where  $z$  is the ion charge and  $e$  is the proton charge. The Bjerrum length  $b_L$  and the inverse of the Debye length  $\kappa$  are given by [83]

$$b_L = \frac{e^2}{4\pi\varepsilon_\beta\varepsilon_0 kT} \quad (4.9)$$

and [90]

$$\kappa = \sqrt{\frac{2N_A I e^2}{\varepsilon_\beta \varepsilon_0 kT}} \quad (4.10)$$

where  $N_A$  and  $I$  are the Avogadro's number and the ionic strength of the liquid, respectively.

## 4.5 Calculation of the theoretical Equilibrium Film Thicknesses

To calculate the equilibrium film thickness for alumina samples, the contributions  $P_{vdW}$ ,  $P_C$ ,  $P_{ELD}$ , and  $P_{ST}$  were calculated using parameters from the literature. The van der Waals pressure was estimated using Eq. 4.3 and 4.4 for a liquid sodium aluminosilicate glass film ( $\varepsilon_\beta = 10$  [91],  $n_\beta = 1.51$  [54]) located between

two flat alumina surfaces ( $\varepsilon_\alpha = 11.6$ ,  $n_\alpha = 1.752$ ) [84]. The capillary pressure was calculated as a function of the relative density and grain size from the sintering trajectories shown in Figure 4.2, using Eq. 4.6, assuming a surface tension of the sodium aluminosilicate glass of  $\gamma_{glass} = 387 \text{ N/m}$  [92]. The structural disjoining pressure was calculated using the heat of fusion of carnegieite ( $35.8 \text{ J/cm}^3$ ) for the constant  $a$ , and a structural correlation length of  $0.3 \text{ nm}$  (approximate size of a  $\text{SiO}_4^{4-}$  tetrahedron). The heat of fusion of carnegieite was chosen since its chemical composition is close to the chemical composition of the grain boundary phase investigated here. It is reported in the literature that considerable ordering of intergranular films can extend up to  $1.5 \text{ nm}$  into the intergranular film before they can be assumed completely amorphous [93]. Therefore, a high ordering factor of 0.75 was assumed.

The electric double layer pressure was calculated as a function of film thickness  $h$  using Eq. 4.8-4.10, with  $z = 1$  ( $\text{Na}^+$  ion charge) and  $\varepsilon_\beta = 10$ . The electrostatic potential  $\psi_s$  and ionic strength  $I$  are difficult to estimate, since they are not reported in the literature for the present system. Literature reports estimating equilibrium film thicknesses based on Clarke's model assume values for  $\psi_s$  within a reasonable range of up to  $1.5 \text{ V}$  [83, 94]. In this work we estimate  $\psi_s$  and  $I$  based on the composition and structure of sodium aluminosilicate glass. It is reported in the literature [95] that all  $\text{Al}^{3+}$  ions in sodium aluminosilicate glasses are in tetrahedral coordination if  $\text{Na}/\text{Al} \geq 1$ , and the local charge deficit of an  $\text{AlO}_4^{5-}$  tetrahedron (compared to the  $\text{SiO}_4^{4-}$  tetrahedron) is compensated by an associated  $\text{Na}^+$ . Excess  $\text{Na}^+$  ions that are not required for this charge compensation act as network modifiers in the glass. For  $\text{Na}/\text{Al} < 1$ , there are not enough  $\text{Na}^+$  ions to stabilize all  $\text{Al}^{3+}$  ions in tetrahedral coordination, and excess  $\text{Al}^{3+}$  ions can form triclusters or are in octahedral coordination [95].

In this model we assume for  $\text{Na}/\text{Al} > 1$  in the glass that  $\text{Na}^+$  ions compensating the charge of an  $\text{AlO}_4^{5-}$  tetrahedron are not mobile due to electrostatic attraction between the charged  $\text{AlO}_4^{5-}$  tetrahedron and the  $\text{Na}^+$  ion, whereas excess  $\text{Na}^+$  ions are assumed to be available as charge carriers. For the samples investigated here an  $I$  of  $2.25 \text{ mol/l}$  was calculated. If we assume that a fraction  $f_{cc}$  of the charge carriers segregate to the immediate particle/grain surface, a charge carrier density  $\sigma$  can be calculated by

$$\sigma = \frac{(c_{Na} - c_{Al}) f_{cc} V_{glass} N_A}{V_m \pi d^2} \quad (4.11)$$

where  $c_{Na}$  and  $c_{Al}$  are the concentration of  $\text{Na}^+$  and  $\text{Al}^{3+}$  ions in the glass, respectively,  $V_{glass}$  is the volume of glass around one particle/grain,  $V_m$  is the molar volume of the glass, and  $d$  is the particle/grain diameter. The electrostatic potential can then be calculated by [83]:

$$\psi_s = \sinh^{-1} \left( \frac{\sigma 2\pi z e b_L}{\kappa} \right) \frac{2kT}{ze} \quad (4.12)$$

The composition of the glass phase in the samples estimated from the phase diagram changes during heating, and consequently the Na/Al ratio changes as shown in Figure 4.5.  $\psi_s$  changes during heating because of the changing charge carrier concentration, the increasing grain boundary area, and the increasing grain size during densification. Figure 4.6 shows the change in  $\psi_s$  during heating, assuming a glass density of 2.45 g/cm<sup>3</sup> and 75% of the charge carriers segregate to the particle/grain surface ( $f_{cc} = 0.75$ ). The estimated values for  $\psi_s$  are reasonable when compared to  $\psi_s$  values used in the literature [83].

Figure 4.7 shows the individual contributions to the equilibrium film thickness plotted as a function of film thickness for a sample with 529 ppm  $\text{Na}_2\text{O}$  and 603 ppm  $\text{SiO}_2$  at 1525°C and a relative density of 93%. It can be seen that the net pressure, i.e. the sum of the acting pressures, is 0 MPa for a film thickness of 1.7 nm, which corresponds to the equilibrium film thickness.

From the above discussion it is apparent that  $P_{vdW}$ ,  $P_{CP}$ , and  $P_{ELD}$  change during densification. The film thickness at which the net pressure is 0 MPa (i.e., the equilibrium film thickness) was calculated for samples at different relative densities during the sintering process, and the calculated equilibrium film thicknesses are shown in Figure 4.8. It should be noted that  $P_{vdW}$  and  $P_C$  are a function of temperature, since the parameters they are calculated from are functions of temperature, glass composition, refractive indices, dielectric constants, and surface tension. However, investigations showed that the changes in  $P_{vdW}$  and  $P_C$  due to the changing temperature are insignificant, and therefore, these contributions were assumed to be constant. Figure 4.8 shows that the equilibrium film thickness does not depend on the amount of glass phase, but decreases as a function of relative density from 2.2 nm at ~60% relative density to 1.6 nm at 98% relative density, as

seen in Figure 4.7.

It is interesting to note that for film thicknesses  $> 1$  nm  $P_C$  and  $P_{ST}$  control the equilibrium thickness, and the contributions from  $P_{vdW}$  and  $P_{ELD}$  are negligible. At film thicknesses  $> 1$  nm  $P_{ST}$  is not expected to change as a function of density, and, therefore, the equilibrium thickness during densification is governed by the change in  $P_C$ . For film thicknesses  $< 1$  nm  $P_{ELD}$ ,  $P_{ST}$ , and  $P_{vdW}$  significantly contribute to the force balance and  $P_C$  is negligible.

Figure 4.9 shows plots of the development of the grain boundary thickness as a function of relative density for different glass concentrations. The trajectory of the equilibrium film thickness (see also Figure 4.8) represents the grain boundary thickness if enough glass phase is present to form a film with equilibrium thickness. The three trajectories labeled with 529/103 ppm Na<sub>2</sub>O/SiO<sub>2</sub>, 529/203 ppm Na<sub>2</sub>O/SiO<sub>2</sub>, and 529/603 ppm Na<sub>2</sub>O/SiO<sub>2</sub> are the estimated grain boundary thicknesses based on the amount of glass phase that is present in the samples. For all glass concentrations, the grain boundary thickness first decreases during initial and intermediate stage sintering. This decrease in grain boundary thickness is due to the increase in grain boundary area with increasing relative density, since the liquid glass phase is distributed over a larger grain boundary area. At the end of the intermediate sintering stage and during final stage sintering grain growth begins, which results in a reduction of the grain boundary area and, therefore, an increase in grain boundary thickness.

For samples with 529/103 ppm Na<sub>2</sub>O/SiO<sub>2</sub> and 529/203 ppm Na<sub>2</sub>O/SiO<sub>2</sub> the grain boundary thicknesses determined from the amount of glass phase are less than the equilibrium film thickness, and therefore, the grain boundary thickness is limited by the amount of glass phase in the sample. For samples with 529/603 ppm Na<sub>2</sub>O/SiO<sub>2</sub> the glass phase concentration in the sample is close to the glass phase concentration necessary to form a film of equilibrium thickness, and the grain boundary thickness is limited by the amount of glass phase or the equilibrium film thickness, depending on the relative density. For samples with higher glass concentrations, the grain boundary thickness is determined by the equilibrium film thickness.

## 4.6 High-resolution TEM

The predicted grain boundary thicknesses were compared to grain boundary thicknesses measured from high-resolution TEM images of samples with different glass concentrations. Figure 4.10 shows high resolution TEM images of the grain boundaries of samples with 0.066 vol.% (529/203 ppm Na<sub>2</sub>O/SiO<sub>2</sub>), 0.21 vol.% (529/603 ppm Na<sub>2</sub>O/SiO<sub>2</sub>), and 0.36 vol.% glass phase (1000/1000 ppm Na<sub>2</sub>O/SiO<sub>2</sub>) after 3 h at 1525°C. The thicknesses of the amorphous grain boundary as measured from the TEM images are 1.0 nm, 1.7 nm and 1.9 nm, respectively.

As seen in Figure 4.9 the measured grain boundary thicknesses agree well with the predicted grain boundary thicknesses. For a sample of 96% relative density and 0.073 vol.% glass phase the predicted grain boundary thickness is 0.9 nm, and the measured grain boundary thickness is 1.0 nm (Figure 4.10a). The equilibrium grain boundary thickness for this sample is 1.6 nm. However, the glass phase concentration is only high enough to form a 1.0 nm thick film. For the sample with 0.21 vol.% (529/603 ppm Na<sub>2</sub>O/SiO<sub>2</sub>) and a relative density of 93% the measured grain boundary thickness of 1.7 nm agrees well with the estimated equilibrium film thickness of 1.7 nm. The glass phase concentration in this sample is high enough to form a film with a thickness of ~2.2 nm, however, the grain boundary thickness is limited by the equilibrium film thickness. For samples with even higher glass concentrations of 0.36 vol.% the glass phase concentration is high enough to form a grain boundary thickness > 3.5 nm, however, the grain boundary thickness determined by TEM is 1.9 nm, which is close to the value of the equilibrium film thickness of 1.7 nm.

Figure 4.9d shows a sample with 0.03 vol.% glass phase (29/103 ppm Na<sub>2</sub>O/SiO<sub>2</sub>). There is no amorphous film in the grain boundaries because for samples with low SiO<sub>2</sub> concentrations such as 103 ppm the theoretically predicted grain boundary is less than a monolayer, and the amount of SiO<sub>2</sub> is insufficient to form a continuous amorphous film in the grain boundaries. However, EDS analysis shows that there is still SiO<sub>2</sub> segregated to the grain boundaries. Note that the maximum sintering temperature of the samples in this work is 1525°C. At higher sintering temperatures a higher glass phase concentration is expected, and, therefore, thicker grain boundaries would be observed.

## 4.7 The effect of changes in powder chemistry

### 4.7.1 $\text{Na}_2\text{O}/\text{SiO}_2$ ratio

For the results above a  $\text{Na}_2\text{O}/\text{SiO}_2$  ratio  $\geq 0.5$  in the sample was assumed, which results in a  $\text{Na}_2\text{O}/\text{SiO}_2$  ratio of 0.5 in the glass phase. For  $\text{Na}_2\text{O}/\text{SiO}_2$  ratios  $< 0.5$  the composition of the glass phase is expected to change, and consequently the grain boundary thickness is expected to change as a function of chemistry.

Figure 4.11 shows a high resolution TEM image of a grain boundary of a sample containing 0.17 vol.% glass phase (29/603 ppm  $\text{Na}_2\text{O}/\text{SiO}_2$ ) and a molar  $\text{Na}_2\text{O}/\text{SiO}_2$  ratio of 0.1 after 3 h at 1525°C, and the measured grain boundary is  $\sim 1.0$  nm thick. Based on the amount of impurities a grain boundary thickness of 2.2 nm is expected in those samples, which indicates that for this chemical composition an equilibrium grain boundary thickness [75] is reached at  $\sim 1.0$  nm. Investigations on how the capillary pressure and van der Waals pressure change as a result of the changed glass chemistry show that the differences in the resulting pressures are negligible. Therefore, the reduction can be attributed to a reduction in the repulsive  $P_{ST}$  and  $P_{ELD}$ .

The Na/Al ratio in the glass phase of the sample with 29/603 ppm  $\text{Na}_2\text{O}/\text{SiO}_2$  is  $< 1$ , and all  $\text{Na}^+$  ions are assumed to stabilize  $\text{Al}^{3+}$  ions in tetrahedral coordination. Therefore, no  $\text{Na}^+$  ions are available as charge carriers, and  $P_{ELD}$  is assumed to be zero. If  $P_{ELD}$  is assumed to be zero and  $P_{ST}$  is the same as for higher  $\text{Na}_2\text{O}/\text{SiO}_2$  ratios, the change in equilibrium film thickness is  $< 0.1$  nm. This confirms the earlier conclusion that  $P_{ST}$  is the dominant repulsive pressure at film thicknesses  $\geq 1$  nm, and that  $P_{ELD}$  is insignificant for the equilibrium grain boundary thicknesses investigated here. This means  $P_{ST}$  has to decrease as the  $\text{Na}_2\text{O}/\text{SiO}_2$  ratio in the sample decreases. Computer simulations showed that the ordering of sodium silicate glass between two alumina surfaces increases with increasing  $\text{Na}_2\text{O}/\text{SiO}_2$  ratio [96]. Therefore, it is reasonable to assume a lower ordering parameter  $\tau_0$  for the sample with a molar  $\text{Na}_2\text{O}/\text{SiO}_2$  ratio of 0.1. For example, if an ordering parameter of 0.25 is assumed the calculated equilibrium film thickness is  $\sim 1.0$  nm for samples with a relative density of 93%, which is close to the observed grain boundary thickness seen in Figure 4.11.

### 4.7.2 MgO-doped Bayer alumina

The influence of MgO on the sintering of Bayer alumina was reported in chapter 3, and it was shown that MgO increases the solubility of SiO<sub>2</sub> in the alumina lattice. Therefore, the reduction of SiO<sub>2</sub> on the grain boundaries by this process has to be taken into account when the grain boundary thickness is calculated. Figure 4.12 shows high resolution TEM images of grain boundaries of the MgO-doped powder with a) 60/82 ppm Na<sub>2</sub>O/SiO<sub>2</sub>, b) 60/582 ppm Na<sub>2</sub>O/SiO<sub>2</sub>, and c) 560/582 ppm Na<sub>2</sub>O/SiO<sub>2</sub> after 3 h at 1525°C and the amorphous film thicknesses are 0 nm, 0.5 nm, and 0.8 nm, respectively. For the sample containing 60 ppm Na<sub>2</sub>O and 82 ppm SiO<sub>2</sub> no amorphous film is expected because the amount of liquid phase in this sample is not sufficient to form a monolayer, similar to the MgO-free powder samples with 103 ppm SiO<sub>2</sub> seen in Figure 4.9d.

For the samples with 60/582 ppm Na<sub>2</sub>O/SiO<sub>2</sub> and 560/582 ppm Na<sub>2</sub>O/SiO<sub>2</sub> the grain boundaries are substantially thinner than the theoretical calculation of ~2.2 nm. As reported in previous work, the reduced grain boundary thickness is due to a co-dissolution process of Mg<sup>2+</sup> and Si<sup>4+</sup> into the alumina lattice, which reduces the amount of liquid phase in the grain boundaries. A maximum of 380 ppm MgO and 380 ppm SiO<sub>2</sub> dissolve into the alumina lattice assuming that equivalent amounts of SiO<sub>2</sub> and MgO go into solid solution, which leaves 202 ppm SiO<sub>2</sub> in the grain boundaries that can form a liquid phase. With 202 ppm SiO<sub>2</sub> in the grain boundaries an amorphous film with a thickness of ~0.8 nm is calculated, which agrees well with the observed grain boundary thicknesses of 0.5 and 0.8 nm for the samples containing 560/582 ppm Na<sub>2</sub>O/SiO<sub>2</sub> and 60/582 ppm Na<sub>2</sub>O/SiO<sub>2</sub>, respectively.

## 4.8 Conclusion

A model that describes the dynamic change in grain boundary chemistry and thickness during densification of Bayer alumina was developed. SiO<sub>2</sub> and Na<sub>2</sub>O impurities form a glass phase during heating, which accumulates in particle contacts due to capillarity. The chemistry and concentration of this glass phase changes as a function of temperature. During sintering the grain boundary area changes as a result of densification and grain growth, which affects the glass phase distribution

and, therefore, leads to the observed dynamic change in grain boundary thickness as a function of relative density.

An intergranular film of equilibrium thickness can form between particles/grains if the glass phase concentration is sufficient, and an interparticle force balance governs the grain boundary thickness. We demonstrated that for grain boundary thicknesses  $\geq 1.0$  nm the contributions that control the equilibrium intergranular film thickness are the attractive capillary pressure and the repulsive structural disjoining pressure. If the glass phase concentration in the sample is insufficient to form an intergranular film of equilibrium thickness the grain boundary thickness is determined by the glass phase concentration in the sample. Changes in powder chemistry such as changing the  $\text{Na}_2\text{O}/\text{SiO}_2$  ratio or the  $\text{MgO}$  concentration affect the concentration of glass phase in the sample and the interparticle force balance, which leads to a change in grain boundary thickness. Grain boundary thicknesses measured from high-resolution TEM images agree well with predicted values.

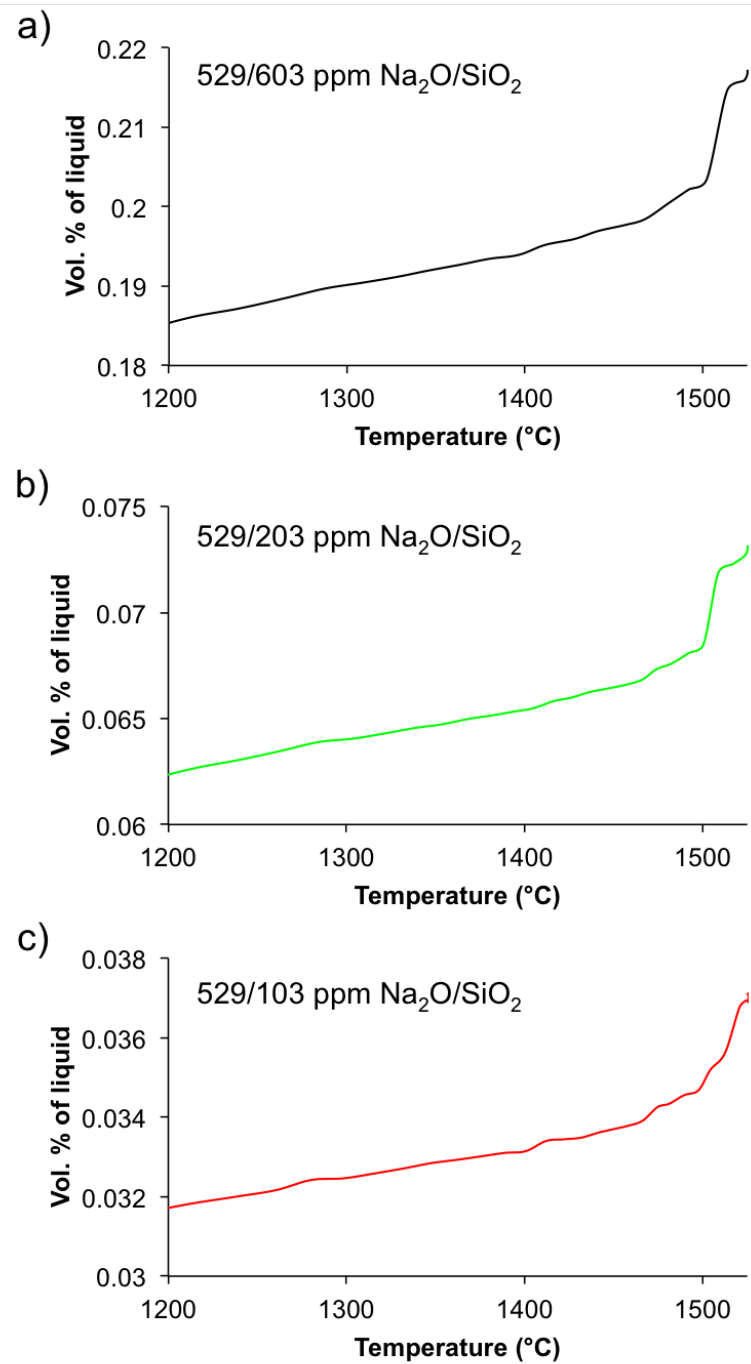


**Figure 4.1.** Increase in concentration of liquid phase as a function of temperature for MgO-free powder samples with 529 ppm Na<sub>2</sub>O and different SiO<sub>2</sub> concentrations.

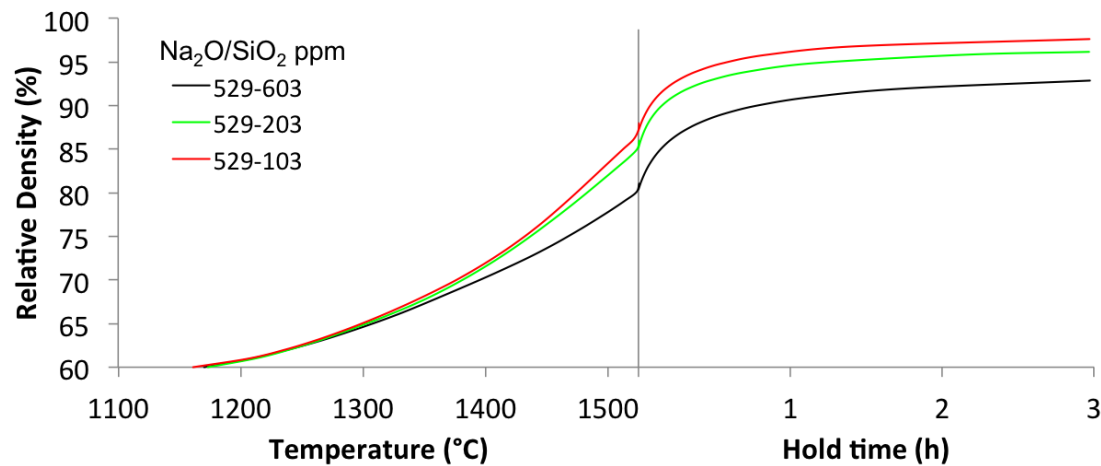


**Figure 4.2.** Relative density as a function of temperature and hold time determined from dilatometry for MgO-free powder samples with 529 ppm  $\text{Na}_2\text{O}$  and different  $\text{SiO}_2$  concentrations.

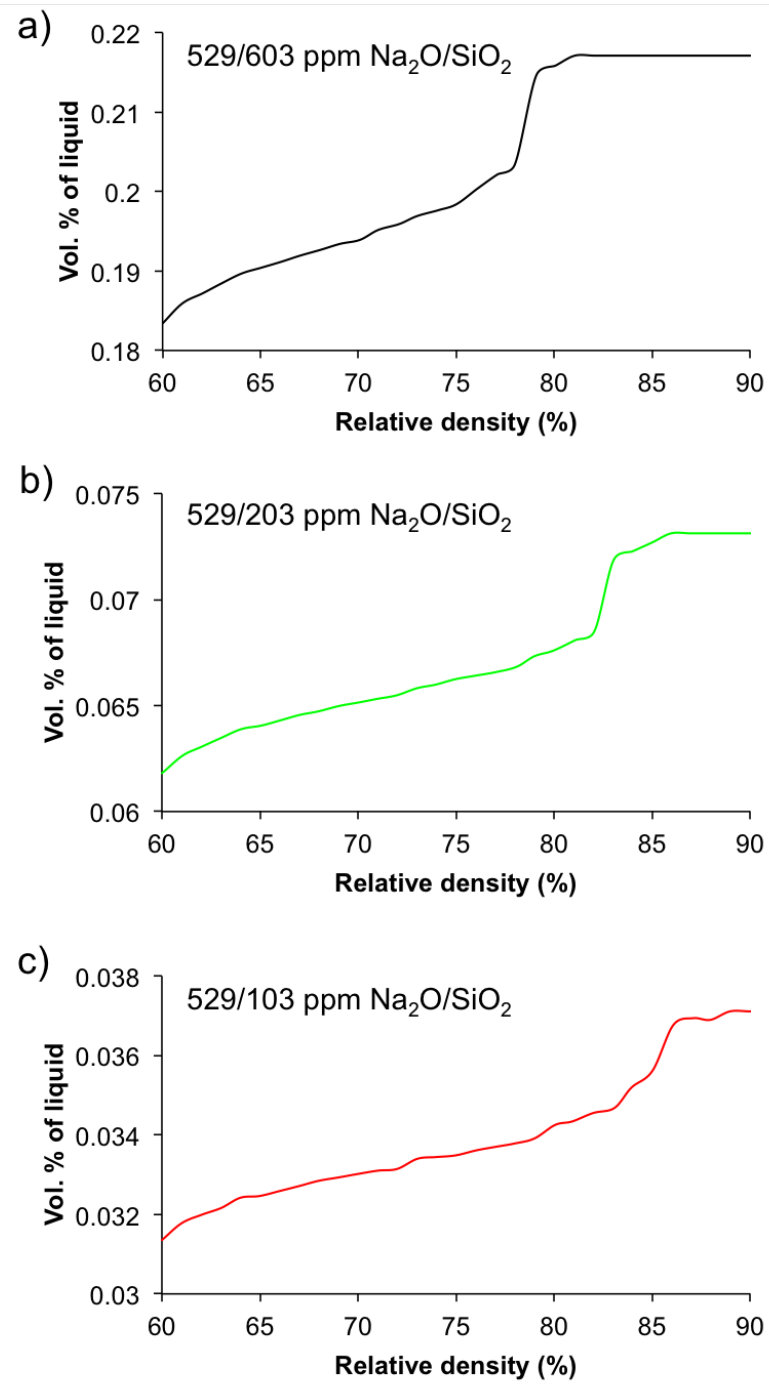


**Figure 4.3.** Liquid phase concentration as a function of relative density for MgO-free powder samples with 529 ppm Na<sub>2</sub>O and different SiO<sub>2</sub> concentrations.

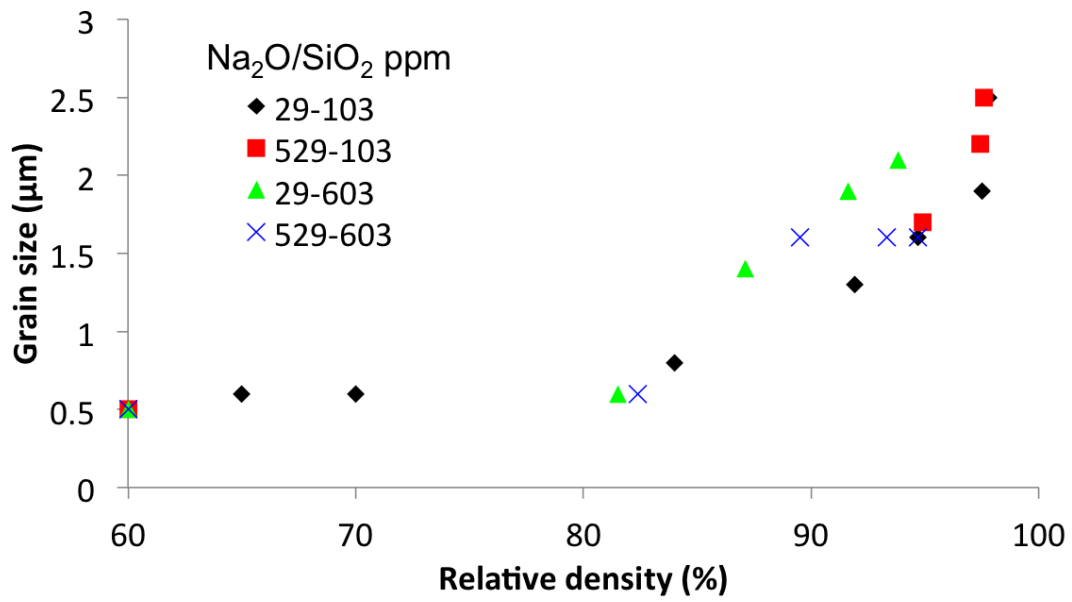


**Figure 4.4.** Grain size - density trajectories as a function of  $\text{Na}_2\text{O}$  and  $\text{SiO}_2$  concentration for MgO-free alumina.

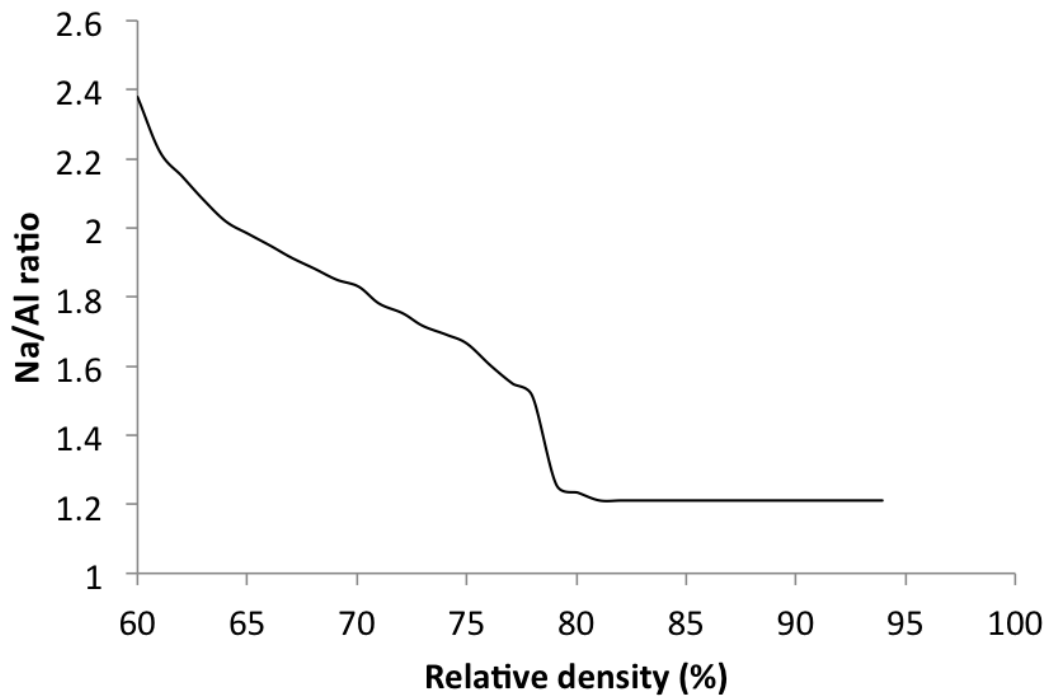


**Figure 4.5.** Change in Na/Al ion ratio in the liquid phase during sintering of samples with  $\text{Na}_2\text{O}/\text{SiO}_2$  ratios  $> 0.5$ .

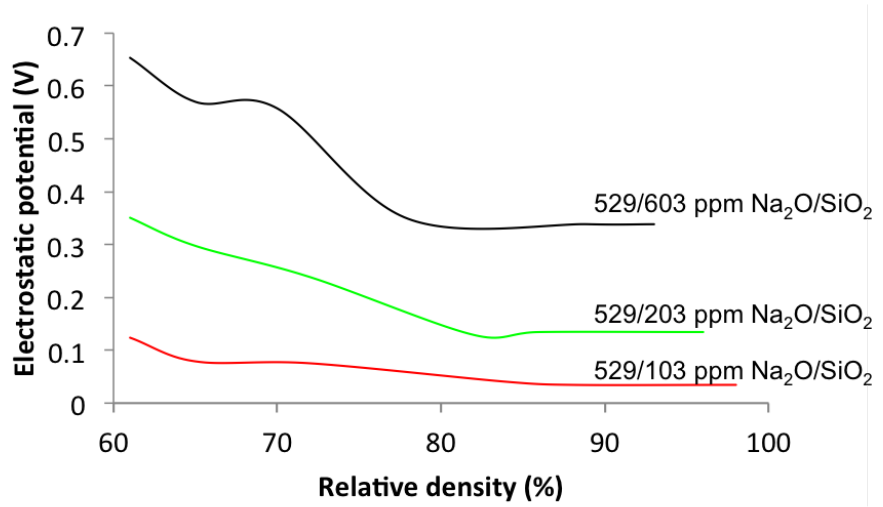


**Figure 4.6.** Development of the electrostatic potential as a function of relative density. For MgO-free powder samples with 529 ppm  $\text{Na}_2\text{O}$  and different  $\text{SiO}_2$  concentrations.

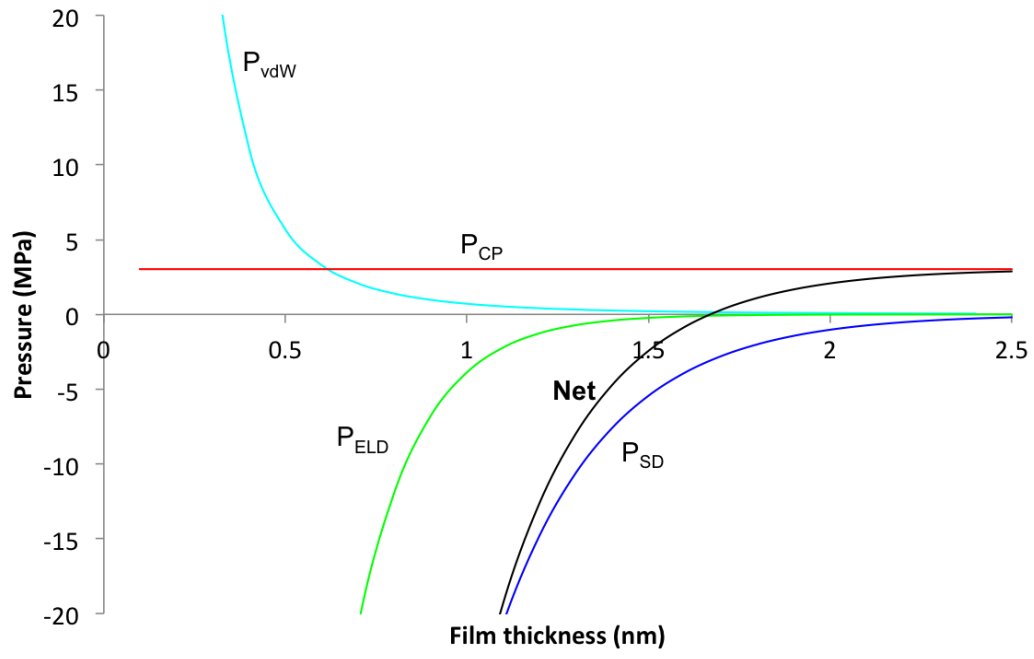


**Figure 4.7.** Contributions to the equilibrium film thickness as a function of film thickness for MgO-free powder samples with 529/603 ppm Na<sub>2</sub>O/SiO<sub>2</sub> at a relative density of 93%.

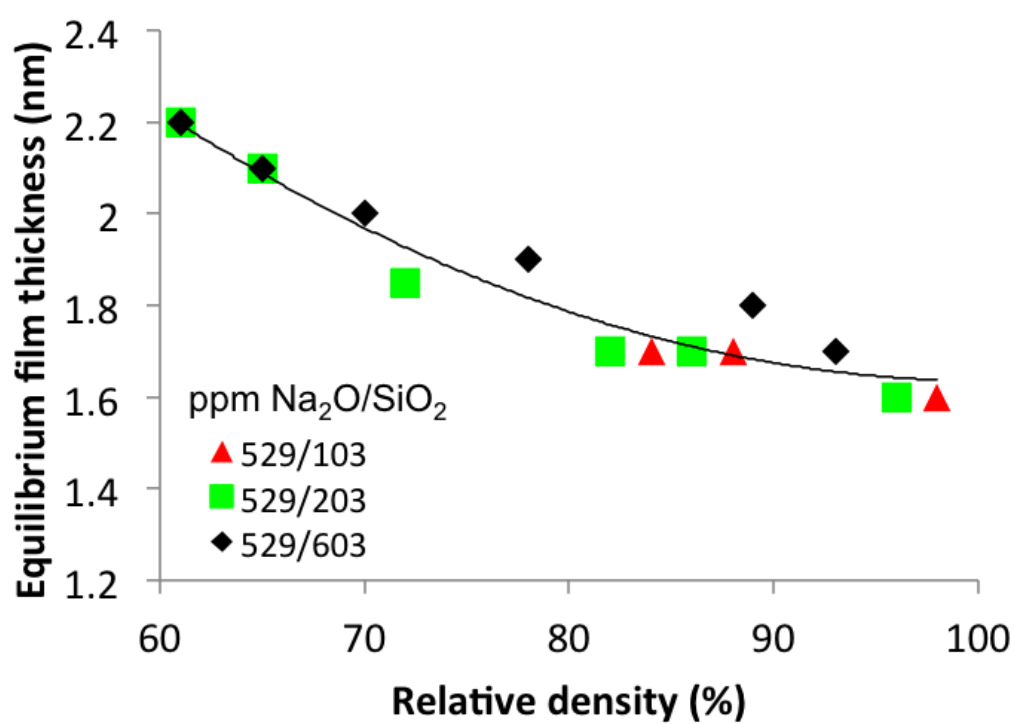


**Figure 4.8.** Calculated equilibrium film thickness for MgO-free powder samples at different chemistries as a function of relative density.

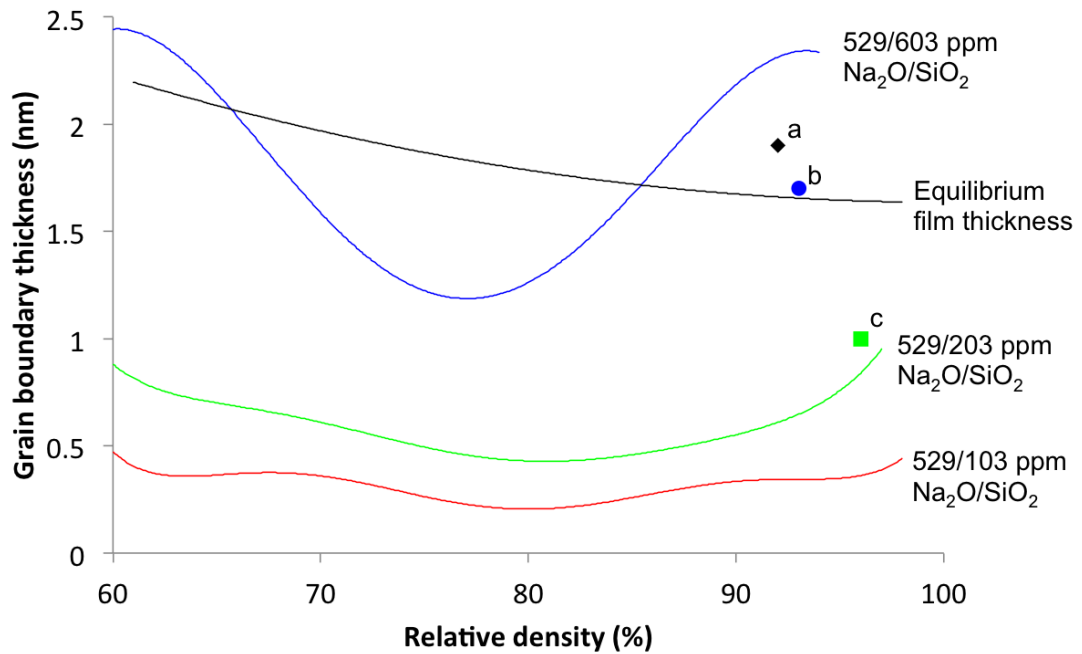


**Figure 4.9.** Calculated grain boundary thicknesses as a function of relative density for MgO-free powder samples. The trajectories labeled with 529/603 ppm  $\text{Na}_2\text{O}/\text{SiO}_2$ , 529/203 ppm  $\text{Na}_2\text{O}/\text{SiO}_2$ , and 529 ppm  $\text{Na}_2\text{O}/\text{SiO}_2$  were calculated based on the liquid phase concentration and sintering stage. The equilibrium film thickness was calculated based on Clarke's model. The calculated grain boundary thicknesses are compared to measured grain boundary thicknesses (data points a: 1000/1000 ppm  $\text{Na}_2\text{O}/\text{SiO}_2$ , b) 529/603 ppm  $\text{Na}_2\text{O}/\text{SiO}_2$ , c) 529/203 ppm  $\text{Na}_2\text{O}/\text{SiO}_2$  after heating at 1525°C for 3 h).

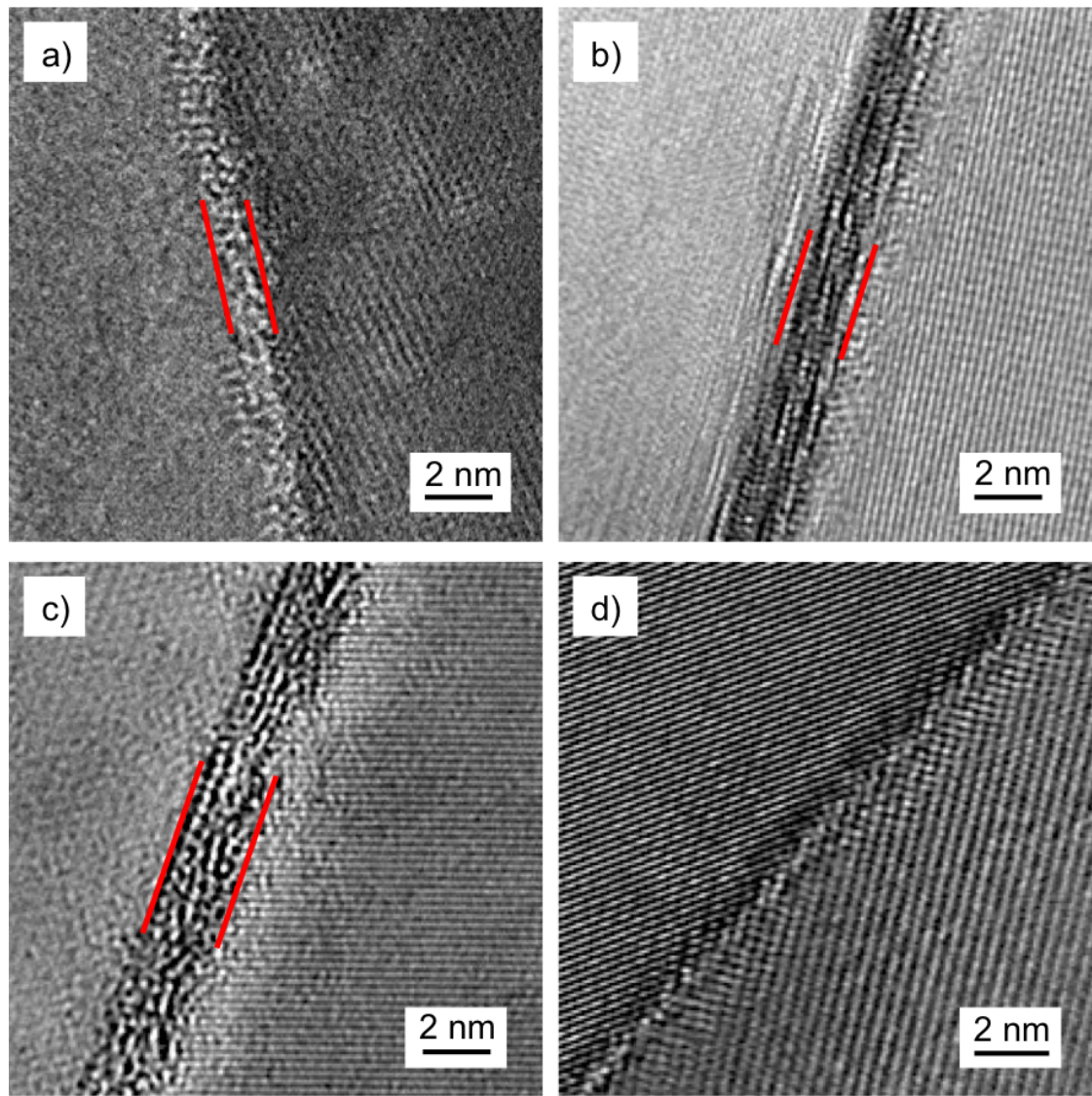


**Figure 4.10.** TEM images of MgO-free powder samples with a) 529/203 ppm  $\text{Na}_2/\text{SiO}_2$ , b) 529/603 ppm  $\text{Na}_2/\text{SiO}_2$ , c) 1000/1000 ppm  $\text{Na}_2/\text{SiO}_2$ , and d) 29/103 ppm  $\text{Na}_2/\text{SiO}_2$  after sintering at  $1525^\circ\text{C}$  for 3 h.

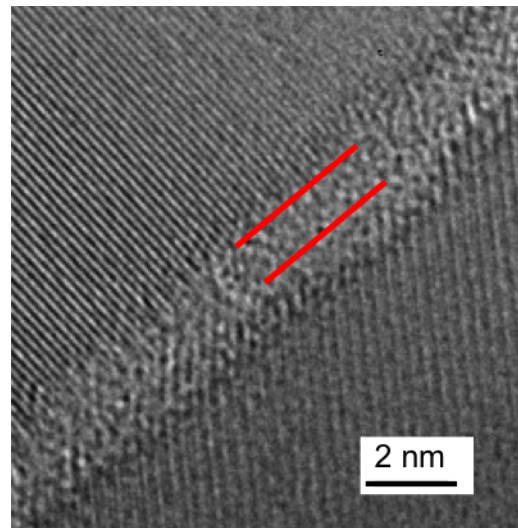


**Figure 4.11.** TEM image of a MgO-free powder sample with 29/603 ppm Na<sub>2</sub>O/SiO<sub>2</sub>.

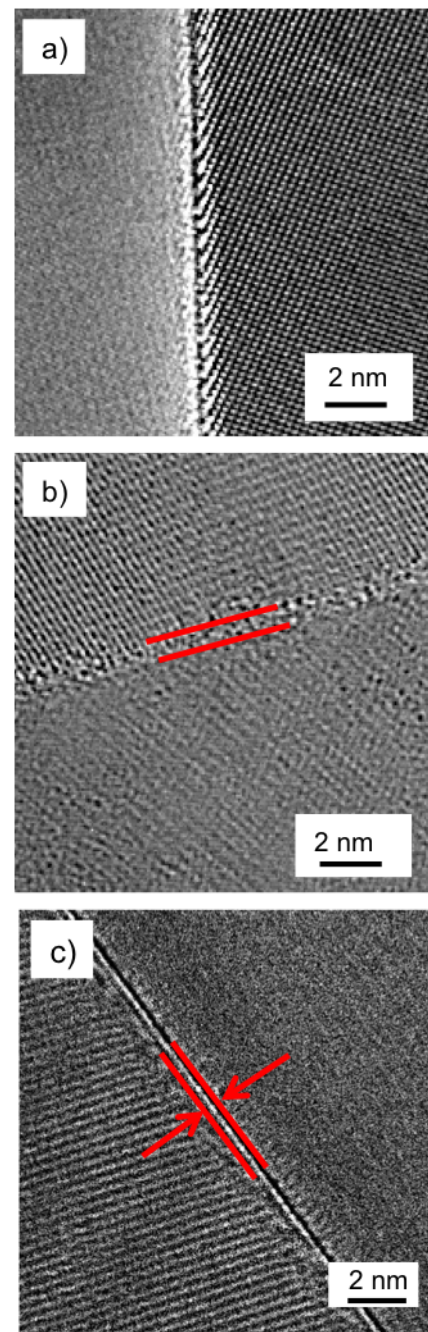


**Figure 4.12.** TEM images of MgO-doped (380 ppm) powder samples with a) 60/82 ppm Na<sub>2</sub>O/SiO<sub>2</sub>, b) 60/582 ppm Na<sub>2</sub>O/SiO<sub>2</sub>, and c) 560/582 ppm Na<sub>2</sub>O/SiO<sub>2</sub>. After heating at 1525°C for 3 h.

# Chapter 5 |

# Second phase formation in Bayer alumina

## 5.1 Introduction

Second phases such as spinel [1], calcium hexaluminate [97], and  $\beta$ -Al<sub>2</sub>O<sub>3</sub> [44], are known to form during the sintering of Bayer alumina as a result of dopants and impurities such as MgO, CaO, and Na<sub>2</sub>O. For Bayer aluminas,  $\beta$ -Al<sub>2</sub>O<sub>3</sub> (Na<sub>2</sub>O·11Al<sub>2</sub>O<sub>3</sub>) is of particular interest because Na<sub>2</sub>O is present up to a few hundred ppm. Rankin and Merwin [42] were the first to observe the formation of a new alumina phase in the high Al<sub>2</sub>O<sub>3</sub> region in the system CaO-Al<sub>2</sub>O<sub>3</sub>-MgO. They believed it was an allotropic modification of Al<sub>2</sub>O<sub>3</sub>, and named it  $\beta$ -Al<sub>2</sub>O<sub>3</sub>. However, later work clarified that there is a relation between the alkali content in the Al<sub>2</sub>O<sub>3</sub> and the formation of  $\beta$ -Al<sub>2</sub>O<sub>3</sub> [98], and that  $\beta$ -Al<sub>2</sub>O<sub>3</sub> is an alkali aluminate, rather than an allotropic form of Al<sub>2</sub>O<sub>3</sub> [49]. Ridgway et al. [43] reported that the Na<sub>2</sub>O content in Bayer process alumina is sufficient to form  $\beta$ -Al<sub>2</sub>O<sub>3</sub>. Four types of beta aluminas have been reported; two of them,  $\beta$ -Al<sub>2</sub>O<sub>3</sub> (Na<sub>2</sub>O·11Al<sub>2</sub>O<sub>3</sub>) and  $\beta''$ -Al<sub>2</sub>O<sub>3</sub> (Na<sub>2</sub>O·5Al<sub>2</sub>O<sub>3</sub>), form in the binary system Na<sub>2</sub>O-Al<sub>2</sub>O<sub>3</sub> and these phases can dissolve up to 2.5 and 5 wt.% MgO, respectively [48]. The other two beta aluminas,  $\beta'''$ -Al<sub>2</sub>O<sub>3</sub> and  $\beta''''$ -Al<sub>2</sub>O<sub>3</sub> are found at higher MgO concentrations in the ternary system Na<sub>2</sub>O-Al<sub>2</sub>O<sub>3</sub>-MgO [46, 48]. For completeness it should be mentioned that the existence of a  $\beta'$ -Al<sub>2</sub>O<sub>3</sub> (Na<sub>2</sub>O·7Al<sub>2</sub>O<sub>3</sub>) has been reported, but subsequent literature is in agreement that  $\beta'$ -Al<sub>2</sub>O<sub>3</sub> is actually  $\beta$ -Al<sub>2</sub>O<sub>3</sub> with excess Na<sub>2</sub>O [46, 48].

The fabrication and stability of  $\beta$ -Al<sub>2</sub>O<sub>3</sub> powder has been extensively reported for the fabrication of the solid electrolyte in Na-S batteries. Most  $\beta$ -Al<sub>2</sub>O<sub>3</sub> powder synthesis studies use sodium carbonate and alumina [48, 49, 99], which when heated to 1100°C leads to the formation of  $\beta''$ -Al<sub>2</sub>O<sub>3</sub> and decomposes to  $\beta$ -Al<sub>2</sub>O<sub>3</sub> and NaAlO<sub>2</sub> at >1500°C. The equilibrium vapor pressure of Na<sub>2</sub>O over  $\beta$ -Al<sub>2</sub>O<sub>3</sub> has been reported to be "appreciable" at >1400°C [48], and thus  $\beta$ -Al<sub>2</sub>O<sub>3</sub> can decompose to  $\alpha$ -Al<sub>2</sub>O<sub>3</sub> by volatilization of Na<sub>2</sub>O. Gallup [57] investigated the high temperature stability of  $\beta$ -Al<sub>2</sub>O<sub>3</sub> under different atmospheres and reported that  $\beta$ -Al<sub>2</sub>O<sub>3</sub> can transform to  $\alpha$ -Al<sub>2</sub>O<sub>3</sub> at 1300°C when heated in hydrogen or vacuum atmosphere. Interestingly,  $\beta$ -Al<sub>2</sub>O<sub>3</sub> did not convert to  $\alpha$ -Al<sub>2</sub>O<sub>3</sub> after heating for 1 h at 1500°C in air, but fully converted when heated for 10 min at 1600°C.

There has been little study of  $\beta$ -Al<sub>2</sub>O<sub>3</sub> formation in  $\alpha$ -Al<sub>2</sub>O<sub>3</sub> ceramics even though  $\beta$ -Al<sub>2</sub>O<sub>3</sub> grains in  $\alpha$ -Al<sub>2</sub>O<sub>3</sub> ceramics can greatly impact electrical and structural properties. Duncan and Creyke [44] investigated the formation and stability of  $\beta$ -Al<sub>2</sub>O<sub>3</sub> in  $\alpha$ -Al<sub>2</sub>O<sub>3</sub> ceramics and reported that  $\beta$ -Al<sub>2</sub>O<sub>3</sub> forms at Na<sub>2</sub>O concentrations as low as 0.04 wt.% if 0.25 wt.% MgO is present. An increase in  $\beta$ -Al<sub>2</sub>O<sub>3</sub> content was observed for powders with higher Na<sub>2</sub>O and MgO concentrations. They showed by electron-probe microanalysis that there is a higher concentration of Na<sub>2</sub>O and MgO in the  $\beta$ -Al<sub>2</sub>O<sub>3</sub> grains, and that  $\beta$ -Al<sub>2</sub>O<sub>3</sub> is stable in dense  $\alpha$ -Al<sub>2</sub>O<sub>3</sub> samples (24 mm diameter x 7 mm thick) up to 1650°C in static air. In flowing air, however,  $\beta$ -Al<sub>2</sub>O<sub>3</sub> decomposes to  $\alpha$ -Al<sub>2</sub>O<sub>3</sub> even in the center of the sample.

To date, there is no systematic study on the effect of Na<sub>2</sub>O and SiO<sub>2</sub> on the formation of  $\beta$ -Al<sub>2</sub>O<sub>3</sub> during the sintering of MgO-doped Bayer alumina powders. The goals of this work are to identify the stages and mechanisms of  $\beta$ -Al<sub>2</sub>O<sub>3</sub> formation in  $\alpha$ -Al<sub>2</sub>O<sub>3</sub> ceramics during sintering and to determine how specific chemistries affect  $\beta$ -Al<sub>2</sub>O<sub>3</sub> formation.

## 5.2 Experimental

A 380 ppm MgO-doped Bayer alumina (99.92% pure, Almatis, Inc., Leetsdale, PA, USA) was chosen to investigate the formation of  $\beta$ -Al<sub>2</sub>O<sub>3</sub>. Physical and chemical characteristics of the powder are shown in Table 5.1. The powder was doped with up to 1000 ppm Na<sub>2</sub>O and 1000 ppm SiO<sub>2</sub> using sodium acetate (NaC<sub>2</sub>H<sub>3</sub>O<sub>2</sub>·3H<sub>2</sub>O, ACS grade, BDH, West Chester, PA), and TEOS (Si(OC<sub>2</sub>H<sub>5</sub>)<sub>4</sub>,

98%, Aldrich Chemical Company, Inc., Milwaukee, WI), respectively. The detailed doping procedures were described in previous chapters. After drying the powders were sieved to  $-106\text{ }\mu\text{m}$ , dry pressed at 170 MPa, and subsequently cold isostatically pressed at 200 MPa (CIP, Autoclave Engineers, Erie, PA) to form  $\sim 3$  mm tall cylindrical samples with 6 mm and 12.7 mm in diameter. The samples were sintered in a box furnace at  $10^\circ\text{C}/\text{min}$  to  $1200^\circ\text{C}$  and then at  $5^\circ\text{C}/\text{min}$  to the final temperature between  $1450^\circ\text{C}$  and  $1600^\circ\text{C}$ , followed by a hold time of up to 8 h. The sintered samples were ground to half their initial height and polished to a surface finish of  $1\text{ }\mu\text{m}$ . The crystal structure of the second phase was identified by x-ray diffraction (XRD, X’Pert Pro MPD, PANalytical B.V., The Netherlands) using Cu K $\alpha$  radiation. The concentration of  $\beta\text{-Al}_2\text{O}_3$  grains was determined on a minimum area of  $0.1\text{ mm}^2$  from the center of the samples using scanning electron microscopy (SEM, Phenom ProX; Phenom-World B.V., Eindhoven, The Netherlands). SEM micrographs obtained from backscattered electrons were used to detect  $\beta\text{-Al}_2\text{O}_3$  grains. The contrast, brightness, and sharpness of the obtained SEM images were adjusted to improve the visibility of the second phases. The size of the  $\beta\text{-Al}_2\text{O}_3$  grains was measured from the SEM images (length and thickness) and an area fraction was estimated. Considering the stereology of randomly oriented, platelet shaped  $\beta\text{-Al}_2\text{O}_3$  grains [100] the estimated area fraction was assumed to be equal to the volume fraction of  $\beta\text{-Al}_2\text{O}_3$  in the samples. The chemical composition of the second phase was determined by energy dispersive x-ray spectroscopy (EDS, Phenom ProX; Phenom-World B.V., Eindhoven, The Netherlands). Note that the samples for SEM analysis were not coated with a conducting material since such coatings can obscure second phases.

### 5.3 Results

Figure 5.1 shows an example of second phases observed in sintered Bayer alumina. The second phase grains are platelet shaped, as evident from the high aspect ratio of the second phase grains. Initial studies showed that the detection of this second phase is challenging because no second phase grains are observed after thermal etching and in unetched samples the second phase grains can only be observed if a backscattered electron detector is used, as seen in Figure 5.1. Furthermore, coatings that are typically applied on insulating samples to achieve sufficient electrical

conductivity for SEM analysis can obscure the second phase grains, and therefore the samples were not coated.

Figure 5.2 shows the XRD pattern of a 99% dense Bayer alumina sample doped with 1060 ppm Na<sub>2</sub>O and 582 ppm SiO<sub>2</sub> and sintered at 1525°C for 5 h. The small amount of second phase was indexed and identified as  $\beta$ -Al<sub>2</sub>O<sub>3</sub> (PDF number: 98-001-2968). The estimated amount of  $\beta$ -Al<sub>2</sub>O<sub>3</sub> from Rietveld analysis is 0.6 wt.% and EDS analysis reveals that the  $\beta$ -Al<sub>2</sub>O<sub>3</sub> grains contain higher concentrations of MgO and Na<sub>2</sub>O relative to the surrounding matrix. As noted earlier, the Al<sub>2</sub>O<sub>3</sub>-Na<sub>2</sub>O-MgO phase diagram shows that  $\beta$ -Al<sub>2</sub>O<sub>3</sub> can dissolve up to 2.5 wt% MgO [48].

Samples were heated for up to 8 h at 1525°C to determine when  $\beta$ -Al<sub>2</sub>O<sub>3</sub> forms during sintering and Figure 5.3 shows micrographs of MgO-doped Bayer alumina samples doped with 560 ppm Na<sub>2</sub>O and 82 ppm SiO<sub>2</sub> after heating for 0 h, 1 h, and 8 h. The relative densities of the samples were 92%, 97%, and 99%, respectively. It can be seen that the  $\beta$ -Al<sub>2</sub>O<sub>3</sub> grains are 4 - 10  $\mu$ m long and their size does not change as a function of sintering time. However the number of  $\beta$ -Al<sub>2</sub>O<sub>3</sub> grains increases with increasing sintering time. To estimate how the amount of  $\beta$ -Al<sub>2</sub>O<sub>3</sub> changes as a function of sintering time and powder chemistry the number density of  $\beta$ -Al<sub>2</sub>O<sub>3</sub> grains per unit area was determined.

The kinetics of  $\beta$ -Al<sub>2</sub>O<sub>3</sub> formation in MgO-doped Bayer alumina is shown in Figure 5.4 as a function of powder chemistry. Most  $\beta$ -Al<sub>2</sub>O<sub>3</sub> grains form within the first hour at 1525°C, and after that the number density of  $\beta$ -Al<sub>2</sub>O<sub>3</sub> grains does not change as a function of hold time for all chemistries. For example, samples with 560 ppm Na<sub>2</sub>O and 82 ppm SiO<sub>2</sub> form  $\sim$ 320  $\beta$ -Al<sub>2</sub>O<sub>3</sub> grains/mm<sup>2</sup> after 0 h at 1525°C (92% relative density), and the amount of  $\beta$ -Al<sub>2</sub>O<sub>3</sub> increases to  $>1000$   $\beta$ -Al<sub>2</sub>O<sub>3</sub> grains/mm<sup>2</sup> after 1 h at 1525°C (97% relative density), but does not change upon further heating. Samples with 560 ppm Na<sub>2</sub>O and 182 ppm SiO<sub>2</sub> form  $\sim$ 130  $\beta$ -Al<sub>2</sub>O<sub>3</sub> grains/mm<sup>2</sup> after 0 h at 1525°C (89% relative density), and  $\sim$ 600  $\beta$ -Al<sub>2</sub>O<sub>3</sub> grains/mm<sup>2</sup> after 1 h at 1525°C (97% relative density). Samples with lower Na<sub>2</sub>O and/or higher SiO<sub>2</sub> concentrations form less  $\beta$ -Al<sub>2</sub>O<sub>3</sub> grains for all hold times, as seen in Figure 5.4.

Figure 5.5 shows the number density of  $\beta$ -Al<sub>2</sub>O<sub>3</sub> grains in MgO-doped Bayer alumina samples with 82 ppm SiO<sub>2</sub>, and Figure 5.6 shows some of the corresponding micrographs. In samples with 60 and 185 ppm Na<sub>2</sub>O  $\beta$ -Al<sub>2</sub>O<sub>3</sub> grains with a length

of 3 - 13  $\mu\text{m}$  form, and if the  $\text{Na}_2\text{O}$  concentration is increased to 560 and 1060 ppm, the number density of  $\beta\text{-Al}_2\text{O}_3$  increases and the length of the  $\beta\text{-Al}_2\text{O}_3$  grains decreases to 4 - 10  $\mu\text{m}$  and 2 - 7  $\mu\text{m}$ , respectively.

The number density of  $\beta\text{-Al}_2\text{O}_3$  in  $\text{MgO}$ -doped Bayer alumina decreases for all  $\text{Na}_2\text{O}$  concentrations if the  $\text{SiO}_2$  concentration is increased, as shown in Figure 5.7a, whereas the size of the  $\beta\text{-Al}_2\text{O}_3$  grains increases with increasing  $\text{SiO}_2$  concentration, as seen when the micrographs in Figure 5.5 are compared to the micrographs in Figure 5.8. For example, samples with 185 ppm  $\text{Na}_2\text{O}$  and 82 ppm  $\text{SiO}_2$  form 3 - 13  $\mu\text{m}$  long  $\beta\text{-Al}_2\text{O}_3$  grains (Figure 5.5a) and if the  $\text{SiO}_2$  concentration is increased to 182 ppm the number density of  $\beta\text{-Al}_2\text{O}_3$  grains decreases significantly, and the  $\beta\text{-Al}_2\text{O}_3$  grains are  $\sim 15 \mu\text{m}$  long (Figure 5.8a). No  $\beta\text{-Al}_2\text{O}_3$  was observed in samples with 582 ppm  $\text{SiO}_2$  and  $\text{Na}_2\text{O}$  concentrations of 60-560 ppm.

The effect of  $\text{Na}_2\text{O}$  and  $\text{SiO}_2$  shows that the formation of  $\beta\text{-Al}_2\text{O}_3$  is a function of the  $\text{Na}_2\text{O}/\text{SiO}_2$  ratio. Figure 5.7b shows that no  $\beta\text{-Al}_2\text{O}_3$  forms in  $\text{MgO}$ -doped Bayer alumina samples with  $\text{Na}_2\text{O}/\text{SiO}_2$  ratios  $< 0.7$ , and only a small amount of  $\beta\text{-Al}_2\text{O}_3$  forms in samples with  $\text{Na}_2\text{O}/\text{SiO}_2$  ratios of 0.7 - 2.0. For higher  $\text{Na}_2\text{O}/\text{SiO}_2$  ratios the amount of  $\beta\text{-Al}_2\text{O}_3$  increases linearly to as much as  $\sim 1880$  grains/ $\text{mm}^2$  for a  $\text{Na}_2\text{O}/\text{SiO}_2$  ratio of  $\sim 13$ .

A theoretical volume fraction of  $\beta\text{-Al}_2\text{O}_3$  was estimated based on the chemical formula of  $\beta\text{-Al}_2\text{O}_3$  ( $\text{Na}_2\text{O}\cdot 11\text{Al}_2\text{O}_3$ ) and the amount of  $\text{Na}_2\text{O}$  in the samples, as seen in Table 5.2. It can be seen that the theoretically estimated amount of  $\beta\text{-Al}_2\text{O}_3$  that can form based on the amount of  $\text{Na}_2\text{O}$  in the samples is higher than the observed amount of  $\beta\text{-Al}_2\text{O}_3$  in the samples. This difference can be explained by  $\text{Na}_2\text{O}$  volatilization during sintering, as shown in Chapter 3. Taking into account that  $\sim 40\%$  of the  $\text{Na}_2\text{O}$  volatizes during heating (Figure 3.12 Chapter 3), the expected amount of  $\beta\text{-Al}_2\text{O}_3$  in the samples is close to the observed amount of  $\beta\text{-Al}_2\text{O}_3$ , as seen in Table 5.2.

## 5.4 Interpretation and mechanisms of $\beta\text{-Al}_2\text{O}_3$ formation

It was shown by TEM and EDS analysis that insoluble impurities and dopants such as  $\text{Na}_2\text{O}$ ,  $\text{MgO}$ ,  $\text{CaO}$  and  $\text{SiO}_2$  segregate to the grain boundaries during sintering

of alumina, and second phases can form if a critical impurity concentration in the grain boundaries is exceeded [1]. For example, a segregation and precipitation map for MgO in ultrahigh purity alumina, which predicts the formation of spinel as a function of MgO concentration and grain size, was proposed in the literature [1]. However, the presence of several impurities and dopants in Bayer alumina can affect the critical concentrations of impurities and dopants in grain boundaries, and the formation of second phases can strongly depend on the concentration and ratios of several impurities and dopants. For example, in previous chapters it was shown that SiO<sub>2</sub>, MgO, and Na<sub>2</sub>O form a liquid grain boundary phase during sintering of Bayer alumina, and the critical concentration of Na<sub>2</sub>O to form  $\beta$ -Al<sub>2</sub>O<sub>3</sub> depends on the amount of siliceous glass phase that forms, since the glass phase consists of 20-30 mol% Na<sub>2</sub>O. Furthermore, it was shown that MgO and SiO<sub>2</sub> co-dissolve into the alumina grains during final stage sintering, which reduces the concentration of SiO<sub>2</sub> in the grain boundaries and thus the amount of Na<sub>2</sub>O that can be dissolved in the glass phase.

The above discussion indicates that MgO plays an important role for  $\beta$ -Al<sub>2</sub>O<sub>3</sub> formation in Bayer alumina. To gain insight into how MgO affects  $\beta$ -Al<sub>2</sub>O<sub>3</sub> formation an additional set of experiments with a Bayer alumina with 2 ppm MgO ("MgO-free") was completed. The powder was doped to concentrations between 2 and 1002 ppm MgO and different Na<sub>2</sub>O and SiO<sub>2</sub> concentrations of up to 1029 ppm and 1000 ppm, respectively, and heated at 1525°C for 3 h. Figures 5.8 and 5.9 show the influence of powder chemistry on the number density of  $\beta$ -Al<sub>2</sub>O<sub>3</sub> grains and microstructures, respectively. It can be seen that no  $\beta$ -Al<sub>2</sub>O<sub>3</sub> forms in samples with 2 ppm MgO and 29 ppm Na<sub>2</sub>O, but the amount of  $\beta$ -Al<sub>2</sub>O<sub>3</sub> increases with increasing MgO concentration (Figure 5.9a).

In the Bayer alumina powder with 2 ppm MgO no second phase formation was observed for Na<sub>2</sub>O concentrations of 29 ppm, and only a very small amount ( $\sim$ 10 grains/mm<sup>2</sup>) of  $\beta$ -Al<sub>2</sub>O<sub>3</sub> forms in samples with 529 ppm Na<sub>2</sub>O, which indicates that most Na<sub>2</sub>O is segregated to the grain boundaries, but the Na<sub>2</sub>O concentration is not sufficient to form  $\beta$ -Al<sub>2</sub>O<sub>3</sub>. Note that the presence of 103 ppm SiO<sub>2</sub> in the Bayer alumina powder with 2 ppm MgO affects the formation of  $\beta$ -Al<sub>2</sub>O<sub>3</sub>. When the Na<sub>2</sub>O concentration is increased to 1029 ppm the amount of  $\beta$ -Al<sub>2</sub>O<sub>3</sub> increases significantly to 470 grains/mm<sup>2</sup> (Figure 5.9b), which indicates that grain boundaries supersaturate during sintering and  $\beta$ -Al<sub>2</sub>O<sub>3</sub> forms.

No or only a very small amount of  $\beta$ -Al<sub>2</sub>O<sub>3</sub> forms in samples with 2 ppm MgO if the SiO<sub>2</sub> concentration is increased to 203 ppm or higher. It was demonstrated by high resolution TEM and EDS that SiO<sub>2</sub> segregates to the grain boundaries and forms an amorphous glass phase. With increasing SiO<sub>2</sub> concentration in the sample the glass phase can dissolve more Na<sub>2</sub>O without precipitating  $\beta$ -Al<sub>2</sub>O<sub>3</sub>, and, therefore, increasing SiO<sub>2</sub> in a sample decreases the amount of  $\beta$ -Al<sub>2</sub>O<sub>3</sub>. This hypothesis is supported by an additional experiment with an ultrahigh purity alumina (AKP-50) with only 11 ppm SiO<sub>2</sub>. The powder was doped to 502 ppm Na<sub>2</sub>O and heated at 1525°C for 0 h and it can be seen in Figure 5.11 that a substantial amount of  $\beta$ -Al<sub>2</sub>O<sub>3</sub> ( $\sim$ 1100 grains/mm<sup>2</sup>) has formed. In Bayer alumina samples with 529 ppm Na<sub>2</sub>O, 2 ppm MgO, and 103 ppm SiO<sub>2</sub> form only  $\sim$ 10  $\beta$ -Al<sub>2</sub>O<sub>3</sub> grains/mm<sup>2</sup>.

When the MgO concentration in Bayer alumina is increased to 252 ppm or higher  $\beta$ -Al<sub>2</sub>O<sub>3</sub> forms at a Na<sub>2</sub>O concentration as low as 29 ppm. It is hypothesized that more  $\beta$ -Al<sub>2</sub>O<sub>3</sub> forms with increasing MgO concentration because MgO removes SiO<sub>2</sub> from the grain boundaries by co-dissolving into the alpha alumina matrix during final stage sintering, as explained earlier. This co-dissolution mechanism significantly decreases the amount of Na<sub>2</sub>O that can be dissolved in the liquid grain boundary phase, leading to the nucleation and growth of  $\beta$ -Al<sub>2</sub>O<sub>3</sub>.

If it is assumed that MgO and SiO<sub>2</sub> form the defect complex proposed earlier, and if it is assumed that MgO and SiO<sub>2</sub> co-dissolve at equal amounts and that all MgO is consumed by this process, MgO-doped powder samples (380 ppm MgO) with 82 and 182 ppm SiO<sub>2</sub> do not have any SiO<sub>2</sub> left in the grain boundaries. This reduction in the amount of SiO<sub>2</sub> in the grain boundaries reduces the solubility of Na<sub>2</sub>O significantly, leading to the precipitation of  $\beta$ -Al<sub>2</sub>O<sub>3</sub>. Samples with 582 ppm SiO<sub>2</sub> have 202 ppm SiO<sub>2</sub> left in the grain boundaries after 380 ppm MgO and SiO<sub>2</sub> co-dissolve into the alumina lattice, and the solubility of Na<sub>2</sub>O in the liquid grain boundary phase is still high enough that only few  $\beta$ -Al<sub>2</sub>O<sub>3</sub> grains form in this sample.

The co-dissolution of SiO<sub>2</sub> and MgO into the alumina lattice and the formation of the majority of the  $\beta$ -Al<sub>2</sub>O<sub>3</sub> grains happens at the same time, between 0 and 3 h at 1525°C at relative densities  $>$  90%, which supports the hypothesis that  $\beta$ -Al<sub>2</sub>O<sub>3</sub> nucleates and grows as a result of supersaturation of the liquid grain boundary phase when MgO reduces the SiO<sub>2</sub> concentration in the grain boundaries. However,

samples with 560 ppm Na<sub>2</sub>O and 82 ppm SiO<sub>2</sub> form more  $\beta$ -Al<sub>2</sub>O<sub>3</sub> than samples with 560 ppm Na<sub>2</sub>O and 182 ppm SiO<sub>2</sub>, even though no SiO<sub>2</sub> should be left in the grain boundaries of both samples. One reason could be that not all 380 ppm MgO and SiO<sub>2</sub> are consumed by this co-dissolution process, and a small amount SiO<sub>2</sub> might remain on the grain boundaries. Another possible explanation is that MgO has an additional effect on the formation of  $\beta$ -Al<sub>2</sub>O<sub>3</sub> in  $\alpha$ -Al<sub>2</sub>O<sub>3</sub>. It has been reported that MgO supports the formation of  $\beta$ -Al<sub>2</sub>O<sub>3</sub> in alumina, and samples with 560 ppm Na<sub>2</sub>O and 82 ppm SiO<sub>2</sub> have 100 ppm more MgO left in the grain boundaries than samples with 560 ppm Na<sub>2</sub>O and 182 ppm SiO<sub>2</sub>. MgO might facilitate the formation of  $\beta$ -Al<sub>2</sub>O<sub>3</sub> since EDS analysis shows the presence of MgO in the  $\beta$ -Al<sub>2</sub>O<sub>3</sub> grains.

## 5.5 Summary

The effect of powder chemistry on the formation of  $\beta$ -Al<sub>2</sub>O<sub>3</sub> in  $\alpha$ -Al<sub>2</sub>O<sub>3</sub> was investigated. The number density of  $\beta$ -Al<sub>2</sub>O<sub>3</sub> grains increases with increasing Na<sub>2</sub>O and MgO concentrations and decreases with increasing SiO<sub>2</sub> concentration, whereas the size of the  $\beta$ -Al<sub>2</sub>O<sub>3</sub> grains decreases with increasing Na<sub>2</sub>O and MgO concentration and increases with increasing SiO<sub>2</sub> concentration. The majority of  $\beta$ -Al<sub>2</sub>O<sub>3</sub> grains form within the first hour at 1525°C at densities >90%, at the same stage at which MgO and SiO<sub>2</sub> were shown to co-dissolve into the  $\alpha$ -Al<sub>2</sub>O<sub>3</sub> grains. It was concluded that the mechanism of  $\beta$ -Al<sub>2</sub>O<sub>3</sub> formation in Bayer alumina is by precipitation from the liquid grain boundary phase. The liquid glass phase in the grain boundaries supersaturates with Na<sub>2</sub>O when the amount of SiO<sub>2</sub> in the grain boundaries is reduced by the co-dissolution of MgO and SiO<sub>2</sub> into the alumina lattice, which leads to the precipitation of  $\beta$ -Al<sub>2</sub>O<sub>3</sub>.

**Table 5.1.** Physical and chemical characteristics of the alumina powder used in this study.

	MgO-doped
	Bayer alumina
BET ( $\text{m}^2/\text{g}$ )	7.3
$D_{50}$ ( $\mu\text{m}$ )	0.4
	ICP (ppm)
$\text{Al}_2\text{O}_3$	99.92%
$\text{SiO}_2$	82
$\text{Na}_2\text{O}$	60
$\text{Fe}_2\text{O}_3$	140
$\text{CaO}$	51
$\text{TiO}_2$	8
MgO	380

**Table 5.2.** Estimated amount of  $\beta$ -Al<sub>2</sub>O<sub>3</sub> in MgO-doped Bayer alumina samples after 3 h at 1525°C.

Concentration of Na <sub>2</sub> O in the sample (ppm)	Theoretical vol.% of $\beta$ -Al <sub>2</sub> O <sub>3</sub>		Measured amount of $\beta$ -Al <sub>2</sub> O <sub>3</sub> 3h 1525°
	No Na <sub>2</sub> O volatizes	Assuming 40 % of of Na <sub>2</sub> O volatizes	
60	0.14	0.08	0.18
185	0.42	0.25	0.25
310	0.71	0.43	0.38
560	1.28	0.77	0.65
1060	2.42	1.45	0.49

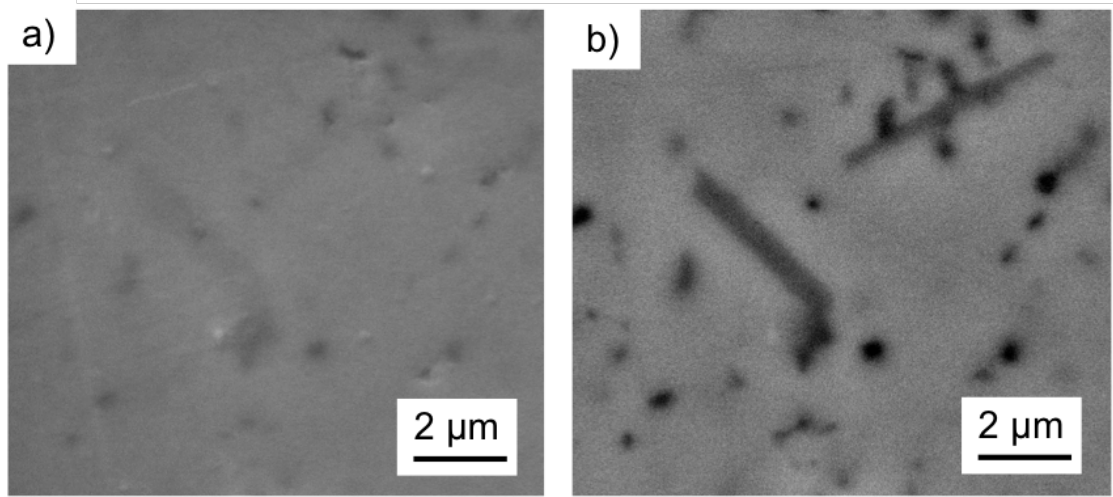


**Figure 5.1.** Micrographs of MgO-doped Bayer doped with 560 ppm Na<sub>2</sub>O and 82 ppm SiO<sub>2</sub> after 3 h at 1525°C obtained using a) a secondary electron detector and b) a backscattered electron detector.

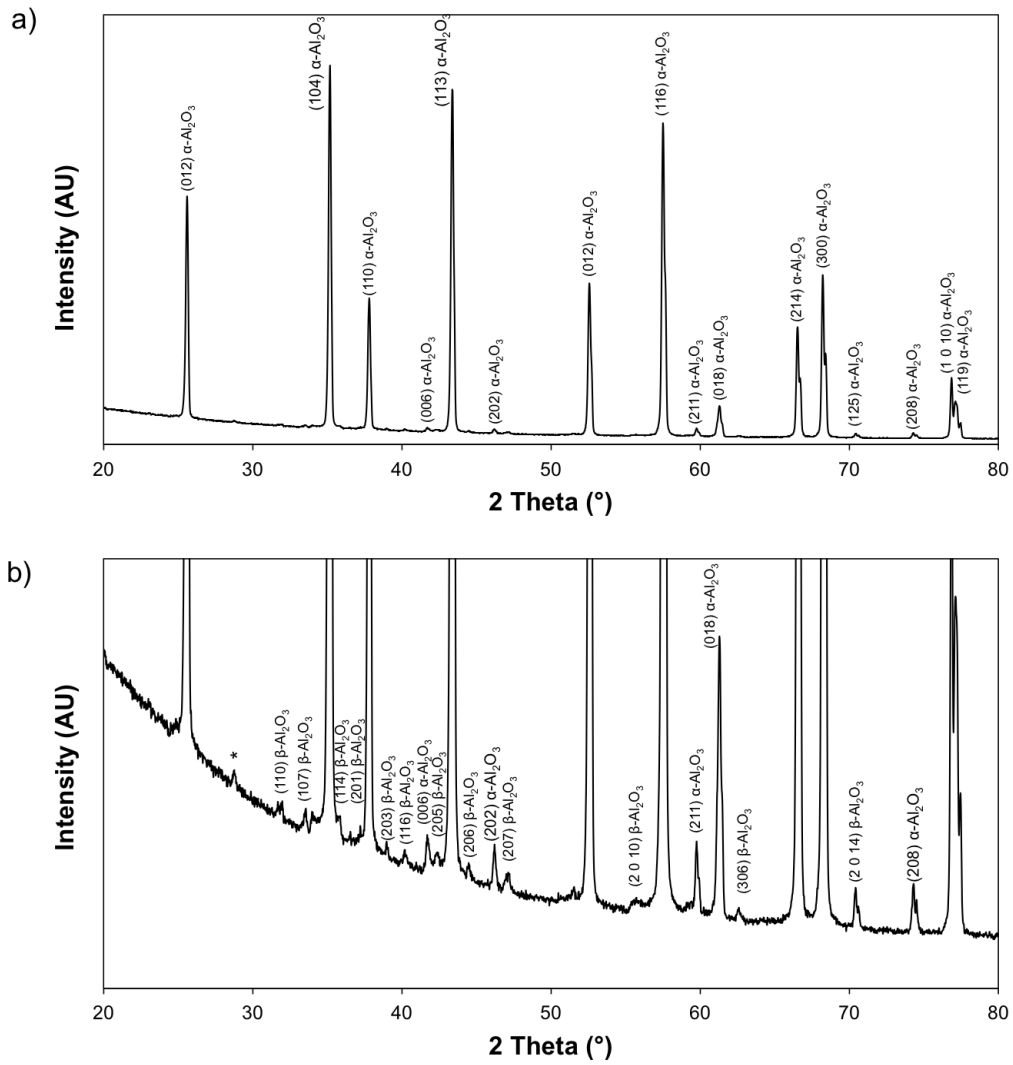


**Figure 5.2.** a) XRD pattern and b) zoomed-in XRD pattern of a sample with 1060 ppm Na<sub>2</sub>O, 82 ppm SiO<sub>2</sub>, and 380 ppm MgO after sintering at 1525°C for 5 h. All observed peaks except for one (\*) can be assigned to either  $\alpha$ -Al<sub>2</sub>O<sub>3</sub> or  $\beta$ -Al<sub>2</sub>O<sub>3</sub>.

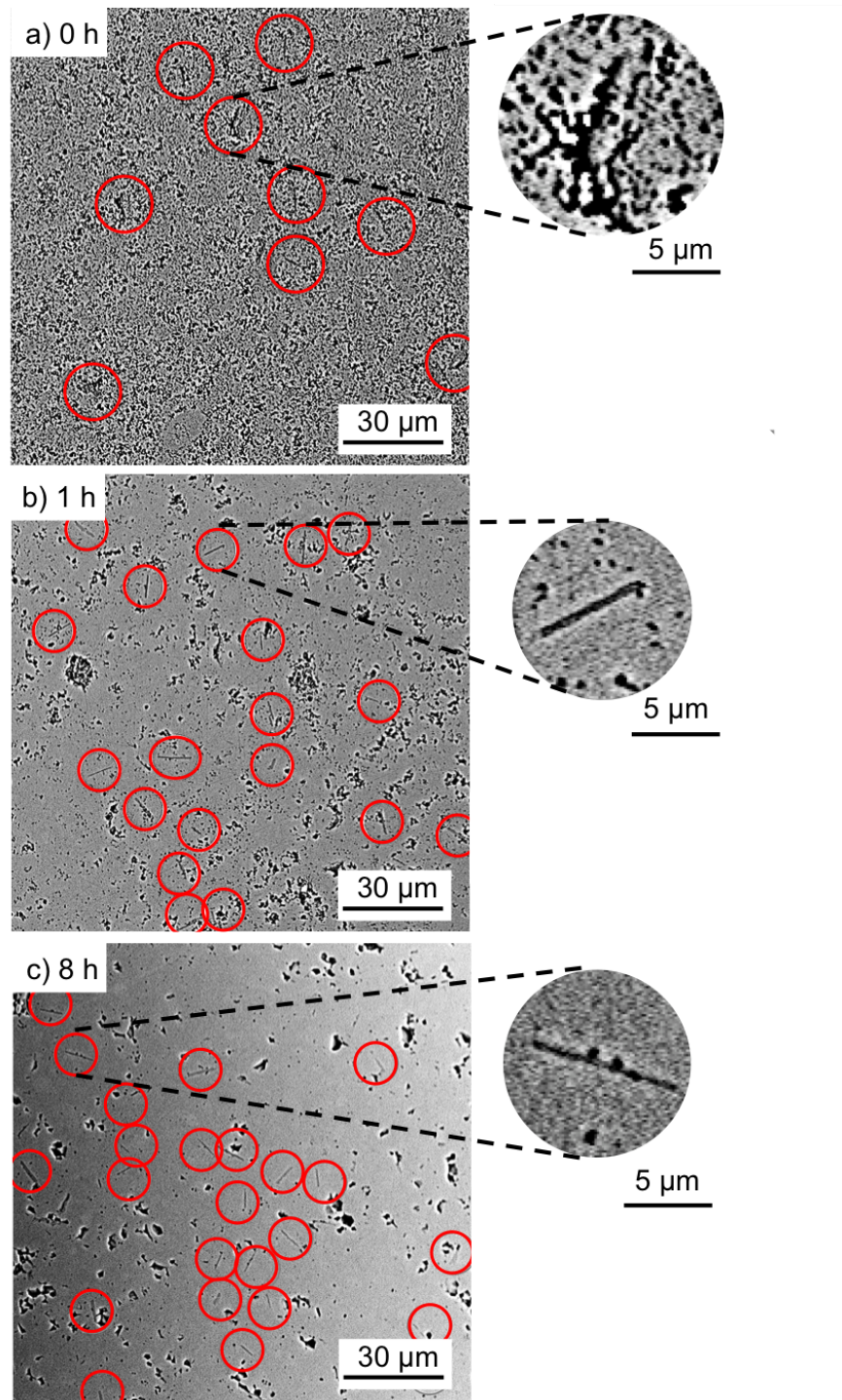


**Figure 5.3.** Micrographs showing  $\beta$ - $\text{Al}_2\text{O}_3$  grains (red circles) in MgO-doped Bayer alumina samples with 82 ppm SiO<sub>2</sub> and 560 ppm Na<sub>2</sub>O after sintering at 1525°C for a) 0 h, b) 1 h, and c) 8 h.

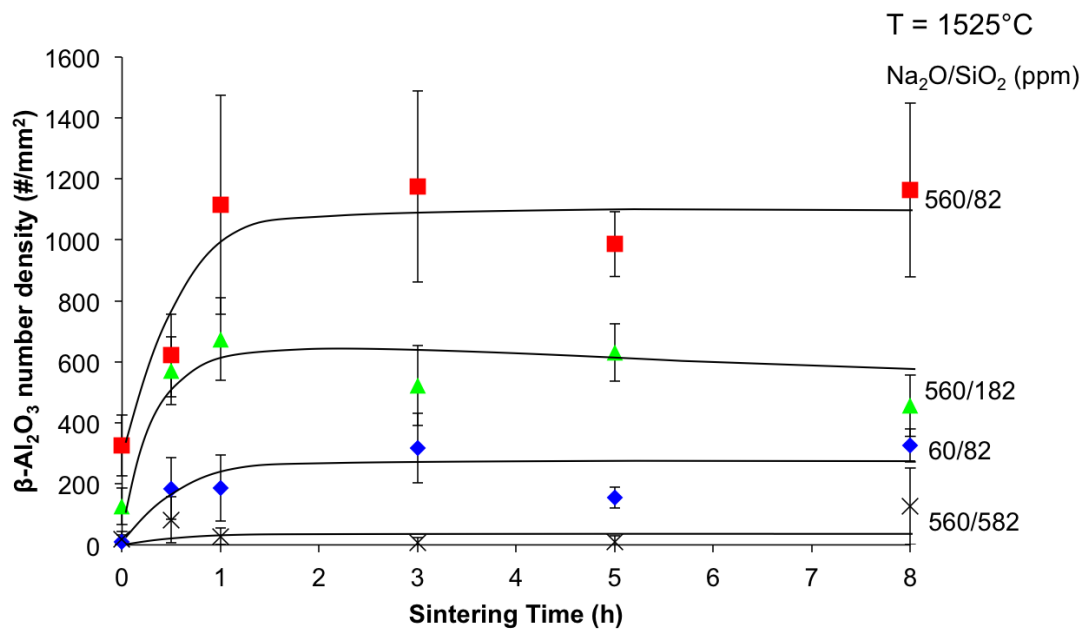


**Figure 5.4.** Kinetics of  $\beta$ - $\text{Al}_2\text{O}_3$  formation for different powder chemistries of MgO-doped powder samples.

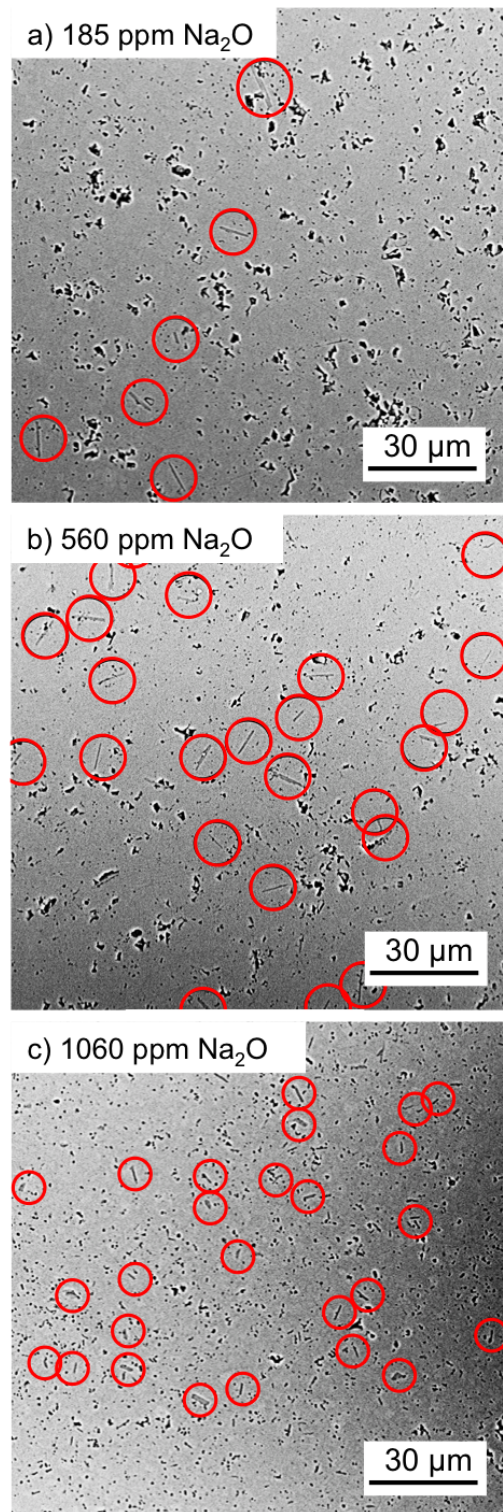


**Figure 5.5.** Micrographs showing  $\beta$ -Al<sub>2</sub>O<sub>3</sub> grains (red circles) in MgO-doped Bayer alumina samples with 82 ppm SiO<sub>2</sub> and a) 185 ppm Na<sub>2</sub>O, b) 560 ppm Na<sub>2</sub>O, and c) 1060 ppm Na<sub>2</sub>O after sintering at 1525°C for 3 h.

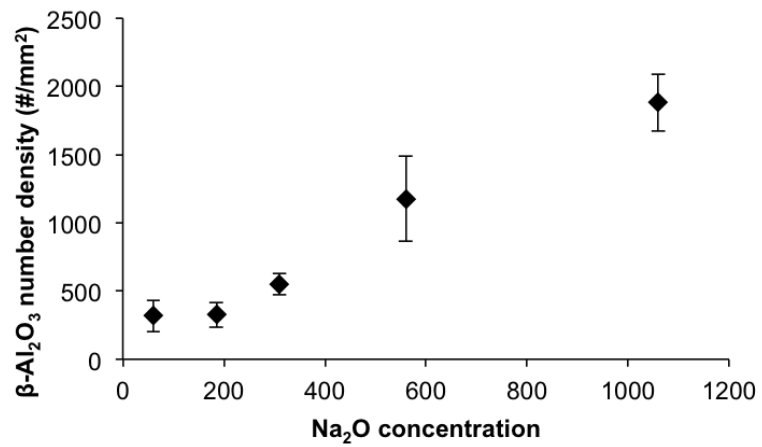


**Figure 5.6.** Formation of  $\beta\text{-Al}_2\text{O}_3$  a function of  $\text{Na}_2\text{O}$  concentration in MgO-doped Bayer alumina.

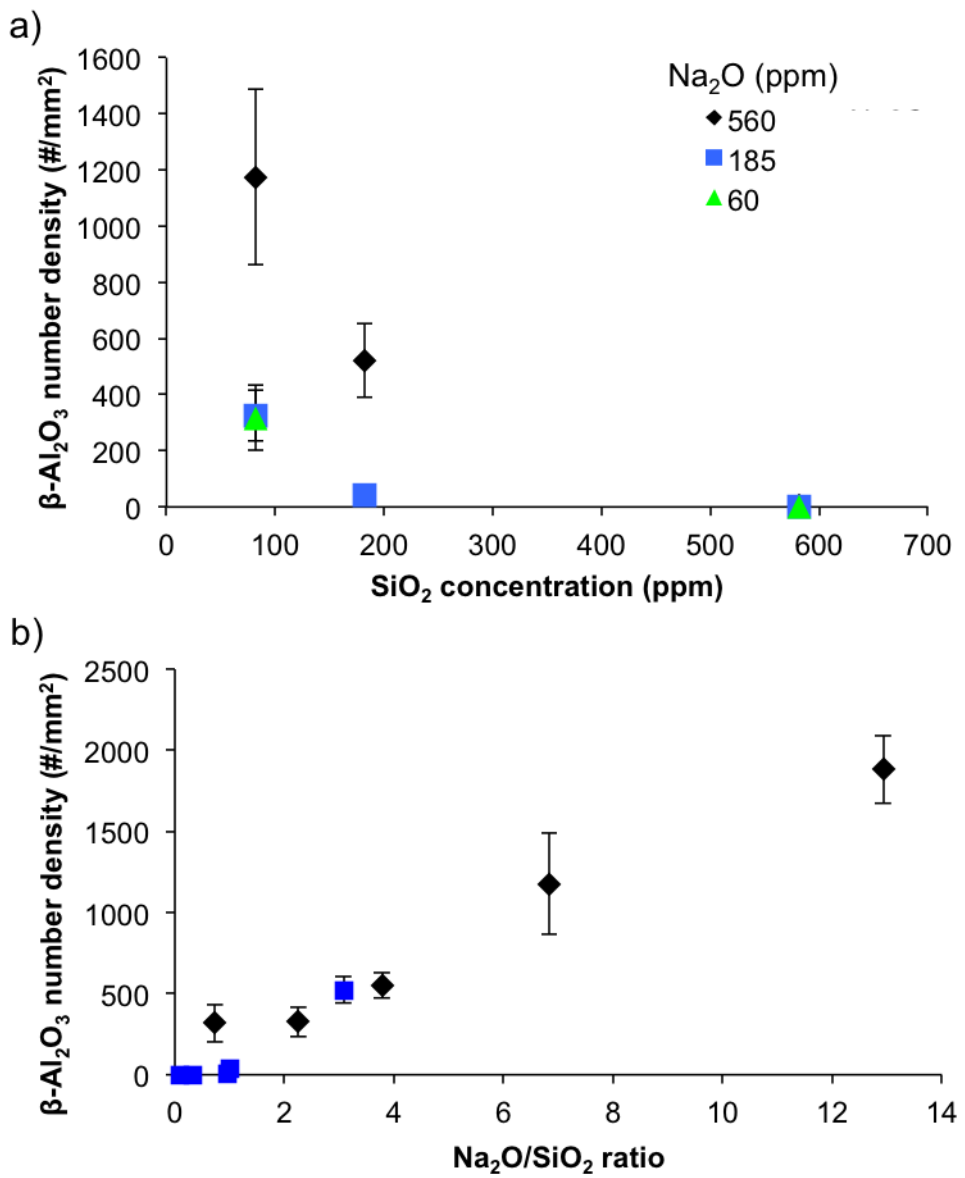


**Figure 5.7.** Formation of  $\beta\text{-Al}_2\text{O}_3$  in  $\text{MgO}$ -doped powder samples a function of a)  $\text{SiO}_2$  concentration for different  $\text{Na}_2\text{O}$  concentrations, and b)  $\text{Na}_2\text{O}/\text{SiO}_2$  ratio. In b) the black diamonds are samples with 82 ppm  $\text{SiO}_2$  and the blue squares are samples with 182 and 582 ppm  $\text{SiO}_2$ .

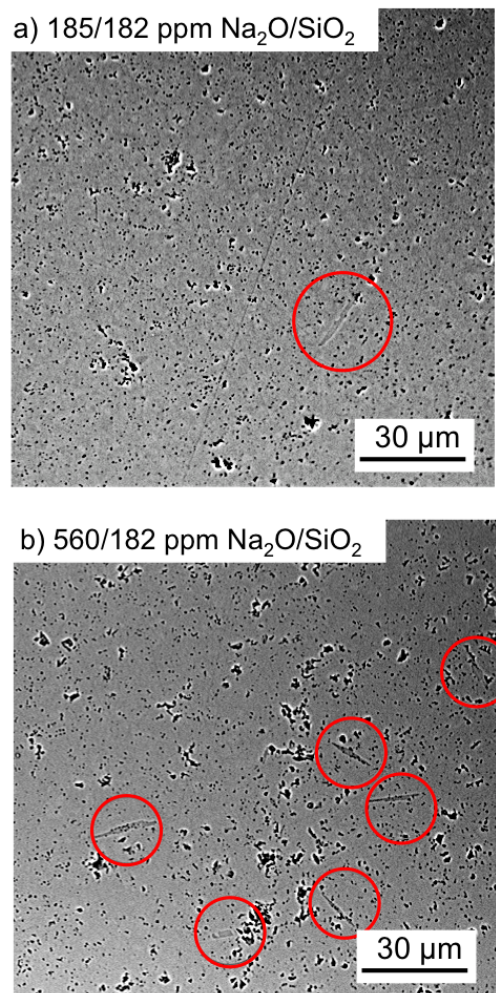


**Figure 5.8.** Micrographs showing  $\beta$ -Al<sub>2</sub>O<sub>3</sub> grains (red circles) in MgO-doped Bayer alumina samples with a) 185/182 ppm Na<sub>2</sub>O/SiO<sub>2</sub> and b) 560/182 ppm Na<sub>2</sub>O/SiO<sub>2</sub> after sintering at 1525°C for 3 h.

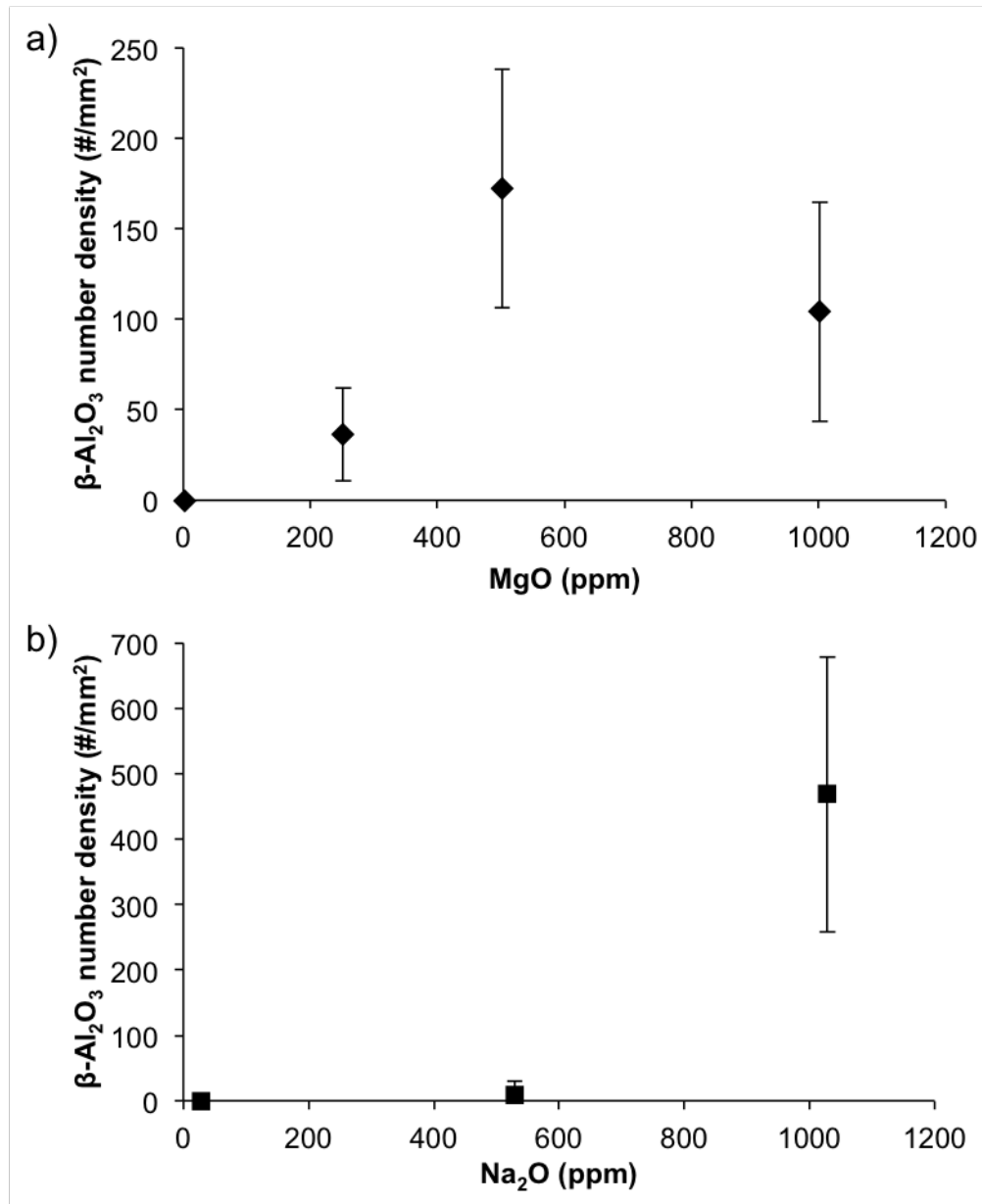


**Figure 5.9.** Formation of  $\beta$ -Al<sub>2</sub>O<sub>3</sub> in MgO-free powder samples as a function of a) MgO concentration (29 ppm Na<sub>2</sub>O) and b) Na<sub>2</sub>O concentration (2 ppm MgO) after 3 h at 1525°C.

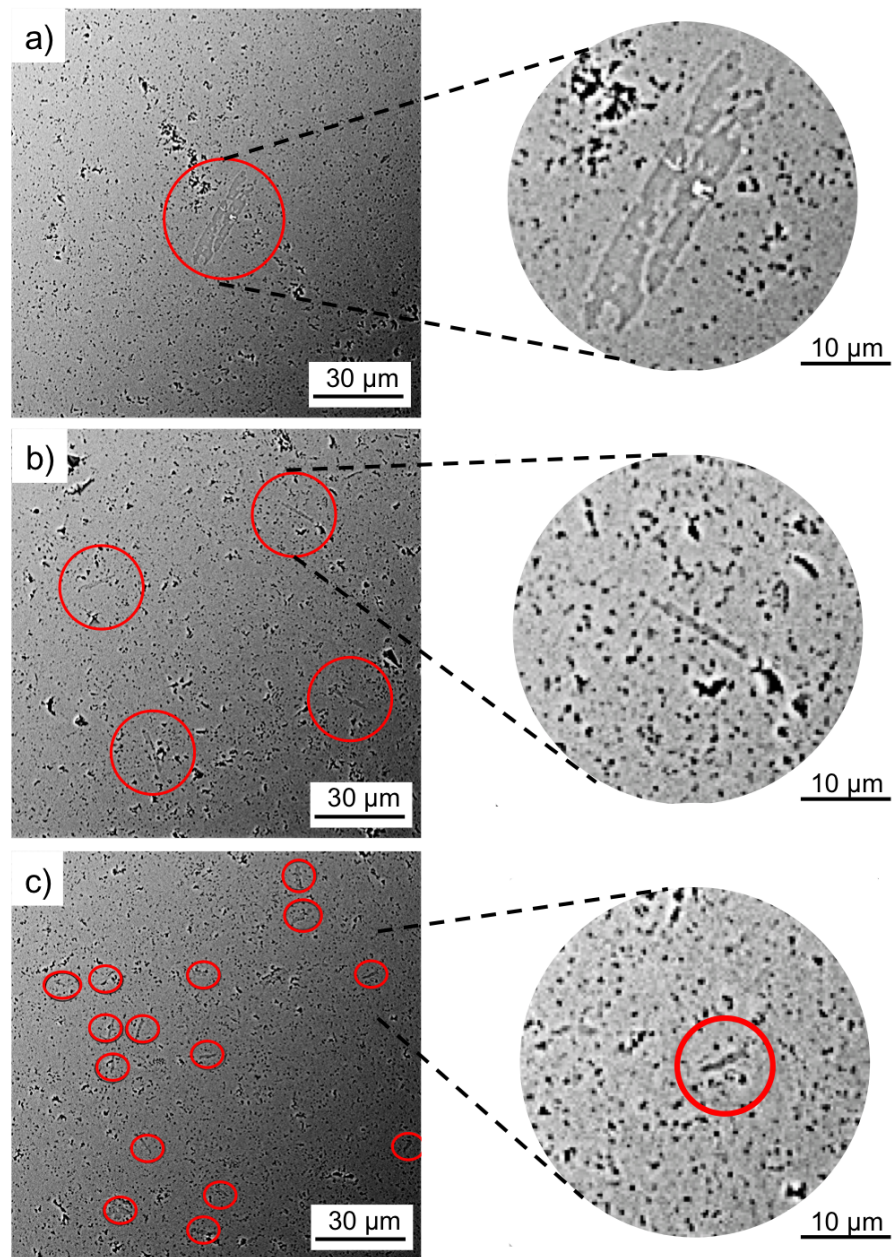


**Figure 5.10.** Micrographs showing  $\beta$ -Al<sub>2</sub>O<sub>3</sub> grains (red circles) in Bayer alumina samples with a) 1002 ppm MgO, 1000 ppm SiO<sub>2</sub>, 29 ppm Na<sub>2</sub>O, b) 2 ppm MgO, 1000 ppm SiO<sub>2</sub>, 1029 ppm Na<sub>2</sub>O, c) 1002 ppm MgO, 1000 ppm SiO<sub>2</sub>, 1029 ppm Na<sub>2</sub>O after 3 h at 1525°C.

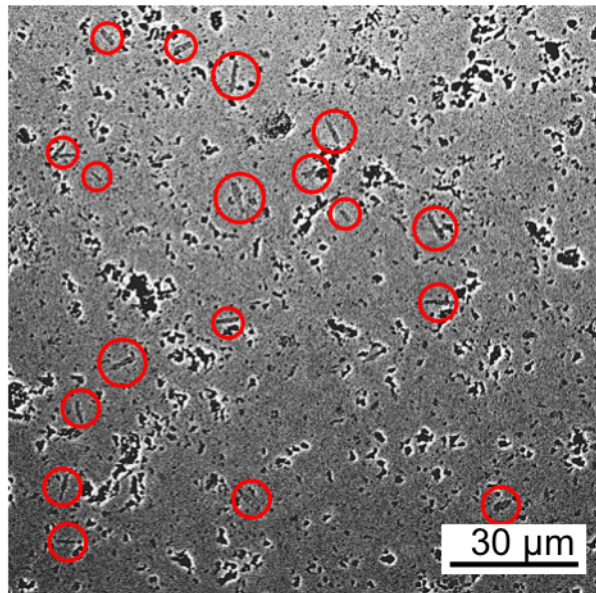


**Figure 5.11.** Micrograph showing  $\beta$ -Al<sub>2</sub>O<sub>3</sub> grains (red circles) in an ultra high purity powder sample with 502 ppm Na<sub>2</sub>O, 2 ppm MgO, and 11 ppm SiO<sub>2</sub> after sintering at 1525°C for 3 h.

# Chapter 6 |

# A Critique of the Master Sintering Curve Analysis of Sintering Processes

## 6.1 Introduction

The master sintering curve (MSC) approach was developed by Su and Johnson [101] to generalize the densification behavior of a sintering powder with a single curve for the entire sintering time/temperature profile. The MSC approach is based on a combined-stage sintering model developed by Hansen et al [102], given as:

$$\frac{1}{\rho} \frac{d\rho}{dt} = \frac{3\gamma\Omega}{k_B T} \left( \frac{\delta D_b \Gamma_b}{G^4} + \frac{D_v \Gamma_v}{G^3} \right) \quad (6.1)$$

where  $\rho$  is relative density of the powder compact,  $d\rho/dt$  is densification rate,  $\gamma$  is surface energy,  $\Omega$  is molar volume,  $k_B$  is Boltzmann's constant,  $T$  is absolute temperature,  $G$  is grain size,  $D$  is diffusion coefficient,  $\delta$  is grain boundary thickness, and  $\Gamma$  is a geometric scaling factor. The subscripts  $b$  and  $v$  represent grain boundary and volume diffusion mechanisms, respectively. The MSC was originally derived to simplify the combined-stage sintering model (Eq. 6.1) to account for only a single diffusion mechanism, and by considering diffusion as thermally-activated with an activation energy  $Q$ . The resulting equation is given as:

$$\frac{1}{\rho} \frac{d\rho}{dt} = \frac{3\gamma\Omega}{k_B T} \left( \frac{D\Gamma}{G^n} \right) \quad (6.2)$$

where

$$D = D_0 e^{-Q/RT} \quad (6.3)$$

and  $R$  is the ideal gas constant. Eq. 6.2 is re-written to collect microstructural parameters on the left hand side and temperature dependent parameters on the right hand side:

$$\frac{k_B G^n}{3\rho\gamma\Omega\Gamma D_0} \frac{d\rho}{dt} = \frac{1}{T} \exp\left(-\frac{Q}{RT}\right) = \frac{d\Theta}{dt} \quad (6.4)$$

Eq. 6.4 can be integrated to give:

$$\frac{k_B}{\gamma\Omega\Gamma D_0} \int_{\rho_0}^{\rho} \frac{(G(\rho))^n}{3\rho\Gamma(\rho)} d\rho = \int_0^t \frac{1}{T} \exp\left(-\frac{Q}{RT}\right) dt = \Theta \quad (6.5)$$

Equation 6.5 describes the sintering behavior for an arbitrary time-temperature profile, and the integral over this profile with respect to time is termed the work of sintering  $\Theta$ . The MSC is obtained by plotting  $\rho$  versus  $\Theta$ . The left hand side of Eq. 6.5 is not solved, because many of the parameters are unknown. However, as long as these parameters are independent of time and temperature, data plotted in this way will collapse into a single continuous curve for a single value of  $Q$ . It is interesting to note that the MSC analysis is independent of the sintering mechanism and, as a generalized model, was applied to other thermally activated process such as grain growth [103] and binder decomposition [104, 105].

In practice,  $Q$  is a fitting parameter for which the best-fit MSC is obtained over a range of heating rates by determining the minimum mean residual. Assuming arbitrary values for  $Q$  in Eq. 6.5, the mean residual square is calculated by [106]

$$\text{Mean residual square} = \sqrt{\frac{1}{\rho_s - \rho_0} \int_{\rho_0}^{\rho_s} \frac{\sum_{i=1}^N \left( \frac{\Theta_i}{\Theta_{avg}} - 1 \right)^2}{N} d\rho} \quad (6.6)$$

where  $N$  is the number of experimental data points gathered at a series of heating rates and a sintered density  $\rho_s$ , and  $Q_{avg}$  is the average of all  $Q_i$  over  $N$ . The  $Q$  value that yields the minimum mean residual square is the  $Q$  value at which the MSC trajectories obtained from the densification curves at different heating rates yield the best fit and converge onto a single curve. Because of the mechanistic nature of the model, the  $Q$  parameter is usually referred to in the literature as the

'activation energy' for sintering.

MSC analysis has been applied to ceramic powders formed and densified by a variety of techniques. For high purity alumina, the reported  $Q$  values vary drastically, as seen in Table 6.1. In Su and Johnson's original work [101],  $Q$  values of 440 and 488 kJ/mol were determined by minimum mean residuals and iso-strain analysis, respectively, for an ultrafine, ultrahigh purity alumina (AKP-50, Sumitomo Chemical America, Inc.). These results showed that the activation energy obtained from minimum mean residuals is in close agreement with the activation energies determined by conventionally used methods. Using the same powder, Tatami et al. [107] determined a  $Q$  of 555 kJ/mol, and when the powder was doped with 2000 ppm MgO, a  $Q$  of 880 kJ/mol was determined. Pouchly et al. [108] estimated the  $Q$  of two different ultrahigh purity alumina powder graded (Taimicron TM-DAR, Taimei Chemicals and RC-HP DBM, Reynolds Chemicals) to be 770 and 640 kJ/mol, respectively, and attributed the difference in  $Q$  to the difference in particle size of 110 nm and 240 nm, respectively. Aminzare et al. [109], reported  $Q$  values of 700 and 605 kJ/mol for alumina (Taimicron TM-DAR, Taimai Chemicals) samples prepared by dry pressing and pressure filtration, respectively. Using the same alumina powder grade (Taimicron TM-DAR, Taimai Chemicals), Guillon and Langer [110] reported a  $Q$  of 290 kJ/mol for  $\text{Al}_2\text{O}_3$  densified by spark plasma sintering (SPS). They attributed the lower  $Q$  value to the effect of the high heating rates of 35 - 150°C/min during SPS.  $Q$  values of up to 1064 kJ/mol were reported by Shao et al. [111] for granulated and dry pressed alumina powder (350 nm, 99.9%, Dalian Luming Nanometer Material Ltd.). They explained the higher  $Q$  values as an effect of slower heating rates (0.5 and 5°C/min) on densification.

The effect of heating rate on densification was explained by Harmer and Brook [112] as due to the relative time the material is heated under conditions favoring surface and grain boundary diffusion. They reasoned that a slow heating process favors surface diffusion and particle coarsening because surface diffusion usually has a lower activation energy than densification mechanisms such as grain and volume diffusion. Samples heated at slow rates spend relatively longer times at lower temperatures and, therefore, experience more particle coarsening prior to reaching the temperatures where densification occurs. Thus, the sintering driving force provided by surface area is higher during the densification stage when ceramics are fired at higher heating rates since these samples do not undergo as much coarsening

prior to densification. In MSC analysis, these relative changes in mechanism result in lower  $Q$  values at faster heating rates. However, it is assumed in the MSC analysis that sintering occurs by a single mechanism for the heating conditions used to collect densification data. Since data for MSC analysis is performed by heating samples at different heating rates, the contributions from surface diffusion and grain boundary diffusion vary, and it is questionable if the  $Q$  values obtained can be used for mechanistic interpretations. Furthermore, it is not apparent what other parameters, additionally to the heating rate, cause the large variability of the reported  $Q$  values.

In this work we investigate how forming techniques and powder chemistry affect the  $Q$  parameter and the shape of the MSC for a commercial specialty alumina powder. We explore how forming process-induced differences in relative green density, microstructural homogeneity and shrinkage anisotropy affect the value of  $Q$ . We also investigate how the assumption of a constant microstructure (i.e., grain size) at high density affects the MSC fit and  $Q$  value. A series of Na<sub>2</sub>O-doped samples were studied to determine how changes in densification mechanism affect the value of  $Q$ . Based on these experiments, we discuss the limits and accuracy of the MSC approach and then determine how MSC can be used in a constructive, practical way to predict the sintering of a specific powder.

## 6.2 Experimental Procedure

To examine the impact of the forming technique on the MSC, we prepared undoped alumina (CT3000 LS SG, Almatis, Inc., Leetsdale, PA) samples by dry pressing, slip casting and tape casting. The powder was a specialty reactive alumina (99.8%) with an average particle diameter of  $\sim 0.3 \mu\text{m}$ . Two sets of samples were prepared by uniaxial dry pressing. For one set, the as-received powder was sieved to -106  $\mu\text{m}$  and uniaxially dry pressed at 30 MPa. The powder handling for the second set was designed to produce a soft granule powder by dispersing it in ethanol with 5 wt.% polyethylene glycol (PEG 600, Alfa Aesar, Ward Hill, MA, USA). After ball milling for 24 h, the dried powder was sieved to -106  $\mu\text{m}$  and samples were lightly pressed at 30 MPa. For uniaxial dry pressing a bar shaped die was used, where the long axis was perpendicular to the pressing direction to minimize density gradients. Both sample types were iso-pressed at 200 MPa after removing the

organic processing aids by heating at 600°C for 12 h in air.

For tape casting, a slurry was prepared by ball milling 26 vol.% alumina powder with 29.7 vol.% xylene (ACS Reagent grade, Avantor Performance Materials, Inc., Center Valley, PA, USA), 32.3 vol.% ethanol (200 proof), and 2.1 vol.% blown menhaden fish oil (Grade Z-3, Tape Casting Warehouse, Morrisville, PA, USA). After 24 h, 5.2 vol.% polyvinyl butyral (PVB B-98, Tape Casting Warehouse, Morrisville, PA, USA), 2.3 vol.% polyalkylene glycol (PAG, UCON50HB2000, Tape Casting Warehouse, Morrisville, PA, USA) and 2.5 vol.% butyl benzyl phthalate (BBP S-160, Tape Casting Warehouse, Morrisville, PA, USA) were added and the mixture was ball milled for another 24 h. Subsequently 1 drop of cyclohexane (99+, Alfa Aesar, Ward Hill, MA, USA) per 20 g of alumina powder was added and the slurry was stirred for an additional 45 min. The slurry was tape cast on a silicone-coated Mylar<sup>TM</sup> carrier tape using a doctor blade gap height of 305 µm. After drying, the tape was cut, stacked, uniaxially pressed at 70°C for 10 min at minimal pressure to tack the layers together, and then isostatically laminated at 74°C and 20 MPa for 30 min.

For non-aqueous slip casting, 28.9 vol.% powder was dispersed in xylene with 3.8 vol.% Menhaden fish oil, ball milled for 24 h, and slip cast. For aqueous slip casting 44.6 vol.% alumina powder was dispersed in deionized water with 6.3 vol.% Darvan C (R. T. Vanderbilt Company, Inc., Norwalk, CT, USA). The pH of the Darvan and water mixture was adjusted to 11 using 5 M NH<sub>4</sub>OH before the alumina powder was added. The slurry was ball milled for 24 h and then slip cast. In both cases the mold consisted of a PVC tube (20 mm diameter) on a plaster of Paris plate.

The polymer processing aids were burned out of all samples by heating at 600°C for 12 h in air. All samples were cold isostatically pressed at 200 MPa (CIP, Autoclave Engineers, Erie, PA). The samples were subsequently cut and ground into 3 x 3 x 15 mm<sup>3</sup> bars for dilatometry studies. The long axis of the dilatometry samples is perpendicular to the casting direction during slip casting and parallel to the casting direction for tape cast samples. The bars were heated to 1525°C or 1595°C at 5, 10, and 20°C/min in a thermomechanical analyzer (TMA; Linseis PT1600, Robbinsville, NJ) and held at temperature for 5 min to record the linear shrinkage of the samples. The thermal expansion of the test fixture was removed by blank experiments, and the thermal expansion contribution of the samples to the

dilatometry curves was subtracted from the dimensions measured in-situ using the cooling curves of the samples measured in the TMA. To ensure accurate shrinkage values the initial nonzero value of the dilatometry data was eliminated, as described in the literature [106].

To examine how changes in chemistry affect the MSC analysis, we studied a series of non-aqueous slip cast  $\text{Na}_2\text{O}$ -doped aluminas. The alumina powder was doped with up to 1000 ppm  $\text{Na}_2\text{O}$  using sodium acetate ( $\text{NaC}_2\text{H}_3\text{O}_2 \cdot 3\text{H}_2\text{O}$ , ACS grade, BDH, West Chester, PA). The detailed doping procedure is reported in chapter 2.

## 6.3 Results and Discussion

### 6.3.1 The effect of forming on $Q$

During initial studies, we observed different degrees of anisotropic shrinkage as a function of the forming method. For example, the dilatometry curves of the non-aqueous slip cast samples during heating to 1525°C at 5, 10, and 20°C/min are shown in Figure 6.1. The shrinkage was measured in the z-direction, i.e., the direction parallel to the capillary (i.e. shear) force of the plaster of Paris mold during slip casting, and in the x/y-direction, perpendicular to the capillary force. Anisotropic shrinkage was observed for all heating rates. Samples heated at 5°C/min have a higher shrinkage in the z-direction than in the x/y-direction throughout the entire sintering process, whereas samples heated at 10 and 20°C/min show slightly more shrinkage in the x/y-direction in the initial stage of densification followed by a crossover in the shrinkage and much more shrinkage in the z-direction at higher densities. The anisotropic shrinkage was quantified with a shrinkage anisotropy factor  $k$ , which is the ratio of the shrinkage in x/y-direction to the shrinkage in z-direction. Figure 6.2 shows how  $k$  changes as a function of relative density and heating rate for the non-aqueous slip cast samples heated at different heating rates during densification. Interestingly, the shrinkage anisotropy factor changes significantly as a function of heating rate during densification and there is much less change in  $k$  at the slowest heating rate. Relative density was calculated using the shrinkage anisotropy factor and is plotted as a function of temperature in Figure 6.3. The mean residuals were calculated as a function of  $Q$  (Eq. 6.6), and

the minimum is at  $Q = 550$  kJ/mol (Figure 6.4). The relatively sharp minimum provides evidence that a single MSC curve is a good fit for the measured TMA data.

When shrinkage in the z-direction is assumed to represent isotropic shrinkage (i.e.  $k=1$ ), then  $Q$  increases to 625 kJ/mol. Figure 6.5 compares the MSCs obtained when the shrinkage anisotropy was accounted for (550 kJ/mol) or by assuming isotropic shrinkage (no correction for anisotropy). This example demonstrates the importance of determining whether the sample shrinks anisotropically during the density measurements used to construct the MSC, and the need to correct for anisotropic shrinkage to determine an accurate value  $Q$  and MSC. Note that the curves at all three heating rates coincide.

Figure 6.6 shows the corresponding MSC curves of samples formed by various techniques and heated to 1525°C. The measurements were corrected for shrinkage anisotropy as described above. The total shrinkage anisotropy was  $\sim 0.75$  for slip cast and tape cast samples, and  $\sim 0.92$  for dry pressed samples. It is clear that  $Q$  changes as a function of forming technique, which is, in part, due to different green densities. The sample prepared by non-aqueous slip casting has a green density of 59% and the lowest  $Q$  (550 kJ/mol), followed by the sample prepared by aqueous slip casting with a green density of 58% and a  $Q$  of 650 kJ/mol. The samples prepared by dry pressing (no PEG) and tape casting have green densities of 57% and 55%, respectively, and both samples have a  $Q$  of 730 kJ/mol. The dry pressed sample with 5 wt.% PEG has a green density of 55% and the highest activation energy with 810 kJ/mol. It can thus be observed that  $Q$  decreases as the green density increases and that the shape and position of the MSC changes as a function of forming technique (Figure 6.6). Aminzare et al. [109] also observed that  $Q$  is sensitive to the forming technique and concluded that samples prepared by pressure filtration have a lower  $Q$  than dry pressed samples as a result of better sample homogeneity as evidenced by the higher green density. As shown in this work, the effect of green density on  $Q$  is complicated. For example, the samples prepared by tape casting and dry pressing with 5 wt.% PEG have the same green density of 55%, but different  $Q$  values of 730 kJ/mol and 810 kJ/mol, respectively, and different MSC shapes. This suggests that other sample characteristics, in addition to green density, influence  $Q$ , such as pore size, pore size distribution, and particle/pore orientation. Given that the curves shown in Figure 6.6 diverge at

very low density it can be assumed that additional factors, i.e. factors that are assumed to be constant in MSC analysis such as  $D_0$ , are highly variable and depend strongly on process history. The magnitude of differences observed suggest that these variables are extremely important in understanding differences in sintering behavior. Such changes are not related to activation energy and have been largely overlooked or ignored in prior literature.

### 6.3.2 MSC at high densities

The final densities used in the MSC analysis of the samples discussed above are  $\leq 90\%$ . Above 90% density we observed that the MSC curves for different heating rates diverge and thus dramatically influences the value of  $Q$ . Figure 6.7a shows the densification curves of dry pressed samples sintered to  $>95\%$  density when heated to 1595°C at different heating rates and held for 5 min. The minimum mean residual analysis yielded  $Q = 700 \text{ kJ/mol}$  (Figure 6.7b) and Figure 6.7c shows the resulting MSC. It can be seen that  $Q = 700 \text{ kJ/mol}$  gives a good fit at low densities, but the trajectories begin to diverge at densities  $>90\%$  (see Fig 6.7c insert).

To account for the effect of bulk density on densification we determined the activation energy at some relative densities by plotting  $\ln(-T \cdot d\rho/dt)$  vs.  $1/T$  and determining the slopes of the resulting linear curves of the isodensities. Figure 6.8 shows the development of the apparent activation energy obtained from iso-density analysis,  $Q_{iso}$ , and it can be seen that  $Q_{iso}$  is  $\sim 700 \text{ kJ/mol}$  and increases slightly with increasing relative density. At densities  $>85\%$   $Q_{iso}$  increases somewhat more rapidly, and at densities  $>95\%$   $Q_{iso}$  increases drastically to  $>1800 \text{ kJ/mol}$ . This change in  $Q_{iso}$  explains the divergence of the MSC trajectories obtained from the different heating rates using  $Q_{MSC} = 700 \text{ kJ/mol}$ .

At densities  $<90\%$  the activation energy obtained from the minimum mean residuals  $Q_{MSC}$ , which is used to obtain the MSC, is reasonably close to the activation energies obtained from the iso-density analysis,  $Q_{iso}$ , resulting in a good fit at all heating rates. However, at densities  $>90\%$  where we observe divergence in the MSCs, the values of  $Q_{iso}$  are  $>100 \text{ kJ/mol}$  greater than the  $Q_{MSC}$  value used to construct the MSC. Although the idea of variable activation energy is understandable, it is not physically realistic to consider that the activation energy for sintering is intrinsically a function of  $\rho$ . It is more likely that this increase in

$Q_{iso}$  and the divergence of the MSC at high densities is caused by microstructural or mechanistic changes that are not accounted for in the MSC model.

### 6.3.3 Quantification of the MSC shape

A way to account for microstructural changes is analyzing the shape of the MSC, since it is determined by the evolution of the microstructural parameters in the left hand side of Eq. 5. Microstructural evolution can be described quantitatively by:

$$C = \frac{k_B G^n}{3\gamma\Omega\Gamma D_0} \quad (6.7)$$

By rearranging Eq. 6.4,  $C$  can be determined as a function of relative density:

$$C = \rho \frac{d\Theta}{d\rho} \quad (6.8)$$

In Figure 6.9 it can be seen that  $C$  increases by more than 5 orders of magnitude between 57% and 98% relative density. The increase in  $C$  is partially due to the 8-fold increase in grain size from 0.3 to 2.4  $\mu\text{m}$  during sintering of the sample to 98% relative density. Assuming that grain boundary diffusion controls densification ( $n=4$ ), the coarsening of the microstructures accounts for an increase in  $C$  of  $\sim 3.5$  orders of magnitude. The remaining  $\sim 2$  orders of magnitude increase in  $C$  are most likely due to an increase in the geometric factor  $\Gamma$ , since it is a function of relative density and the only parameter that is expected to change considerably with temperature. Note that the obtained trajectories for  $C$  also diverge above 90% relative density, similar to the MSCs.

While we can hypothesize about the factors that influence the MSC shape, the actual shape of the MSC cannot be understood based on the existing MSC analysis methodology, because one or more parameters in Eq. 6.7 vary with time and temperature in a complex manner. To gain insight into the development of the shape of the MSC the individual parameters in Eq. 6.7 need to be investigated. For example, grain size evolution could be tracked as a function of density and extracted from the  $C$  parameter. Assuming that the divergence of the MSCs at densities  $>90\%$  is caused by differences in grain size as a result of different heating rates only, this divergence in MSC shape at densities  $>90\%$  could be corrected. If the development of the geometry factor  $\Gamma$  could be quantified and separated from

the  $C$  parameter, we should be able to assign a constant value for  $C$ , and the  $Q$  value that results from MSC analysis should represent the true activation energy for sintering. However, such an analysis would assume that  $\Gamma$  can be quantified on a sufficiently accurate level, and that grain size and  $\Gamma$  are the only factors in Eq. 6.7 that change as a function of relative density.

### 6.3.4 Influence of powder chemistry

Figure 6.10 shows the MSCs of  $\text{Na}_2\text{O}$ -doped samples formed by non-aqueous slip casting. It can be seen that  $Q$  changes as a function of  $\text{Na}_2\text{O}$  concentration and increases from 550 kJ/mol for samples with no  $\text{Na}_2\text{O}$  dopant to 700 and 730 kJ/mol for samples doped with 250 and 500 ppm  $\text{Na}_2\text{O}$ , respectively.  $Q$  decreases to 690 kJ/mol when the concentration is further increased to 1000 ppm  $\text{Na}_2\text{O}$ . The position of the MSC changes as a function of  $\text{Na}_2\text{O}$  concentration as well and the effect of  $\text{Na}_2\text{O}$  concentration on the MSC is complicated.

### 6.3.5 Limitations of the MSC analysis

Anisotropic shrinkage is commonly observed in slip cast parts since the capillary force cause particles in the slurry to align during slip casting. It should be noted that the degree of shrinkage anisotropy strongly depends on the particle morphology and forming technique (i.e. magnitude of shear force exerted on the particles and ease of reorientation). For samples that were prepared by colloidal forming techniques, such as slip casting and tape casting, the degree anisotropic shrinkage has to be taken into account during the MSC analysis, otherwise the densities calculated from the dilatometry data alone are inaccurate and thus the calculated value of  $Q$  and the shape of the MSC are incorrect. Likewise, samples formed by uniaxial pressing are often anisotropic but not to the same degree as slurry processed ceramics.

The above results show that a variety of factors such as forming technique and powder chemistry affect the value of  $Q$  and the shape of the MSC in a complicated way, and the reason for this complicated relation lies in the assumption in MSC analysis that sintering is influenced by only one single mechanism. Making this assumption allows MSC analysis to assign an activation energy for sintering that corresponds to this specific sintering mechanism. If this assumption held true, variations in forming technique or chemistry could be analyzed using the MSC

approach and using  $Q$  as an indicator for how the sinterability of a powder changes as a function of powder chemistry and forming technique. However, sintering is typically divided into different stages, all of which are governed by different sintering mechanisms. When multiple mechanisms are involved, each mechanism can be affected differently by such changes and  $Q$  loses its physical meaning as an activation energy for a specific sintering mechanism. As a result,  $Q$  appears to be a function of relative density (Figure 6.8) and the changes in  $Q$  and MSC shape as a function of powder chemistry and forming technique are complicated (Figures 6.9 and 6.10).

For example, we know that initial pore size, pore size distribution, and pore/particle orientation in a green body are highly dependent on the forming technique. Changes in these parameters affect different sintering stages in different ways. During initial stage sintering the sinter undergoes a particle rearrangement process that is driven by capillary forces and therefore highly sensitive to the aforementioned parameters. During final stage sintering the concentration of large pores that can only slowly be eliminated is determined by the forming technique. Mechanistic changes as such can affect  $Q$  in different ways.

Similarly, powder chemistry affects initial stage sintering and intermediate stage sintering in different ways. In previous chapters, it was observed that the onset temperature of sintering increases with higher  $\text{Na}_2\text{O}$  concentration, which has the effect of increasing  $Q$ . The further development of densification was shown to depend heavily on additional factors. For example, samples with  $\text{Na}_2\text{O}/\text{SiO}_2$  ratios  $\sim 1.0$  densify faster during intermediate stage sintering than samples with  $\text{Na}_2\text{O}/\text{SiO}_2$  ratios  $\sim 0.1$  for the same  $\text{SiO}_2$  concentration because  $\text{Na}_2\text{O}$  decreases the viscosity of the siliceous liquid grain boundary phase, and, therefore, enhances diffusion, which would decrease  $Q$ . This demonstrates that powder chemistry influences fundamental sintering mechanisms at different sintering stages and in different ways.

Since the processes and mechanisms of all sintering stages are lumped into one  $Q$  value during MSC analysis, forming technique and powder chemistry may affect the value of  $Q$  and the shape of the MSC, but the changes in sintering behavior and mechanisms cannot be sufficiently described using  $Q$  and the MSC. Therefore, the MSC approach is judged to be insufficient to evaluate forming and powder chemistry effects on sintering. It is recommended that  $Q$  values obtained by MSC

analysis for different powder grades (i.e. chemistries, forming techniques, particle size, etc.) should not be compared or used to draw conclusions about sintering mechanisms.

### 6.3.6 Practical use of the MSC analysis

Even though MSC analysis is insufficient to analyze fundamental differences in sintering behavior due to differences in powder chemistry and forming technique, choosing an appropriate  $Q$  value converges the trajectories of samples obtained from different heating rates onto one MSC, and this  $Q$  value and the obtained MSC can be used to predict densification. As explained in the literature [113,114], the  $Q$  value obtained is an apparent activation energy for the entire sintering process of a sinter and accounts for densification (regardless of mechanism), the retardation of densification due to grain growth, surface diffusion in the early sintering stages, and other processes that potentially influence densification. Consequently,  $Q$  is a fitting parameter that is composed of a variety of factors that influence densification, including the activation energies for sintering of all involved mechanisms.

One of the practical objectives of MSC analysis is to predict the sintered density of samples prepared from a given powder for an arbitrary time/temperature condition. The MSC data provided above and Eq. 6.5 can be used to construct equivalent time/temperature diagrams to predict the density of samples for known heating conditions [109]. Fig. 6.11 is an example of the equivalent time/temperature conditions leading to equivalent densities for non-aqueous processed powder dry pressed samples heated at 10°C/min. The contours shown in Figure 6.11 indicate the equivalent relationships between particular time/temperature treatments and relative densities of 80, 85, 90, and 95%. For example, a relative density of 85% is reached after heating a dry pressed sample at 10°C/min to 1460°C with no hold time. The same density is reached after heating a dry pressed sample from the same powder at 10°C/min to 1400°C and holding for 29 min. It should be noted that the predicted MSC response for >90% sintered density has some inaccuracy due to the discrepancies we noted above for MSC data analysis at >90% density. Despite earlier reservations and limitations, the predictions for equivalent time/temperature conditions leading to 95% density are insightful and, at least, give a semiquantitative measure of the effect of time and temperature on sintering. In the literature it was

proposed to divide the MSC into two regimes of "low density" and "high density" (i.e., <75% and >85%), respectively with two individual  $Q$  values to account for the changes in  $Q$  during densification [108, 115]. While the fundamental reasoning behind assigning two separate  $Q$  values is questionable, considering our conclusion that  $Q$  is a fitting parameter without physical meaning, this could be an useful approach to obtain more accurate density predictions at high densities.

## 6.4 Summary

MSC analysis results in two pieces of information; a  $Q$  value and the MSC curve itself.  $Q$  should not be interpreted as the activation energy for sintering, since multiple mechanisms contribute to its value and processing history and powder chemistry can drastically affect the  $Q$  value and the shape of the MSC. Therefore, comparing  $Q$  between different chemistries is not an appropriate means to interpret fundamental, mechanistic changes in sintering behavior.

It is evident that the MSC is only useful for characterizing the sintering behavior of the specific ceramic powder studied. A number of factors need to be accounted for to obtain accurate  $Q$  values and MSCs including sample shrinkage anisotropy, and limiting the density range to < 90% density to avoid microstructural changes that are not accounted for in the MSC analysis. With more accurate  $Q$  values the MSC approach is a useful tool and "a practical approach to sintering" as originally proposed by Su and Johnson, but is not sufficient to explain fundamental changes in sintering behavior, or to determine the "activation energy" for sintering since basic assumptions made for MSC analysis are insufficient to describe the entire sintering process.

**Table 6.1.**  $Q$  values obtained by MSC analysis for different alumina powders.

Alumina grade	Forming technique	Heat rates (°C/min)	$Q$ (kJ/mol)	Ref.
AKP-50 Sumitomo Chemicals	CIP (270 MPa)	60 to 750°C, 8-45 to 1500°C	440	[101]
AKP-50 Sumitomo Chemicals	Uniaxial pressing (50 MPa) CIP (200 MPa)	3-20 to 1400°C	555	[107]
AKP-50 + 2000 ppm MgO Sumitomo Chemicals	Uniaxial pressing (50 MPa) CIP (200 MPa)	3-20 to 1400°C	880	[107]
Taimicron TM-DAR Taimei Chemicals	CIP (300 MPa)	2-20 to 1500°C	770	[108]
RC-HP DBM Reynolds Chemicals	CIP (300 MPa)	2-20 to 1500°C	640	[108]
Taimicron TM-DAR Taimei Chemicals	Uniaxial pressing (50 MPa) CIP (200 MPa)	2-25 to 1400°C	700	[109]
Taimicron TM-DAR Taimei Chemicals	Pressure filtration (40 MPa)	2-25 to 1400°C	605	[109]
Taimicron TM-DAR Taimei Chemicals	SPS (50 MPa)	35-150 to 1200°C	290	[110]
99.9%, Dalian Luming Nanometer Materials	Uniaxial pressing (80 MPa) CIP (250 MPa)	0.5-5 to 1640°C	1064	[111]

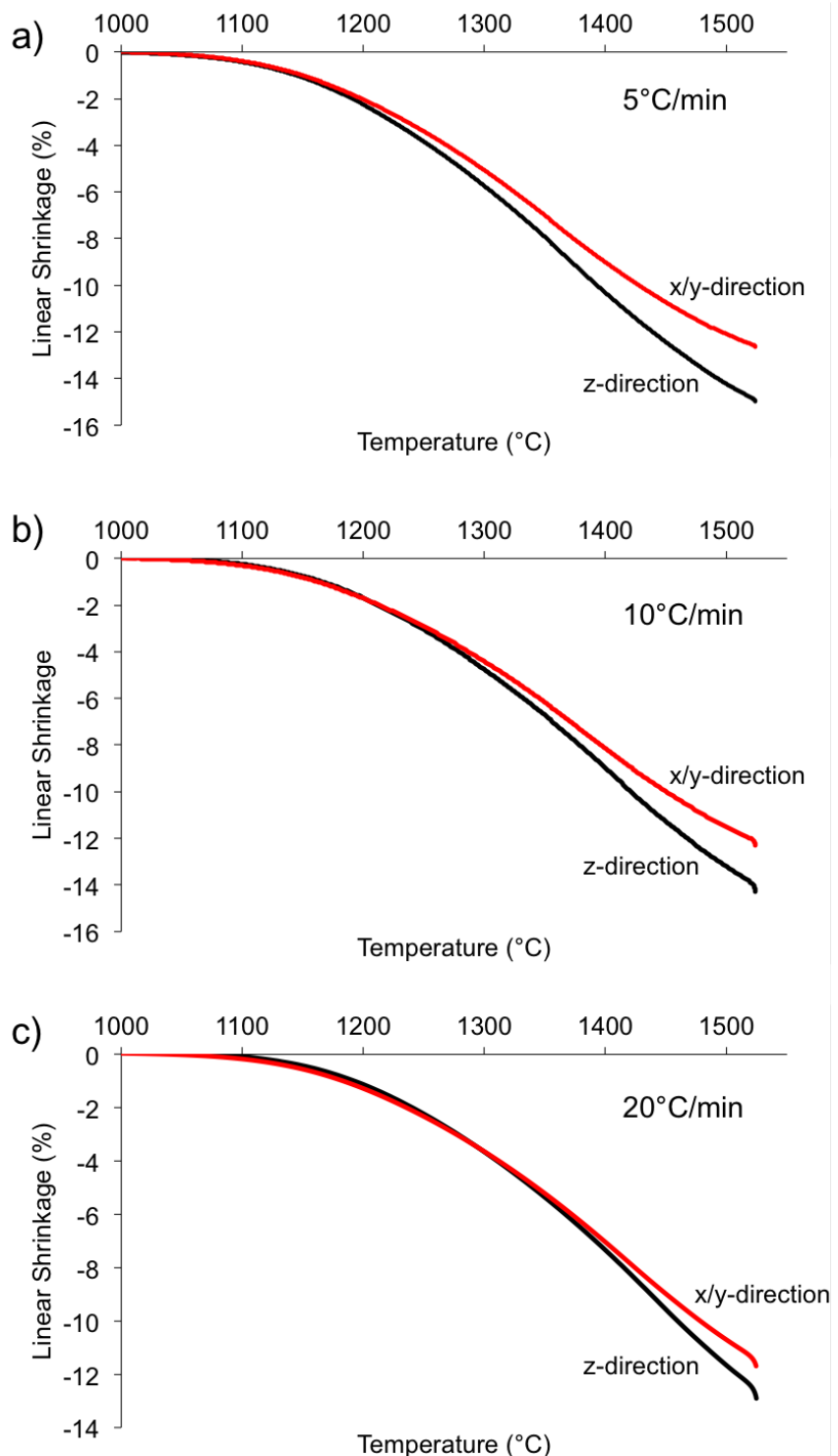


**Figure 6.1.** Dilatometry curves of non-aqueous slip cast CT3000 LS SG samples heated at a) 5°C/min, b) 10°C/min, and c) 20°C/min to 1525°C measured parallel to (z-direction) and perpendicular to (x/y-direction) the capillary force acting during slip casting.

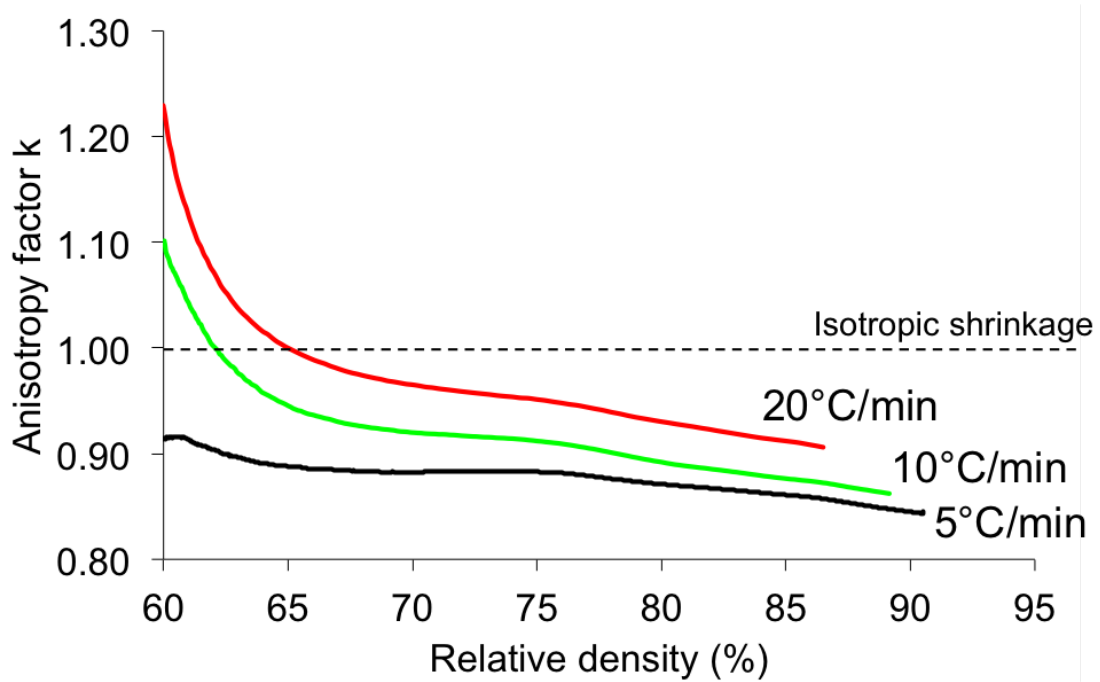


**Figure 6.2.** Development of the shrinkage anisotropy factor for shrinkage,  $k$ , during densification of non-aqueous slip cast samples as a function of relative density for CT3000 LS SG samples heated at different rates.

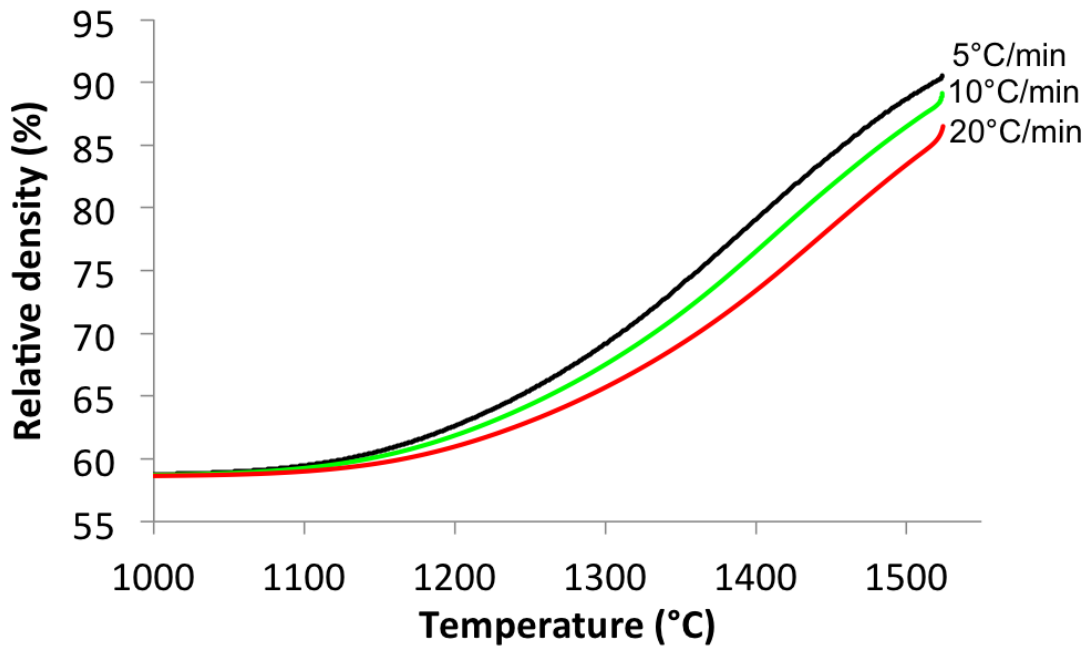


**Figure 6.3.** Development of the relative density corrected for shrinkage anisotropy as a function of temperature for non-aqueous slip cast CT3000 LS SG samples heated at different rates.

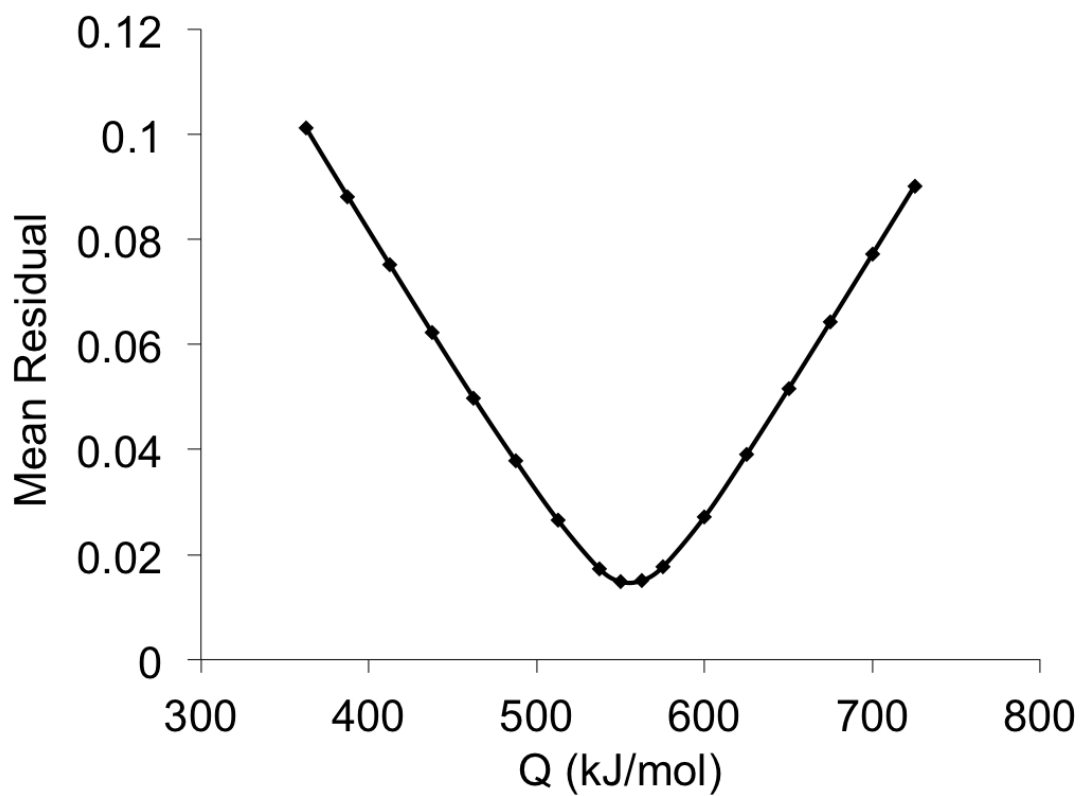


**Figure 6.4.** Mean residuals of the MSCs assuming different values for  $Q$  for non-aqueous slip cast CT3000 LS SG samples.

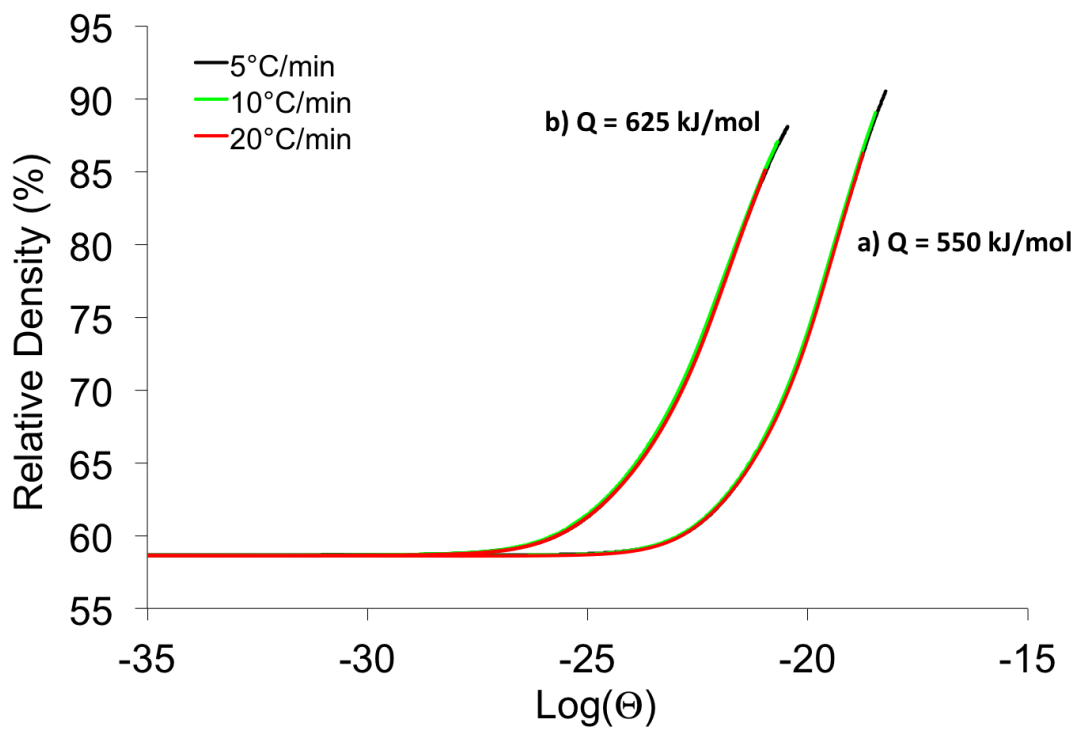


**Figure 6.5.** MSCs of CT3000 LS SG samples prepared by non-aqueous slip casting using a) the  $Q$ -value obtained by accounting for shrinkage anisotropy ( $Q=550 \text{ kJ/mol}$ ) and b) using  $Q$ -value when shrinkage anisotropy was uncorrected for ( $Q = 625 \text{ kJ/mol}$ ).

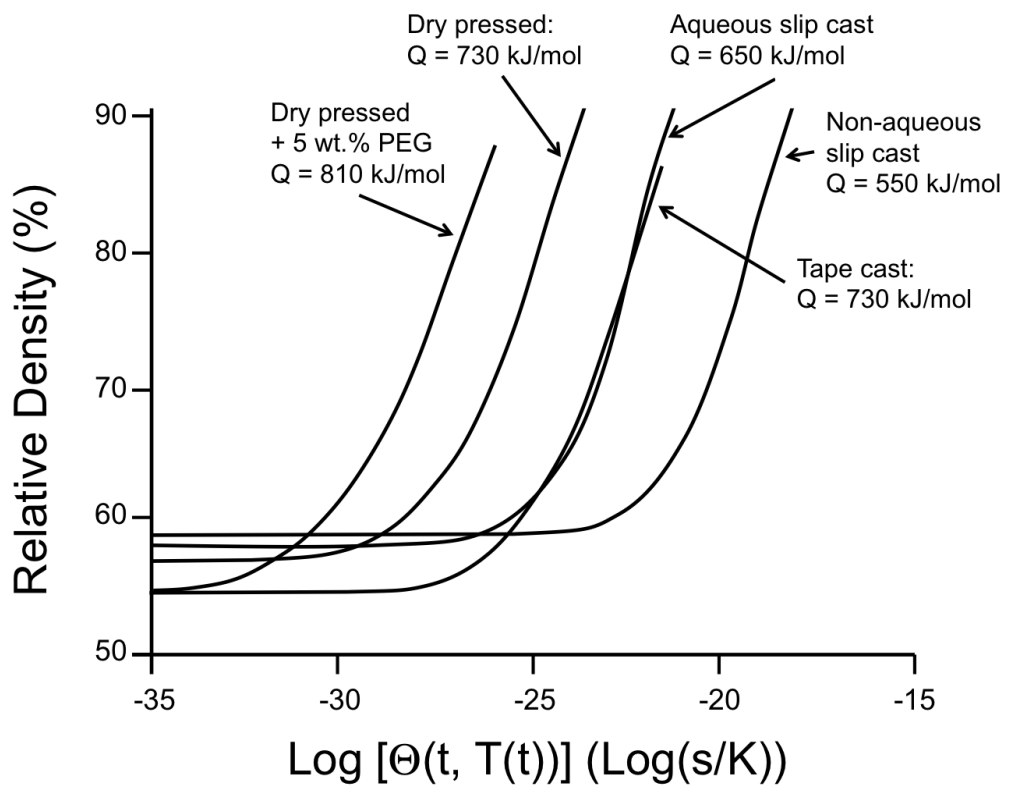


**Figure 6.6.** MSCs and  $Q$ -values of CT3000LS-SG samples obtained from the minimum mean residuals for samples prepared by different forming techniques and accounting for shrinkage anisotropy.

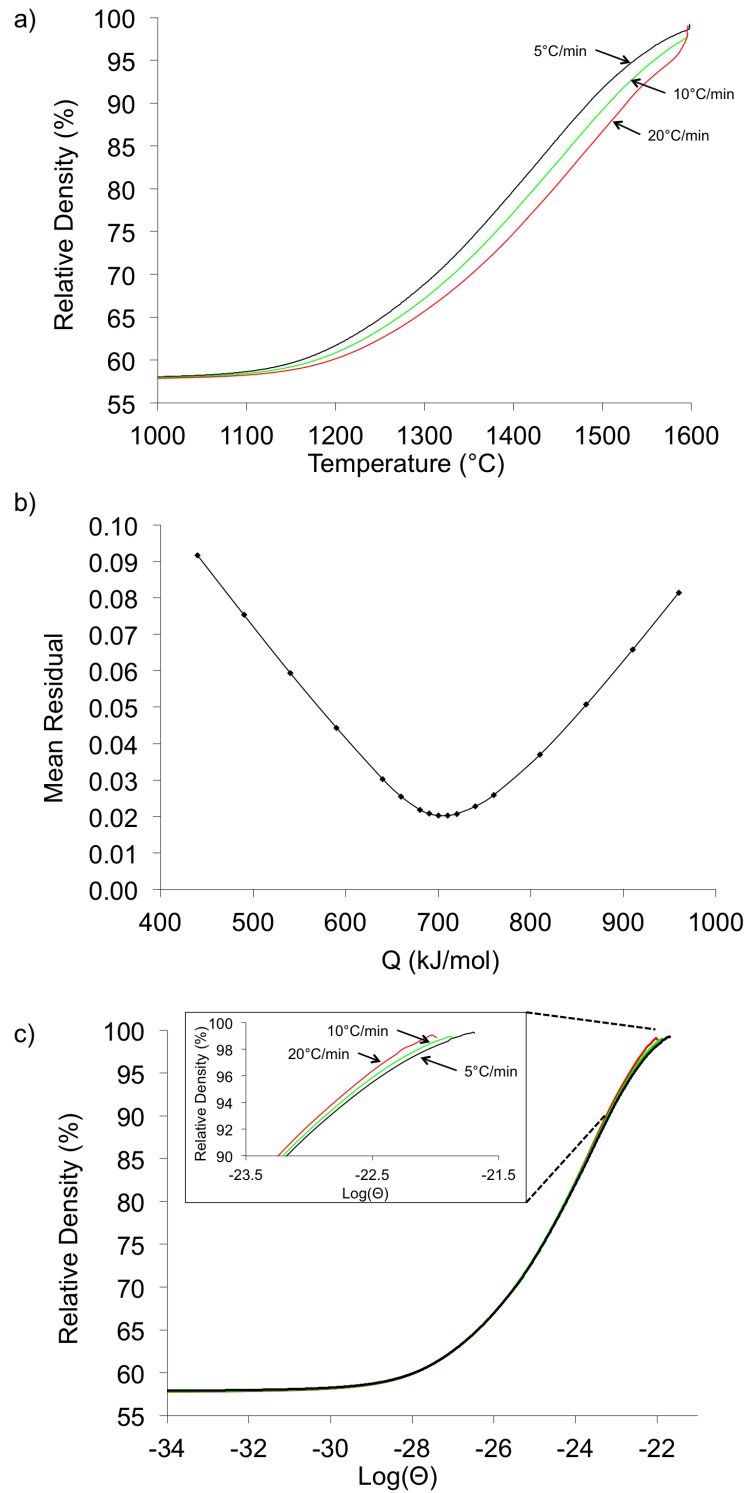


**Figure 6.7.** a) Densification of dry pressed CT3000 LS SG samples at different heating rates, b) mean residuals as a function of  $Q$ , and c) MSC for  $Q = 700$  kJ/mol obtained from the minimum mean residuals, showing divergence at densities  $>90\%$ .

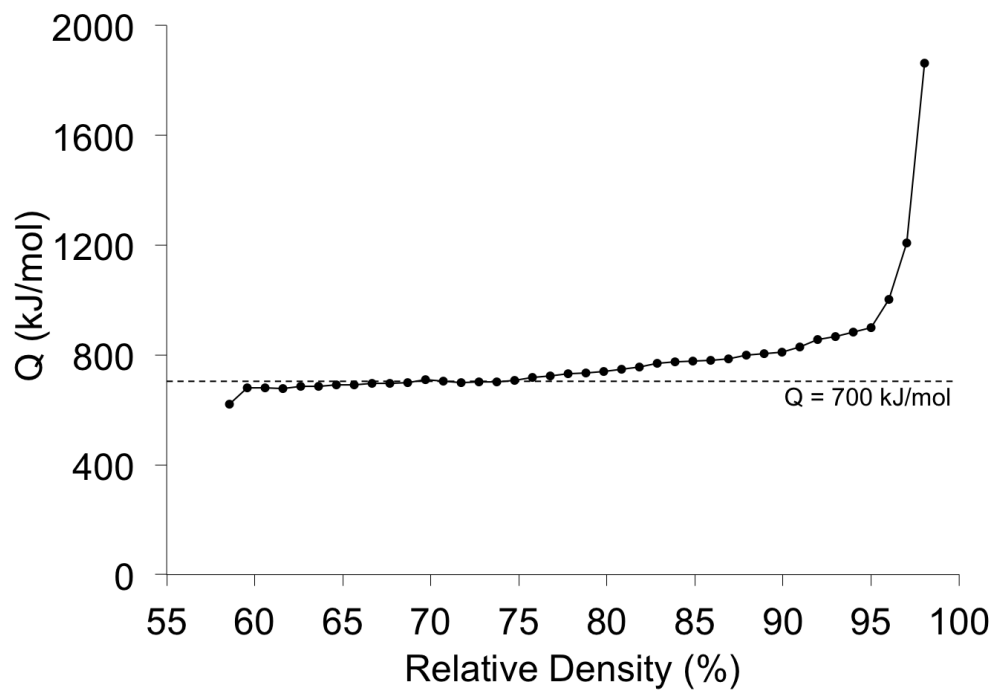


**Figure 6.8.**  $Q$ -values for dry pressed CT3000 LS SG samples as a function of relative density obtained from iso-density analysis.

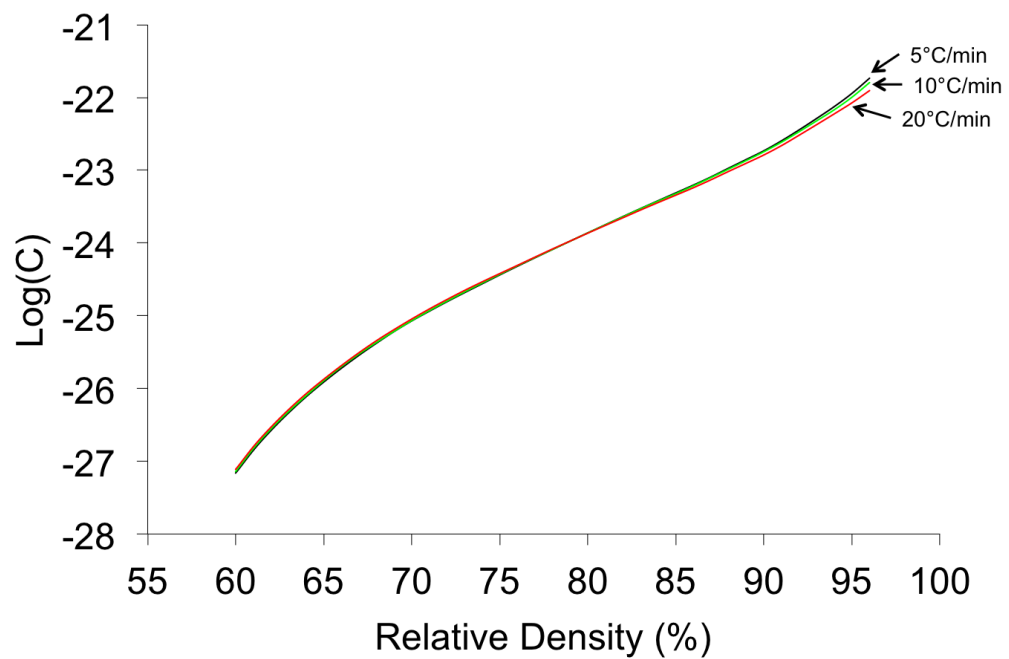


**Figure 6.9.** Development of the microstructural parameters, summarized in the  $C$  parameter, as a function of relative density for dry pressed CT3000 LS SG samples.

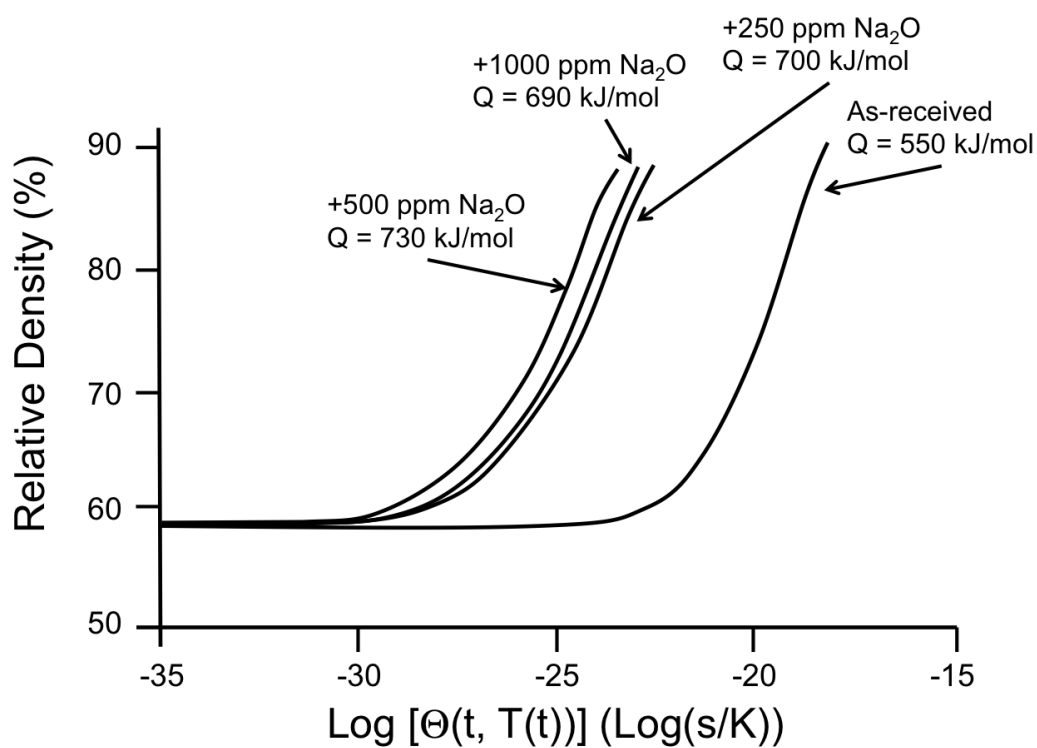


**Figure 6.10.** MSCs and  $Q$ -values for CT3000 LS SG samples prepared by non-aqueous slip casting with different  $\text{Na}_2\text{O}$  concentrations.

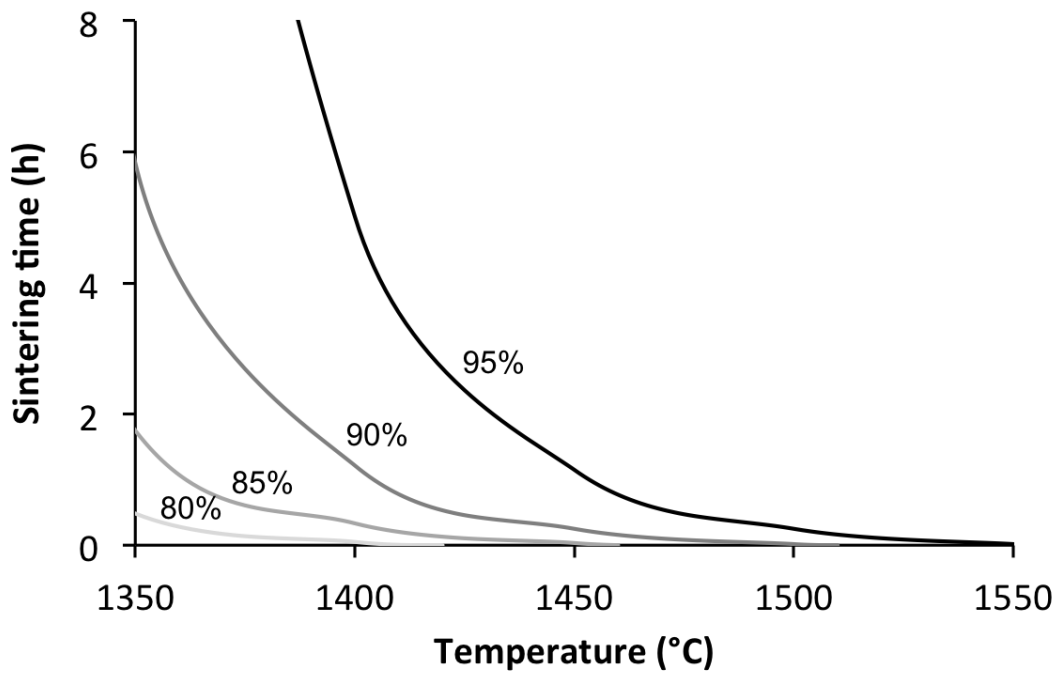


**Figure 6.11.** Equivalent time/temperature diagram for CT3000 LS SG samples prepared by non-aqueous slip casting heated at 10°C/min. The contours may be used to predict heat treatments requirements to achieve a desired density.

# Chapter 7 |

# Summary and Future Work

## 7.1 Summary

The goal of this work was to gain fundamental understanding on how powder chemistry of commercial Bayer alumina affects densification, microstructural evolution, and sintering mechanisms. A large number of investigations has dealt with the effect of impurities and dopants on the sintering of ultrahigh purity alumina. However, there is little research about the effects of impurities that are characteristic of Bayer alumina, such as Na<sub>2</sub>O, specifically in the presence of other impurities and dopants that are known to affect sintering of alumina, such as SiO<sub>2</sub> and MgO. This work systematically investigated cross effects of some impurities and dopants that are characteristic to commercial grade Bayer alumina on densification, microstructural evolution, and fundamental sintering mechanisms.

### 7.1.1 The Effects of Na<sub>2</sub>O and SiO<sub>2</sub> on Liquid Phase Sintering of Bayer Al<sub>2</sub>O<sub>3</sub>

To investigate the effect of Na<sub>2</sub>O and SiO<sub>2</sub> on sintering of MgO-free Bayer alumina samples with up to 1029 and 603 ppm, respectively, were prepared. Dilatometry and sintering kinetics experiments showed that increasing Na<sub>2</sub>O concentrations led to an increased onset temperature of sintering and results in a lower density up to final stage sintering, but no difference in relative density for sintering times of 3 h or longer at 1525°C was observed. Increasing SiO<sub>2</sub> concentrations leads to a significant retardation of densification starting at ~1250°C and after 8 h at 1525°C samples with 603 ppm SiO<sub>2</sub> have 4% lower density than samples with 103 ppm

$\text{SiO}_2$ . In samples with increased  $\text{SiO}_2$  concentrations, such as 603 ppm, the addition of  $\text{Na}_2\text{O}$  increases the density by 1 - 2.5% compared to samples with low  $\text{Na}_2\text{O}$  concentrations.

The observed sintering behavior was explained by a liquid phase sintering model, where the viscosity of the liquid grain boundary phase, and therefore the diffusion coefficient, are determined by the chemical composition of the liquid grain boundary phase. The viscosity of the grain boundary phase is 2 orders of magnitude lower for samples with high  $\text{Na}_2\text{O}/\text{SiO}_2$  ratios, e.g. 0.9 for samples with 529/603 ppm  $\text{Na}_2\text{O}/\text{SiO}_2$ , than the viscosity of the liquid grain boundary phase of samples with low  $\text{Na}_2\text{O}/\text{SiO}_2$  ratios, e.g. 0.1 for samples with 29/603 ppm  $\text{Na}_2\text{O}/\text{SiO}_2$ . Additionally, the solubility of  $\text{Al}_2\text{O}_3$  in the liquid grain boundary phase is increased for samples with higher  $\text{Na}_2\text{O}$  concentrations. Both of these factors lead to enhanced densification in samples with higher  $\text{Na}_2\text{O}/\text{SiO}_2$  ratios. It is concluded that Bayer  $\text{Al}_2\text{O}_3$  densification is controlled by the  $\text{Na}_2\text{O}$  to  $\text{SiO}_2$  ratio.

### **7.1.2 Powder Chemistry Effects on the Sintering of MgO-doped Specialty $\text{Al}_2\text{O}_3$**

$\text{MgO}$  is typically added to commercial alumina powder due to its beneficial effect on sintering. To identify the mechanisms responsible for this beneficial effect, 380 ppm MgO-doped Bayer alumina powder with chemical and physical characteristics similar to the MgO-free powder studied in the first part of this dissertation was used and doped to similar chemistries as the MgO-free Bayer alumina. Dilatometry measurements and sintering kinetics of the MgO-free powder and the MgO-doped powder were compared to identify differences in sintering behavior as a result of MgO-doping. In both powders higher  $\text{SiO}_2$  concentrations retard densification significantly, however, this effect is less severe in the MgO-doped powder than in the MgO-free powder. For example the addition of 500 ppm  $\text{SiO}_2$  results in 4% lower relative density in MgO-free powder samples after sintering at 1525°C for 8 h, but only 2% lower relative density in MgO-doped powder samples. While the  $\text{Na}_2\text{O}/\text{SiO}_2$  ratio has a similar effect in both powders during initial and intermediate stage sintering, i.e. higher  $\text{Na}_2\text{O}/\text{SiO}_2$  ratios increase densification, no effect of the  $\text{Na}_2\text{O}/\text{SiO}_2$  ratio was observed for 380 ppm MgO-doped Bayer alumina samples

during final stage sintering at densities  $\geq 92\%$ .

High resolution TEM showed the presence of a liquid phase in the grain boundaries of MgO-free powder samples and in MgO-doped powder samples during intermediate stage sintering ( $< 92\%$ ). During final stage ( $> 92\%$ ) sintering the thickness of the grain boundary phase in the MgO-doped powder samples is significantly reduced compared to MgO-free powder. EDS analysis showed that MgO and SiO<sub>2</sub> have an increased co-solubility in the alumina lattice where Mg<sup>2+</sup> and Si<sup>4+</sup> compensate for each size and charge difference relative to Al<sup>3+</sup> in the alumina lattice. The thermodynamic stability of such a mechanism was shown by DFT-based first-principles calculations. The reduced amount of SiO<sub>2</sub> on the grain boundaries of MgO-doped alumina leads to enhanced densification compared to MgO-free alumina because SiO<sub>2</sub> has been shown to retard densification.

### **7.1.3 Dynamic development of nanometer scale grain boundaries during liquid phase sintering**

It was shown that grain boundary chemistry and structure drastically affect fundamental sintering mechanisms and, therefore, it is crucial to understand how grain boundaries change during densification. A physical model was developed to describe the dynamic development of grain boundaries in Bayer alumina during densification. The liquid glass phase concentration that forms during sintering is a function of powder chemistry and the glass phase concentration changes during densification because the temperature of the sample changes during heating. The liquid glass phase initially accumulates in the particle contacts due to capillarity, and then the distribution of the glass phase changes during sintering due to the formation of grain boundaries and grain growth, which leads to the observed dynamic change in grain boundary thickness. The model predicts that the grain boundary thickness can be governed by either the glass phase concentration or by an equilibrium grain boundary thickness. If sufficient glass phase is present to form an intergranular film of equilibrium thickness, then the balance between attractive and repulsive colloidal forces determines the grain boundary thickness, and for grain boundary films  $> 1$  nm the main contributions to this force balance are attractive capillary forces and repulsive structural disjoining forces.

Changes in Na<sub>2</sub>O/SiO<sub>2</sub> ratio and/or the addition of MgO changes the concentra-

tion of liquid phase in the sample and the interparticle force balance, and, therefore, changes the grain boundary thickness. It was shown that grain boundary thicknesses measured by high resolution TEM agree well with predicted film thicknesses as a function of powder chemistry.

#### 7.1.4 Second phase formation in Bayer alumina

Bayer alumina has higher impurity concentrations than ultrahigh purity aluminas, which makes these powders more prone to second phase formation, and thus the conditions of formation and the formation process of second phases in Bayer alumina were explored as a function of powder chemistry. XRD showed that  $\beta$ -Al<sub>2</sub>O<sub>3</sub> was the only second phase that forms for the range of chemistries explored in this dissertation. No  $\beta$ -Al<sub>2</sub>O<sub>3</sub> was observed in samples with low Na<sub>2</sub>O and MgO concentrations such as 29 and 2 ppm, respectively. Only a small number of  $\beta$ -Al<sub>2</sub>O<sub>3</sub> grains form when the Na<sub>2</sub>O concentration is  $\leq$ 529 ppm. However, there was a significant increase in the amount of  $\beta$ -Al<sub>2</sub>O<sub>3</sub> observed when the Na<sub>2</sub>O concentration was increased to 1029 ppm. Increasing the MgO concentration in samples with 29 ppm Na<sub>2</sub>O increases the number of  $\beta$ -Al<sub>2</sub>O<sub>3</sub> grains up to 502 ppm, but no further increase in number density of  $\beta$ -Al<sub>2</sub>O<sub>3</sub> grains is observed when the MgO concentration is increased to 1002 ppm. In general, increasing Na<sub>2</sub>O and MgO concentrations leads to an increase in number density and a decrease in  $\beta$ -Al<sub>2</sub>O<sub>3</sub> grain size, but increasing the SiO<sub>2</sub> concentration results in a decrease in number density and increase in  $\beta$ -Al<sub>2</sub>O<sub>3</sub> grain size.

It was shown that SiO<sub>2</sub> and Na<sub>2</sub>O form a liquid grain boundary phase during sintering of alumina, and the amount of  $\beta$ -Al<sub>2</sub>O<sub>3</sub> that forms is determined by the Na<sub>2</sub>O-supersaturation of the liquid grain boundary phase, i.e. the Na<sub>2</sub>O/SiO<sub>2</sub> ratio in the sample. Formation kinetics showed that the majority of beta alumina form within the first hour at 1525°C, which is within the same time as when the grain boundary thickness decreases due to the proposed MgO- and SiO<sub>2</sub> co-dissolution mechanism into the alumina grain. It was concluded that MgO increases the amount of  $\beta$ -Al<sub>2</sub>O<sub>3</sub> because the co-dissolution of MgO and SiO<sub>2</sub> into the alumina grain lowers the SiO<sub>2</sub> concentration in the glassy grain boundaries during final stage sintering. As a result, the Na<sub>2</sub>O/SiO<sub>2</sub> ratio in the grain boundaries increases, which leads to a higher Na<sub>2</sub>O-supersaturation and to an enhanced formation of

$\beta$ -Al<sub>2</sub>O<sub>3</sub>.

### 7.1.5 A Critique of Master Sintering Curve Analysis of Sintering Processes

The objective of this work was to explore if the Master Sintering Curve (MSC) approach can be used as a tool to identify powder chemistry effects on the sintering of Bayer alumina in a fundamental, predictive way. MSC analysis results in an apparent activation energy  $Q$  and the MSC itself. It was shown that processing history and powder chemistry drastically affect the value of  $Q$  and the shape of the MSC but no direct correlation was found between powder chemistry and the MSC shape or  $Q$  since changes in powder chemistry can cause complex variations in sintering mechanisms. Likewise, no direct correlation was found between forming technique, the resulting green density, and  $Q$  or the shape of the MSC because factors such as pore size and pore size distribution, which are known to influence densification, are not accounted for in MSC analysis. Finally, the applicability of MSC at high densities (>90%) is limited by changes in microstructural evolution that occur as a function of densification rate, but are not accounted for in MSC analysis.

It was shown that MSC analysis can be a useful tool for predicting the sintering behavior of a specific powder after its  $Q$  and MSC are accurately determined. For example, shrinkage anisotropy has to be accounted for to determine accurate  $Q$  values and MSCs. Under these conditions MSC analysis is only a useful and practical tool to predict sintering behavior, but again fails to analyze fundamental sintering processes or changes that result from differences in chemical or physical variations of the sintering material.

## 7.2 Future work

This work focused on the effects and cross effects of Na<sub>2</sub>O, SiO<sub>2</sub>, and MgO on the sintering of commercial Bayer alumina and is therefore a step towards a fundamental understanding of the interplay of multiple dopants and impurities during sintering of commercial Bayer alumina. Several paths for future research are proposed below.

The effects of additional impurities that can be found in commercial powders,

specifically CaO, should be investigated. Multiple studies have investigated the effect of CaO on the sintering of ultra-high purity alumina, however, it is crucial to consider the presence of other impurities and dopants. The importance of considering the presence of other impurities and dopants was shown in this work; for example, the effect of Na<sub>2</sub>O on the sintering of Bayer alumina strongly depends on the SiO<sub>2</sub> concentration and the Na<sub>2</sub>O/SiO<sub>2</sub> ratio, and the effect of MgO depends on the SiO<sub>2</sub> concentration. Similar relations could exist between CaO and other impurities and dopants, and it is of great interest to identify such effects. Based on the present investigation and literature reports a variety of hypotheses of the effect of CaO on the sintering of Bayer alumina are reasonable. Initial and intermediate stage sintering in Bayer alumina are governed by a liquid phase sintering mechanism, due to the presence of SiO<sub>2</sub>, which forms a siliceous glass phase in the grain boundaries. At these sintering stages Na<sub>2</sub>O and MgO were shown to affect the properties of the liquid grain boundary phase by acting as a network modifier. It is likely that CaO behaves in a similar manner. However, calcium silicate glass melts are known to exhibit liquid-liquid miscibility gaps that are influenced by the MgO, Na<sub>2</sub>O, and Al<sub>2</sub>O<sub>3</sub> concentrations [116]. This suggests that glass phases of different compositions can be present at the same time, which could significantly affect sintering, since diffusion is controlled by viscosity and, therefore, the composition of the liquid phase. Furthermore, different concentrations in CaO can affect second phase formation. For example, CaO by itself forms calcium hexaluminate (CaO·6Al<sub>2</sub>O<sub>3</sub>) in alumina, which can form a solid solution with  $\beta$ -Al<sub>2</sub>O<sub>3</sub> in the high alumina region of the Na<sub>2</sub>O-SiO<sub>2</sub>-CaO-Al<sub>2</sub>O<sub>3</sub> system [49]. Different ratios and concentrations of impurities and dopants might lead to different amounts and types of second phases, and, therefore, the influence of CaO on the formation of second phases should be investigated.

Grain boundaries of ceramics have been extensively researched over the past decades because their structure and chemistry determine sintering mechanisms and many properties of ceramics, such as corrosion, mechanical, and electrical properties. In this work the chemical composition and structure of grain boundaries was investigated to gain insight into sintering mechanisms and to explain the observed sintering behavior. Therefore, samples were quenched from the sintering temperature to room temperature to "freeze" the chemistry and structure at the sintering temperature. However, ceramic parts for most applications are cooled at

much slower rates, which can drastically affect grain boundary structure, thickness, and chemistry, and the grain boundaries investigated in this work may not be representative for grain boundaries in slow cooled Bayer alumina ceramic parts. The influence of cooling rate on the chemistry and structure of grain boundaries of Bayer alumina should be investigated to gain insight into how properties are affected by different powder chemistries and grain boundary characteristics. The development of time-temperature-transformation (TTT) diagrams for grain boundaries [117] as a function of powder chemistry could be a powerful tool to design grain boundaries and tailor the properties of alumina ceramics.

In this dissertation a physical model was developed to predict the dynamic development of grain boundaries during densification. A potential application for such predictions is to determine the applicability of different sintering models, i.e. solid-state sintering or liquid phase sintering. For samples with high SiO<sub>2</sub> concentrations, such as 603 ppm, it was demonstrated that sintering at 1525°C can be analyzed using a liquid phase sintering model, and for samples with low SiO<sub>2</sub> concentrations, such as 103 ppm, the grain boundary structure and chemistry at 1525°C suggests that a solid state sintering model is more appropriate to analyze sintering. However, it was also demonstrated that the structure and chemistry of the grain boundaries are a function of additional parameters, such as temperature, relative density, powder chemistry, and grain size. For example, the grain boundary thickness first decreases and then increases as a function of relative density, which implies that for certain glass phase concentrations there can be a transition from liquid phase sintering to solid state sintering and vice versa. Another example is the effect of MgO on final stage sintering of Bayer alumina. It was shown that during initial and intermediate stages alumina with 582 ppm SiO<sub>2</sub> densifies by a liquid phase sintering mechanism. However, if MgO is present then MgO and SiO<sub>2</sub> form a solid solution in the alumina grains during final stage sintering, which reduces the amount of SiO<sub>2</sub> in the grain boundaries, and, depending on the MgO concentration, sintering should be analyzed using a solid state sintering model. This described mechanism suggests that transitions from liquid phase sintering to solid state sintering and vice versa are possible during densification. It would be interesting to investigate in greater detail the effects of such transitions on the sintering process.

# Bibliography

- [1] ZUO, F., C. CARRY, S. SAUNIER, S. MARINEL, and D. GOEURIOT (2013) “Comparison of the microwave and conventional sintering of alumina: effect of MgO doping and particle size,” *Journal of the American Ceramic Society*, **96**(6), pp. 1732–1737.
- [2] GAVRILOV, K. L., S. J. BENNISON, K. R. MIKESKA, J. M. CHABALA, and R. LEVI-SETTI (1999) “Silica and magnesia dopant distributions in alumina by high-resolution scanning secondary ion mass spectrometry,” *Journal of the American Ceramic Society*, **82**(4), pp. 1001–1008.
- [3] FRUEH, T., E. KUPP, C. COMPSON, J. ATRIA, and G. MESSING (2016) “The effects of Na<sub>2</sub>O and SiO<sub>2</sub> in liquid phase sintering of Bayer Al<sub>2</sub>O<sub>3</sub>,” *Journal of the American Ceramic Society*, **99**(7), pp. 2267–2272.
- [4] KANG, S. J. L. (2004) *Sintering*, Elsevier Butterworth-Heinemann, Oxford.
- [5] COBLE, R. L. (1962), “Transparent alumina and method of preparation,” .
- [6] ——— (1962) “Sintering alumina: effect of atmospheres,” *Journal of the American Ceramic Society*, **45**(3), pp. 123–127.
- [7] ——— (1961) “Sintering crystalline solids,” *Journal of applied physics*, **32**(5), pp. 787–799.
- [8] BENNISON, S. J. and M. P. HARMER (1990) “A history of the role of MgO in the sintering of  $\alpha$ -Al<sub>2</sub>O<sub>3</sub>,” in *Ceramic Transactions 7, Sintering of Advanced Ceramics* (C. A. Handwerker, J. E. Blendell, and W. A. Kaysser, eds.), Am. Ceram. Soc., Westerville, pp. 13–49.
- [9] JORGENSEN, P. J. and J. H. WESTBROOK (1964) “Role of Solute Segregation at Grain Boundaries During Final-Stage Sintering of Alumina,” *Journal of the American Ceramic Society*, **47**(7), pp. 332–338.
- [10] JORGENSEN, P. J. (1965) “Modification of sintering kinetics by solute segregation in Al<sub>2</sub>O<sub>3</sub>,” *Journal of the American Ceramic Society*, **48**(4), pp. 207–210.

- [11] JOHNSON, W. C. and R. L. COBLE (1978) “A Test of the Second-Phase and Impurity-Segregation Models for MgO-Enhanced Densification of Sintered Alumina,” *Journal of the American Ceramic Society*, **61**(3-4), pp. 110–114.
- [12] HEUER, A. H. (1979) “The role of MgO in the sintering of alumina,” *Journal of the American Ceramic Society*, **62**, pp. 317–318.
- [13] BAE, S. I. and S. BAIK (1993) “Determination of critical concentrations of silica and/or calcia for abnormal grain growth in alumina,” *Journal of the American Ceramic Society*, **76**(4), pp. 1065–1067.
- [14] BAE, I.-J. and S. BAIK (1997) “Abnormal grain growth of alumina,” *Journal of the American Ceramic Society*, **56**, pp. 1149–1156.
- [15] BAE, S. I. and S. BAIK (1994) “Critical concentration of MgO for the prevention of abnormal grain growth in alumina,” *Journal of the American Ceramic Society*, **77**(10), pp. 2499–2504.
- [16] HANDWERKER, C. A., P. A. MORRIS, and R. L. COBLE (1989) “Effects of chemical inhomogeneities on grain growth and microstructure in  $\text{Al}_2\text{O}_3$ ,” *Journal of the American Ceramic Society*, **72**(1), pp. 130–136.
- [17] HANSEN, S. C. and D. S. PHILLIPS (1983) “Grain boundary microstructures in a liquid-phase sintered alumina ( $\alpha\text{-Al}_2\text{O}_3$ ),” *Philosophical Magazine A*, **47**(2), pp. 209–234.
- [18] HARMER, M. P. (1984) “Use of solid-solution additives in ceramic processing,” *Advances in ceramics*, **10**, p. 679.
- [19] BATEMAN, C. A., S. J. BENNISON, and M. P. HARMER (1989) “Mechanism for the role of magnesia in the sintering of alumina containing small amounts of a liquid phase,” *Journal of the American Ceramic Society*, **72**(7), pp. 1241–1244.
- [20] SONI, K. K., A. M. THOMPSON, M. P. HARMER, D. B. WILLIAMS, J. M. CHABALA, and R. LEVI-SETTI (1995) “Solute segregation to grain boundaries in MgO-doped alumina,” *Applied physics letters*, **66**(21), pp. 2795–2797.
- [21] BENNISON, S. J. and M. P. HARMER (1983) “Effect of MgO solute on the kinetics of grain growth in  $\text{Al}_2\text{O}_3$ ,” *Journal of the American Ceramic Society*, **66**(5).
- [22] ROY, S. K. and R. L. COBLE (1968) “Solubilities of magnesia, titania, and magnesium titanate in aluminum oxide,” *Journal of the American Ceramic society*, **51**(1), pp. 1–6.

- [23] DILLON, S. J. and M. P. HARMER (2007) "Multiple grain boundary transitions in ceramics: a case study of alumina," *Acta Materialia*, **55**(15), pp. 5247–5254.
- [24] DILLON, S. J., M. P. HARMER, and G. S. ROHRER (2010) "Influence of interface energies on solute partitioning mechanisms in doped aluminas," *Acta Materialia*, **58**(15), pp. 5097–5108.
- [25] DILLON, S. J., M. TANG, W. C. CARTER, and M. P. HARMER (2007) "Complexion : A new concept for kinetic engineering in materials science," **55**, pp. 6208–6218.
- [26] CANTWELL, P. R., M. TANG, S. J. DILLON, J. LUO, G. S. ROHRER, and M. P. HARMER (2014) "Grain boundary complexions," *Acta Materialia*, **62**, pp. 1–48.
- [27] DILLON, S. J. and M. P. HARMER (2008) "Demystifying the role of sintering additives with "complexion"," *Journal of the European Ceramic Society*, **28**(7), pp. 1485–1493.
- [28] KANG, S.-J. L., M.-G. LEE, and S.-M. AN (2009) "Microstructural Evolution During Sintering with Control of the Interface Structure," *Journal of the American Ceramic Society*, **92**(7), pp. 1464–1471.
- [29] KANG, S.-J. L., S.-Y. KO, and S.-Y. MOON (2016) "Mixed control of boundary migration and the principle of microstructural evolution," *Journal of the Ceramic Society of Japan*, **124**(4), pp. 259–267.
- [30] JO, W., D.-Y. KIM, and N.-M. HWANG (2006) "Effect of Interface Structure on the Microstructural Evolution of Ceramics," *Journal of the American Ceramic Society*, **89**(8), pp. 2369–2380.
- [31] COMPSON, C., N. ROSENBERGER, and M. SPREIJ (2013) "The Effect of SiO<sub>2</sub> and Na<sub>2</sub>O content on the Sintering Behavior of Calcined Specialty Aluminas for the Ceramics Industry," *CFI-Ceramic Forum International*, **90**(3), pp. E17–E22.
- [32] SUMITA, S. and H. K. BOWEN (1988) "Effects of foreign oxides on grain growth and densification of sintered Al<sub>2</sub>O<sub>3</sub>," *Ceramic Powder Science II. Transactions*, **1**, pp. 840–847.
- [33] SMOTHERS, W. J. and H. J. REYNOLDS (1954) "Sintering and grain growth of alumina," *Journal of the American Ceramic Society*, **37**(12), pp. 588–595.
- [34] CAHOON, H. P. and C. J. CHRISTENSEN (1956) "Sintering and Grain Growth of  $\alpha$ -Alumina," *Journal of the American Ceramic Society*, **39**(10), pp. 337–344.

- [35] LOUET, N., M. GONON, and G. FANTOZZI (2005) "Influence of the amount of Na<sub>2</sub>O and SiO<sub>2</sub> on the sintering behavior and on the microstructural evolution of a Bayer alumina powder," *Ceramics International*, **31**(7), pp. 981–987.
- [36] *ASTM B962-15, Standard test methods for density of compacted or sintered powder metallurgy (PM) products using Archimedes' principle, ASTM International, West Conshohocken, PA, 2015, www.astm.org.*
- [37] *ASTM E112-13, Standard test methods for determining average grain size, ASTM International, West Conshohocken, PA, 2013, www.astm.org.*
- [38] JUDD, M., B. PLUNKETT, and M. POPE (1974) "The thermal decomposition of calcium, sodium, silver and copper (II) acetates," *Journal of Thermal Analysis and Calorimetry*, **6**(5), pp. 555–563.
- [39] LAMBOTTE, G. and P. CHARTRAND (2013) "Thermodynamic modeling of the (Al<sub>2</sub>O<sub>3</sub>+Na<sub>2</sub>O), (Al<sub>2</sub>O<sub>3</sub>+Na<sub>2</sub>O+SiO<sub>2</sub>), and (Al<sub>2</sub>O<sub>3</sub>+Na<sub>2</sub>O+AlF<sub>3</sub>+NaF) systems," *The Journal of Chemical Thermodynamics*, **57**, pp. 306–334.
- [40] BROWNMILLER, L. and R. BOGUE (1932) "System CaO-Na<sub>2</sub>O-Al<sub>2</sub>O<sub>3</sub>," *Bureau of Standards Journal of Research*, **8**, pp. 289–307.
- [41] PABLO-GALAN, L. and W. R. FOSTER (1959) "Investigation of Role of Beta Alumina in the System Na<sub>2</sub>O-Al<sub>2</sub>O<sub>3</sub>-SiO<sub>2</sub>," *Journal of the American Ceramic Society*, **42**(10), pp. 491–498.
- [42] RANKIN, G. A. and H. E. MERWIN (1916) "THE TERNARY SYSTEM CaO-Al<sub>2</sub>O<sub>3</sub>-MgO." *Journal of the American Chemical Society*, **38**(3), pp. 568–588.
- [43] RIDGWAY, R. R., A. A. KLEIN, and W. J. O'LEARY (1936) "The Preparation and Properties of So-Called "Beta Alumina"," *Transactions of the Electrochemical Society*, **70**(1), pp. 71–88.
- [44] DUNCAN, J. H. and W. E. C. CREYKE (1969) "The formation and stability of  $\beta$ -Al<sub>2</sub>O<sub>3</sub> in  $\alpha$ -Al<sub>2</sub>O<sub>3</sub> Ceramics," *Trans. Brit. Ceram. Soc.*, pp. 137–144.
- [45] SUTORIK, A. C., S. S. NEO, D. R. TREADWELL, and R. M. LAINE (1998) "Synthesis of Ultrafine  $\beta$ "-Alumina Powders via Flame Spray Pyrolysis of Polymeric Precursors," *Journal of the American Ceramic Society*, **81**(6), pp. 1477–1486.
- [46] STEVENS, R. and J. G. P. BINNER (1984) "Structure, properties and production of  $\beta$ -alumina," *Journal of materials science*, **19**(3), pp. 695–715.

- [47] CHRISTIE, J. R., A. J. DARNEll, and D. F. DUSTIN (1978) “Reaction of molten sodium carbonate with aluminum oxide,” *J. Phys. Chem.;(United States)*, **82**(1).
- [48] KUMMER, J. T. (1972) “Beta-alumina electrolytes,” in *Prog. Solid State Chemistry* (H. Reiss and J. O. McCaldin, eds.), 7 Pergamon Press, New York, pp. 141–175.
- [49] VRIES, R. C. and W. L. ROTH (1969) “Critical Evaluation of the Literature Data on Beta Alumina and Related Phases: I, Phase Equilibria and Characterization of Beta Alumina Phases,” *Journal of the American Ceramic Society*, **52**(7), pp. 364–369.
- [50] TERAI, R. and R. HAYAMI (1975) “Ionic diffusion in glasses,” *Journal of Non-Crystalline Solids*, **18**(2), pp. 217–264.
- [51] KWON, O.-H. and G. L. MESSING (1990) “Kinetic Analysis of Solution-Precipitation During Liquid-Phase Sintering of Alumina,” *Journal of the American Ceramic Society*, **73**(2), pp. 275–281.
- [52] ——— (1991) “A theoretical analysis of solution-precipitation controlled densification during liquid phase sintering,” *Acta metallurgica et materialia*, **39**(9), pp. 2059–2068.
- [53] PARK, C. W. and D. Y. YOON (2000) “Effects of SiO<sub>2</sub>, CaO<sub>2</sub>, and MgO additions on the grain growth of alumina,” *Journal of the American Ceramic Society*, **83**(10), pp. 2605–2609.
- [54] DAY, D. E. and G. E. RINDONE (1962) “Properties of soda aluminosilicate glasses: I, refractive index, density, molar refractivity, and infrared absorption spectra,” *Journal of the American Ceramic Society*, **45**(10), pp. 489–496.
- [55] WU, G., E. YAZHENSKIKH, K. HACK, and M. MÜLLER (2015) “Viscosity model for oxide melts relevant to fuel slags. Part 2: The system SiO<sub>2</sub>-Al<sub>2</sub>O<sub>3</sub>-CaO-MgO-Na<sub>2</sub>O-K<sub>2</sub>O,” *Fuel Processing Technology*, **138**, pp. 520–533.
- [56] POPOVIC, A., L. BENCZE, J. KORUZA, B. MALIC, and M. KOSEC (2012) “Knudsen effusion mass spectrometric approach to the thermodynamics of Na<sub>2</sub>O-Nb<sub>2</sub>O<sub>5</sub> system,” *International Journal of Mass Spectrometry*, **309**, pp. 70–78.
- [57] GALLUP, J. (1935) “The transformation of aluminum oxide from the beta to the alpha form,” *Journal of the American Ceramic Society*, **18**(1-12), pp. 144–148.

- [58] BAE, S. I. and S. BAIK (1993) “Sintering and grain growth of ultrapure alumina,” *Journal of Materials Science*, **28**(15), pp. 4197–4204.
- [59] PARK, C. W. and D. Y. YOON (2000) “Grain growth of alumina,” **609**(3), pp. 2605–2609.
- [60] MAO, H., O. FABRICHNAYA, M. SELLEBY, and B. SUNDMAN (2005) “Thermodynamic assessment of the MgO-Al<sub>2</sub>O<sub>3</sub>-SiO<sub>2</sub> system,” *Journal of Materials Research*, **20**(04), pp. 975–986.
- [61] SHANG, S., Y. WANG, D. KIM, and Z.-K. LIU (2010) “First-principles thermodynamics from phonon and Debye model: Application to Ni and Ni<sub>3</sub>Al,” *Computational Materials Science*, **47**(4), pp. 1040–1048.
- [62] WANG, Y., Z.-K. LIU, and L.-Q. CHEN (2004) “Thermodynamic properties of Al, Ni, NiAl, and Ni<sub>3</sub>Al from first-principles calculations,” *Acta Materialia*, **52**(9), pp. 2665–2671.
- [63] LIU, X. L., B. K. VANLEEUWEN, S. SHANG, Y. DU, and Z.-K. LIU (2015) “On the scaling factor in Debye-Grüneisen model: A case study of the Mg-Zn binary system,” *Computational Materials Science*, **98**, pp. 34–41.
- [64] SHANG, S., Y. WANG, and Z.-K. LIU (2007) “First-principles elastic constants of  $\alpha$ - and  $\theta$ -Al<sub>2</sub>O<sub>3</sub>,” *Applied Physics Letters*, **90**(10), pp. 101909–1–101909–3.
- [65] KRESSE, G. and J. FURTHMÜLLER (1996) “Efficiency of ab-initio total energy calculations for metals and semiconductors using a plane-wave basis set,” *Computational Materials Science*, **6**(1), pp. 15–50.
- [66] KRESSE, G. and D. JOUBERT (1999) “From ultrasoft pseudopotentials to the projector augmented-wave method,” *Physical Review B*, **59**(3), pp. 1758–1775.
- [67] BLÖCHL, P. (1994) “Projector augmented-wave method,” *Physical Review B*, **50**(24), p. 17953.
- [68] PERDEW, J. and Y. WANG (1992) “Accurate and simple analytic representation of the electron-gas correlation energy,” *Physical Review B*, **45**(23), p. 13244.
- [69] MONKHORST, H. and J. PACK (1976) “Special points for Brillouin-zone integrations,” *Physical Review B*, **13**(12), pp. 5188–5192.
- [70] ATKINSON, K. J. W., R. W. GRIMES, M. R. LEVY, Z. L. COULL, and T. ENGLISH (2003) “Accommodation of impurities in  $\alpha$ -Al<sub>2</sub>O<sub>3</sub>,  $\alpha$ -Cr<sub>2</sub>O<sub>3</sub> and  $\alpha$ -Fe<sub>2</sub>O<sub>3</sub>,” *Journal of the European Ceramic Society*, **23**(16), pp. 3059–3070.

- [71] GRIMES, R. W. (1994) “Solution of MgO, CaO, and TiO<sub>2</sub> in  $\alpha$ -Al<sub>2</sub>O<sub>3</sub>,” *Journal of the American Ceramic Society*, **77**(2), pp. 378–384.
- [72] LAGERLÖF, K. P. D. and R. W. GRIMES (1998) “The defect chemistry of sapphire ( $\alpha$ -Al<sub>2</sub>O<sub>3</sub>),” *Acta materialia*, **46**(16), pp. 5689–5700.
- [73] XIANG, X., G. ZHANG, X. WANG, T. TANG, and Y. SHI (2015) “A new perspective on the process of intrinsic point defects in  $\alpha$ -Al<sub>2</sub>O<sub>3</sub>,” *Physical Chemistry Chemical Physics*, **17**(43), pp. 29134–29141.
- [74] SARSAM, J., M. W. FINNIS, and P. TANGNEY (2013) “Atomistic force field for alumina fit to density functional theory,” *The Journal of chemical physics*, **139**(20), p. 204704.
- [75] SUBRAMANIAM, A., C. T. KOCH, R. M. CANNON, and M. RÜHLE (2006) “Intergranular glassy films: An overview,” *Materials Science and Engineering A*, **422**(1-2), pp. 3–18.
- [76] LOUET, N., H. REVERON, and G. FANTOZZI (2008) “Sintering behaviour and microstructural evolution of ultrapure  $\alpha$ -alumina containing low amounts of SiO<sub>2</sub>,” *Journal of the European Ceramic Society*, **28**, pp. 205–215.
- [77] JAIN, A., S. ONG, G. HAUTIER, W. CHEN, W. RICHARDS, S. DACEK, S. CHOLIA, D. GUNTER, D. SKINNER, and G. CEDER (2013) “The Materials Project: A materials genome approach to accelerating materials innovation,” *Apl Materials*, **1**(1), p. 11002.
- [78] “Materials Project,” .  
URL <http://www.materialsproject.org>
- [79] GRAHAM, J. (1960) “Lattice spacings and colour in the system alumina - chromic oxide,” *Journal of Physics and Chemistry of Solids*, **12**, pp. 349–350.
- [80] BERGERHOFF, G., R. HUNDT, R. SIEVERS, and I. D. BROWN (1983) “The inorganic crystal structure data base,” *Journal of Chemical Information and Computer Sciences*, **23**(2), pp. 66–69.
- [81] KARLSRUHE, F. I. Z., “Inorganic Crystal Structure Database,” .
- [82] RAGHAVAN, V. (2010) “Al-Fe-O (Aluminum-iron-oxygen),” *Journal of Phase Equilibria and Diffusion*, **31**(4), p. 367.
- [83] CLARKE, D. R., T. M. SHAW, A. P. PHILIPSE, and R. G. HORN (1993) “Possible electrical double-layer contribution to the equilibrium thickness of intergranular glass films in polycrystalline ceramics,” *Journal of the American Ceramic Society*, **76**(5), pp. 1201–1204.

- [84] CLARKE, D. R. (1987) “On the equilibrium thickness of intergranular glass phases in ceramic materials,” *Journal of the American Ceramic Society*, **70**(1), pp. 15–22.
- [85] KINGERY, W. D. (2004) “Densification during sintering in the presence of a liquid phase. I. Theory,” *Journal of Applied Physics*, **30** (1959).
- [86] LEE, S.-M. and S.-J. L. KANG (1998) “Theoretical analysis of liquid-phase sintering: Pore filling theory,” *Acta Materialia*, **46**(9), pp. 3191–3202.
- [87] SHAW, T. M. (1986) “Liquid redistribution during liquid-phase sintering,” *Journal of the American Ceramic Society*, **69**(1), pp. 27–34.
- [88] SVOBODA, J., H. RIEDEL, and R. GAEBEL (1996) “A model for liquid phase sintering,” *Acta Materialia*, **44**(8), pp. 3215–3226.
- [89] GERMAN, R. M. (2016) “Sintering trajectories: Description on how density, surface area, and grain size change,” *JOM*, **68**(3), pp. 878–884.
- [90] ISRAELACHVILI, J. (2011) *Intermolecular and Surface Forces*.
- [91] HSIEH, C., H. JAIN, and E. I. KAMITSOS (1996) “Correlation between dielectric constant and chemical structure of sodium silicate glasses,” *Journal of Applied Physics*, **80**(3), pp. 1704–1712.
- [92] LYON, K. (1942) “Calculation of surface tensions of glasses,” *Journal of The American Ceramic Society*, **27**(6), pp. 25–28.
- [93] ZHANG, S. and S. H. GAROFALINI (2005) “Molecular dynamics computer simulations of the interface structure of calcium-alumino-silicate intergranular films between combined basal and prism planes of  $\alpha\text{-Al}_2\text{O}_3$ ,” *Journal of the American Ceramic Society*, **88**(1), pp. 202–209.
- [94] TANAKA, I., H.-J. KLEEBE, M. K. CINIBULK, J. BRULEY, D. R. CLARKE, and M. RÜHLE (1993) “Calcium concentration dependence of the intergranular film thickness in silicon nitride,” *Journal of the American Ceramic Society*, **77**(4), pp. 911–914.
- [95] TOPLIS, M. J., D. B. DINGWELL, and T. LENCI (1997) “Peraluminous viscosity maxima in  $\text{Na}_2\text{O}$   $\text{Al}_2\text{O}_3$   $\text{SiO}_2$  liquids: The role of triclusters in tectosilicate melts,” *Geochimica et Cosmochimica Acta*, **61**(13), pp. 2605–2612.
- [96] LITTON, D. A. and S. H. GAROFALINI (1999) “Atomistic structure of sodium and calcium silicate intergranular films in alumina,” *Journal of Materials Research*, **14**(4), pp. 1418–1429.

- [97] CINIBULK, M. (1995) "Thermal stability of some hexaluminates at 1400°C," *Journal of Materials Science Letters*, **14**, pp. 651–654.
- [98] STILLWELL, C. V. (1926) "The Color of the Ruby," *J. Phys. Chem.*, **30**, pp. 1441–1466.
- [99] RAY, A. K. and E. C. SUBBARAO (1975) "Synthesis of sodium beta and beta" alumina," **10**(6), pp. 583–590.
- [100] UNDERWOOD, E. E. (1972) "The Mathematical Foundations of Quantitative Stereology," in *Stereology and Quantitative Metallography* (G. Pellissier and S. Purdy, eds.), ASTM International, West Conshohocken, pp. 3–38.
- [101] SU, H. and D. L. JOHNSON (1996) "Master Sintering Curve: a practical approach to sintering," *Journal of American Ceramics Society*, **79**(12), pp. 3211 – 3217.
- [102] HANSEN, J. D., R. P. RUSIN, M.-H. TENG, and D. L. JOHNSON (1992) "Combined-Stage Sintering Model," *Journal of the American Ceramic Society*, **75**(5), pp. 1129–1135.
- [103] PARK, S. J., J. M. MARTIN, J. F. GUO, J. L. JOHNSON, and R. M. GERMAN (2006) "Grain Growth Behavior of Tungsten Heavy Alloys Based on the Master Sintering Curve Concept," *Metallurgical and Materials Transactions A*, **37**, pp. 9–16.
- [104] DIANTONIO, C. B., K. G. EWSUK, and D. BENCOE (2005) "Extension of Master Sintering Curve Theory to Organic Decomposition," *Journal of the American Ceramics Society*, **2728**, pp. 2722–2728.
- [105] AGGARWAL, G., S.-J. PARK, I. V. I. SMID, and R. M. GERMAN (2007) "Master Decomposition Curve for Binders Used in Powder Injection Molding," *Metallurgical and Materials Transactions A*, pp. 606–614.
- [106] BLAINE, D. C., S. J. PARK, P. SURI, and R. M. GERMAN (2006) "Application of work-of-sintering concepts in powder metals," *Metallurgical and Materials Transactions A: Physical Metallurgy and Materials Science*, **37**(9), pp. 2827–2835.
- [107] TATAMI, J., Y. SUZUKI, T. WAKIHARA, T. MEGURO, and K. KOMEYA (2006) "Control of Shrinkage during Sintering of Alumina Ceramics Based on Master Sintering Curve Theory," *Key Engineering Materials*, **317-318**, pp. 11–14.
- [108] POUCHLY, V. and K. MACA (2009) "Master sintering curves of two different alumina powder compacts," *Processing and Application of Ceramics*, **3**(4), pp. 177–180.

- [109] AMINZARE, M., F. GOLESTANI-FARD, O. GUILLON, M. MAZAHERI, and H. R. REZAIE (2010) “Sintering behavior of an ultrafine alumina powder shaped by pressure filtration and dry pressing,” *Materials Science and Engineering A*, **527**(16-17), pp. 3807–3812.
- [110] GUILLON, O. and J. LANGER (2010) “Master sintering curve applied to the Field-Assisted Sintering Technique,” *Journal of Materials Science*, **45**(19), pp. 5191–5195.
- [111] SHAO, W. Q., S. O. CHEN, D. LI, H. S. CAO, Y. C. ZHANG, and S. S. ZHANG (2009) “Prediction and control of microstructure evolution for sub-microscale  $\alpha$ -Al<sub>2</sub>O<sub>3</sub> during low-heating-rate sintering based on the master sintering curve theory,” *Journal of the European Ceramic Society*, **29**(1), pp. 201–204.
- [112] HARMER, M. P. and R. J. BROOK (1981) “Fast firing - Microstructural benefits,” *Trans. Brit. Ceram. Soc.*, **80**, p. 147.
- [113] WANG, S.-Y. and M.-H. TENG (2010) “Why a master sintering curve model can be applied to the sintering of nano-sized particles ?” *Journal of Alloys and Compounds*, **504**, pp. S336–S339.
- [114] REITERER, M. W. and K. G. EWSUK (2009) “An Analysis of Four Different Approaches to Predict and Control Sintering,” *Journal of the American Ceramic Society*, **92**, pp. 1419–1426.
- [115] MACA, K., V. POUCHLÝ, K. BODIŠOVÁ, P. ŠVANČÁREK, and D. GALUSEK (2014) “Densification of fine-grained alumina ceramics doped by magnesia, yttria and zirconia evaluated by two different sintering models,” *Journal of the European Ceramic Society*, **34**(16), pp. 4363–4372.
- [116] KINGERY, W. D., P. B. VANDIVER, I.-W. HUANG, and Y.-M. CHIANG (1983) “Liquid-liquid immiscibility and phase separation in the quaternary systems Ka<sub>2</sub>O-Al<sub>2</sub>O<sub>3</sub>-CaO-SiO<sub>2</sub> and Na<sub>2</sub>O-Al<sub>2</sub>O<sub>3</sub>-CaO-SiO<sub>2</sub>,” *Journal of Non-Crystalline Solids*, **54**, pp. 163–171.
- [117] CANTWELL, P. R., S. MA, S. A. BOJARSKI, G. S. ROHRER, and M. P. HARMER (2016) “Expanding time temperature-transformation (TTT) diagrams to interfaces: A new approach for grain boundary engineering,” *Acta Materialia*, **106**, pp. 78–86.

## Vita

### Tobias Frueh

Tobias Frueh was born in Ellwangen/Jagst, Germany in 1990 and was raised in Ammelbruch, Germany. Tobias received his Bachelor of Science degree in Nanoscience and Technology in May 2013 and his Master of Science degree in Materials Science and Engineering in January 2015, both from the University of Erlangen-Nuremberg, Germany. During his Masters education, he studied for one year at The Pennsylvania State University, USA to conduct the research for his Masters Thesis and was co-advised by Professor Andreas Roosen and Professor Gary Messing. After completing his Master of Science degree Tobias continued his graduate studies at The Pennsylvania State University and was advised by Professor Gary L. Messing. After graduation, Tobias joined Almatis GmbH in Ludwigshafen, Germany as Application and Market Development Engineer.

#### List of Publications:

- Tobias Frueh, Elizabeth R. Kupp, Charles Compson, Joe Atria, Nils Rosenberger and Gary L. Messing, "Modal interpretation of Sintering Kinetics Based on Dilatometry," chi/Ber. DKG, 92, E1-4 (2015).
- Tobias Frueh, Elizabeth R. Kupp, Charles Compson, Joe Atria and Gary L. Messing, "The Effect of Na<sub>2</sub>O and SiO<sub>2</sub> on Liquid Phase Sintering of Bayer Al<sub>2</sub>O<sub>3</sub>," J. Am. Ceram. Soc., 99, 2267-2272 (2016).
- Gary L. Messing, Stephen Poterala, Yunfei Chang, Tobias Frueh, Elizabeth R. Kupp, Beecher H. Watson III, Rebecca L. Walton, Michael J. Brova, Anna-Katharina Hofer, Raul Bermejo, Richard J. Meyer, "Texture-engineered ceramics - Property enhancements through crystallographic tailoring" Journal of Materials Research, <https://doi.org/10.1557/jmr.2017.207> (2017).
- Tobias Frueh, Cassie Marker, Elizabeth R. Kupp, Charles Compson, Joe Atria, Jennifer L. Gray, Zi-Kui Liu, and Gary L. Messing, "Powder Chemistry Effects on the Sintering of MgO-doped Specialty Al<sub>2</sub>O<sub>3</sub>," accepted in J. Am. Ceram. Soc.
- Tobias Frueh, I. O. Ozer, S. F. Poterala, Elizabeth R. Kupp, Charles Compson, Joe Atria and Gary L. Messing, "A Critique of Master Sintering Curve Analysis of Sintering Processes," submitted for publication.
- Tobias Frueh, Elizabeth R. Kupp, Charles Compson, Joe Atria, and Gary L. Messing, "Dynamic development of nanometer scale grain boundaries during liquid phase sintering," preparing for submission.
- Tobias Frueh, Elizabeth R. Kupp, Charles Compson, Joe Atria, and Gary L. Messing, "Second phase formation in Bayer alumina," preparing for submission.